

# Neutronics Experiments and Analysis Related to Strong Moderation Heterogeneity in LWRs

THÈSE N° 5284 (2012)

PRÉSENTÉE LE 9 MARS 2012

À LA FACULTÉ DES SCIENCES DE BASE

LABORATOIRE DE PHYSIQUE DES RÉACTEURS ET DE COMPORTEMENT DES SYSTÈMES

PROGRAMME DOCTORAL EN PHYSIQUE

ÉCOLE POLYTECHNIQUE FÉDÉRALE DE LAUSANNE

POUR L'OBTENTION DU GRADE DE DOCTEUR ÈS SCIENCES

PAR

**Dominik Rätz**

acceptée sur proposition du jury:

Prof. O. Schneider, président du jury

Prof. R. Chawla, directeur de thèse

Dr F. Jatuff, rapporteur

Dr G. Perret, rapporteur

Prof. G. Rimpault, rapporteur



ÉCOLE POLYTECHNIQUE  
FÉDÉRALE DE LAUSANNE

Suisse  
2012



for Regula, Lia, and Anina





# Abstract

The Supercritical-Water-Cooled Reactor (SCWR) is the Generation IV reactor concept most closely related to current light water reactors (LWRs). The SCWR builds on the vast experience with today's LWRs and supercritical coal-fired power plants. Water at supercritical state is used as moderator and coolant, and reaches a temperature of about 500 °C at the core outlet, which enables a much higher thermal efficiency ( $\sim 44\%$ ) than possible with current-day LWRs.

In the operating range of an SCWR, the supercritical water density can become as low as one seventh of the density of water at room temperature. In order to ensure a thermal neutron spectrum, large moderator regions are introduced into the fuel assembly designs, resulting in lattices with strong moderation heterogeneity. As such, the neutronics of these assemblies differs significantly from that of standard LWRs, and lies outside the validated domain of reactor physics codes. Previous comparisons between the deterministic code CASMO-4 and reference calculations carried out with the Monte Carlo code MCNP4C showed large differences in calculated pin-wise reaction rate distributions in perturbed SCWR lattices. The experimental validation of standard reactor physics codes for SCWR-representative neutronics conditions is thus clearly of key importance for the further development of this technology. The goal of this thesis is to provide an experimental database for such validation and to assess the level of performance of current-day codes for SCWR analysis.

An SCWR-like fuel lattice, based on a Japanese assembly design proposal from 2001, has been investigated in the PROTEUS zero-power research reactor at the Paul Scherrer Institute. Measurements have been carried out on the unperturbed test lattice, as also on six other PROTEUS configurations corresponding to different types of perturbations of the reference lattice. The investigated perturbations include control rod related effects, moderator density changes, and the replacement of a fuel pin with gadolinium-poisoned fuel. For each experimental configuration, pin-wise distributions of the total fission rate ( $F_{\text{tot}}$ ) and the  $^{238}\text{U}$  capture rate ( $C_8$ ), as well as of their ratio ( $C_8/F_{\text{tot}}$ ), have been obtained across the assembly and compared to computed values. The neutronics codes used for the calculations are the LWR assembly code CASMO-4E and the Monte Carlo code MCNPX. Additionally, the reactivity effects of removing individual pins from the unperturbed SCWR-like lattice have been measured and compared to predictions obtained using the two codes.

The pin-wise reaction rate distributions predicted with MCNPX have been found to agree within two standard deviations with the measured values for the unperturbed, as well as all the perturbed, configurations. The  $1\sigma$  uncertainty was in the order of 0.4%, 0.8%, and 2.2% for  $F_{\text{tot}}$ ,  $C_8$ , and  $C_8/F_{\text{tot}}$ , respectively. MCNPX could thus be validated for the various SCWR-like conditions investigated and has, in turn, been used to validate CASMO-4E on simplified geometries. For

---

the latter purpose, the unperturbed and perturbed SCWR-like lattices were modeled as reflected assemblies, and reaction rate distributions predicted with the two codes were compared. For the unperturbed lattice and for the configurations with local perturbations of the neutron absorption, the agreement between the codes was within  $\sim 1\%$  for all reaction rates. However, for lattices with locally perturbed moderation conditions, CASMO-4E was initially found to overestimate the reaction rates in the vicinity of the perturbations by up to 5%. The discrepancies were identified as resulting from the default leakage treatment in CASMO-4E, which applies a  $DB^2$  correction in a homogenized sense across the lattice. In this way, cases with a global leakage gradient were not being treated properly. Usage of the optional input card BZ2, which allows a region-wise leakage treatment, resolved this problem, and the codes then agreed mostly within 1% for all the configurations.

The pin removal worth measurements in the unperturbed SCWR-like lattice have provided integral data complementary to the reaction rate distributions. MCNPX results were found to agree with experiment within the statistical uncertainty of typically  $\sim 10\%$  ( $1\sigma$ ). The comparison of reflected-assembly results from MCNPX and CASMO-4E yielded significant differences in the calculated pin removal worths (up to  $4.3\sigma$ ). A decomposition analysis of these differences has indicated that the discrepancies, especially for the better moderated pin positions, are linked to the calculation of the additional moderator effect caused by the pin removal.

Finally, the transferability of the code validation, carried out under the PROTEUS experimental conditions, to the most recently proposed SCWR assembly designs has been assessed. Since, under power-reactor conditions, the moderator and coolant water densities are considerably lower in the proposed SCWR assemblies than that in the PROTEUS test lattices, their neutron spectra are much harder. Assembly-averaged values of the integral parameters  $C_8/F_{\text{tot}}$  and  $F_8/F_{\text{tot}}$  have been found to be as much as 65% and 80% higher, respectively, than for the PROTEUS reference lattice. However, the agreement between CASMO-4E and MCNPX predictions for the proposed SCWR assembly designs is still very good, indicating that the accuracy of the deterministic calculations does not deteriorate markedly when considering these new designs under power-reactor conditions.

**Keywords:** SCWR, HPLWR, code validation, neutronics, lattice physics, moderation heterogeneity, CASMO, MCNPX, PROTEUS, reaction rates, reactivity worths

# Kurzfassung

Der Superkritische-Wasser-Gekühlte Reaktor (SCWR) ist dasjenige Generation IV Reaktorkonzept, das den heutigen Leichtwasserreaktoren (LWRs) am ähnlichsten ist. Der SCWR basiert auf der grossen Erfahrung mit modernen LWRs und superkritischen Kohlekraftwerken. Als Kühlmittel und Moderator wird Wasser in superkritischem Zustand verwendet. Es erreicht Temperaturen von zirka 500 °C am Reaktorausgang, was einen erheblich höheren Wirkungsgrad ( $\sim 44\%$ ) ermöglicht, als mit den heutigen LWRs.

Die Wasserdichte kann im Betriebsbereich eines SCWR auf einen Siebtel der Dichte bei Raumtemperatur sinken. Um ein thermisches Neutronenspektrum zu gewährleisten, müssen grosse Moderatorzonen im Brennelement untergebracht werden, was in diesem zu grossen Heterogenitäten der Neutronenmoderation führt. Aus diesem Grund unterscheidet sich die Neutronik eines SCWR-Brennelements deutlich von derjenigen eines LWR-Brennelements und liegt ausserhalb der validierten Domäne von Reaktorphysik-Rechenprogrammen. Frühere Vergleiche zwischen dem deterministischen Rechenprogramm CASMO-4 und Referenzrechnungen, die mit dem Monte Carlo Programm MCNP4C durchgeführt wurden, zeigten grosse Unterschiede in den berechneten Werten der pinweisen Reaktionsratenverteilungen in gestörten SCWR Gittern. Die experimentelle Validierung von gewöhnlichen Reaktorphysik-Rechenprogrammen unter SCWR-repräsentativen Zuständen ist daher von zentraler Bedeutung für die Weiterentwicklung dieser Technologie. Das Ziel dieser Doktorarbeit ist die Bereitstellung einer experimentellen Datenbank für eine derartige Validierung und die Eruierung des gegenwärtigen Leistungsgrades von modernen Neutronik-Rechenprogrammen für die SCWR Analyse.

Ein SCWR-ähnliches Brennstoffgitter, das auf einem japanischen Designvorschlag eines Brennelements aus dem Jahr 2001 basiert, wurde am Nullleistungs-Versuchsreaktor PROTEUS am Paul Scherrer Institut untersucht. Messungen wurden sowohl am ungestörten Versuchsgitter, als auch an sechs anderen PROTEUS Konfigurationen mit unterschiedlichen Arten von Störungen des Referenzgitters durchgeführt. Die eingebrachten Störungen dienten zur Untersuchung der im Zusammenhang mit Kontrollstäben stehenden Effekte, der Änderungen der Modertordichte und dem Ersetzen eines Brennstabes mit Gadolinium-vergiftetem Brennstoffmaterial. Für jede experimentelle Konfiguration wurden pinweise Verteilungen sowohl der Spaltrate ( $F_{\text{tot}}$ ) und der  $^{238}\text{U}$  Einfangsrate ( $C_8$ ), als auch deren Verhältnis ( $C_8/F_{\text{tot}}$ ) gemessen. Die erhaltenen Resultate wurden anschliessend mit berechneten Werten verglichen. Die verwendeten Neutronik-Rechenprogramme sind das deterministische Programm CASMO-4E, das zur Berechnung von LWR-Brennelementen entwickelt wurde, und das Monte Carlo Programm MCNPX. Zusätzlich wurden die Reaktivitätseffekte, die beim Ausziehen eines einzelnen Brennstabes aus dem ungestörten Referenzgitter auftreten, gemessen und verglichen mit den Vorhersagen von den zwei Rechenprogrammen.

---

Die Berechnungen der pinweisen Verteilungen der Reaktionsraten mit MCNPX stimmten innerhalb von zwei Standardabweichungen mit den gemessenen Werten überein. Dies gilt für den ungestörten Referenzfall, wie auch für jede der sechs gestörten Konfigurationen. Die  $1\sigma$ -Unsicherheit lag bei 0.4%, 0.8% und 2.2% entsprechend für  $F_{\text{tot}}$ ,  $C_8$  und  $C_8/F_{\text{tot}}$ . Demzufolge konnte MCNPX für die untersuchten SCWR-ähnlichen Bedingungen validiert werden und wurde anschliessend für die Validierung von CASMO-4E für vereinfachte Geometrien verwendet. Um Letzteres zu tun, wurden das ungestörte und sämtliche gestörten SCWR-ähnlichen Gitter als reflektierte Brennelement modelliert und die mit CASMO-4E und MCNPX berechneten Werte für die Reaktionsratenverteilungen miteinander verglichen. Für das ungestörte Gitter und für die Konfigurationen in denen die Neutronenabsorption lokal gestört wurde, stimmten die Berechnungsprogramme für alle Reaktionsraten innerhalb von  $\sim 1\%$  überein. Für Gitter mit lokal gestörten Moderationsbedingungen wurde aber anfänglich eine Überschätzung der Reaktionsraten nahe der Störungen von bis zu 5% festgestellt. Die Ursache dieser Abweichungen kam von der in CASMO-4E programmierten Standartoption für die Berechnung der Leckage, die eine homogenisierte DB<sup>2</sup> Korrektur über das ganze Brennstoffgitter anwendet. Auf diese Weise werden Fälle mit globalem Leckage-Gradienten nicht korrekt behandelt. Die Verwendung der optionalen Inputkarte BZ2, die eine regionale Behandlung der Leckage erlaubt, hat dieses Problem behoben und die Rechenprogramme zu einem Grad an Übereinstimmung von meist innerhalb 1% gebracht.

Die gemessenen Änderungen der Reaktivität, die beim Ausziehen von einzelnen Brennstäben aus dem Referenzgitter auftreten, haben die experimentelle Datenbank um komplementäre integrale Messungen erweitert. MCNPX Resultate stimmten innerhalb der statistischen Unsicherheit von typischerweise  $\sim 10\%$  ( $1\sigma$ ) mit den Experimenten überein. Der Vergleich der berechneten Werte von CASMO-4E und MCNPX in reflektierter Geometrie ergab signifikante Abweichungen (bis zu  $4.3\sigma$ ). Eine Zerlegungsanalyse dieser Differenzen hat ergeben, dass diese, speziell für besser moderierte Brennstabpositionen, im Zusammenhang mit der Berechnung des zusätzlichen Moderationseffektes durch den ausgezogenen Stab stehen.

Abschliessend wurde die Übertragbarkeit der Validierung der Rechenprogramme, die unter PROTEUS-eigenen experimentellen Bedingungen durchgeführt wurde, auf die aktuell vorgeschlagenen SCWR Brennelementdesigns ermittelt. Da die Kühlmittel- und Moderatorichten unter Leistungsreaktor-Bedingungen in diesen deutlich geringer sind, sind ihre Neutronenspektren entsprechend härter. Auf ein Brennelement bezogene Durchschnittswerte der integralen Parameter  $C_8/F_{\text{tot}}$  und  $F_8/F_{\text{tot}}$  wurden bis zu 65% und 80% höher als im PROTEUS Referenzgitter berechnet. Dennoch ist die Übereinstimmung zwischen CASMO-4E und MCNPX Vorhersagen für die vorgeschlagenen SCWR Brennelementdesigns sehr gut. Dies deutet an, dass sich die Genauigkeit der deterministischen Berechnungen nicht wesentlich verschlechtert, wenn diese neuen Designs unter Leistungsreaktor-Bedingungen betrachtet werden.

**Schlüsselwörter:** SCWR, HPLWR, Validierung, Neutronik, Gitterphysik, Moderationsheterogenität, CASMO, MCNPX, PROTEUS, Reaktionsraten, Reaktivitätswerte

# Contents

<b>Abstract</b>	<b>iii</b>
<b>Kurzfassung</b>	<b>v</b>
<b>Nomenclature</b>	<b>xi</b>
<b>1 Introduction</b>	<b>1</b>
1.1 Current Status of Nuclear Power . . . . .	2
1.1.1 Generation IV . . . . .	4
1.1.2 Situation in Switzerland . . . . .	8
1.2 Importance of Well Validated Computational Tools . . . . .	8
1.3 Scope of the present research . . . . .	9
Bibliography . . . . .	12
<b>2 Thesis Background</b>	<b>13</b>
2.1 The PROTEUS Research Reactor . . . . .	13
2.1.1 General Description and Past Programs . . . . .	13
2.1.2 Multi-Zone Layout of the Reactor . . . . .	15
2.1.3 The LWR-PROTEUS Program . . . . .	18
2.2 Supercritical-Water-Cooled Reactor (SCWR) . . . . .	21
2.2.1 History of SCWR Design . . . . .	22
2.2.1.1 Stage 1: the 1950's and 60's . . . . .	22
2.2.1.2 Stage 2: the 1990's . . . . .	24
2.2.1.3 Stage 3: 2000 Onwards . . . . .	25
2.2.2 Latest Thermal SCWR Designs . . . . .	26
2.2.2.1 The Japanese Design . . . . .	26
2.2.2.2 The European Design . . . . .	29
2.2.2.3 Other SCWR Concepts . . . . .	31
2.2.3 The SCWR-like Lattice in PROTEUS . . . . .	34
Bibliography . . . . .	37
<b>3 Experiments and Measurement Techniques</b>	<b>43</b>
3.1 PROTEUS Test Zone Configurations . . . . .	43
3.1.1 Unperturbed Lattice . . . . .	44
3.1.2 Control-Rod Insertion Effects . . . . .	44
3.1.3 Insertion of Water Tanks . . . . .	46
3.1.4 Removal of the Central Fuel Pin . . . . .	49
3.1.5 Replacement of the Central Pin by Gadolinium-Poisoned Fuel . . . . .	50
3.2 Reaction Rate Measurement Techniques . . . . .	51
3.2.1 The Measurement Principle . . . . .	51
3.2.2 The Gamma Scanning Machine . . . . .	54
3.2.3 Analysis of Obtained Spectra . . . . .	55
3.2.3.1 Corrections . . . . .	56

3.2.3.2	The MATLAB Routine . . . . .	62
3.2.3.3	Uncertainties and Uncertainty Propagation . . . . .	63
3.2.3.4	Choosing Gamma Lines . . . . .	66
3.3	Reactivity Measurements . . . . .	69
3.3.1	Compensation Technique . . . . .	69
3.3.2	Measurement Procedure . . . . .	71
	Bibliography . . . . .	73
<b>4</b>	<b>Neutronics Modeling of the SCWR-Like Lattice</b>	<b>75</b>
4.1	Codes . . . . .	75
4.1.1	MCNPX . . . . .	75
4.1.1.1	Method . . . . .	75
4.1.1.2	KCODE Option . . . . .	76
4.1.1.3	Limitations . . . . .	77
4.1.2	CASMO-4E . . . . .	77
4.1.2.1	Methodology . . . . .	78
4.1.2.2	Limitations . . . . .	81
4.2	Considered Models for the SCWR-Like Test Lattice . . . . .	82
4.3	Validation Strategy . . . . .	87
	Bibliography . . . . .	89
<b>5</b>	<b>Reaction Rate Distributions: Unperturbed Lattice</b>	<b>91</b>
5.1	Characterization of the Test Lattice . . . . .	91
5.2	Verification of Experimental Results . . . . .	95
5.2.1	Reproducibility of Measurements . . . . .	95
5.2.2	Symmetry Check . . . . .	96
5.3	Comparison of MCNPX Whole-Reactor Calculation with Experiment . . . . .	99
5.3.1	Comparison Between Computed and Measured $F_{\text{tot}}$ and $C_8$ Distributions . . . . .	99
5.3.2	Comparison Between Computed and Measured $C_8/F_{\text{tot}}$ Values . . . . .	101
5.4	Comparison Between CASMO-4E and MCNPX . . . . .	104
	Bibliography . . . . .	107
<b>6</b>	<b>Reaction Rate Distributions: Perturbed Lattices</b>	<b>109</b>
6.1	Control Rod Related Perturbations . . . . .	109
6.1.1	Comparison of the Perturbed and Unperturbed Lattices (Reduced Geometry Model Results) . . . . .	110
6.1.2	Comparison of MCNPX Whole-Reactor Calculations with Experiments . . . . .	112
6.1.2.1	Aluminum Rods in the Central Moderator Regions . . . . .	112
6.1.2.2	Steel Rods in the Central Moderator Regions . . . . .	113
6.1.3	Comparison of CASMO-4E and MCNPX Reduced Geometry Models . . . . .	116
6.1.3.1	Aluminum Rods in Central Moderator Regions . . . . .	116
6.1.3.2	Steel Rods in Central Moderator Regions . . . . .	118
6.1.4	Investigation of Discrepancies . . . . .	118
6.2	Moderation Density Variations . . . . .	120
6.2.1	Characterization of the Perturbed Lattices (Reduced Geometry Model Results) . . . . .	120
6.2.2	Comparison of MCNPX Whole-Reactor Calculations with Experiments . . . . .	123
6.2.3	Comparison of CASMO-4E and MCNPX Reduced Geometry Models . . . . .	125
6.3	Removing the Central Pin and Replacing it with Gadolinium-Poisoned Fuel . . . . .	129
6.3.1	Characterization of the Perturbed Lattices (Reduced Geometry Model Results) . . . . .	129
6.3.2	Comparison of MCNPX Whole-Reactor Calculations with Experiments . . . . .	131

6.3.3	Comparison of CASMO-4E and MCNPX Reduced Geometry Models . . .	133
6.4	Chapter Summary . . . . .	139
	Bibliography . . . . .	141
<b>7</b>	<b>Reactivity Effects</b>	<b>143</b>
7.1	Pin Removal Worths in the Unperturbed Configuration . . . . .	144
7.1.1	Measurements and Calculations . . . . .	145
7.1.2	Results . . . . .	146
7.1.2.1	Experimental Values . . . . .	146
7.1.2.2	MCNPX Whole-Reactor Calculations . . . . .	147
7.1.2.3	Reduced Geometry Calculations . . . . .	147
7.1.2.4	Comparison of Reactivity Worth Ratios . . . . .	149
7.1.3	Decomposition of Reactivity Effects . . . . .	150
7.1.3.1	Pin-Wise Decomposition . . . . .	151
7.1.3.2	Decomposition in Terms of Pin Types . . . . .	153
7.2	PROTEUS Whole-Reactor $k_{\text{eff}}$ Values for the Different Configurations . . . . .	161
7.2.1	MCNPX Whole-Reactor $k_{\text{eff}}$ Values for the Critical Configurations . . . . .	162
7.2.2	Inter-Model Comparison of Relative Whole-Reactor $k_{\text{eff}}$ Changes . . . . .	168
	Bibliography . . . . .	171
<b>8</b>	<b>Transferability of the PROTEUS Experiments to SCWR Design</b>	<b>173</b>
8.1	Transferability to Reduced Geometry Calculations . . . . .	174
8.2	Transferability to Different SCWR Assembly Designs . . . . .	176
8.2.1	Integral Parameter Comparison . . . . .	177
8.2.2	Pin-wise Comparisons of Reaction Rates . . . . .	179
8.2.3	Investigation of Reaction Rate Distributions as Calculated by MCNPX . . . . .	180
8.2.4	Further Studies for the Transferability to the European HPLWR Design . . . . .	182
8.2.4.1	Integral Parameter Comparison . . . . .	182
8.2.4.2	Pin-Wise Comparison of Reaction Rates . . . . .	185
8.2.4.3	Investigation of Reaction Rate Distributions as Calculated by MCNPX . . . . .	187
8.2.5	Chapter Summary . . . . .	189
	Bibliography . . . . .	190
<b>9</b>	<b>Conclusions and Recommendations for Future Work</b>	<b>191</b>
9.1	Main Results . . . . .	191
9.1.1	Reaction Rate Distributions in the Unperturbed SCWR-like Lattice . . . . .	192
9.1.2	Reaction Rate Distributions in the Perturbed SCWR-like Lattices . . . . .	193
9.1.3	Fuel Pin Removal Worths in the Unperturbed Lattice . . . . .	195
9.1.4	PROTEUS $k_{\text{eff}}$ Changes for the Different Configurations . . . . .	196
9.1.5	Transferability of the PROTEUS Experiments to SCWR Design . . . . .	196
9.2	Recommendations for Future Work . . . . .	197
9.2.1	New Experiments at the PROTEUS Zero-Power Facility . . . . .	197
9.2.2	Other Aspects . . . . .	199
	Bibliography . . . . .	201
	<b>Appendix A: Reduced Geometry Input Decks for the Unperturbed Configuration</b>	<b>203</b>
A.1	CASMO-4E Input . . . . .	203
A.2	MCNPX Input . . . . .	205
	<b>Acknowledgements</b>	<b>211</b>
	<b>Curriculum Vitæ</b>	<b>213</b>





# Nomenclature

## Abbreviations

ABS	absorptions
ABWR	Advanced Boiling Water Reactor
AECL	Atomic Energy of Canada Limited
AGR	Advanced Gas-cooled Reactor
ANL	Argonne National Laboratory
AR	autorod
ave	average
B&W	Babcock & Wilcox
BOC	beginning of cycle
BWR	boiling water reactor
CANDU	Canadian pressure-tube heavy-water reactor
CAP	captures
CPU	central processing unit
CR	control rod
DNB	departure from nucleate boiling
ENDF/B	Evaluated Nuclear Data File
ENSDF	Evaluated Nuclear Structure Data File
FA	fuel assembly
FIS	fissions
FM	fundamental mode
FSC	fission source
GFR	Gas-cooled Fast Reactor
GIF	Generation IV International Forum
HCLWR	High Conversion Light Water Reactor
HP-Ge	high purity germanium
HPLWR	High Performance Light Water Reactor
HTR	High Temperature Reactor
IT	internal transition
JEFF	Joint Evaluated Fission and Fusion File
KAERI	Korea Atomic Energy Research Institute
LEAK	leakage
LFR	Lead-cooled Fast Reactor
LWR	light water reactor
MCNPX	Monte Carlo N-Particle extended
MOX	mixed oxide
MSR	Molten-Salt Reactor
NU-FIS	productions
pcm	percent mille

ppb	parts per billion
PWR	pressurized water reactor
RIF	region integrated flux
RPI	Renselaer Polytechnic Institute
RPV	reactor pressure vessel
SCOTT-reactor	Supercritical Once-Through Tube reactor
SCWR	Supercritical-Water-Cooled Reactor
SFR	Sodium-cooled Fast Reactor
SPPR	Supercritical Pressure Power Reactor
St	steel
SWFR	Supercritical Water-cooled Fast Reactor
SWR	single water rods
VHTR	Very-High Temperature Reactor

## Symbols

$Abs_{fuel}$	absorptions in the fuel
$Abs_{struc}$	absorptions in structural material
$Abs_{tot}$	total absorption rate
$Abs_{water}$	absorptions in water
$A_x$	attenuation correction factor for $^{235}U$ fissions
$B$	branching ratio
$B^2$	buckling
$B_c^2$	critical buckling
$b_{eff}$	delayed neutron fraction
$C$	Calculation
$C_8$	$^{238}U$ capture rate
$C_8/F_{tot}$	ratio of $^{238}U$ capture rate to total fission rate
$C_{Capt}$	measured count rate (Captures)
$C_{Fiss}$	measured count rate (Fissions)
$D$	dimension
$d$	fraction of the activity coming from the present irradiation
$\Delta$	rate of change
$E$	experiment, energy
$\epsilon, e$	efficiency
$eARU$	equivalent autorod unit
$F_8$	fission rate in $^{238}U$
$F_{tot}$	total fission rate
$k_{eff}$	effective multiplication factor
$k_{inf}$	infinite multiplication factor
$\Lambda$	neutron generation time
$\lambda$	decay constant
$M^2$	migration area
$MWe$	megawatt electric
$MWt$	megawatt thermal
$n$	neutron density
$\nu$	total average number of neutrons born per fission
$\Omega$	solid angle
$p$	power
$P$	neutron population

---

$\Psi$	Spectral index (ratio of neutrons below 4 eV to the total neutron flux)
$p_{1x}$	fraction of atoms that populate state x by decay of state 1
$P/D$	Pitch-to-diameter ratio
$\text{Prod}_{\text{tot}}$	total production rate
p-value	probability of measuring a set of data with worse agreement than the present sample
$\rho$	reactivity
®	registered trademark
$R^2$	coefficient of determination (linear fit)
$r_x$	ratio of fissions in $^{23x}\text{U}$ to total fissions
s	fission source
$\sigma$	standard deviation
$\Sigma_f$	macroscopic fission cross section
$s_i$	fission source in state i
$\Sigma_s$	macroscopic scattering cross section
$\Sigma_t$	total macroscopic cross section
$T_c$	cooling time
$T_i$	irradiation time
$T_m$	measurement time
v	velocity
$x_i$	number of atoms in state i
yc	cumulative fission yield
$\text{Yd}_x$	average activity during the measurement of the fission product emitting $\gamma$ -ray of interest
yi	individual fission yield
z	integrated activity



# 1 Introduction

Nuclear power plants can make an important contribution towards meeting the world's future energy demands. Efforts are being made internationally to develop next-generation nuclear energy systems which fulfill more stringent economic, ecological, safety, and proliferation criteria. Within the Generation IV International Forum (GIF), six promising concepts have been selected for further investigation. Of these concepts, the Supercritical-Water-Cooled Reactor (SCWR) is the one most closely related to the well established technological experience available with conventional Light Water Reactors (LWRs). Water at a supercritical state is used to remove heat from the core, which allows higher working-fluid temperatures to run the turbine. This enhances the thermal efficiency of the power plant from 33% to approximately 44%.

Although this concept has been studied in Japan since the early 1990's [1], there is no consensus yet on key design features, including the optimal layout of the fuel assembly. This is mainly due to the large variation of the density of supercritical water across the core. The density variation leads to a high degree of neutron moderation heterogeneity and makes it difficult to assess reliable values for important parameters such as power peaking factors and reactivity effects of system perturbations. These need to be known to reasonable accuracy in order to further advance the SCWR design process.

Results of modern neutron transport codes, such as the probabilistic MCNPX [2] and the deterministic CASMO-4E [3], agree well for reactor lattices with a regular moderator and fuel distribution. Recent calculations of advanced LWR configurations with large heterogeneities in fuel/moderation conditions representative of SCWR lattices, however, have indicated considerable differences between deterministic and probabilistic codes [4]. There has thus been a growing need for the experimental validation of calculational predictions for such configurations. In the framework of the doctoral thesis, specific investigations are carried out with the explicit goal of studying, both experimentally and analytically, how the basic neutron physics and safety-related integral parameters of an LWR can be influenced by strongly heterogeneous moderation regions across the fuel assembly.

The main objective is to study the influence of large heterogeneities in the fuel/moderator distribution on the predictive performance of both deterministic assembly codes (e.g. CASMO-4E) and Monte Carlo methods (e.g. MCNPX). To achieve this, the test zone of the zero-power research reactor PROTEUS (see Sec. 2.1) has been loaded with a reference lattice representative

of an SCWR concept (unperturbed configuration) and a range of perturbations have been implemented to investigate this SCWR-like lattice. In each of these configurations, appropriate integral measurements (principally, pin-by-pin reaction rate distributions) are carried out, and the experimental results obtained are compared to probabilistic and deterministic predictions.

An important aspect of the research is the investigation of the transferability of the affected comparisons, between calculations and the PROTEUS experiments, to the validation of typical SCWR neutronics calculations. Thus, it is expected that a certain experimental evaluation will be rendered possible, for some of the performance goals which have been set for the SCWR as a Generation IV system.

In this opening chapter, an overview of the current status of nuclear power worldwide is given first (Sec. 1.1). The situation in Switzerland is explicitly discussed in Sec. 1.1.2. Thereafter, Sec. 1.2 briefly discusses the importance of well validated computational tools, which is an important aspect of this work. Finally, in Sec. 1.3, the outline of this thesis is presented.

## 1.1 Current Status of Nuclear Power

Today, 13% of the electricity produced worldwide comes from the 446 operating nuclear power plants. Together, they produce about 376 Gigawatts of electricity. In the US alone, 104 reactors are in operation (see Fig. 1.1). Other important nuclear countries are France, Japan, Russia, Canada, South Korea, and India. The vast majority of the reactors are Generation II light water reactors (Pressurized Water Reactors (PWRs) and Boiling Water Reactors (BWRs)). While the world's electricity production is constantly rising, the number of power plants has been more or less constant. Therefore, the nuclear share of electricity production has been decreasing.

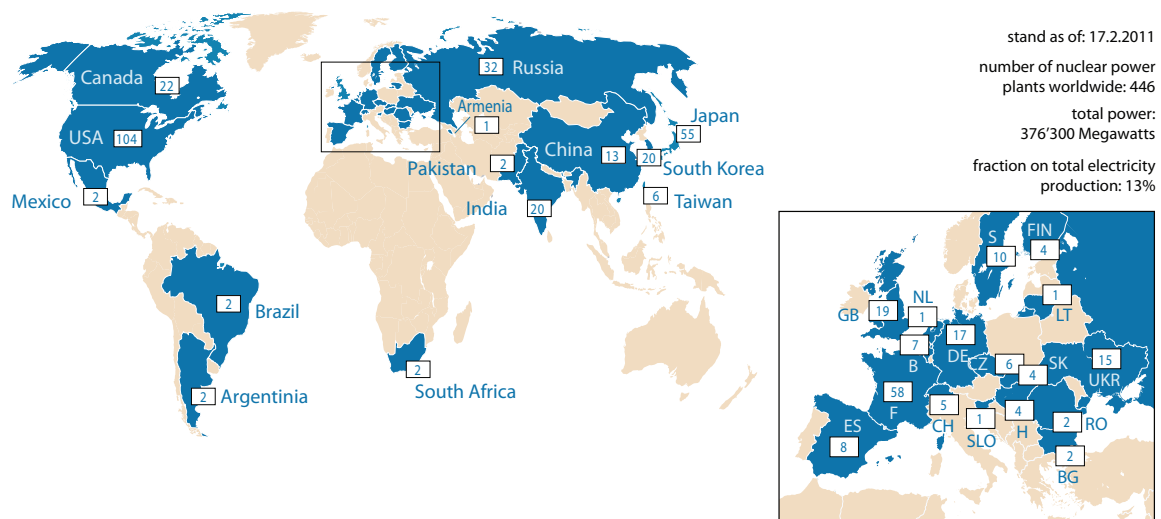


Figure 1.1: Nuclear power plants in operation worldwide [5].

More than three-quarters of nuclear power plants have been in operation for longer than 20 years. The aging of important components such as the reactor pressure vessel has been less severe than expected, and lifetime extensions have become common. Despite these trends, many reactors will be taken out of operation in the next decade or two.

The discussion about global warming and electricity production that generates less carbon dioxide has triggered a nuclear renaissance around the world. Many countries have realized the advantages of nuclear power production, e.g. low carbon dioxide emissions, low fuel costs, and overall inexpensive electricity production. As of today, 64 nuclear power plants are under construction, 27 of them being in China and 11 in Russia (see Fig. 1.2). In South Korea, 6 new units are under construction and in India 5.

Apart from the 64 reactors currently being built, there are 150 units being planned. There are 43 new reactors projected in China, 20 in the US, 18 in India, 13 in Russia and 12 in Japan. In Europe, while just 6 reactors are under construction (1 in France, 1 in Finland, 2 in the Slovak Republic, and 2 in Bulgaria), 19 new plants are projected. Additionally, several countries have announced their interest in building nuclear power plants: Albania, Belarus, Croatia, Estonia, Ireland, Italy, Latvia, Norway, Poland, Portugal, Turkey, and Serbia [6].

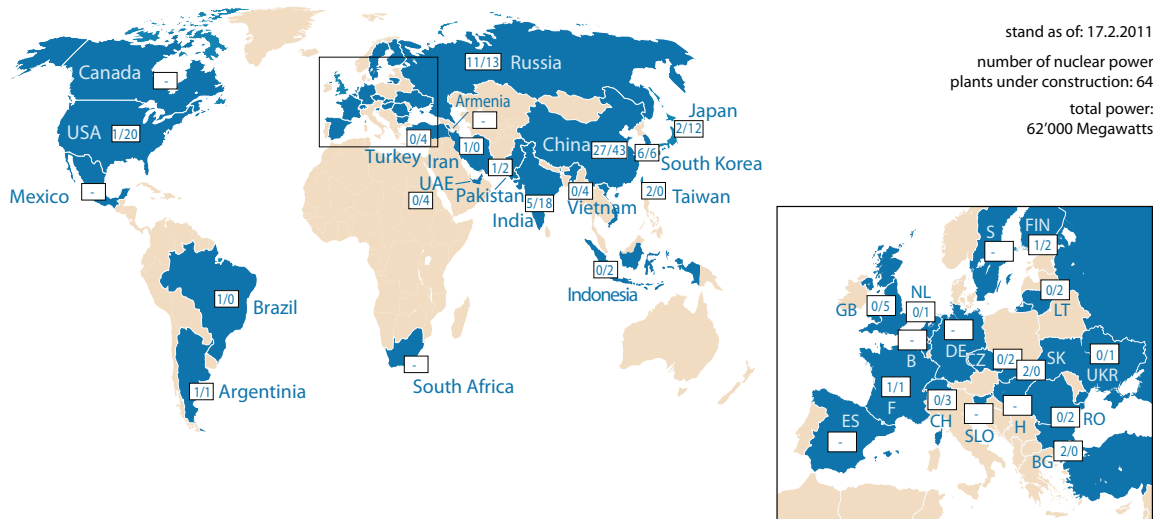


Figure 1.2: Nuclear power plants under construction (value on the left) and projected (value on the right) worldwide [5].

However, the most recent events in Japan may have a major influence on the electricity generation policy of many countries. Following the strongest earthquake ever measured in Japan (9.0 on the Richter scale) and a tsunami wave more than 15 meter high, the Japanese nuclear power plant Fukushima I has suffered severe damage on four of its six nuclear reactors. After the loss of off-site power and the diesel generators, the cooling systems stopped functioning. In the aftermath, emergency measures had to be taken, using seawater to cool the reactors and the spent fuel storage pools. Considerable amounts of radioactive materials have been released into the environment, and the nearby civil population has had to be evacuated. These tragic events

may stop the nuclear renaissance, maybe not globally, but possibly in some countries that can afford to produce their electricity differently. Italy, for one, has interrupted its plans to reembark upon nuclear power generation, and Germany has decided to shut all its nuclear power plants by 2022.

Nevertheless, several major countries that strongly depend on cheap electricity to drive their economy will find it advantageous to maintain their nuclear strategy. The most important of these are China, India, and Russia. Together, they have 43 reactors under construction and another 74 that are being planned. In addition, highly industrialized countries that depend on their export products being produced with cheap electricity, such as the US and Japan itself, will not be willing to pay the price for a drastic strategy change in electricity production. Thus, the Fukushima I disaster, while influencing the electricity generation policy of some countries, should not stop the global trend to build new nuclear power plants.

### 1.1.1 Generation IV

While almost all of the nuclear power plants currently in operation feature Generation II type reactors, i.e. PWRs, BWRs, and CANDUs (Canadian pressure-tube heavy water reactors), most of the reactors under construction or in planning will be light water reactors of Generation III type (see Fig. 1.3). The lifetime of these reactors is foreseen to be in the order of 60 years. This generation of reactors will then be replaced by Generation IV type reactors, which feature superior economics, ecology, safety, and proliferation resistance.

In July 2001, the Generation IV International Forum (GIF) was chartered. Its purpose is to coordinate the collaborative efforts of the world's most important nuclear technology nations, in the context of developing next generation nuclear energy systems capable of meeting the world's future energy demands. It was first signed by nine countries. Switzerland acceded later in 2002. Eight technology goals have been defined for the Generation IV systems in the areas of sustainability, economics, safety and reliability, and proliferation resistance and physical protection. The overall aim is to have a next generation of nuclear energy systems, that meets all the above mentioned criteria, ready for deployment by the year 2030.

The first task that the GIF faced was to narrow down the many possible reactor concepts to a smaller number of most promising technologies. Based on the GIF goals, experts around the world selected the six most promising concepts for further R&D work by the member countries. The eight general goals, defined by the GIF are [7]:

**Sustainability-1** Generation IV nuclear energy systems will provide sustainable energy generation that meets clean air objectives and provides long-term availability of systems and effective fuel utilization for worldwide energy production.

**Sustainability-2** Generation IV nuclear energy systems will minimize and manage their nuclear



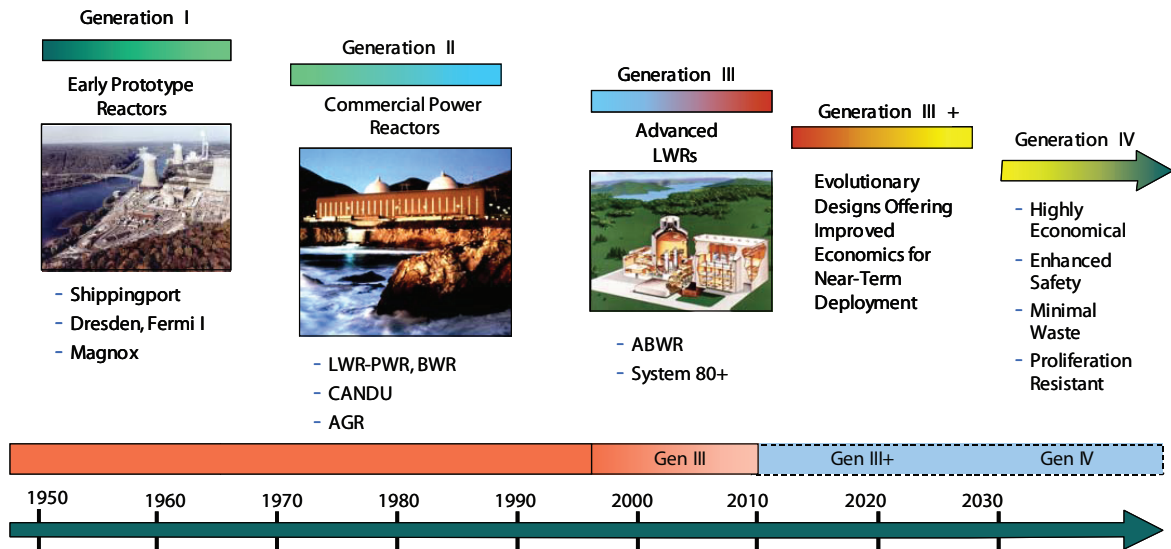


Figure 1.3: Overview of the different generations of nuclear power plants [7].

waste and notably reduce the long-term stewardship burden, thereby improving protection for the public health and the environment.

**Economics-1** Generation IV nuclear energy systems will have a clear life-cycle cost advantage over other energy sources.

**Economics-2** Generation IV nuclear energy systems will have a level of financial risk comparable to other energy projects.

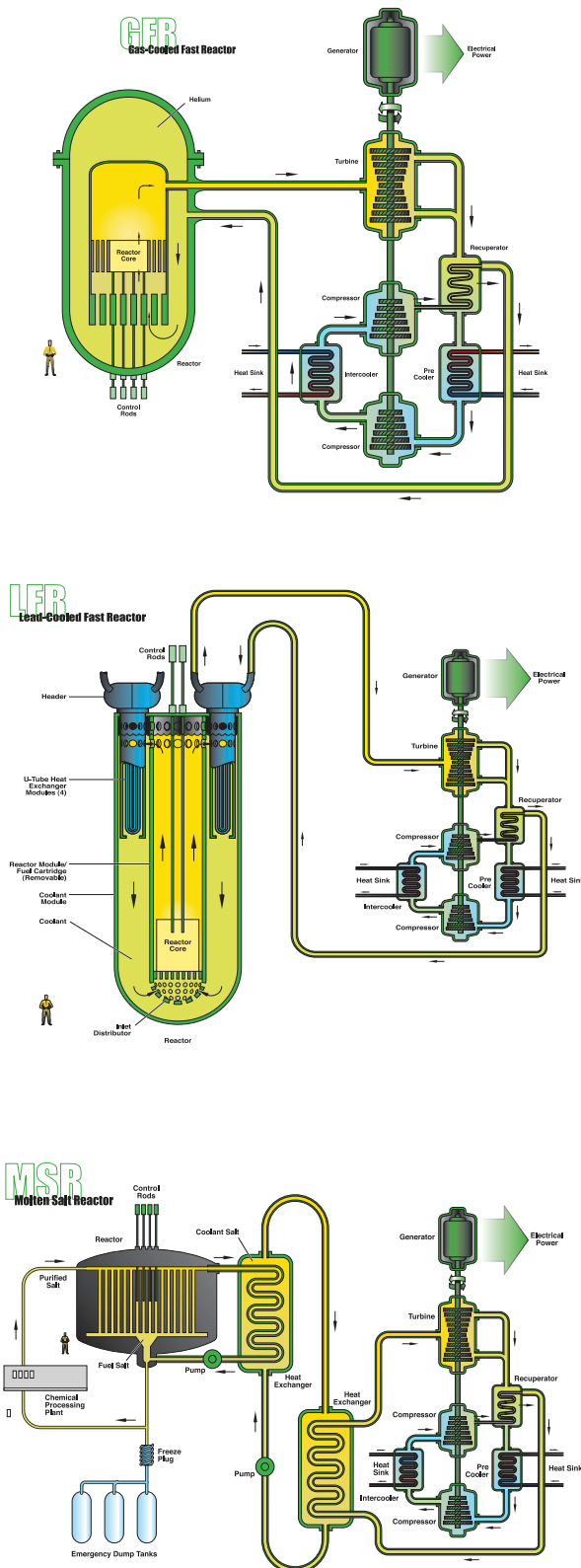
**Safety and Reliability-1** Generation IV nuclear energy systems operations will excel in safety and reliability.

**Safety and Reliability-2** Generation IV nuclear systems will have a very low likelihood and degree of reactor core damage.

**Safety and Reliability-3** Generation IV nuclear energy systems will eliminate the need for off-site emergency response.

**Proliferation resistance and Physical Protection** Generation IV nuclear energy systems will increase the assurance that they are very unattractive and the least desirable route for diversion or theft of weapons-usable materials, and provide increased physical protection against acts of terrorism.

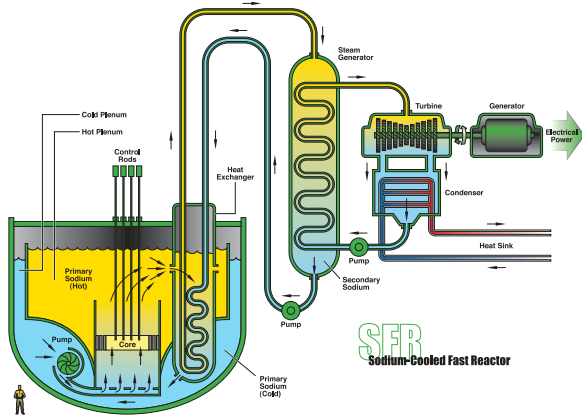
In 2002, the first GIF R&D Roadmap was established, introducing the following six selected concepts:



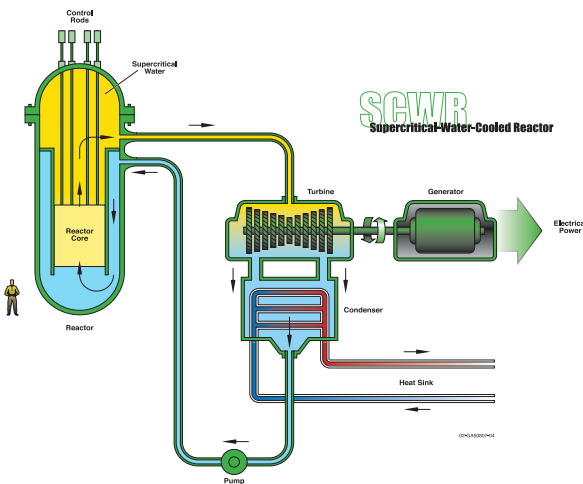
“**GFR** - The main characteristics of the gas-cooled fast reactor are fissile self-sufficient cores with fast neutron spectrum, robust refractory fuel, high operating temperature, high efficiency electricity production, energy conversion with a gas turbine and full actinide recycling possibly associated with an integrated on-site fuel reprocessing facility.” [7]

“**LFR** - The lead-cooled fast reactor system is characterized by a fast-neutron spectrum and a closed fuel cycle with full actinide recycling, possibly in central or regional fuel cycle facilities. The coolant could be either lead (preferred option), or lead/bismuth eutectic. The LFR can be operated as a breeder; a burner of actinides from spent fuel, using inert matrix fuel; or a burner/breeder using thorium matrices.” [7]

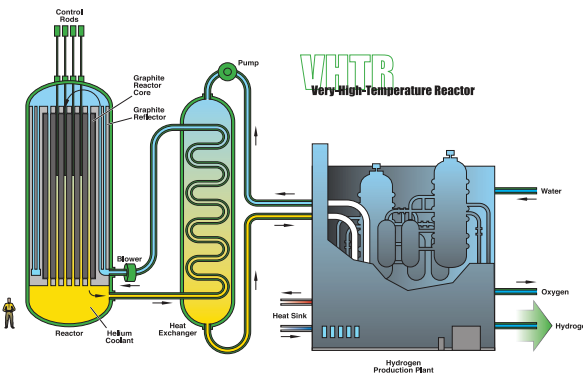
“**MSR** - The molten-salt reactor system embodies the very special feature of a liquid fuel. MSR concepts, which can be used as efficient burners of TRU from spent LWR fuel, have also a breeding capability in any kind of neutron spectrum ranging from thermal (with a thorium based fuel cycle) to fast (with the U-Pu fuel cycle). Whether configured for burning or breeding, MSRs have considerable promise for the minimization of radiotoxic nuclear waste.” [7]



“**SFR** - The sodium-cooled fast reactor system uses liquid sodium as the reactor coolant, allowing high power density with low coolant volume fraction. The reactor can be arranged in a pool layout or a compact loop layout. Reactor size options under consideration range from small (50 to 300 MWe) modular reactors to larger reactors (up to 1500 MWe).” [7]



“**SCWR** - Supercritical-Water-Cooled Reactors are a class of high-temperature, high-pressure water-cooled reactors operating with a direct energy conversion cycle and above the thermodynamic critical point of water (374 °C, 22.1 MPa). The higher thermodynamic efficiency and plant simplification opportunities afforded by a high-temperature, single-phase coolant translate into improved economics. A wide variety of options are currently considered: both thermal-neutron and fast-neutron spectra are envisaged and both pressure vessel and pressure tube configurations are considered.” [7]



“**VHTR** - The very-high temperature reactor is a next step in the evolutionary development of high-temperature reactors. The VHTR is a helium gas-cooled, graphite-moderated, thermal neutron spectrum reactor with a core outlet temperature greater than 900 °C, and a goal of 1000 °C, sufficient to support production of hydrogen by thermo-chemical processes.” ... “The VHTR is primarily dedicated to the cogeneration of electricity and hydrogen, as well as to other process heat applications.” [7]

Table 1.1: The six reactor concepts selected by the GIF.

### 1.1.2 Situation in Switzerland

In Switzerland, 40% of the electricity production comes from five nuclear power plants. The oldest one, operating since 1969, is a pressurized water reactor located at Beznau (see Fig. 1.4) and produces 365 MW electrical output. In 1972, a second unit, Beznau-2, and the boiling water reactor Mühleberg went into operation, producing today 365 MW and 373 MW electrical output, respectively. Seven years later, in 1979, the pressurized water reactor at Gösgen started electricity generation (985 MW electrical output). Leibstadt, the youngest nuclear power plant in Switzerland, was commissioned in 1984 and produces today 1165 MW of electricity.

The three older reactors (Beznau-1 and -2, and Mühleberg) are foreseen to operate until about 2020, Gösgen and Leibstadt until about 2035. Because of the expiring of long-term electricity import contracts with France in 2020, Switzerland faces an electricity production gap that will have to be closed. Currently, extensive discussions are going on to determine the future electricity policy of the country. In 2008, three general license applications were submitted to replace the older plants. The complex application and licensing process was expected to take up to 15 to 20 years until a possible new reactor would go into operation.

Switzerland is one of the countries in which nuclear power is intensely debated. As for the global trend, after the accidents at Three Mile Island and Chernobyl, it seemed unthinkable that another nuclear reactor would ever be built in Switzerland. However, the discussion on global warming and CO<sub>2</sub> emissions led to a reconsideration of nuclear technology and the acceptance of it had been constantly growing until the accident in Fukushima. The latter has had a strong impact on public opinion and, at the current time, it seems unlikely that a public referendum during the next few years would yield a decision in favor of nuclear energy.

## 1.2 Importance of Well Validated Computational Tools

As calculational tools, computer codes are of utmost importance during the entire lifetime of a nuclear power plant. Codes that predict the thermal-hydraulic or neutronic behavior (or a combination thereof) are extensively used during the design and operational phase of every reactor. These codes have usually been tested and validated on a broad variety of reactor designs. However, the results obtained from a given calculation can only be trusted if the application under consideration is within the validation domain of the code. The further away one gets from the validation domain, the higher is the uncertainty on the validity and accuracy of the results.

The reactor concepts of the fourth generation have major differences compared to today's LWRs. The SCWR is the reactor concept most closely related to standard LWRs, the systems for which most codes are well validated. However, even the SCWR has major differences relative to common light water reactors. For one, there is the obvious difference that the reactor core is cooled and moderated by water in supercritical state. There is much less validation of thermal-hydraulics



Figure 1.4: The nuclear power plants in Switzerland [8].

codes dealing with supercritical water. The reactor physics side of the problem, i.e. the neutron balance and distribution in the core, is also very different from an LWR since - apart from the moderation heterogeneity - the average volumetric ratio of moderator to fuel needs to be much larger in an SCWR due to the lower density of supercritical water, which can become as low as one seventh that of water at room temperature.

### 1.3 Scope of the present research

As mentioned earlier, the influence of large heterogeneities in the fuel/moderator distribution on the predictive performance of deterministic (CASMO-4E) and probabilistic (MCNPX) reactor physics codes are investigated in the currently presented research. A series of experiments has been conducted at the zero-power research reactor PROTEUS, in order to establish an appropriate validation basis. An unperturbed SCWR-like test lattice has served as reference case, against which code performance has been compared for six configurations with various perturbations. In each of these cases, measured pin-by-pin reaction rate distributions have been compared with the corresponding calculational results from CASMO-4E and MCNPX. Additionally, pin removal reactivity worths have been measured in the reference case and have also been compared to calculated values. Following the validation of the codes for the presently considered configurations, the applicability of these findings to the most recently proposed SCWR power reactor assembly designs has been investigated.

This thesis is organized in 9 chapters:

A more detailed background of the work is given in Chapter 2, which introduces the zero power research facility PROTEUS, at which the experimental part of the thesis has been conducted. Secondly, the Supercritical-Water-Cooled Reactor (SCWR), which has been discussed only briefly in the introduction, is described in more detail. Along with the basic design features, the history of the concept and a survey of the ongoing research in various countries around the world are given.

Chapter 3 introduces the measurement techniques employed in the experiments. The first part of the chapter discusses the scope of the conducted experiments and gives detailed information on the measured configurations. The main part of the chapter is dedicated to the gamma scanning technique which was used to derive reaction rate distributions across the fuel lattice. Finally, the measurement technique used to obtain fuel pin reactivity worths - by applying the reactivity compensation technique - is presented.

In Chapter 4, the calculational tools are introduced. The methods employed in the probabilistic code MCNPX and the deterministic code CASMO-4E, which were used for the prediction of the experimentally measured reaction rate ratios and fuel pin removal worths, are discussed along with their limitations. The different computational models that were used for the calculations are presented. In the last part of the chapter, the validation strategy, which has been developed and employed currently, is discussed.

Chapter 5 gives a detailed characterization of the unperturbed reference SCWR-like fuel lattice based on reaction rate distributions. Following this, two consistency checks of the experimental results are discussed: the reproducibility of the measurements and the symmetry of the results. In the third part, the measured reaction rates are compared to the whole-reactor calculations carried out using MCNPX. The final section of this chapter is dedicated to the comparison between CASMO-4E and MCNPX calculations at the assembly level.

As in the previous chapter, Chapter 6 reports on the validation of the computer codes based on experimentally derived reaction rate distributions, but this time in perturbed lattice configurations. The perturbations that are introduced in Sec. 3.1, are grouped here into three categories, each of them being discussed in a separate section. The first section investigates control rod related effects, the second the effects of moderator density changes, and the third the effect of removing a fuel pin and replacing it with gadolinium poisoned fuel. For each of the perturbed configurations, whole-reactor MCNPX predictions are validated against experimental results. Then, MCNPX and CASMO-4E calculations are compared at the assembly level.

Chapter 7 covers pin removal reactivity worths in the reference test lattice and  $k_{\text{eff}}$  values calculated for the different critical PROTEUS configurations. It is divided into the corresponding two main sections. In the first section, fuel pin removal worths in the unperturbed lattice, i.e. the effect on  $k_{\text{eff}}$  of the system upon removal of a single fuel pin, are discussed. The obtained

experimental results are compared with MCNPX and CASMO-4E calculations. To get more information on the individual contributors to the total reactivity effect, a decomposition analysis is done for the assembly-level models of both codes. The second section deals with whole-reactor reactivity predictions of the unperturbed and perturbed PROTEUS configurations.

In order to assess the validity of CASMO-4E and MCNPX calculations for SCWR assembly designs which are currently being proposed, the transferability of measurements in the PROTEUS SCWR-like test lattice is investigated in Chapter 8. In a first step, the transferability of the experimentally derived results to assembly-level calculations of the investigated SCWR-like lattice is assessed. Next, the transferability of these assembly-level calculations to SCWR power reactor assemblies is checked.

Finally, Chapter 9 presents the conclusions of the thesis and offers recommendations for future work.

# Bibliography

- [1] Y. Oka, S. Koshizuka, and T. Yamasaki. Direct Cycle Light Water Reactor Operating at Supercritical Pressure. *Journal of Nuclear Science and Technology*, 29(6):585–588, 1992.
- [2] Denise B. Pelowitz. *MCNPX User's Manual*, 2.5.0 edition, 2005. LA-CP-05-0369.
- [3] Joel Rhodes, Kord Smith, and Malte Edenius. *CASMO-4E, Extended Capability CASMO-4, User's Manual*. Studsvik Scandpower, 2004. SSP-01/401Rev2.
- [4] F. Jatuff, K. Macku, and R. Chawla. On the accuracy of reactor physics calculations for square HPLWR fuel assemblies. *Annals of Nuclear Energy*, 33:198–207, 2006.
- [5] Nuklearforum Schweiz. *Kernkraftwerke der Welt*. 2011. <http://www.nuklearforum.ch>.
- [6] World Nuclear Association. Emerging nuclear energy countries, March 2011. <http://www.world-nuclear.org>.
- [7] U.S. DOE Nuclear Energy Research Advisory Committee and the Generation IV International Forum. A Technology Roadmap for Generation IV Nuclear Energy Systems. Technical Report GIF-002-00, December 2002.
- [8] Nuklearforum Schweiz. *Kernenergie für die Schweiz*. Fourth edition, 2010.



## 2 Thesis Background

This chapter provides general background information which is necessary in order to understand the framework of this thesis and the conducted work. It is split into two sections. Sec. 2.1 describes the PROTEUS zero power research reactor. This facility provided the experimental results for the thesis, and its setup as well as its history as research reactor are discussed. Sec. 2.2 introduces the concept of the Supercritical-Water-Cooled Reactor (SCWR) and discusses the current status of international research on the subject. The history of the SCWR is also presented.

### 2.1 The PROTEUS Research Reactor

#### 2.1.1 General Description and Past Programs

The PROTEUS zero-power research facility is a driven reactor system consisting of a central test zone surrounded by buffer and driver regions. The setup of the surrounding zones depends on the system being investigated. Figure 2.1 shows a cutaway view of the whole reactor system. It is basically a cylinder of graphite, which is 3304 *mm* high and has a diameter of 3262 *mm*. In the center of this cylinder, there is a 22-sided polygonal cavity with an equivalent diameter of 1255 *mm*, which accommodates the test zone, as well as a buffer and an inner (D<sub>2</sub>O-moderated) driver region. The innermost part of the graphite block itself is used as the outer (graphite-moderated) driver region. Concrete doors are located on top of the reactor, and these can be opened horizontally when the reactor is not in operation.

The advantage of such a driven system is its flexibility and versatility in terms of being able to study different reactor concepts. One can, with relatively little fuel, build a test zone representative of a given reactor concept. At its center, the constructed test zone closely resembles the power reactor one wishes to study, in terms of neutron energy spectrum and neutron balance.

Since the reactor went into operation in 1968, various reactor concepts of rich diversity have been studied at PROTEUS. The first experimental program, in the 1970's, was dedicated to gas-cooled fast reactor (GCFR) designs, which offered the possibility to use natural uranium resources in a much more efficient way, while at the same time enabling high coolant temperatures to be

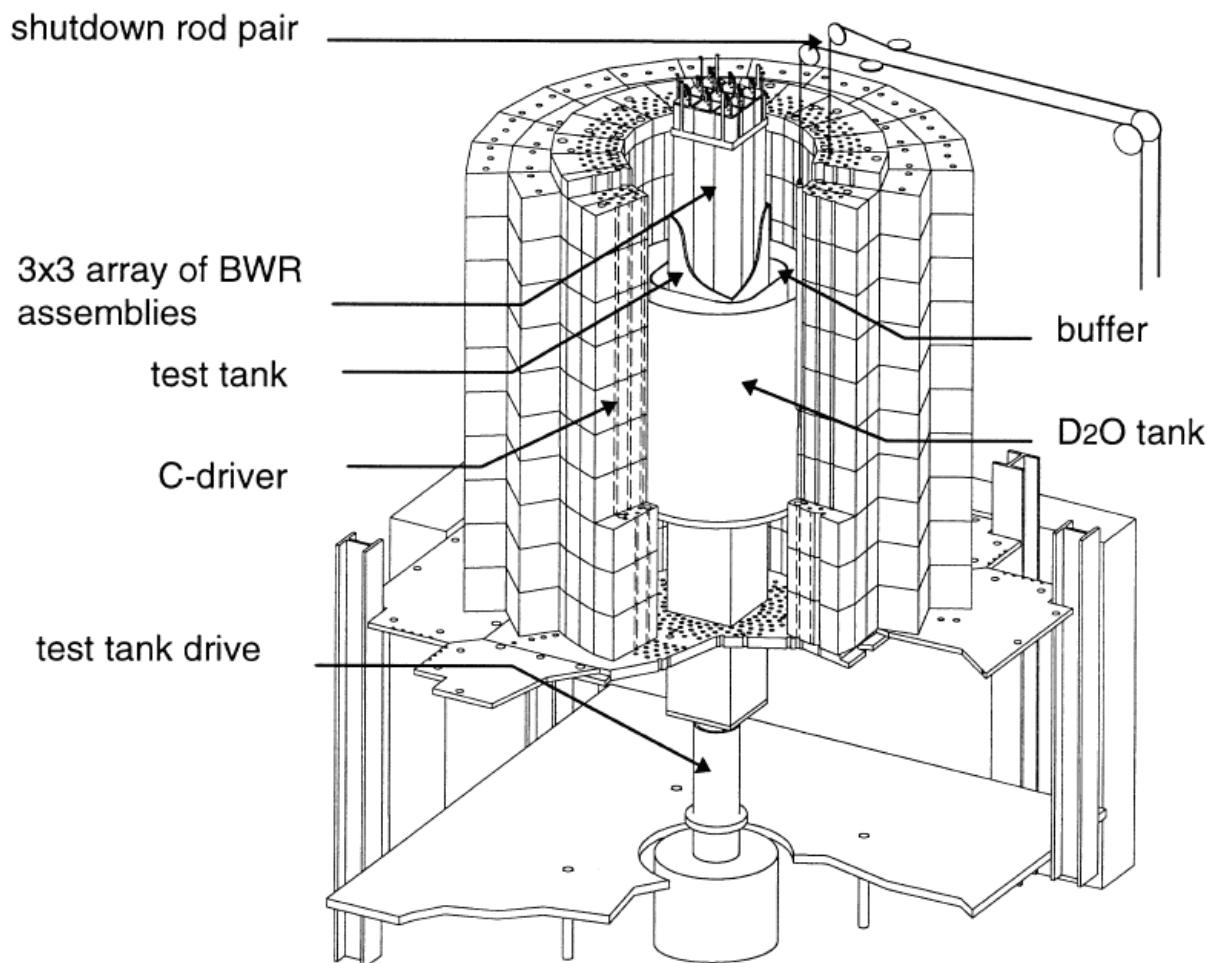


Figure 2.1: Cutaway view of the PROTEUS zero-power reactor

reached for the energy conversion process. These are the important reasons why the interest in the GCFR has become large again and why this reactor type has been selected as one of the Generation IV concepts.

The next program, in the 1980's, was on high conversion light water reactors (HCLWRs). Here, the motivation is to improve the uranium utilization in LWRs. The plutonium content of the fuel is high and the moderator-to-fuel ratio is low, compared to a standard light water reactor. This produces a strongly undermoderated neutron spectrum, which is much harder than in normal LWRs and enables a high conversion ratio to be achieved.

A further reactor concept was studied in the early 1990's, the pebble-bed high temperature reactor (HTR). The basic fuel in such reactors is in the form of coated particles of enriched  $\text{UO}_2$ . A fuel element consists of a "pebble" of graphite of 6 cm diameter, in the central part of which the coated fuel particles are embedded. For this particular program, the entire inner cavity of PROTEUS was filled with fuel pebbles, and no buffer or driver zones were used.

From 1998 to 2006, the research reactor was employed for the light water reactor program LWR-PROTEUS. The main goals of the program have been to experimentally investigate (a) power distributions in fresh, strongly heterogeneous BWR fuel assemblies and (b) the reactivity effects of single, highly burnt  $\text{UO}_2$  and MOX fuel pins in a fresh PWR assembly mock-up. The ability of computational tools to correctly calculate the investigated characteristics of modern LWR fuel assemblies could thus be validated against accurate experimental data. The PROTEUS test zone for these experiments was designed to hold full-length BWR fuel assemblies, which were loaned by the Swiss utilities. Up to nine assemblies could be inserted into the vertically movable test tank. Subsection 2.1.3 describes this program in more detail.

At the end of the LWR-PROTEUS program, the test zone was modified to accommodate an SCWR-like lattice. This reference test lattice has served as the basis for the present investigations and is described in greater detail in Subsection 2.2.3. It should be mentioned that this test lattice has also served for preliminary experiments related to the LIFE@PROTEUS program, which aims to study the interfaces between fresh and spent fuel ([1, 2]).

### 2.1.2 Multi-Zone Layout of the Reactor

Figure 2.2 shows a cross section of the PROTEUS reactor. The different zones are clearly visible. These are, starting from the inside: the test zone, shown here containing the SCWR-like fuel lattice; the buffer zone; the  $\text{D}_2\text{O}$  driver zone; the C-driver zone; and the reflector zone. Each zone is described shortly in the following.

The test zone consists of an aluminum tank, which is filled with moderator and the SCWR-like fuel lattice. The test-region is surrounded by the buffer zone. It contains a tight lattice of natural uranium rods. Around the buffer zone is located the  $\text{D}_2\text{O}$  driver zone, which is filled

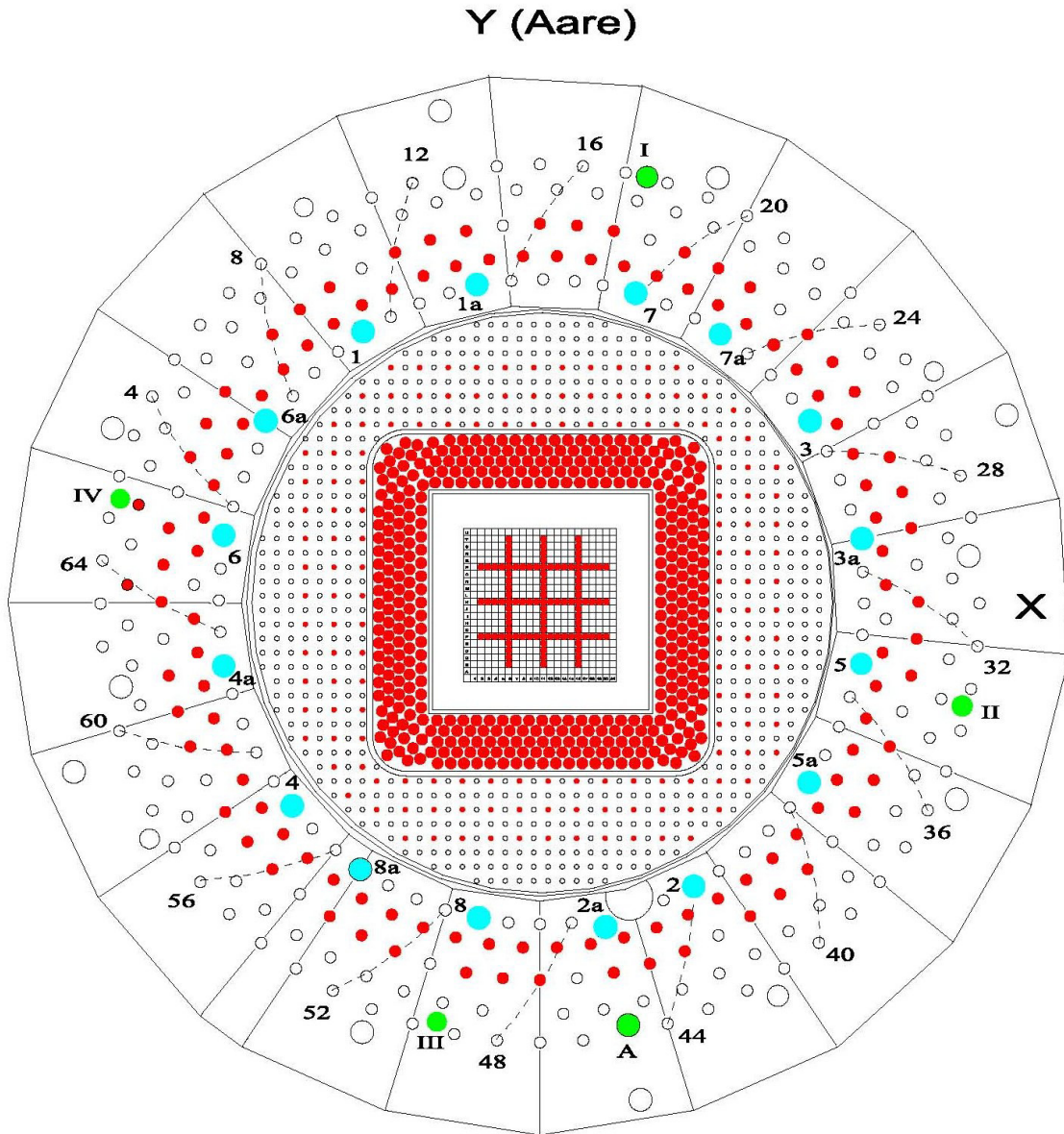


Figure 2.2: Cross section view of PROTEUS

with pure heavy water and a lattice of 5% enriched  $\text{UO}_2$  fuel. In this region, the basic square shape of the test zone and the buffer zone is transitioned into the round shape of the C-driver zone and the graphite reflector zone. Around the  $\text{D}_2\text{O}$  zone is the C-driver zone which consists of a cylinder of graphite with five annular rings of drillings, which can be filled with fuel pins (also 5% enriched  $\text{UO}_2$ ). The safety and shut-down rods are located in this region. They are arranged in the innermost circle of drillings. The outermost zone is the graphite reflector, which is a solid cylinder of graphite containing four zebra control rods and the start-up sources of the reactor.

The physics of a multi-zone system is more complex than that of a single zone reactor. The test zone contains the experimental lattice. It has to be laid out such that the neutron spectrum in the central region resembles the spectrum of the corresponding single-zone critical reactor, i.e. the fundamental-mode spectrum, as closely as possible. For this to be achieved, the test zone has to be large in comparison to dimensions characterizing the neutronics of the test lattice, e.g. the diffusion length. The natural uranium metal pins in the buffer zone are arranged in a tight hexagonal lattice and have no moderator between them. The buffer zone decouples the neutron spectra of the test zone and the driver zones, in that it absorbs thermal neutrons from the outer driver zones and produces fast neutrons through fissions in  $^{235}\text{U}$ . The neutron spectrum inside the buffer zone thus approaches a fast spectrum. The resulting intermediate energy neutron spectrum incident on the test zone greatly facilitates the establishing of its own characteristic neutron spectrum, i.e. the fundamental-mode spectrum, in its central region.

The surrounding driver regions ( $\text{D}_2\text{O}$  driver and graphite driver) provide neutrons to the subcritical test zone to drive the entire system critical. As mentioned, the standard driver fuel in PROTEUS consists of 5% enriched  $\text{UO}_2$ . The number of fuel pins in the graphite driver can be varied in order to reach criticality. The greater the reactivity needed from the driver region, the larger is the number of drillings loaded in the graphite driver. The surrounding graphite reflector is dimensioned to reflect as many neutrons as possible back towards the inner zones, thereby reducing the number of neutrons that leak out of the system.

All safety and control elements, as well as the instrumentation channels of the reactor, are located in the graphite driver region or adjacent to it, close to where the thermal neutron flux is at its maximum. By this arrangement, one can avoid disturbing effects from these elements on the neutron spectrum inside the test zone. On the other hand, this requires that the test zone by itself is sufficiently subcritical, such that, considering the system as a whole, the neutronic importance of the driver regions remains high. This is necessary in order to ensure that the reactivity worths of the safety and control rods are high enough. There are eight shut-down rods and also eight safety rods located at the inner boundary of the graphite driver region. Four “zebra” control rods are located at the outer edge of the graphite driver. They can be controlled by the operator in order to compensate reactivity changes during the experiment (in the order of a few tens of cents). Additionally, there is an autorod in the graphite driver which automatically compensates small reactivity fluctuations and drifts (in the order of several tenths of a cent).

For each new test zone configuration in PROTEUS, one needs to carry out an “approach-to-critical”, i.e. to load the fuel in a controlled manner before reaching a critical configuration. With the D<sub>2</sub>O and buffer zones already loaded, one starts with inserting the new sub-critical lattice to be studied in the test zone and thereafter loads the C-driver zones step-by-step to reach the final critical system. After each step, one obtains, via the count rates of appropriately positioned neutron detectors, a measure of the subcritical  $k_{\text{eff}}$  of the system and extrapolates the number of C-driver fuel pins that are needed to reach criticality. Then, one inserts half of the estimated number of fuel pins and measures the subcritical multiplication once again. In this manner, one slowly approaches the critical loading and avoids the risk of reaching a significantly super-critical configuration (a positive reactivity of more than 30 cents).

The advantages of a driven reactor system such as PROTEUS are numerous. Investigations on a certain type of reactor are possible with a minimal amount of fuel (and other associated materials, such as moderator), because only a representative test lattice of the reactor needs to be built. This has a large effect on the costs of the experiment. The system is flexible and versatile. A large range of test zone conditions (even with  $k_{\infty} < 1$ ) can be studied by changes of the driver loading alone. One thereby omits undesirable perturbations of the test zone which would influence the measurements. Additionally, all the necessary reactor safety and control elements are located in the graphite driver zone, which again prevent the experimental zone from being perturbed. In addition, the test zone is relatively large (45x45 cm) and, in the case of PROTEUS, high enough (4.5 m) to accommodate different types of test lattices, including full-length LWR fuel assemblies. Limitations concern test zone configurations that are too reactive and lessen the importance of the driver region and the therein located control and safety elements, as also test lattices whose large diffusion lengths make them impossible to study even with the use of a buffer zone.

### 2.1.3 The LWR-PROTEUS Program

The LWR-PROTEUS program was a scientific collaboration between PSI and the Swiss nuclear utilities (*swissnuclear*), with the basic aim of experimental validation of reactor physics codes for modern LWR fuel assemblies. This has been necessary due to the increase in complexity of these assemblies (especially of BWR assemblies), which have been developed to enhance fuel utilization and increase burnup. The measured reactor physics parameters of primary interest have been reaction rate distributions (radial and axial), reaction rate ratios, and reactivity worths of individual fuel pins. The experimental program consisted of three phases, as discussed below.

Phase I of the LWR-PROTEUS program [3] was dedicated to the investigation of fresh industrial BWR assemblies provided by the Swiss utilities. Nine (an array of 3 x 3 elements) SVEA-96+ fuel assemblies from Westinghouse were inserted into the experimental test zone of PROTEUS (see Fig. 2.3). Measurements were made in the central assembly, the surrounding eight assemblies serving to achieve near-to fundamental-mode spectral conditions therein.

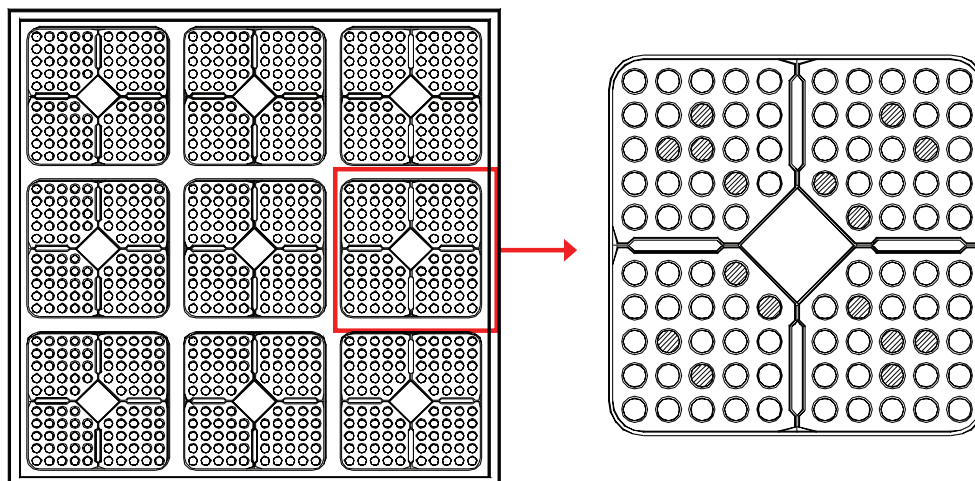


Figure 2.3: Cross section view of the PROTEUS test zone layout (on the left) and of a Westinghouse SVEA-96+ BWR fuel assembly (on the right). The dark shaded fuel pins contain the burnable poison gadolinium.

The SVEA-96+ is a highly heterogeneous fuel assembly based on a square 10 x 10 matrix of fuel pins. However, 4 lattice positions in the center of the assembly are not occupied, which leaves 96 fuel pins in the array (hence the name). In order to achieve uniform power distribution throughout the lifetime of the assembly in the reactor, a number of geometric and material heterogeneities have been introduced. A wide spread of uranium enrichments - between 2% and 5% - is employed (up to six different values in a single assembly) in the radial direction. Additionally, there are two axial enrichment zones. Up to 16 fuel pins containing gadolinium as burnable absorber are introduced. There are four water-bypass wings between each quadrant of the assembly and a central, diamond shaped water channel. A number of changes of the test zone configuration were investigated in the Phase I program, including the effect of changing moderator densities, introducing absorber plates (Hf and B<sub>4</sub>C) and asymmetric loading of the fuel assemblies to simulate channel bowing. The main results were published by Jatuff et al. in 2001 [4] and by Murphy et al. in 2002 [5].

The central fuel assembly of the Phase I reference configuration was replaced with a PWR mock-up in Phase II [6] (see Fig. 2.4). The focus of this phase laid on the investigation of highly burnt LWR fuel (well above 50 GWd/t for UO<sub>2</sub> as well as for MOX fuel). The central assembly was inserted into a separate tank in order to enable moderation conditions to be achieved different from those in the surrounding BWR assemblies. The central test assembly had a square 11 x 11 fuel pin matrix in which the central fuel pin was replaced by a guide tube. Highly burnt fuel samples, provided by the Swiss nuclear power plants (where they had been burnt under well documented conditions), were inserted into the lattice through this guide tube. A special transport flask and sample changer was constructed, in which the highly radioactive samples were stored. This device could be mounted on top of the reactor (inside the concrete shielding) and the fuel samples could be lowered into the core automatically. In this phase, mainly reactivity



differences between burnt and fresh fuel samples were measured, using the sample changer which could hold up to six fuel pin samples. The principal results were published by Murphy et al. in 2006 [7].

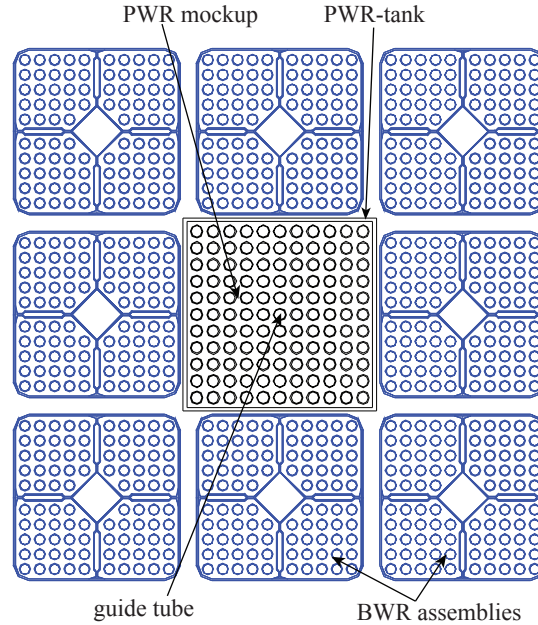


Figure 2.4: Cross section view of the PROTEUS test zone layout as implemented during Phase II of the LWR-PROTEUS program.

Phase III of the LWR-PROTEUS program was essentially an extension of Phase I [8]. The layout of the test zone was similar, but with even more advanced fuel assemblies: nine Westinghouse Optima2 BWR assemblies were inserted into the experimental zone of PROTEUS. These elements contain part-length fuel pins in order to compensate the axial change in hydrogen (water) density in a power reactor (BWR). Reaction rate distributions were measured across the central fuel assembly, and the results were reported by Murphy et al.[9] and Perret et al. [10].

It was as the last step of the Phase III program (III.4) that an SCWR-like fuel lattice (see next section) was set up in the PROTEUS test zone. This configuration was used as a transition between the LWR-PROTEUS and the LIFE@PROTEUS (Large Scale Irradiated Fuel Experiments) [2] programs. As mentioned earlier, the latter program aims to experimentally characterize the interfaces between zones of highly burnt and fresh fuel. This is an important topic for code validation since the continuous increase of burnup levels in LWRs leads to the frequent occurrence of such interfaces. The SCWR-like configuration was primarily used to develop measurement techniques to assess fission rates in re-irradiated spent fuel [1, 11]. Additionally, the SCWR-like lattice was investigated in terms of reaction rate distributions and pin removal worths, this experimental characterization and the corresponding code validation constituting the main part of this thesis.



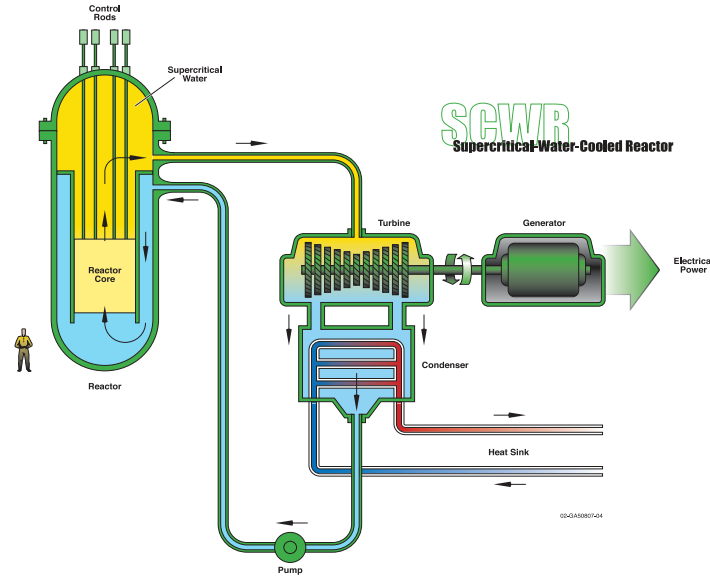


Figure 2.5: A possible layout of an SCWR [14].

## 2.2 Supercritical-Water-Cooled Reactor (SCWR)

The Supercritical-Water-Cooled Reactor (SCWR) is one of the six Generation IV International Forum (GIF) concepts that have been chosen for extensive collaborative R&D efforts. The SCWR [12, 13] builds on the combination of the vast experience with today's LWRs and supercritical coal-fired power plants. Water at supercritical state is used as moderator and coolant; the core output temperature of the supercritical water is around 500 °C, which enables a much higher overall plant efficiency (approximately 44%) than possible with current-day LWRs. Water at supercritical state has a highly varying density, depending on its temperature; the value can be as low as  $0.1 \text{ g/cm}^3$  at the exit of an SCWR core.

An SCWR operates at high pressure (in the order of 25 MPa) and, due to its high temperature (approximately 280 °C at the core entry point and above 500 °C at the exit), the water is above the thermodynamic critical point (374 °C, 22.1 MPa). A simplified, possible layout of an SCWR is shown in Fig. 2.5. The spectrum can either be thermal or fast, depending on the design of the reactor core. The supercritical water is heated in the reactor and fed directly to the turbine. After the turbine, it passes through the condenser, which serves as heat sink. It is then pumped back into the reactor core. Throughout the entire cycle, the water remains at supercritical state, as illustrated in Fig. 2.6. The SCWR has a number of major advantages compared to a LWR:

- much higher overall plant efficiency;
- a lower coolant mass flow rate per unit thermal power due to the higher enthalpy of the supercritical water, resulting in a lower coolant-mass inventory;

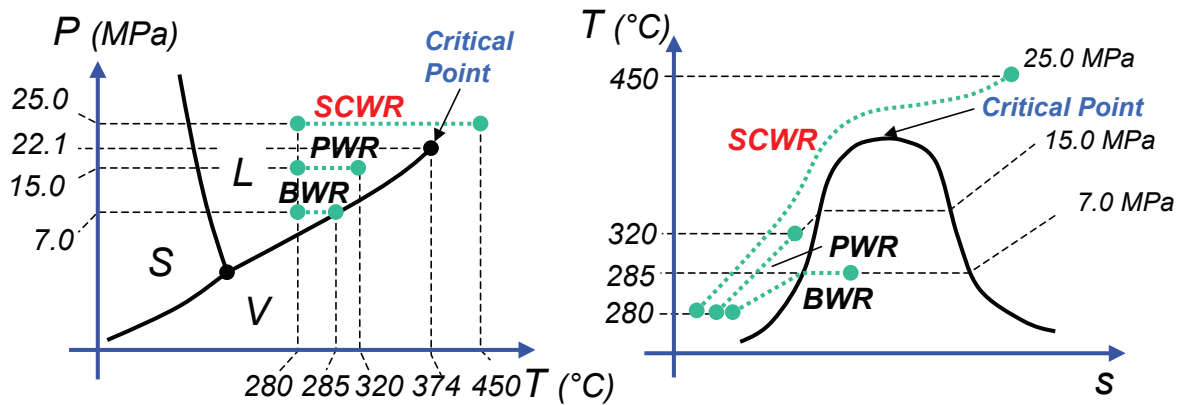


Figure 2.6: Operation conditions of an SCWR as compared to a BWR and a PWR [15].

- no possibility of departure from nucleate boiling (DNB) or dry-out because the water can not evaporate;
- elimination of steam dryers, generators, and separators.

Two direct consequences of the above-mentioned advantages are the significant reduction in containment size, as illustrated in Fig. 2.7, and an overall simplification of the plant because several major LWR components are not necessary. This increases the safety of the plant, which is one of the most important goals of the GIF initiative.

## 2.2.1 History of SCWR Design

### 2.2.1.1 Stage 1: the 1950's and 60's

The concept of using water at supercritical state to cool a reactor had already been established in the late 1950's. At that time, both Westinghouse and General Electric studied this idea under the names Supercritical Pressure Power Reactor (SPPR) and Supercritical-Water-Cooled Reactor (SCWR) [17]. The first design of Westinghouse, from 1957, was a water moderated (at 260 °C), low pressure supercritical water cooled core. Because of the fear of instabilities due to the rapid changes of physical properties of water with temperature, the designers decided not to let the coolant exceed the critical point in the reactor, where the critical point denotes the conditions above which distinct liquid and gas phases cease to exist (for water at 374 °C and 22.1 MPa). Furthermore, due to the fear of radioactive contamination in the turbines, they chose an indirect cycle which lowered the thermal efficiency of the plant design to about 30%.

General Electric made a conceptual design of a heavy water moderated, light water cooled, supercritical reactor with a once-through cooling system in 1959. The coolant passed the core

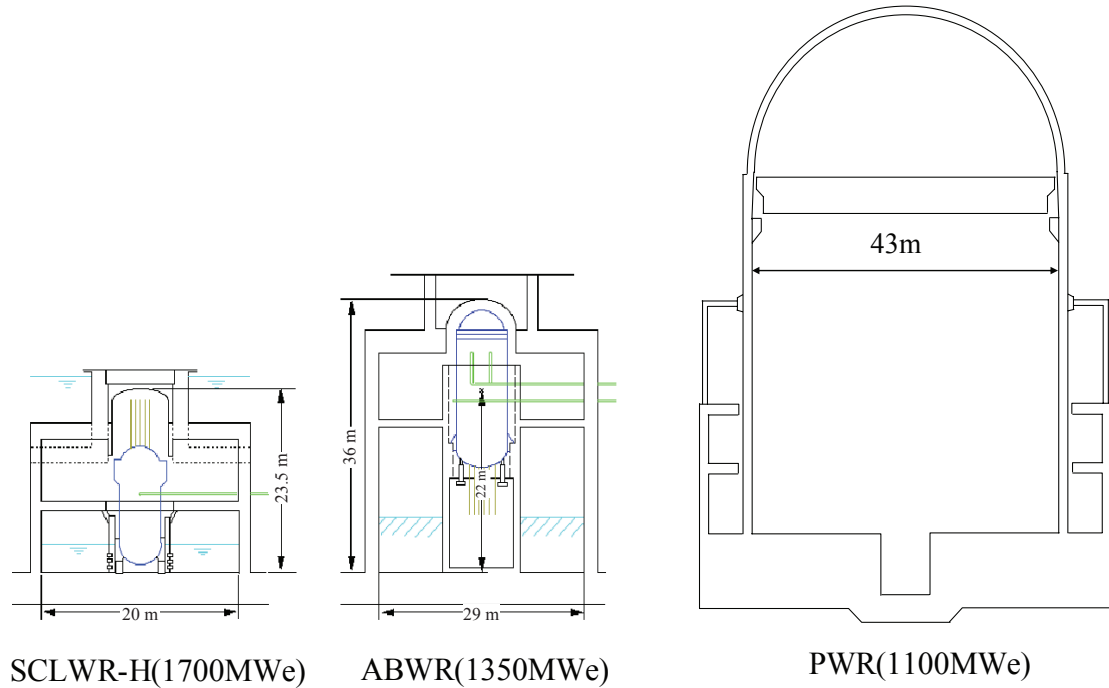


Figure 2.7: Illustration of the reduced containment size as compared to current LWRs [16].

four times. In between core passes, the coolant went through two heat exchangers and, after the fourth pass through the core, it entered the supercritical turbine at a temperature above  $600\text{ }^{\circ}\text{C}$ . The high operating conditions of temperature and pressure ( $37.9\text{ MP}$ ) were selected on the basis of the first supercritical, fossil-fired power plants operating at that time. The concepts of Westinghouse and General Electric were reviewed by the Argonne National Laboratory (ANL) in 1960 [18].

In 1962, Westinghouse presented another design which used supercritical water as coolant. It was the SCOTT-reactor (Supercritical Once-Through Tube reactor), which used a solid block of graphite as moderator through which several hundred vertical pressure tubes were penetrating. The water exited the core at  $556\text{ }^{\circ}\text{C}$  after four consecutive passes and was then fed directly to the turbine. A series of reports were published up until 1968. After that, both companies pursued conventional BWR and PWR designs.

Steam-cooled fast reactors were studied in the 1960's. Most of the concepts used steam at subcritical pressure as a coolant, but there was one concept by the Babcock & Wilcox Company (B&W) which used low density supercritical water as coolant. It operated on a direct-cycle principle in which part of the superheated coolant from the outlet was led to a boiler and mixed with feedwater to produce steam. Safety concerns regarding the emergency core cooling capabilities due to high power density and a positive reactivity coefficient were the reason to stop development. A more detailed description of the early high temperature water-cooled reactor concepts can be found in [19].

### 2.2.1.2 Stage 2: the 1990's

According to the open literature, there were only three countries performing research on supercritical water type reactors between 1990 and 2000: Canada, Russia, and Japan. In Canada, AECL (Atomic Energy of Canada Limited) extended its studies of CANDU reactors to the employment of supercritical water as coolant as part of a program, generically called CANDU-X, which aimed at significant cost reductions through improvement of efficiency and simplification of the plant [20]. The range of concepts covered conventional indirect cycle with forced convection, as well as reactors with dual cycle (hybrid of direct and indirect cycles) and natural convection. In 1992, Russia presented the B-500 SKDI concept, which was a further development of PWRs [21]. It was cooled by natural circulation and the steam generators were contained within the reactor pressure vessel. The coolant outlet temperature was around  $380\text{ }^{\circ}\text{C}$ , which led to a small increase of thermal efficiency to 38.1%.

In the 1990's, the most extensive research on Supercritical-Water-Cooled Reactors was conducted in Japan. Several different concepts were investigated. Both thermal and fast systems were considered. In 1992, Oka et al. [22] reported on a conceptional design of a Supercritical-Water-Cooled Reactor containing zirconium hydride rods to enhance the moderation. The core height was set to  $5.7\text{ m}$  and the fuel pitch-to-diameter ratio (P/D) was reduced because of thermal-hydraulic considerations. Because of the neutron absorption in the zirconium hydride rods, the fuel enrichment had to be increased to 5.6% on average. Another disadvantage of zirconium hydride is the resulting large amount of radioactive waste. These shortcomings could be resolved by using water tubes instead of zirconium hydride rods. Okano et al. [23] compared three different types of water tubes for the SCLWR core: single, semi-double and full-double water tubes. The core with full-double water tubes was found to be superior in terms of moderation, because the axial change in coolant density was the smallest.

In 1996, an SCLWR with double-tube water rods was designed in detail and named SCLWR-WR [24]. The entire coolant flowed upward through the inner tube and downward through the outer tube of the water rod, before it flowed upward again to cool the fuel rods. With this, the axial power distribution was flattened, and the core height decreased. A hexagonal fuel lattice with three pins on each side was chosen, with the central seven pins replaced by a full double tube. Control rods were located inside the water tubes. The thermal efficiency of the system was 40.8%. Tanaka et al. recommended the adoption of single water tubes because of simplicity [25]. One year later, a detailed design study of an SCLWR employing single water rods (SCLWR-SWR) was reported [26]. The characteristics of this reactor were similar to the full double-tube case. The thermal efficiency was 40.7%, and the coolant outlet temperature  $397\text{ }^{\circ}\text{C}$ .

In 1998, Dobashi et al. [27] proposed a core which was further improved by increasing the coolant outlet temperature. Supercritical fossil-fired power plants had been demonstrating the feasibility of coolant outlet temperatures far above  $500\text{ }^{\circ}\text{C}$ . In this study, an SCLWR core with high outlet temperature was designed (SCLWR-H). At these temperatures, zirconium is no longer suitable as cladding material. It was replaced by a Ni-based alloy. The single tube water rod was adopted

due to simplicity. Two alternative cores were discussed, one with ascending-flow type water rods (conventional case) and one with descending-flow type rods. The descending type was superior in terms of coolant outlet temperature because there was no mixing of coolant between the fuel channel and the water rods above the core. As before, a hexagonal fuel lattice was proposed with water tubes and control rods in the central positions. Dobashi et al. found that the descending-flow type water tubes were necessary to raise the coolant outlet temperature to above  $500\text{ }^{\circ}\text{C}$  and at the same time keep the cladding surface temperature below  $620\text{ }^{\circ}\text{C}$ . The high temperature version of the SCLWR increased the coolant outlet temperature to  $508\text{ }^{\circ}\text{C}$ , and thereby the thermal efficiency to 44.0%

Simultaneously, a fast spectrum version of the SCLWR was developed called SCFR. Indirect and direct cycle concepts, as also fast breeder and fast converter reactors, were studied. Also a high temperature version of the SCFR was developed, the SCFR-H [28, 29, 30, 31, 32, 33].

### 2.2.1.3 Stage 3: 2000 Onwards

As mentioned in Subsection 1.1.1, the Generation IV International Forum (GIF) was founded in 2001, which has been an important step in the development of next generation reactors because GIF coordinates the corresponding R&D efforts of its member countries. In the first two years after its foundation, GIF focused on the selection of possible advanced concepts for further investigations. More than 100 experts chose the six most promising nuclear reactor concepts, among them the Supercritical-Water-Cooled Reactor (SCWR). The member countries have been free to decide upon the project in which they want to participate. Up till the year 2009, three members had committed themselves to the SCWR project: Canada, Euratom and Japan. The Republic of Korea has expressed interest in the concept and is observing the developments.

Canada has developed the supercritical water cooled version of the CANDU reactor (CANDU-X) [34, 35]. It is the only country investigating the topic of supercritical water in a pressure tube reactor. The economic evaluation has led to an estimated capital cost reduction of 40 – 50%, compared to current CANDU reactors. The core outlet temperature is  $625^{\circ}\text{C}$ , which enables the net thermal efficiency to be 48%, which is the highest value among the SCWR concepts.

Europe started its own SCWR project called the High Performance Light Water Reactor (HPLWR) after the foundation of GIF, as part of the Fifth Framework Program of the European Commission Community Research. The project yielded a clear state-of-the-art report on HPLWR technology, determination of its technical merit and economic feasibility, and recommendations for future R&D work. As continuation of this program, the HPLWR-Phase 2 project was launched in September 2006 under the Sixth Framework Program, bringing together eight member states. The HPLWR reference plant uses supercritical coolant pressure of about 25 MPa and a coolant outlet temperature of more than  $500^{\circ}\text{C}$  to reach the envisaged net thermal efficiency of 44% [12].

Japan has kept working extensively on the various SCWR-concepts it developed earlier. While

the research during the 1990's was focused on hexagonal lattices, a square assembly layout was proposed in 2001 in which arrays of four-by-four fuel pins were taken out and replaced by moderator channels [13]. This layout was altered and optimized during the following years [36, 37]. Control rods and burnable absorbers were inserted into the assemblies. Since 2006, the focus has been laid on the fast version of the SCWR, the supercritical water-cooled fast reactor (SWFR) [38, 39, 40, 41].

Recently, China and Korea have become interested in the SCWR concept as well and started to participate in the ongoing research. While Korea's work is based on the Japanese design proposals [42, 43], China's research has been more focused on the basic assembly design, and they have made a proposal for a thermal assembly of their own [44].

### 2.2.2 Latest Thermal SCWR Designs

This section reviews the state-of-the-art of thermal SCWR designs. The Japanese and the European designs are the two furthest developed projects. In parallel, Canada has been progressing on the development of the SCWR version of their CANDU reactor. Besides the three signatory countries of the GIF SCWR project, only China and Korea have been working on this concept, according to open literature.

#### 2.2.2.1 The Japanese Design

The current Japanese concept for an SCWR power plant has a reactor cooled by water at 25 MPa, with the temperature varying from 280 °C to 500 °C [45]. 121 square fuel assemblies of 300 x 300 mm cross section make up the reactor core. The core thermal output is 2744 MWt and the electrical output is 1200 MWe; hence the thermal efficiency is 43.8%. The average discharge burnup is 45 GWd/t. The reactor pressure vessel (RPV) resembles a PWR vessel closely. A schematic of the plant is shown in Fig. 2.8. As for all other SCWR plant designs, the heat exchangers and the turbines are more compact due to the high enthalpy coolant, and steam separation systems and steam generators are not necessary.

The reactor pressure vessel, along with the reactor core, is shown in Fig. 2.9. There is no active component inside the RPV, i.e. no coolant circulation pumps. The inner diameter of the RPV is 4.3 m and the total height is 15 m [46]. On the right hand side of Fig. 2.9, the feed water distribution is shown. Most of the feed water (91.1%) is led to the upper dome and only 8.1% goes through the downcomer at the periphery of the core. The core consists of two regions of fuel assemblies, an inner region and a peripheral region. While the moderating water that is flowing through the water rods (see detailed description below) is always descending, the coolant water in the fuel channels is descending in the peripheral fuel assemblies and ascending in the inner fuel assemblies. The feed water in the upper dome is split between the water rods of the inner and peripheral fuel assemblies (30.0% and 19.7%, respectively), and the fuel channels of

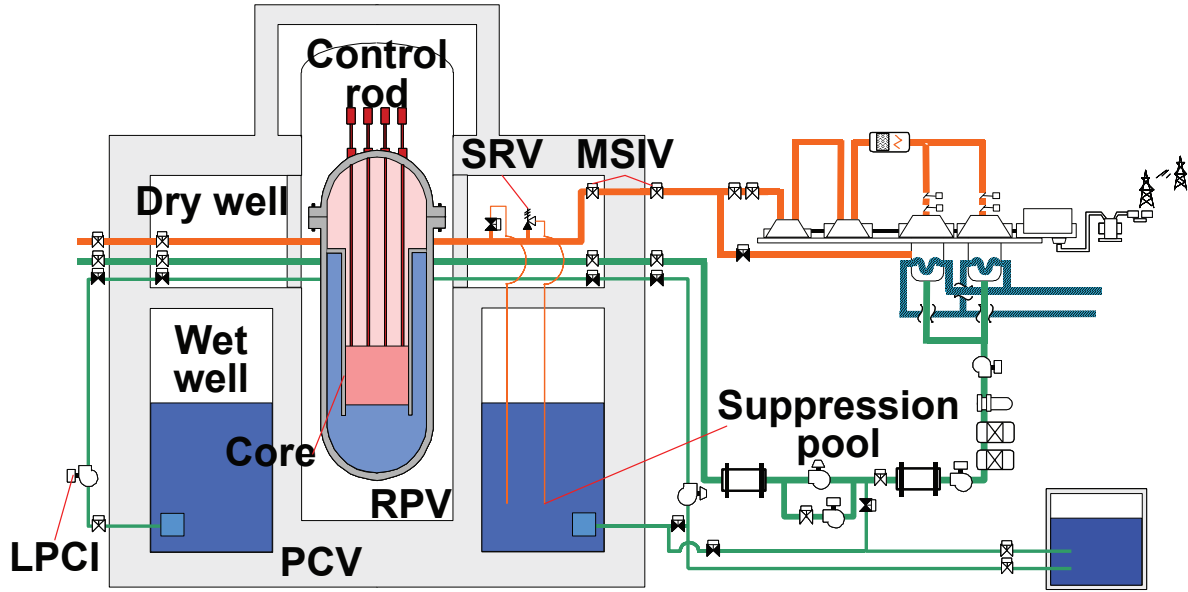


Figure 2.8: Schematic of the latest thermal SCWR power plant design from Japan [46].

the peripheral region (42.2%). After this water has descended through the various channels, it is mixed in the lower plenum with the water from the downcomer, and all the water is led through the fuel channels of the inner fuel assemblies, where it is heated up to 500 °C before it exits the core.

One of the 121 fuel assemblies in the core is shown in Fig. 2.10. It consists of 300 fuel pins which are arranged in a square array. Throughout the assembly, large water rods (also called moderation channels) are inserted, each replacing a 3-by-3 array of fuel pins. 36 of these water rods are inside the array of fuel pins, and an additional 24 rectangular shaped water rods surround the fuel assembly. The fuel pin is similar to an LWR fuel pin and made out of enriched  $\text{UO}_2$ . Its outer diameter is 10.2 mm and it is clad with 0.63 mm of stainless steel. In order to achieve the average discharge burnup of 45 GWd/t, the average fuel enrichment is 6.11%, there being two axial zones of different enrichments. The relatively high average enrichment is necessary because of the higher neutron absorption in the structural material (non-zircaloy cladding) as compared to an LWR. In each assembly, a cluster-type  $\text{B}_4\text{C}$  control rod can be inserted into the 16 central water rods.

The water rods are insulated by means of a layer of  $\text{ZrO}_2$ , which is clad in 0.2 mm stainless steel. This is necessary because of the large temperature difference between the water rods and the fuel channels and the corresponding high thermal stress. In order to compensate for the excess reactivity at the beginning of the cycle (BOC), burnable poison ( $\text{Gd}_2\text{O}_3$ ) is added uniformly to 40 out of the 300 fuel pins of the assembly. These fuel pins are located at the peripheral

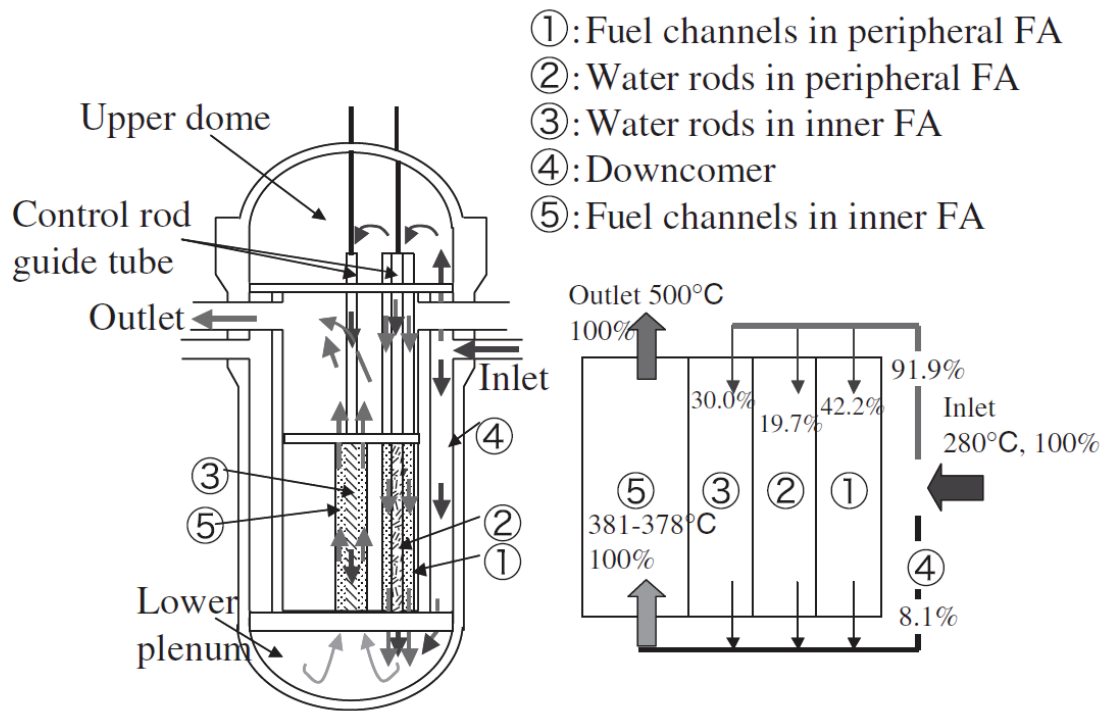


Figure 2.9: Cross section of the reactor pressure vessel of the latest Japanese thermal SCWR design and the water flow scheme through the core [45].

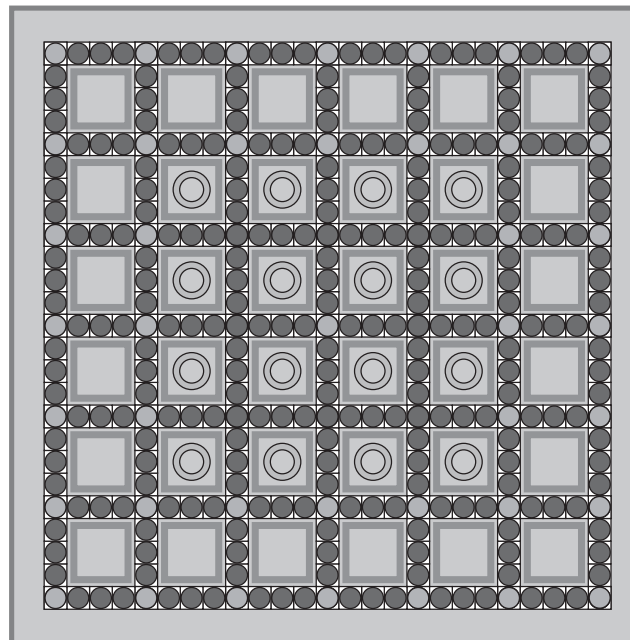


Figure 2.10: Fuel assembly layout of the latest thermal SCWR design from Japan. The dark grey circles depict UO<sub>2</sub> fuel pins and the light circles indicate gadolinium poisoned fuel pins. Control rods are inserted into the 16 central water rods [45].



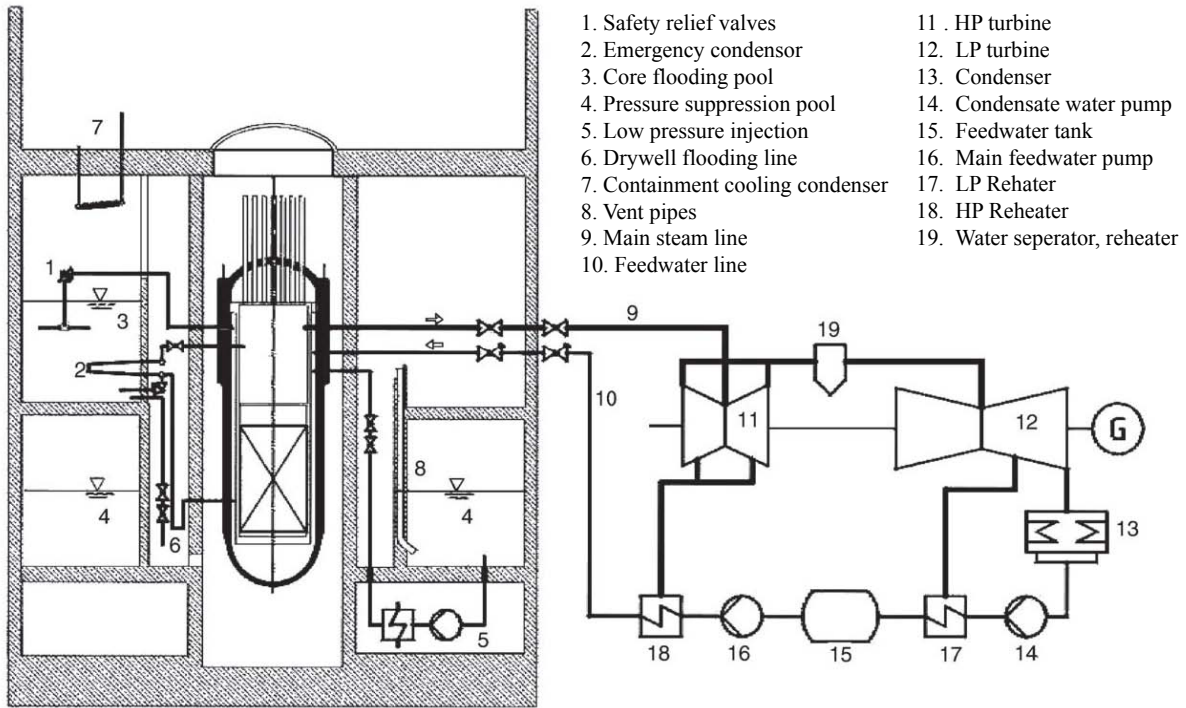


Figure 2.11: Schematic of the European SCWR power plant design, called HPLWR [12].

intersections of columns and rows of fuel pins.

### 2.2.2.2 The European Design

The European version of an SCWR power plant (called an HPLWR, as mentioned earlier) is shown in Fig. 2.11. As in a boiling water reactor, the exiting steam from the RPV is directly fed to the high pressure steam turbine. A heat exchanger between the high pressure and the low pressure steam turbines reheats the supercritical water to approximately 480 °C [12]. The containment is a cylinder of 20 m inner diameter, made out of reinforced concrete and equipped with an inner liner. Following the GIF objectives, major passive safety systems are planned, such as a passive heat removal system as well as a passive flooding system for the RPV.

In order to avoid hot spots which may be caused by a non-uniform power profile and to reach the target coolant outlet temperature, the water traverses the core three times, as illustrated in Fig. 2.12. As for the Japanese design, the water at the core inlet is split up. The majority of it is led to the upper part of the RPV, where it is distributed among all the assemblies as moderator. From there, it flows downward through the moderator channels and between the assemblies, and is then mixed with the remaining part of the feed water that has come through the downcomer to the lower mixing chamber [47]. Up until this point, the water has been heated up from 280 °C to 310 °C. In a second step, all the water ascends through the fuel channels of the 52 assembly clusters in the center of the core, which make up the evaporator where it gets

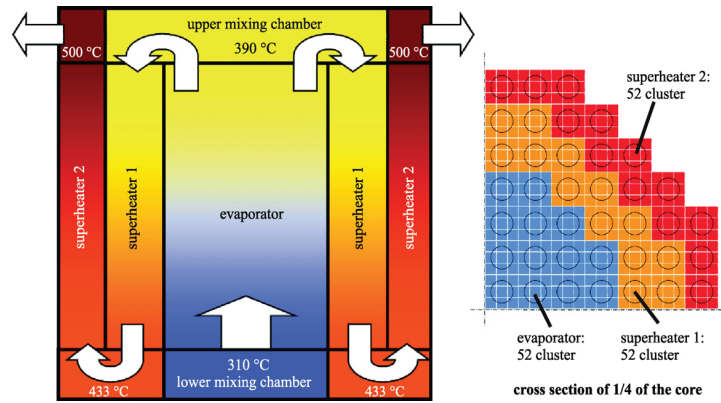


Figure 2.12: The three-pass core concept of the HPLWR, with approximate coolant temperatures on the left and a cross section of the core with the arrangement of fuel assembly clusters on the right [48].

heated up to approximately 390 °C. In the upper mixing chamber, it is mixed by coolant jets and led to the first superheater (another 52 assembly clusters), through which it descends and heats up to 433 °C. As a final step, it once again rises through the 52 assembly clusters at the periphery of the core, which form the second superheater and raise the coolant temperature to the core outlet temperature of 500 °C.

The thermal hydraulic development of the three-pass core and its assemblies is quite advanced, and detailed design proposals have been reported [48]. The RPV is 14.26 *m* high and has an inner diameter of 4.47 *m*. The active height of the core is 4.2 *m*. Its cylindrical shell is made out of 45 *cm* thick stainless steel, and there are four cold and four hot nozzles to transport the coolant.

An HPLWR assembly consists of 40 UO<sub>2</sub> fuel pins, arranged in a 7-by-7 square matrix, with the 9 central pins (3-by-3) replaced by a large moderator box. Fig. 2.13 shows an assembly cluster, where 9 assemblies are grouped together into a single unit in order to ease the handling. The gap between two assemblies is 10 *mm* wide, in order to let enough moderator flow through and ensure that the pins at the periphery of the assembly are as well moderated as the pins close to the inner moderator box, thereby flattening the power profile of the assembly. The fuel pins have an outer cladding diameter of 8 *mm*, with a pitch of 9.44 *mm*. The assembly box wall is made out of stainless steel, has a thickness of 2.5 *mm*, and an outer size of 72.5 *mm*. The inner moderator box is also made out of stainless steel and has an inner side length of 25.3 *mm*.

The complicated path, which the coolant has to go through, brings additional requirements to the fuel assembly design. In order to provide as much flexibility as possible for the burnup optimization, and hence for the reshuffling of assemblies after a power production cycle, it is necessary that the assemblies are designed such that they can be used as evaporator as well as superheater elements. However, the coolant flow direction in the first superheater is opposite to

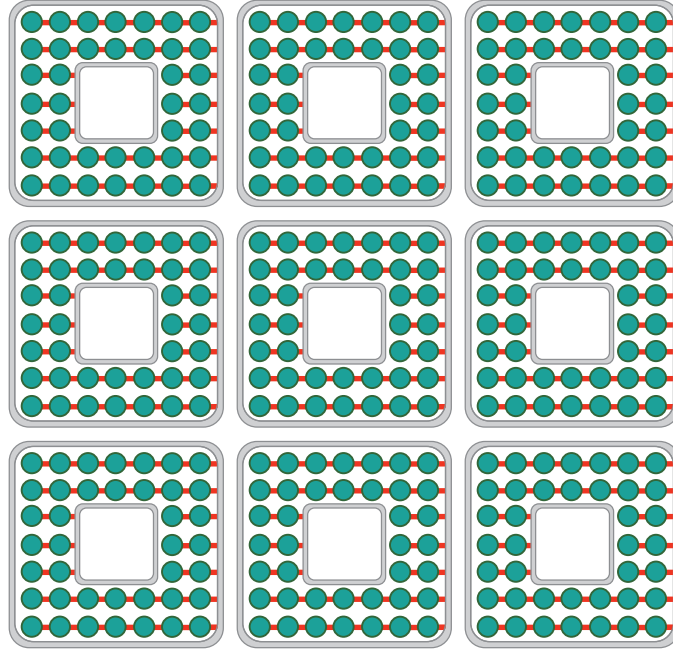


Figure 2.13: Assembly cluster of the European HPLWR, consisting of 9 fuel assemblies. Each assembly consists of 40  $\text{UO}_2$  fuel pins which are wrapped with a wire to avoid hot spots [48].

that in the evaporator and the second superheater, which implies that the spacers need to mix the coolant equally well in both flow directions. Therefore, a single type of wire of 1.34 mm diameter is wrapped around each fuel rod.

The core is controlled by means of control rod spiders, which can be lowered into the assembly clusters. Thereby, a control rod is inserted into the central assembly and into each of the four middle assemblies on the sides of the cluster.

### 2.2.2.3 Other SCWR Concepts

Besides the two furthest-advanced SCWR concepts discussed above, there are three other designs worth mentioning. As indicated earlier, China has recently become active in the field and has proposed an SCWR with a mixed-spectrum core [49]. While for the thermal-spectra SCWR designs, there are concerns in terms of complicated assembly layouts and large hot-channel factors, the fast-spectra designs will have considerable non-uniformities in the circumferential distribution of heat production. The fast spectrum however allows a much higher fuel utilization and a higher power density. In order to overcome the problems of both types of spectra, a mixed-spectrum design has been developed, consisting of a fast zone at the center of the core and a thermal zone at the periphery (see Fig. 2.14).

The feed water (280 °C) is directed into the upper dome of the reactor where it is distributed

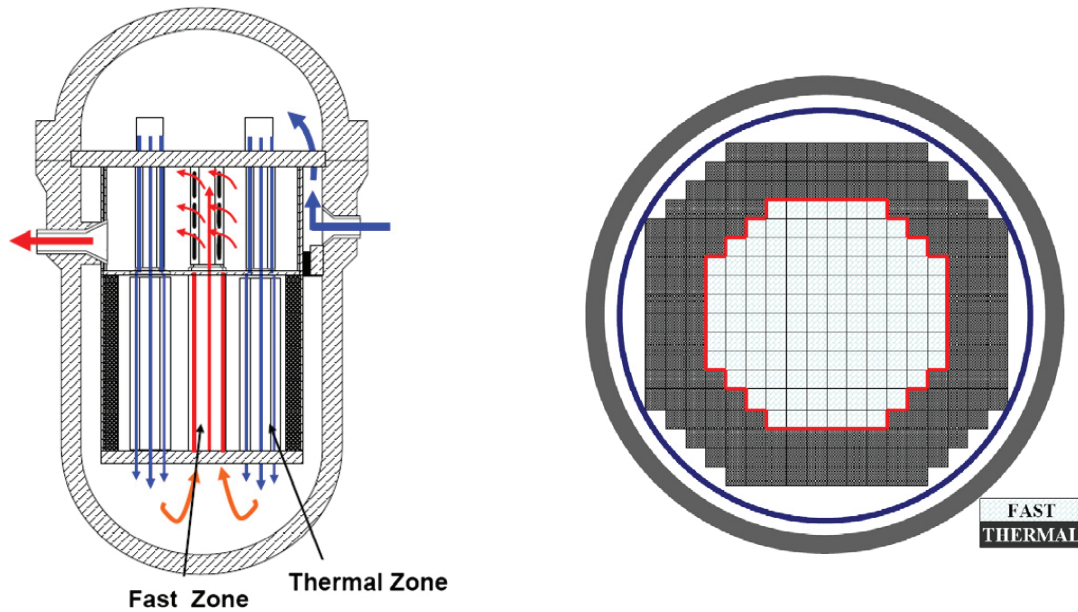


Figure 2.14: Chinese design of a mixed-spectrum SCWR, with the fast zone at the center of the core and the thermal zone at its periphery [49].

among the 164 thermal fuel assemblies. A quarter of the water mass goes through the moderator channels, and the rest descends through the fuel channels to the bottom of the core where it is mixed with the water from the moderator channels. All the water then ascends through the fuel channels of the 120 assemblies of the central fast zone, where it reaches the core exit temperature of  $510\text{ }^{\circ}\text{C}$ . The active height of the thermal zone is  $4.5\text{ m}$ , but the height of the fast zone is only  $2.0\text{ m}$  in order to increase neutron leakage and thus assure a negative void coefficient. The fuel assemblies of the thermal zone are subdivided into axial zones with different enrichments.

The layout of the fuel assemblies of the thermal zone is shown in Fig. 2.15. There are 180 fuel pins in a 18-by-18 square matrix with 9 large moderator channels, each replacing a 4-by-4 array of pins. The basic difference between the Chinese and the Japanese assembly designs is that in the Japanese layout the rows and columns of fuel pins are only a single pin thick. Therefore, the fuel pins in the center of the assembly have a moderator channel on either side, while the pins at the periphery have only one moderator channel adjacent to them. This leads to a non-uniform radial power distribution in the assembly [44]. To flatten the power distribution, the Chinese design has two fuel-pin thick columns and rows in the assembly, surrounded by a single-pin thick border. When putting two assemblies next to each other, the moderator is evenly distributed among all the regions of the assembly.

The Korea Atomic Energy Research Institute (KAERI) has proposed a modified version of the Japanese SCLWR-H [27] called the SCWR-R. In order to reduce the hot channel coefficient of the core, an internal coolant recirculation system has been introduced. Jet pumps installed in the downcomer of the reactor cause the coolant to recirculate between the core and the downcomer [43]. The basic reactor layout is given in Fig. 2.16, along with an eighth-assembly illustration.  $\text{UO}_2$  fuel pins of different enrichments are distributed in the  $21 \times 21$  square fuel pin array with a

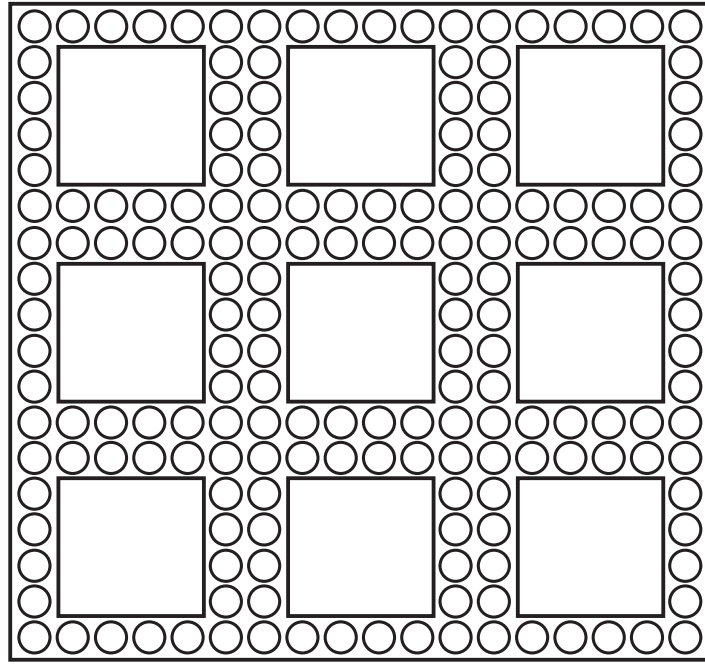


Figure 2.15: The Chinese fuel assembly design, with two fuel-pin thick columns and rows of fuel inside the lattice and a single-pin thick border [44].

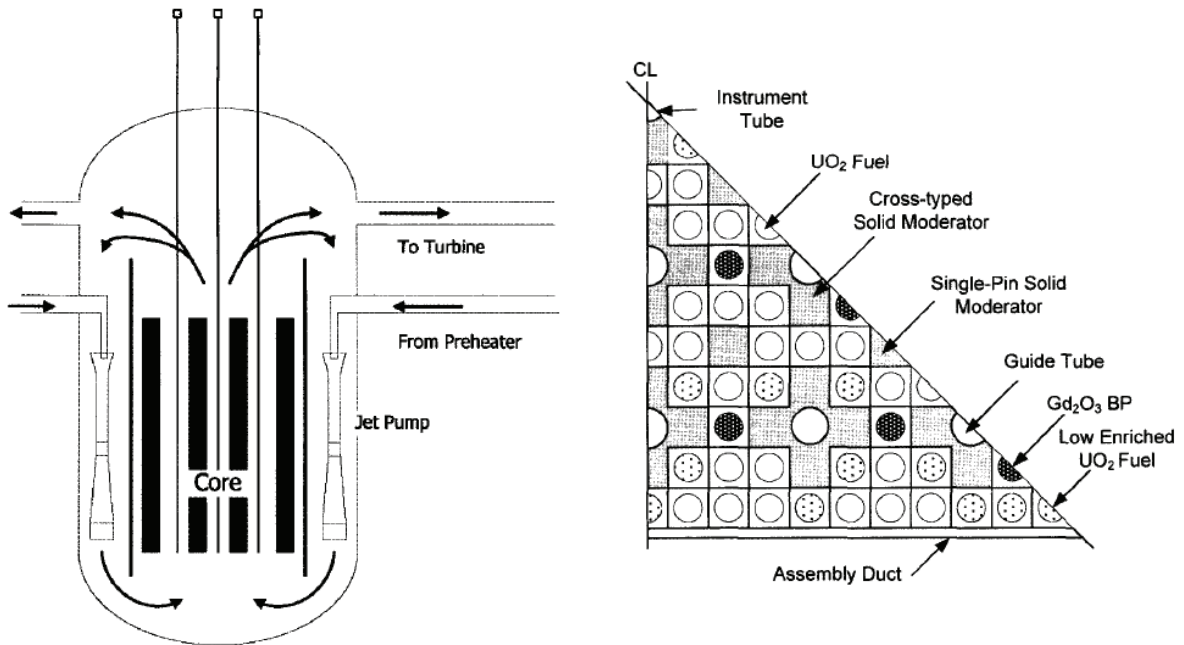


Figure 2.16: The SCWR-R design proposal from the Korea Atomic Energy Research Institute [43]. This is a modified version of the Japanese SCLWR-H with an additional coolant recirculation system inside the reactor.

pitch of 1.15 *cm*. The assembly consists of 300 fuel pins, 25 cruciform solid-moderator pins, and 16 single solid-moderator pins. The fuel pins are axially divided into three different enrichment zones. As solid moderator,  $\text{ZrH}_2$  is used. Additionally, fuel pins containing 10 w% of gadolinium as burnable poison are inserted into the assembly. Their number depends on the axial zone as well.

As mentioned earlier, Canada has been developing the SCWR version of the CANDU reactor [35]. The envisaged electrical power is 1220 *MW* with a thermal efficiency of 48%. This is achieved with a core outlet temperature of 625 °C. Compared to LWRs, the CANDU reactor is more flexible from the viewpoint of employing supercritical water as coolant, because of its pressure tube concept which already separates the coolant from the moderating heavy water. Therefore, the fuel assembly design does not have to be re-engineered in a fundamental sense as is the case for the LWR assemblies. However, increasing the system pressure and the coolant temperature still requires considerable R&D work on the materials side.

### 2.2.3 The SCWR-like Lattice in PROTEUS

The SCWR-like lattice inserted into the PROTEUS test zone is depicted on the right hand side of Fig. 2.17. The experiments reported on in this thesis were conducted using this test lattice. It is based on the Japanese SCWR assembly design proposed by Yamaji et al in 2001 [13], which is shown on the left hand side of Fig. 2.17. The  $\text{UO}_2$  fuel pins available for constructing the test zone (the standard PROTEUS driver fuel, see Sec. 2.1) were slightly larger (outer diameter of 12.2 *mm* instead of 10.2 *mm*). Furthermore, for reasons related to operational safety margins in PROTEUS, the outermost “ring” of pins had to be omitted (see Fig. 2.17 caption).

The fuel is fresh 5% enriched  $\text{UO}_2$  of 932 *mm* active height. The diameter of the  $\text{UO}_2$  pellets is 10.16 *mm* and they are clad in 1 *mm* thick aluminum. The fuel pins are held in position by a lattice ground plate and two lattice spacer plates. There are 105 fuel pins in the PROTEUS test lattice layout (The difference of 80 fuel pins, as compared to the Yamaji lattice, comes from omitting the outermost ring of pins). The 16 moderator channels each replace a 4-by-4 array of fuel pins. However, there are no structural walls introduced into the PROTEUS test lattice, so that there is no physical separation between the “coolant” of the fuel channels and the moderator in the moderation channels. There is effectively a single liquid employed, namely a mixture of 67.2%  $\text{H}_2\text{O}$  and 32.8%  $\text{D}_2\text{O}$ , to approximately simulate the water density of a PWR at operating temperature.

Due to the homogeneous enrichment and square geometry of the assembly, the system has an octagonal symmetry. Ignoring the boundary effects, the lattice becomes even more symmetric. In fact, there are only three generic fuel pin positions, which are constantly repeated. These generic pin positions are:

- The fuel pins at the intersections of rows and columns of pins (*corner pins*).

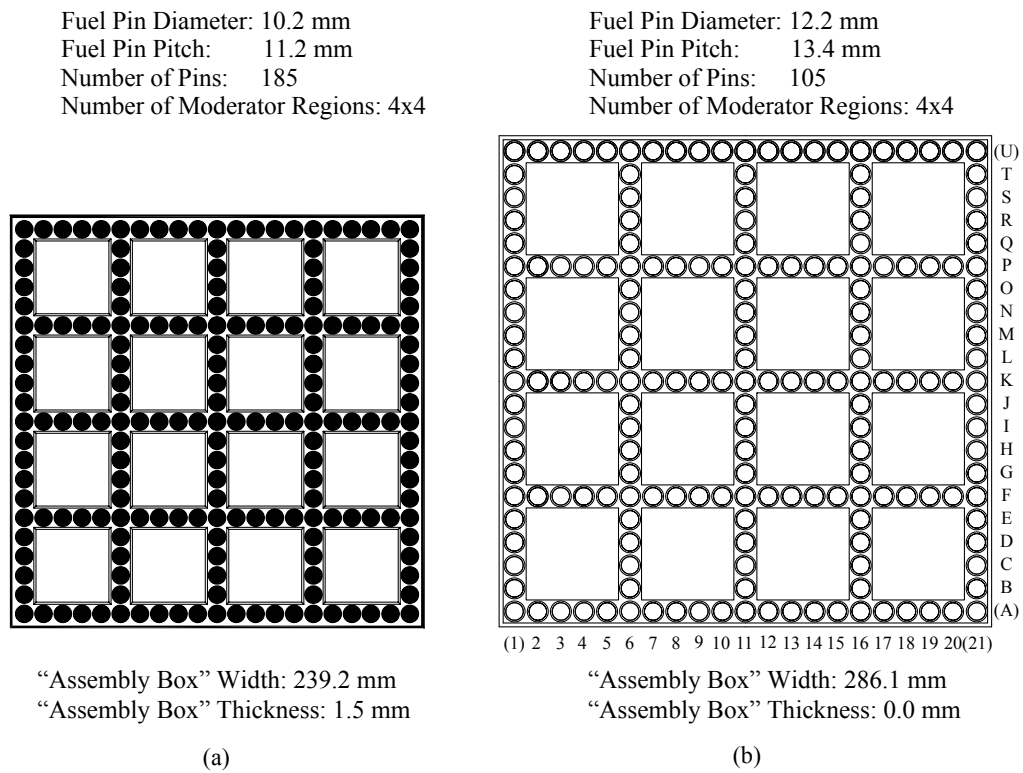


Figure 2.17: (a) Square SCWR fuel assembly proposed by Yamaji et al., 2001 [13]; (b) Reference test lattice used in PROTEUS (the outermost columns (1 & 21) and rows (A & U) of fuel pins had to be omitted in the actually implemented test zone, as indicated by the indices in brackets).

- The fuel pins neighboring a corner pin (*neighbors* or *neighboring pins*).
- The fuel pins which are not adjacent to one of the corner pins. Due to their large distance from the corner pins: *remotes* or *remote pins*.

The experiments, which have served as basis for code validation, were done on this test lattice, with and without specific perturbations being considered. The measured configurations are described in detail in the next chapter, along with the employed measurement techniques.



# Bibliography

- [1] H. Kröhnert, G. Perret, M.F. Murphy, and R. Chawla. Freshly Induced Short-Lived Gamma-Ray Activity as a Measure of Fission Rates in Lightly Re-Irradiated Spent Fuel. *Nuclear Instruments and Methods in Physics Research Section A*, 624:101–108, 2010.
- [2] M.F. Murphy, G. Perret, O. Köberl, K.A. Jordan, P. Grimm, H. Kröhnert, and M.A. Zimmermann. Large Scale Irradiated Fuel Experiments at PROTEUS Research Program. In *PHYSOR 2010 - Advances in Reactor Physics to Power the Nuclear Renaissance, Pittsburgh, Pennsylvania, USA*, 2010.
- [3] T. Williams, R. Chawla, P. Grimm, O.P. Joneja, R. Seiler, and A.K. Ziver. LWR-PROTEUS - New Experiments at a Zero-Power Facility Using Power Reactor Fuel. In *Proceedings of International Conference on the Physics of Nuclear Science and Technology, Long Island, New York, USA*, pages 720–727, 1998.
- [4] F. Jatuff, P. Grimm, O. Joneja, M. Murphy, A. Lüthi, R. Seiler, R. Brogli, R. Jacot-Guillarmod, T. Williams, S. Helmersson, and R. Chawla. LWR-PROTEUS Verification of Reaction Rate Distributions in Modern 10 x 10 Boiling Water Reactor Fuel. *Nuclear Science and Engineering*, 139:262–272, 2001.
- [5] M. Murphy, A. Lüthi, R. Seiler, P. Grimm, O. Joneja, A. Meister, R. van Geemert, F. Jatuff, R. Brogli, R. Jacot-Guillarmod, T. Williams, S. Helmersson, and R. Chawla. Neutronics Investigations for the Lower Part of a Westinghouse SVEA-96+ Assembly. *Nuclear Science and Engineering*, 141:32–45, 2002.
- [6] R. Chawla A. Meister, P. Grimm. Neutronics Design of LWR-PROTEUS Phase II High-Burnup Fuel Reactivity Measurements. In *Transactions of the American Nuclear Society*, 85, pages 268–269, 2001.
- [7] M.F. Murphy, F. Jatuff, P. Grimm, R. Seiler, R. Brogli, G. Meier, H.-D. Berger, and R. Chawla. Reactivity and Neutron Emission Measurements of Highly Burnt PWR Fuel Rod Samples. *Annals of Nuclear Energy*, 33:760–765, 2006.
- [8] F. Jatuff. Experimental Test Matrix of the LWR-PROTEUS Phase III Experiments. Technical Report AN-41-04-02, Paul Scherrer Institute, Villigen, Switzerland, March 2004.

- [9] M.F. Murphy, F. Jatuff, G. Perret, M. Plaschy, U. Bergmann, and R. Chawla. Comparison of 3D Reaction Rate Distributions Measured in an Optima2 BWR Assembly with MCNPX Predictions. *Annals of Nuclear Energy*, 35:2042–2050, 2008.
- [10] G. Perret, M. Plaschy, M.F. Murphy, F. Jatuff, and R. Chawla. Characterisation of Radial Reaction Rate Distributions Across the 92-Pin Section of a SVEA-96 Optima2 Assembly. *Annals of Nuclear Energy*, 35:478–484, 2008.
- [11] K.A. Jordan and G. Perret. A Delayed Neutron Technique for Measuring Induced Fission Rates in Fresh and Burnt LWR Fuel. *Nuclear Instruments and Methods in Physics Research Section A*, 634:91–100, 2011.
- [12] D. Squarer, T. Schulenberg, D. Struwe, and Y. Oka. High performance light water reactor. *Nuclear Engineering and Design*, 221:167–180, 2003.
- [13] A. Yamaji, Y. Oka, and S. Koshizuka. Conceptual core design of a 1000MWe supercritical pressure light water cooled and moderated reactor. In *ANS/HPS Student Conference, Texas A&M University*, 2001.
- [14] U.S. DOE Nuclear Energy Research Advisory Committee and the Generation IV International Forum. A Technology Roadmap for Generation IV Nuclear Energy Systems. Technical Report GIF-002-00, December 2002.
- [15] J. Buongiorno. The Supercritical-Water-Cooled Reactor (SCWR). In *In Proceedings of: American Nuclear Society, 2002 Winter Meeting*, 2002.
- [16] Y. Oka, S. Koshizuka, Y. Ishiwatari, and A. Yamaji. Overview of Design Studies of High Temperature Reactor Cooled by Supercritical Light Water at the University of Tokyo. In *Proceedings of International Conference on Global Environment and Advanced Nuclear Power Plants (GENES4/ANP2003), Kyoto, Japan*, page 1168, 2003.
- [17] General Electric. Supercritical pressure power reactor, A conceptual design. Technical Report HW-59684, Hanford Laboratories, General Electric, 1959.
- [18] J.F. Marchaterre and M. Petrick. Review of the Status of Supercritical Water Reactor Technology. Technical Report ANL-6202, Argonne National Laboratory, 1960.
- [19] Y. Oka. Review of High Temperature Water and Steam Cooled Reactor Concepts. In *The First International Symposium on Supercritical Water-cooled Reactors. Design and Technology, SCR-2000, University of Tokyo, Japan*, 2000.
- [20] G.R. Dimmick, N.J. Spinks, and R. Duffey. An Advanced CANDU Reactor with Supercritical Water Coolant: Conceptual Design Features. In *The 6th International Conference on Nuclear Engineering, San Diego, California*, 1998.

- 
- [21] V.A. Silin, V.A. Voznesensky, and A.M. Afrov. The Light Water Integral Reactor with natural circulation of the coolant at supercritical pressure B-500 SKDI. *Nuclear Engineering and Design*, 144:327–336, 1993.
- [22] Y. Oka, S. Koshizuka, and T. Yamasaki. Direct Cycle Light Water Reactor Operating at Supercritical Pressure. *Journal of Nuclear Science and Technology*, 29(6):585–588, 1992.
- [23] Y. Okano, S. Koshizuka, and Y. Oka. Design of Water Rod Cores of a Direct Cycle Supercritical-Pressure Light Water Reactor. *Annals of Nuclear Energy*, 21(10):601–611, 1994.
- [24] Y. Okano, S. Koshizuka, and Y. Oka. Core Design of a Direct-Cycle, Supercritical-Pressure, Light Water Reactor with Double Tube Water Rods. *Journal of Nuclear Science and Technology*, 33:365–373, 1996.
- [25] S. Tanaka, Y. Shirai, and M. Mori. Core Design of Supercritical-Pressure Light Water Reactor. In *Proceedings of 4th International Conference on Nuclear Engineering (ICONE-4)*, New Orleans, USA, pages 199–211, 1996.
- [26] K. Dobashi, Y. Oka, and S. Koshizuka. Core and Plant Design of the Power Reactor Cooled and Moderated by Supercritical Light Water with Single Tube Water Rods. *Annals of Nuclear Energy*, 24(16):1281–1300, 1997.
- [27] K. Dobashi, A. Kimura, Y. Oka, and S. Koshizuka. Conceptual Design of a High Temperature Power Reactor Cooled and Moderated by Supercritical Light Water. *Annals of Nuclear Energy*, 25(8):487–505, 1998.
- [28] Y. Oka and K. Kataoka. Conceptual Design of a Fast Breeder Reactor Cooled by Supercritical Steam. *Annals of Nuclear Energy*, 19:243, 1992.
- [29] T. Jevremovic, Y. Oka, and S. Koshizuka. Design of an Indirect-Cycle Steam Cooled Fast Breeder Reactor. *Nuclear Engineering and Design*, 144:337, 1993.
- [30] Y. Oka, T. Jevremovic, and S. Koshizuka. A Direct-Cycle, Supercritical-Water-Cooled Fast Breeder Reactor. *Journal of Nuclear Science and Technology*, 31:83, 1994.
- [31] T. Jevremovic, Y. Oka, and S. Koshizuka. Core Design of a Direct-Cycle, Supercritical-Water-Cooled Fast Breeder Reactor. *Nuclear Technology*, 108:24–32, 1994.
- [32] T. Mukohara, S. Koshizuka, and Y. Oka. Core Design of a High-Temperature Fast Reactor Cooled by Supercritical Light Water. In *Proceedings of the 6th International Conference on Nuclear Engineering (ICONE-6)*, San Diego, USA, 1998.
- [33] Y. Oka, K. Nomura, S. Koshizuka, and T. Mukohara. Supercritical-Pressure Light Water Cooled Fast Reactor, A Competitive Way of FR over LWR. In *Proceedings of the 8th*

- International Conference on Nuclear Engineering (ICONE-8), Baltimore, USA, 2000.*
- [34] H.F. Khartabil, R.B. Duffey, N. Spinks, and W. Diamond. The Pressure-Tube Concept of Generation IV Supercritical Water-Cooled Reactor (SCWR): Overview and Status. In *Proceedings of 2005 International Congress on Advances in Nuclear Power Plants (ICAPP'05), Seoul, Korea, 2005.*
  - [35] D.F. Torgerson, B.A. Shalaby, and S. Pang. CANDU technology for Generation III+ and IV reactors. *Nuclear Engineering and Design*, 236:1565–1572, 2006.
  - [36] T.T. Yi, S. Koshizuka, and Y. Oka. A Linear Stability Analysis of Supercritical Water Reactors, (I) Thermal Hydraulic Stability. *Journal of Nuclear Science and Technology*, 41(12):1166–1175, 2004.
  - [37] T.T. Yi, S. Koshizuka, and Y. Oka. A Linear Stability Analysis of Supercritical Water Reactors, (II) Coupled Neutronic Thermal Hydraulic Stability. *Journal of Nuclear Science and Technology*, 41(12):1176–1186, 2004.
  - [38] J. Yoo, Y. Oka, Y. Ishiwatari, J. Yang, and J. Liu. Subchannel analysis of supercritical light water-cooled fast reactor assembly. *Nuclear Engineering and Design*, 237:1096–1105, 2007.
  - [39] L. Cao, Y. Oka, Y. Ishiwatari, and Z. Shang. Fuel, Core Design and Subchannel Analysis of a Superfast Reactor. *Journal of Nuclear Science and Technology*, 45(2):138–148, 2008.
  - [40] L. Cao, Y. Oka, Y. Ishiwatari, and S. Ikejiri. Three-dimensional core analysis on a super fast reactor with negative local void reactivity. *Nuclear Engineering and Design*, 239:408–417, 2009.
  - [41] S. Ikejiri, Y. Ishiwatari, and Y. Oka. Safety analysis of a supercritical-pressure water-cooled fast reactor under supercritical pressure. *Nuclear Engineering and Design*, 240:1218–1228, 2010.
  - [42] H.-O. Kang and Y.-Y. Bae. Conceptual Design of a Supercritical Water-Cooled Reactor with an Internal Recirculating Flow. In *Proceedings of International Conference on Global Environment and Advanced Nuclear Power Plants (GENES4/ANP2003), Kyoto, Japan, page 1023, 2003.*
  - [43] Y.-Y. Bae, J. Jang, H.-Y. Kim, H.-Y. Yoon, H.-O. Kang, and K.-M. Bae. Research Activities on a Supercritical Pressure Water Reactor in Korea. *Nuclear Engineering and Technology*, 39(4):273–286, 2007.
  - [44] X.J. Liu and X. Cheng. Thermal-Hydraulic and Neutron-Physical Characteristics of a new SCWR Fuel Assembly. *Annals of Nuclear Energy*, 36:28–36, 2009.
  - [45] K. Kamei, A. Yamaji, Y. Ishiwatari, Y. Oka, and J. Liu. Fuel and Core Design of Super

- Light Water Reactor with Low Leakage Fuel Loading Pattern. *Journal of Nuclear Science and Technology*, 43(2):129–139, 2006.
- [46] A. Shioiri, K. Moriya, Y. Oka, H. Mori, and H. Takahashi. Development of Supercritical-water Cooled Power Reactor Conducted by a Japanese Joint Team. In *Proceedings of International Conference on Global Environment and Advanced Nuclear Power Plants (GENES4/ANP2003)*, Kyoto, Japan, page 1121, 2003.
- [47] T. Schulenberg, J. Starflinger, and J. Heinecke. Three pass core design proposal for a high performance light water reactor. *Progress in Nuclear Energy*, 50:526–531, 2008.
- [48] K. Fischer, T. Schulenberg, and E. Laurien. Design of a Supercritical Water-Cooled Reactor with a Three-Pass Core Arrangement. *Nuclear Engineering and Design*, 239:800–812, 2009.
- [49] X.J. Liu, T. Yang, and X. Cheng. Core and Sub-Channel Analysis of SCWR with Mixed Spectrum Core. *Annals of Nuclear Energy*, 37:1674–1682, 2010.



## 3 Experiments and Measurement Techniques

Integral experiments play an important role in the validation of calculational methods and nuclear data libraries. There is a large variety of parameters which can be analyzed, starting from the critical size of a core to safety parameters such as the shut-down worth of safety rods and power distributions in the core. Integral measurements are important because they provide complementary information to differential experiments which are usually carried out at accelerator-based facilities and build the basis for generation of the nuclear data libraries. Integral experiments, on the other hand, give indications on the performance and accuracy of the entire calculational system under consideration. The most frequently measured integral parameters are the effective multiplication factor  $k_{\text{eff}}$ , reaction rates (fission and capture), and reactivity coefficients (e.g. the void coefficient). Kinetic parameters, such as the delayed neutron fraction  $\beta_{\text{eff}}$  and the generation time  $\Lambda$ , are measured in certain dedicated experiments. Throughout this thesis, focus is laid on measuring reaction rate distributions and reactivity effects.

This chapter is divided into three parts. The first section introduces the PROTEUS test zone configurations that were investigated. The techniques to measure reaction rate distributions in the fuel lattice are discussed in Section 2. Finally, Section 3 describes the measurement technique for the reactivity effect of removing a fuel pin from the lattice.

### 3.1 PROTEUS Test Zone Configurations

To achieve the main goal of the thesis – the validation of deterministic and probabilistic nuclear design codes for an SCWR-like fuel lattice – the central test zone of the PROTEUS reactor (see Subsec. 2.1) was loaded with the reference SCWR-like fuel lattice described in Subsec. 3.1.1. This lattice is referred to as unperturbed lattice. To expand the validation base for the computer codes, the assembly was perturbed in various ways (detailed in Subsections 3.1.2 - 3.1.5).

There are two levels of heterogeneities present in the perturbed lattices. The first level is the heterogeneity of the lattice itself, where the matrix of fuel pins is not tightly filled but has several large moderator areas where no fissile material is present (see Subsec. 2.2.3). This has strong effects on the neutron flux profile across the lattice. The second level of heterogeneity corresponds

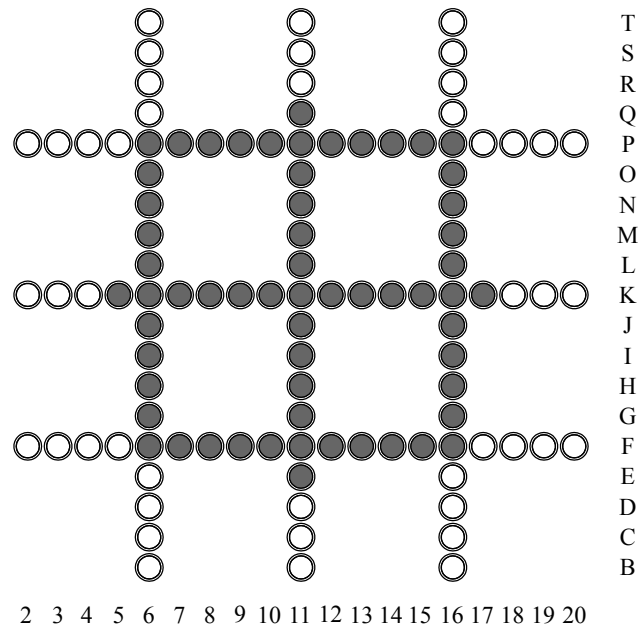


Figure 3.1: Schematic view of the unperturbed test lattice implemented in PROTEUS. The dark grey shaded circles indicate the fuel pins that were measured during the campaign.

to the perturbations themselves which superimpose a local perturbation of the neutron flux upon the already strongly varying neutron flux profile of the unperturbed fuel lattice.

### 3.1.1 Unperturbed Lattice

The unperturbed configuration provides the basis for the present series of experiments. As mentioned, the reference SCWR-like test lattice, discussed in Subsec. 2.2.3, was inserted into the central experimental region of PROTEUS (see Subsection 2.1). Fig. 3.1 illustrates the arrangement of fuel pins and moderator regions of this lattice. The dark grey shaded circles indicate fuel pins that were measured during the campaign. Out of the 105 fuel pins present in the lattice, 61 were measured.

### 3.1.2 Control-Rod Insertion Effects

The insertion of control rods is one of the most relevant perturbations of an SCWR lattice. Ishiwatari et al. [1] proposed in 2003 to insert control rods in the moderator channels. This seems to be the natural choice since the thermal neutron flux has a maximum there and hence does the efficiency of the control rod.

Fig. 3.2 shows a schematic view of the inserted rod positions considered. Four identical rods were introduced into the middle of the four central moderator channels of the unperturbed lattice. They were of similar length (98 cm) as the fuel pins of the experimental region (93 cm) and had



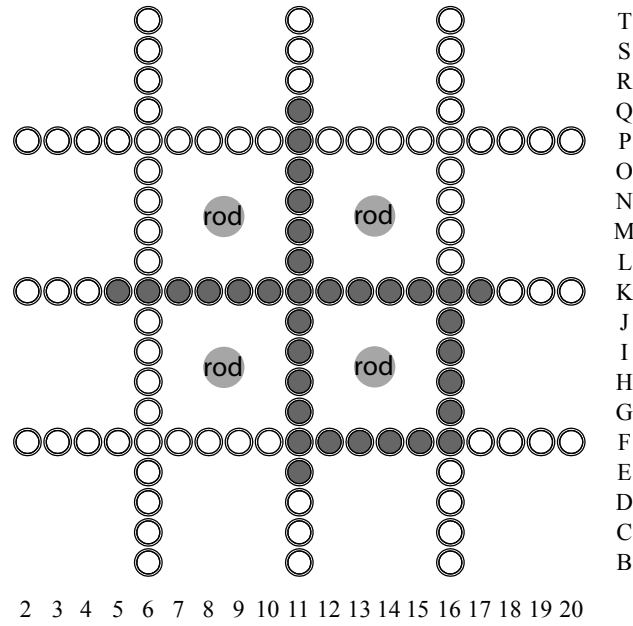


Figure 3.2: Schematic view of the test lattice implemented in PROTEUS, perturbed by four rods inserted into the central moderator channels. The dark grey shaded circles indicate the fuel pins that were measured during the campaign.

a diameter of 2 *cm*.

The insertion of a control rod into a moderator channel has two simultaneous effects that influence the reactivity of the system: the introduction of neutrons absorbing material, and the displacement of moderator which changes the neutron balance and increases the leakage of the system. In order to separate the two effects, two kinds of experimental rods were inserted into the lattice.

The first measurement campaign was conducted for a test lattice configuration with four inserted aluminum rods of 2 *cm* diameter. Each of these was positioned at the exact center of one of the central moderator regions via a conical extension attached to the bottom of the rod, which fitted into the lattice ground plate. Aluminum was chosen because of its low neutron absorption cross-section. The first-order effect of the rods is thus simply moderator displacement. Such use of aluminum is a traditional technique for void simulation in LWR critical experiments [2].

In the second perturbed test lattice configuration related to control rod effects, four steel rods were inserted at the same positions. Their diameters were also 2 *cm*, so that the moderator displacement effect was the same as in the case of the aluminum rods. Steel was chosen in order to observe the absorption effect on the neutron flux, while keeping the change in reactivity of the PROTEUS reactor below certain operational limits (the difference in  $k_{\text{eff}}$  values should be below \$3). The two separate measurement campaigns - with aluminum and steel rods, respectively - enabled a clear separation of the effects of moderator displacement and parasitic absorption.

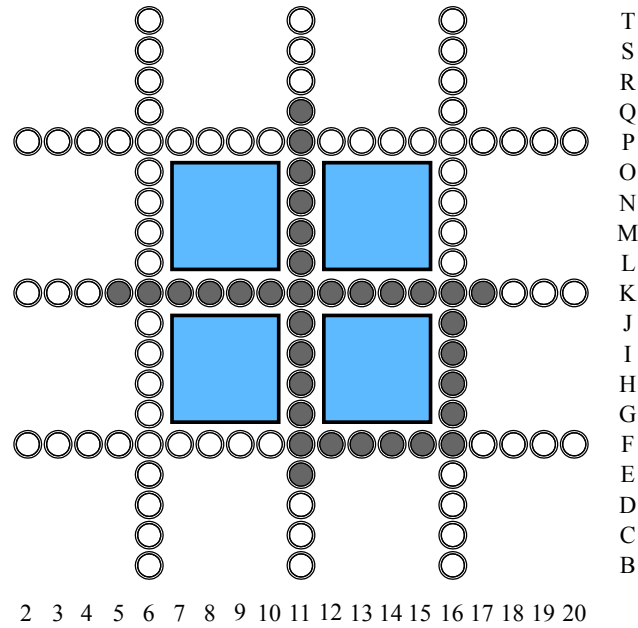


Figure 3.3: Schematic view of the test lattice implemented in PROTEUS, perturbed by four water tanks. The dark grey shaded circles indicate the fuel pins that were measured during the campaign.

### 3.1.3 Insertion of Water Tanks

One important aspect of the SCWR is the different densities of moderator and coolant (both are light water). In order to further increase the efficiency of the moderator regions, the proposed SCWR designs aim at keeping the high density water in the moderator channels separated from the low density water in the cooling channels around the fuel pins through the use of appropriate structural materials. A fraction of the inlet water would enter the reactor vessel above the active core and descend through the moderator channels. It would then get mixed with the rest of the inlet water below the core and finally rise in the cooling channels to the water outlet. When considering a given horizontal plane across the lattice, one thus has lower density coolant adjacent to higher density moderator. This effect is largest at the top of the core, where the moderator has just entered the reactor vessel and the coolant has already passed the entire core and is close to the outlet. It is smallest at the bottom, where the moderator is mixed with inlet water and becomes coolant.

Jatuff et al. [3] have indicated that CASMO-4 and MCNP4C disagree in situations where the water densities vary locally and heterogeneously. Accordingly, the related investigations have considered the effect of partially changing the moderator density in the central section of the SCWR-like test lattice implemented in PROTEUS. This has been achieved by inserting “water tanks” into the four central moderator channels of the test lattice (see Fig. 3.3). The water tanks can be filled with different mixtures of  $H_2O$  and  $D_2O$  in order to simulate specific hydrogen densities and hence, the corresponding moderation efficiencies. The reference mixture in PROTEUS is 32.8%  $D_2O$  and 67.2%  $H_2O$ , which roughly corresponds to the hydrogen density in an oper-

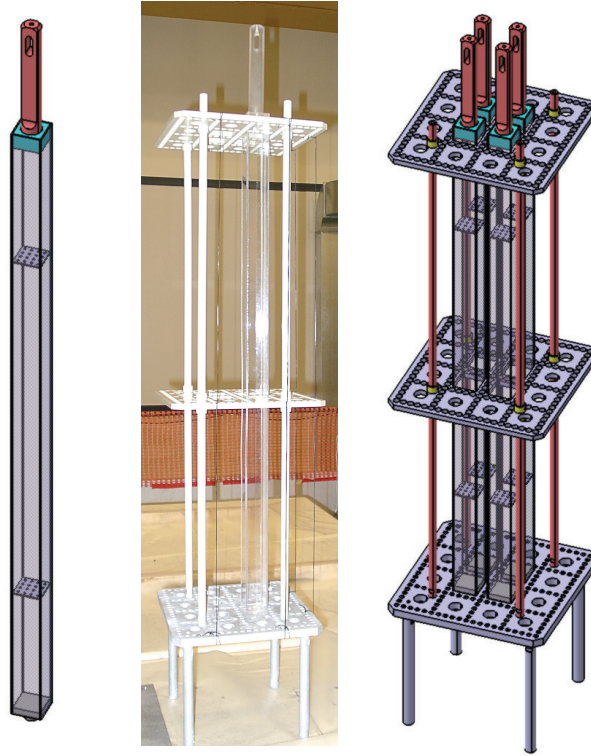


Figure 3.4: The water tanks that were inserted into the PROTEUS test lattice. Schematic of a water tank, on the left hand side; the lattice spacer-plates with an inserted water tank, in the middle; a three-dimensional view of the lattice structure with the inserted water tanks, on the right hand side.

ating pressurized water reactor (PWR). To reduce the perturbing influence on the neutron flux of the structural material, the water tanks were made out of polycarbonate (Makrolon<sup>®</sup>). The hydrogen density of Makrolon<sup>®</sup> ( $0.066 \text{ g/cm}^3$ ) is similar to that of the water mix in PROTEUS ( $0.077 \text{ g/cm}^3$ ). More importantly, there is no strong neutron absorbing isotopes in Makrolon<sup>®</sup>, which is crucial for having representative measurements.

The unusual dimensions of the water tanks ( $46 \text{ mm} \times 46 \text{ mm} \times 1020 \text{ mm}$ ; see Fig. 3.4), along with the additional requirement of making the walls as thin as possible ( $2 \text{ mm}$ ), were challenging and demanded a custom-made production. Each side of the tank was cut out of a polycarbonate plate. The sides were glued together using Acrifix 192<sup>®</sup> which is an organic compound (methyl methacrylate) that would not perturb the neutron flux, since its hydrogen density is comparable with that of the moderator. In order to provide more stiffness to the structure, two support plates of  $2 \text{ mm}$  thickness were glued into the tank  $200 \text{ mm}$  above the bottom and  $200 \text{ mm}$  below the top (see left hand side of Fig. 3.5). Holes were drilled into the support plates so that the liquid could get passed them.

The top part of each water tank consists of a glued-in, square-shaped plug with a handle which can be screwed into a matching drilling in the plug (see middle of Fig. 3.5). The handle can be removed in order to fill the tank with a mixture of  $\text{H}_2\text{O}$  and  $\text{D}_2\text{O}$ . An O-ring is placed

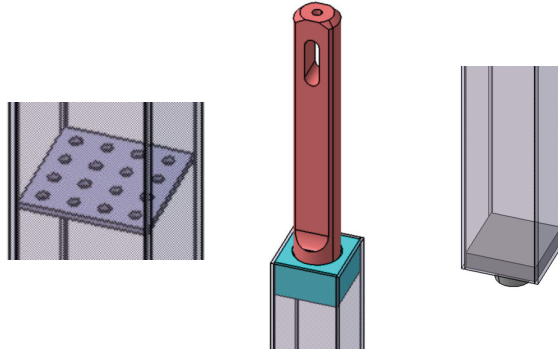


Figure 3.5: Details of the inserted water tanks: on the left, one of two support plates to provide more stiffness to the tank; in the middle, the top plug with the screwed-in handle; on the right, the bottom plug with the conical foot to secure the tank's position in the lattice ground-plate.

between handle and plug to seal the tank. Another glued-in plug seals the water tank at the bottom (right hand side of Fig. 3.5). A conical foot is attached below this plug, such as to fit into the lattice ground-plate and ensure the water tank's correct positioning at the center of the moderator channel.

The outer width of the water tank was 46 mm, only 1 mm smaller than the drilling in the lattice spacer plates. Major difficulties in the production of the tanks were experienced due to the combination of the challenging dimensions and the needed watertightness. The possible occurrence of a leak in one of the water tanks had to be ruled out due to the change of reactivity that a mixing of the fluids could induce. To test the water tanks for leak-tightness they were filled with food-dyed water and laid (horizontally) on blotting paper, such as to show colored areas around the leaks. After identifying the leaks, these were sealed by grinding away a part of the polycarbonate and applying more glue.

To represent possible operating conditions in an SCWR, two mixtures of  $\text{H}_2\text{O}$  and  $\text{D}_2\text{O}$  different from the earlier mentioned standard mixture (67.2%  $\text{H}_2\text{O}$  and 32.8%  $\text{D}_2\text{O}$ ) were filled into the water tanks. These provided the following two perturbed test zone configurations:

1. The water tanks were filled with pure  $\text{H}_2\text{O}$ . The moderator channels in the center thus had a higher hydrogen density than the coolant channels surrounding the fuel pins and the moderator areas at the periphery of the assembly. This is the type of situation that would occur in an SCWR with counter-flowing moderator and coolant under normal operating conditions.
2. The water tanks were filled with a mixture of 66%  $\text{D}_2\text{O}$  and 34%  $\text{H}_2\text{O}$ . In this case, the hydrogen density in the moderator tank approaches the coolant density of an SCWR.

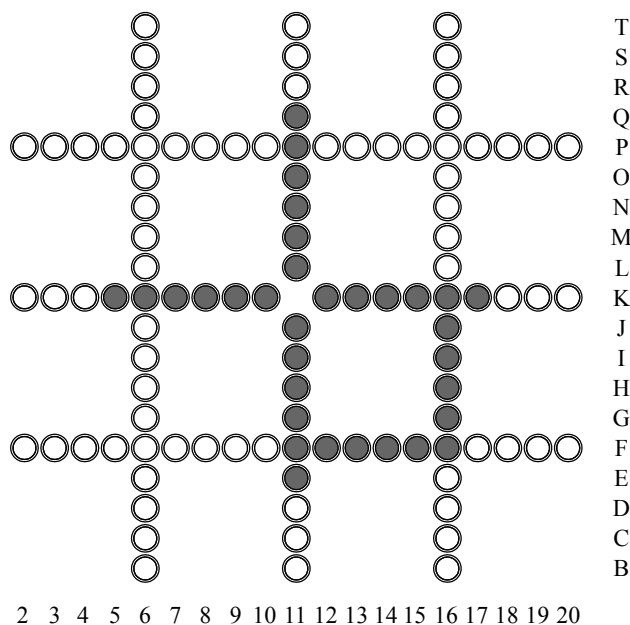


Figure 3.6: Schematic view of the test lattice implemented in PROTEUS, perturbed by removing the central fuel pin (missing pin at position K11). The dark grey shaded circles indicate the fuel pins that were measured during the campaign.

### 3.1.4 Removal of the Central Fuel Pin

The simplest perturbation of a given fuel lattice is the removal of a single fuel pin. The situation where one or more lattice positions are not occupied occurs regularly in the upper parts of BWRs with part-length fuel pins, and is therefore well known and studied. Deterministic and probabilistic computer codes correctly model this kind of perturbation. One would thus not expect to find significant discrepancies between codes when just one fuel pin (e.g. that at the center of the assembly at position K11) is removed from the SCWR-like reference lattice (see Fig. 3.6).

The measurement campaign for the perturbed test zone configuration of Fig. 3.6 was still useful to perform, for two reasons. First, it is an intermediate step to the more severe perturbation of replacing the central fuel pin with a gadolinium-poisoned pin (discussed in Subsection 3.1.5). Secondly, this particular pin is of special interest since its removal has a positive net effect on the reactivity, i.e. one has the unusual situation where one can add reactivity to the system by removing fuel. This peculiarity is due to the strong under-moderation of the central fuel pin (K11) and the less under-moderated neighbors (K10, K12, J11, L11). By removing K11, the neighbors become better moderated and overcompensate the negative effect of removing fissile material. It is clearly of interest to investigate the accuracy with which the tested computer codes can calculate these competing effects in this particular case.

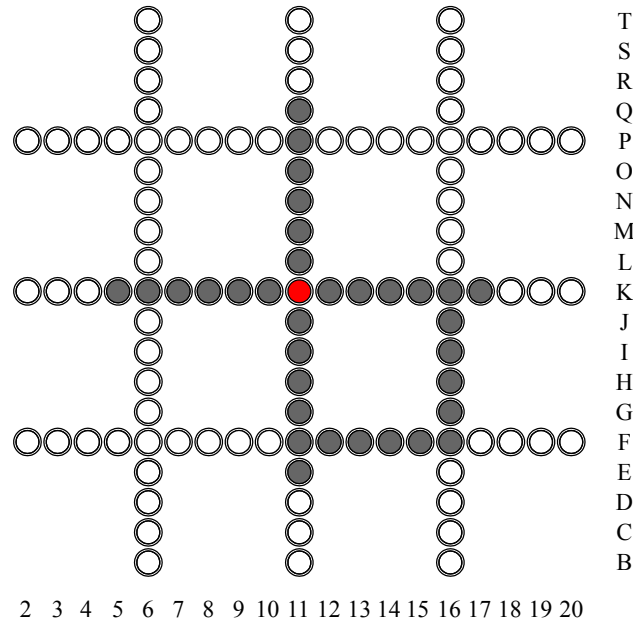


Figure 3.7: Schematic view of the test lattice implemented in PROTEUS, perturbed by replacing the central fuel pin with a gadolinium-poisoned fuel pin (red marked pin at position K11). The dark grey shaded circles indicate the fuel pins that were measured during the campaign.

### 3.1.5 Replacement of the Central Pin by Gadolinium-Poisoned Fuel

Yamaji and Kamei have proposed [4, 5] to insert gadolinium-poisoned fuel into the lattice in order to compensate for the excess reactivity at the beginning of the fuel cycle (BOC). This excess reactivity is necessary to ensure that the reactor maintains criticality until the next refueling outage. Gadolinium acts as burnable poison. At BOC, the gadolinium, due to its large absorption cross-section for thermal neutrons, absorbs thermal neutrons strongly and therefore reduces the reactivity of the system. However, only certain isotopes of gadolinium ( $^{155}\text{Gd}$  and  $^{157}\text{Gd}$ ) have large absorption cross-sections and by absorbing a neutron, they are transformed into Gd isotopes with absorption cross-sections that are several orders of magnitude smaller ( $^{156}\text{Gd}$  and  $^{158}\text{Gd}$  respectively). Therefore, following neutron absorption, the isotopic vector of the introduced gadolinium moves towards a less poisoned composition until, finally, all of the  $^{155}\text{Gd}$  and  $^{157}\text{Gd}$  are transformed into low absorbing isotopes and the Gd is no longer significantly lowering the reactivity of the system.

The replacement of the fuel pin K11 by gadolinium-poisoned fuel (see Fig. 3.7) builds on the previously discussed perturbation of removing the central fuel pin (Subsection 3.1.4). The standard driver fuel of PROTEUS (5% enriched  $\text{UO}_2$ ), which is used in the test zone for the SCWR-like lattice, has been replaced by 3.5% enriched  $\text{UO}_2$  with 3.95w% of natural gadolinium. The poisoned fuel pin also has a different diameter (8.19 mm instead of 10.18 mm) and additional Zircaloy cladding in between the fuel and the standard aluminum cladding used for all driver fuel pins in PROTEUS.

## 3.2 Reaction Rate Measurement Techniques

Measurement of the spatial distributions of the two different integral reaction rates, total fission ( $F_{\text{tot}}$ ) and  $^{238}\text{U}$  capture ( $C_8$ ), is well suited for code validation because one obtains information about the spatial neutron flux distribution at different average energies. The  $C_8$  reaction is sensitive to both the thermal and epithermal range, while  $F_{\text{tot}}$  is mainly sensitive to thermal neutrons in water moderated systems.

The ratio of the two reaction rates, i.e.  $C_8/F_{\text{tot}}$ , is also especially useful for code validation, since a spectral index is obtained in an absolute sense for each location in the lattice. No specific normalization steps are necessary in this case. However, nuclear data related uncertainties (which are quite significant) do not cancel out while analyzing the measurements of the reaction rate ratio. This makes the experimental uncertainties larger than on the relative distributions of the individual reaction rates. It should be noted that, in addition to being a neutron spectrum index,  $C_8/F_{\text{tot}}$  corresponds to the so-called modified conversion ratio, which is a measure of the fuel conversion capacity ( $^{239}\text{Pu}$  production) of the system.

In this section, the measurement techniques used to derive reaction rates are detailed. In the first subsection, the underlying principle of measuring reaction rates with the gamma scanning method is presented. Subsection 3.2.2 covers the hardware which was used to obtain the results, viz. the gamma scanning machine. The details of the analysis are discussed in Subsection 3.2.3, which describes how the reaction rate distributions are deduced from a given set of measured gamma scans.

### 3.2.1 The Measurement Principle

Experimental reaction rate maps for the SCWR-like test lattice implemented in PROTEUS have been derived by measuring the gamma-spectra of freshly irradiated fuel pins. The gamma scanning technique applied is standard art [6] and, in the context of experiments at PROTEUS, has been detailed before by Bergmann et al. [7]. A summary description of the technique is given here.

To deduce the reaction rate distributions across the test lattice, the activity of fission and  $^{238}\text{U}$  capture products inside the fuel pins is measured in the following way. Following a PROTEUS irradiation, fission and capture products are built up in the pins. The majority of these products are non-stable isotopes, and they decay with various half-lives and thereby move towards the isle of stable isotopes. As an example, Fig. 3.8 shows the decay scheme for the fission product mass chain 135 which contains the well known fission products  $^{135}\text{I}$  and  $^{135}\text{Xe}$ .  $^{135}\text{Te}$  decays via a  $\beta^-$ -decay almost immediately (half-life of 19 seconds) to  $^{135}\text{I}$ , which again makes a  $\beta^-$ -decay to  $^{135}\text{Xe}^{\text{m}}$ . The  $\beta^-$ -decay of the metastable state is negligible compared to its internal transition (IT) which happens with a half-life of 15.3 minutes. The ground state of  $^{135}\text{Xe}$  decays with a

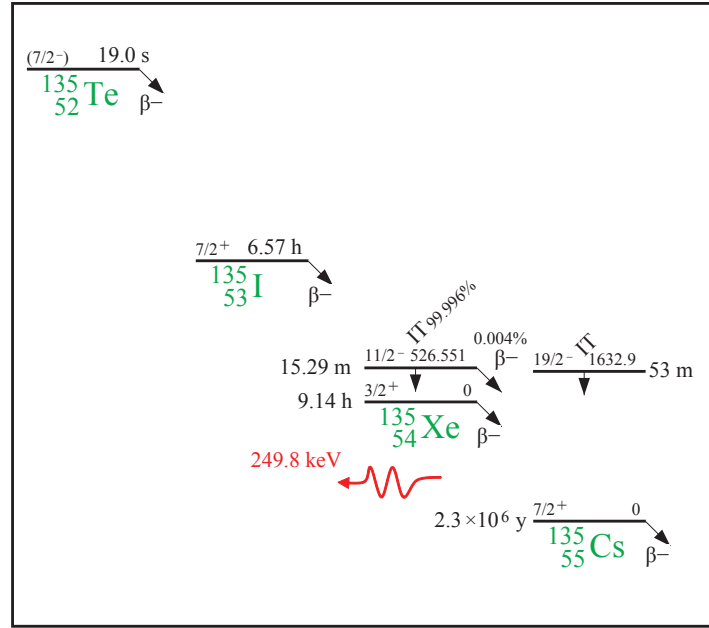


Figure 3.8: The decay scheme of  $^{135}\text{Xe}$

half-life of 9.14 hours entirely to an excited state of  $^{135}\text{Cs}$ . The de-excitation takes place almost immediately by emission of  $\gamma$ -rays. These emitted  $\gamma$ -rays are very characteristic of the decaying isotope. The most prominent  $\gamma$ -ray of this particular decay is at  $249.8 \text{ keV}$ .

If one knows all the necessary nuclear data (such as the fission yields, the branching ratios, the half-lives, and the number of emitted  $\gamma$ -rays of a given energy and per  $\beta^-$ -decay), then one can deduce the number of fissions that took place in the fuel pin from the number of  $\gamma$ -rays of the characteristic energy. Measuring the reaction rate in a fuel pin boils down to counting the number of  $\gamma$ -rays of a certain energy emitted by that fuel pin after the irradiation.

As regards the gamma counting procedure itself, the fuel remains in the core for 2 to 3 hours after the irradiation in order for the very short-lived fission products to decay and thereby lower the activity of the fuel pins. Once the activity is low enough for the fuel to be manageable, fuel pins can be extracted from the reactor and put in front of a gamma-ray detector. This detector records the energy spectrum of the entering  $\gamma$ -rays. Fig. 3.9 depicts a schematic of the detector and the recorded spectrum in the range of 130 to 330 keV. The fuel pin is put in front of a HP-Ge (High Purity Germanium) semiconductor detector. Lead shielding prevents disturbing  $\gamma$ -rays from other sources to enter the system and a collimator is used to generate an axial sensitivity of about 3 cm. A software program [8] analyses the full-energy peak at  $249.8 \text{ keV}$  (the characteristic energy of the  $\gamma$ -ray emitted after the  $\beta^-$ -decay of  $^{135}\text{Xe}$ ), subtracts the background, fits a Gaussian distribution on it, and estimates the number of  $\gamma$ -rays recorded.

The procedure described above is repeated for all the fuel pins of interest. After measuring the chosen fuel pins, one can compare them to each other and construct reaction rate maps over the fuel assembly. An example of the results of such an analysis is given in Fig. 3.10.



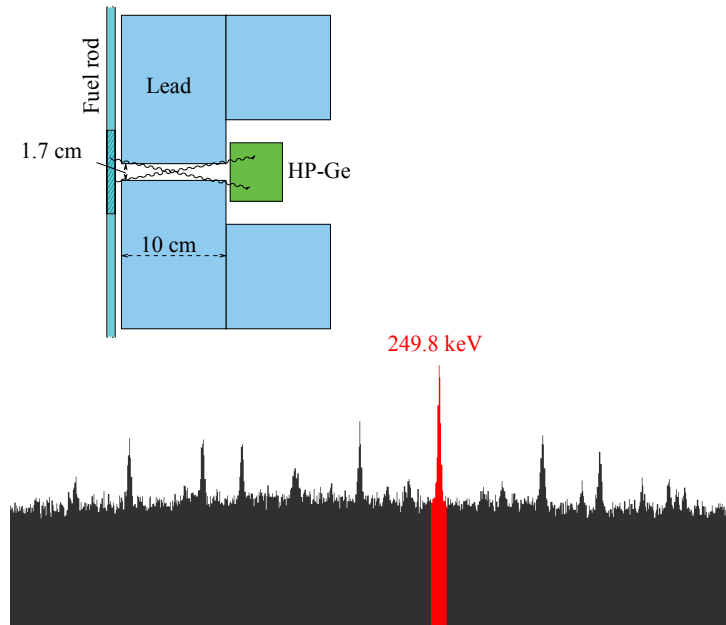


Figure 3.9: Principle of measuring the  $\gamma$ -ray spectrum of a newly irradiated fuel pin

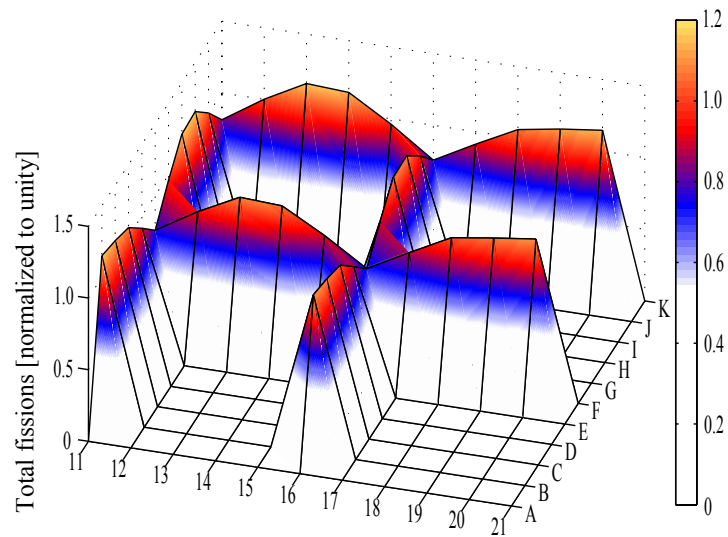


Figure 3.10: Example of an experimentally derived total fission rate map across the south-east quadrant of the SCWR-like fuel lattice in PROTEUS

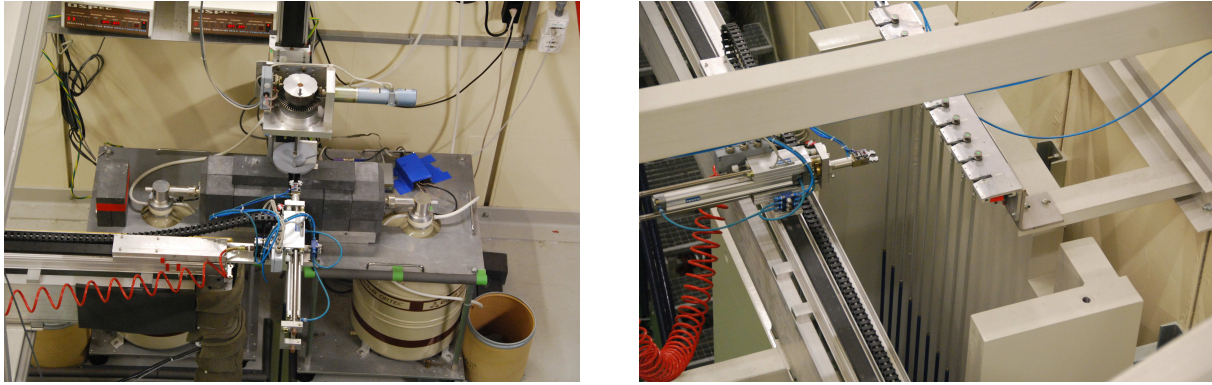


Figure 3.11: The gamma scanning machine: on the left, the detector setup with 2 high purity germanium detectors; on the right, the storage rack where up to 10 fuel pins can be stored

### 3.2.2 The Gamma Scanning Machine

The gamma scanning technique has been implemented at PROTEUS using a special fuel-pin gamma scanning machine. This device has been designed to facilitate measurements in batches of up to ten fuel pins [9]. It consists mainly of two parts: a horizontal drive which collects the fuel pins from a storage rack and transfers them to the second part, viz. a vertical drive which moves the pin through the measurement station.

After the irradiation and a cooling period of approximately two hours, up to ten fuel pins are manually transferred from the reactor to the storage rack (right hand side of Fig. 3.11). From there, the horizontal drive collects the pin to be measured and moves it to the measurement location. There, the vertical drive takes over the fuel pin and elevates it to the desired measurement position.

The measurement station consists of two HP-Ge detectors. The detectors are positioned on either side of the fuel pin (left hand side of Fig. 3.11). The germanium crystals of 5.5 cm diameter were placed at 11.4 cm distance from the center of the fuel pin. The collimator block for each detector is made of lead and is 10 cm thick, 10 cm wide, and 30 cm high. The collimator slit is of rectangular shape, 1.7 cm high and 4.0 cm wide. The height was chosen such that it covers roughly one-and-a-half uranium pellets (1.016 cm high). One can therefore perform axial scans of the fuel pin, even though the exact position of each inter-pellet gap, and hence, the accompanying reduction in fissile material, is unknown. Additional shielding is installed around the detectors. In order to shield the detector from low-energy scattered radiation and X-rays, a 1 mm thick layer of cadmium and copper is installed. A schematic of one of the detectors is given in Fig. 3.9. The energy calibration of the detectors is performed using a  $^{152}\text{Eu}$  point source mounted onto a dummy rod. This is repeated before every irradiation.

The two installed germanium  $\gamma$ -ray detectors are from EG&G Ortec and each is connected to a DSPec multi-channel analyzer, also from EG&G Ortec [8]. The DSPec is a combined spectrometry amplifier and multi-channel analyzer that employs digital signal processing to produce an

optimal pulse shape with good resolution and peak position stability over a wide range of count rates (a rise time of  $6.4 \mu s$  was used). The DSPEC units are controlled by the GammaVision program from EG&G Ortec via Ethernet connections. The program sets and records the values of most controls. It also receives and saves all the measured spectral data. Over the same Ethernet connection, the mechanism of the scanner, i.e. the horizontal and the vertical drive, are controlled. Custom-made programs written with LabView from National Instruments steer the drives as well as the robotic finger which pulls the fuel pins out of the storage and transfers it from the horizontal to the vertical drive.

The fuel pins are measured in cycles, one after another. The gamma spectrum of each pin is recorded over a period of 540 seconds. Additional time is needed for the machine to change the fuel pin being measured. For one measurement cycle of ten fuel pins to be completed, it takes roughly 2.2 hours. Eighteen identical cycles were carried out which led to a total measurement time of approximately 40 hours. A typical experimental campaign consisted of an irradiation on the first day, followed by 40 hours of gamma-scanning measurements. On the third day, the scanned fuel pins were transferred back into the reactor and a new irradiation started. In this manner, up to three irradiations could be done per week. During the gamma scans, the pins were constantly rotated to average out azimuthal variations. They were measured at an elevation which corresponds to the core mid-plane. The gamma-scanning machine is also capable of performing axial scans (not done in the present experiments).

The duration of the irradiation was chosen such that the activity of the fuel pins was high enough to ensure good counting statistics. At the same time, the count rates should not be too high in order to facilitate the handling of the pins and to keep the dead time of the detectors low enough ( $<30\%$ ). The optimal irradiation time was found to be 1 hour at a reactor power of approximately 20 W (thermal neutron flux  $\sim 1 \times 10^8 \text{ n cm}^{-2} \text{ s}^{-1}$  in the graphite region of PROTEUS).

### 3.2.3 Analysis of Obtained Spectra

Gamma spectra of the irradiated fuel pins have been obtained using the machine described above. In this subsection, the method to derive fission and  $^{238}\text{U}$  capture rates from these spectra is detailed.

In principle, the measured count rates  $C_{Fiss}$  and  $C_{Capt}$  are proportional to the total fission rate  $F_{tot}$  and the  $^{238}\text{U}$  capture rate  $C_8$ , respectively. However, a number of corrections and proportionality factors must be taken into account. They will be discussed in detail in the following Subsection (3.2.3.1). The final equations, relating the reaction rates to the count rates, are:

$$F_{tot} = \frac{C_{Fiss}}{eB(r_5A_5Yd_5 + r_8A_8Yd_8)} \quad (3.1)$$

$$C_8 = \frac{C_{Capt}}{eBA d} \quad (3.2)$$

$$\frac{C_8}{F_{tot}} = \frac{C_{Capt} e_{Fiss} B_{Fiss} (r_5A_5Yd_5 + r_8A_8Yd_8)}{C_{Fiss} e_{Capt} B_{Capt} A_{Capt} d_{Capt}} \quad (3.3)$$

Here,  $C_{Capt}$  and  $C_{Fiss}$  are the net counts,  $e$  is the detector efficiency,  $B$  is the branching ratio,  $r_x$  is the ratio of fissions in  $^{23x}\text{U}$  to total fissions (i.e. in  $^{235}\text{U} + ^{238}\text{U}$ ),  $A_x$  is the attenuation correction factor for the  $^{23x}\text{U}$  fissions, and  $Yd_x$  is the activity of the fission product emitting the  $\gamma$ -ray of interest (integrated during the measurement), which results from one fission of isotope  $x$ .  $B$ ,  $e$ ,  $r_x$ ,  $A_x$  are simple factors and can be obtained quite easily. The number of decays  $Yd_x$ , on the other hand, depends also on the fission yields and the fission products which were built up during the previous irradiations (not just the one being studied). In the case of the capture rate  $C_8$  (involving the counting of the 277.6 keV gamma-ray of  $^{239}\text{Np}$ ), there is no fission yield to be taken into account, which is why in Eq. 3.2 only the decay term  $d$  is present.

### 3.2.3.1 Corrections

**Decay Corrections** To calculate the parameters  $Yd_5$  and  $Yd_8$  one needs to know the activity  $z$  of a certain isotope emitting the gamma ray of interest. The activity needs to be integrated over the measurement time  $T_m$ , which was employed after a cooling period  $T_c$  following the irradiation of duration  $T_i$ . The activity however, is directly proportional to the number of nuclei  $N$  of the isotope via the decay constant  $\lambda$ . Most isotopes that emit a useful gamma-ray line are populated via several paths during the build-up of the fission products. An isotope can be a direct fission product but also a decay product from another fission product. For example,  $^{135}\text{Xe}$ , the decay scheme of which is illustrated in Fig. 3.8, can be populated directly, or via the decay of  $^{135}\text{I}$ , or via the decay of  $^{135}\text{Te}$  followed by a decay of  $^{135}\text{I}$  to  $^{135}\text{Xe}$ . Therefore,  $^{135}\text{Xe}$ ,  $^{135}\text{I}$ ,  $^{135}\text{Te}$  are all fission products which contribute to the activity of  $^{135}\text{Xe}$  and hence, to the count rate of the corresponding gamma-ray line at 249.8 keV.

The treatment of all possible paths, from a fission reaction to the fission product of interest, can, in our case, be accounted by a standard scheme which has four distinct states (see Fig. 3.12). State 3 is the ground state of the actual fission product under consideration. State 2 is the isomer state of the ground state, and State 1 is the parent state. State 4 is the daughter state which, upon generation, instantly emits the gamma-ray. The number of gamma-rays per decay of the ground State 3 is given by the branching ratio of the decay path for this state. Therefore, the activity of State 3 is the final parameter of interest. For each of the studied gamma lines, the emitting isotope and its precursors are fitted into this template. States 1, 2, and 3 have non-negligible half-lives, whereas the yield of parent isotopes to state 1 can be considered as instantaneous. To account for the different decay paths, we therefore only needed to use the

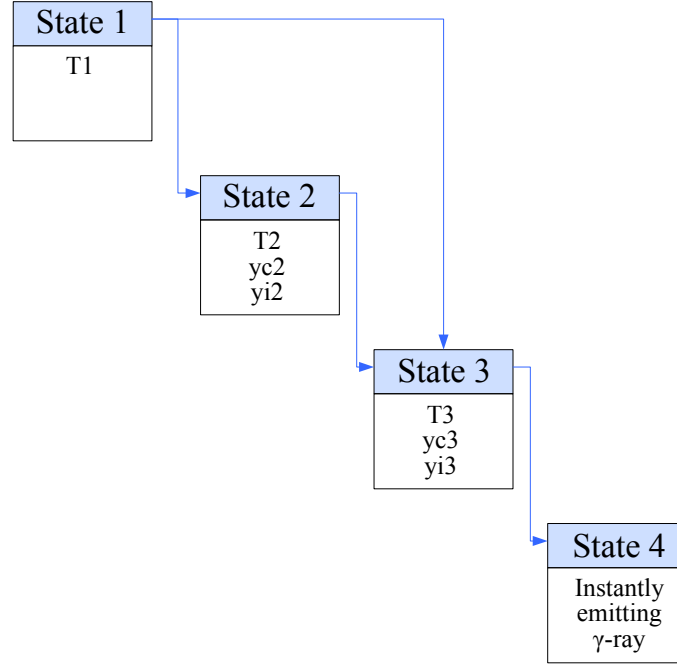


Figure 3.12: The decay scheme of fission products as coded in the MATLAB routine

individual and cumulative fission yields of States 2 and 3.

To calculate the activity of State 3 (integrated over the measurement time  $T_m$ ), one needs to know the number of atoms in States 1, 2, and 3 at all times. The system of equations to be solved is therefore:

$$\frac{\partial x_1}{\partial t} = s_1 - \lambda_1 x_1 \quad (3.4)$$

$$\frac{\partial x_2}{\partial t} = s_2 - \lambda_2 x_2 + p_{12} \lambda_1 x_1 \quad (3.5)$$

$$\frac{\partial x_3}{\partial t} = s_3 - \lambda_3 x_3 + p_{13} \lambda_1 x_1 + \lambda_2 x_2 \quad (3.6)$$

$$p_{12} + p_{13} = 1, \quad s_1 = (yc_3 - yi_3 - yi_2)f, \quad s_2 = yi_2f, \quad s_3 = yi_3f, \quad (3.7)$$

Here,  $x_i$  denotes the number of atoms in State  $i$  with decay constant  $\lambda_i$ , and  $s_i$  is the corresponding fission source.  $yc_i$  is the cumulative fission yield and  $yi_i$  the individual fission yield for State  $i$ .  $p_{12}$  and  $p_{13}$  denote the fractions of atoms that populate State 2 (State 3) by decay of State 1.  $f$  stands for the fission rate, which is assumed to be constant during an irradiation and is zero during the cooling and measurement times. Solving this system of equations, one can deduce  $z$ , the activity integrated over the measurement duration  $T_m$ .

$$\begin{aligned}
z = & \underbrace{s_3 \lambda_3 g_3}_{(1)} + \underbrace{s_2 \frac{\lambda_2 \lambda_3}{\lambda_3 - \lambda_2} (g_2 - g_3)}_{(2)} + \underbrace{s_1 p_{13} \frac{\lambda_1 \lambda_3}{\lambda_3 - \lambda_1} (g_1 - g_3)}_{(3)} + \dots \\
& \underbrace{s_1 p_{12} \frac{\lambda_1 \lambda_3}{\lambda_3 - \lambda_1} \left( \frac{\lambda_2}{\lambda_2 - \lambda_1} (g_1 - g_2) - \frac{\lambda_2}{\lambda_2 - \lambda_3} (g_3 - g_2) \right)}_{(4)}
\end{aligned} \tag{3.8}$$

where

$$g_i = \frac{1}{\lambda_i^2} e^{-\lambda_i T_c} (1 - e^{-\lambda_i T_m}) \cdot (1 - e^{-\lambda_i T_i}). \tag{3.9}$$

The four grouped terms in Eq. 3.8 correspond to four different individual contributions to the total integrated activity  $z$ . Contributor (1) is the number of fissions directly populating State 3, contributor (2) is the number of fissions populating State 2 that decay into State 3. Contributor (3) is the number of fissions populating State 1 that decay directly into State 3, and contributor (4) is the number of fissions populating State 1 that first decay into State 2 and then into State 3. The individual fission sources  $s_1 p_{12}$  and  $s_1 p_{13}$  can be identified as  $(yc_2 - yi_2)f$  and  $(yc_3 - yi_3 - yc_2)f$ , respectively, and Eq. 3.8 can therefore be converted into:

$$z = f(yc_2 a + yi_2 b + yc_3 c + yi_3 d). \tag{3.10}$$

The coefficients  $a$ ,  $b$ ,  $c$ , and  $d$  are considered to be without uncertainties. The cumulative and independent fission yields  $yc$  and  $yi$  on the other hand have non-negligible uncertainties. Because the saturation and decay equations are linear, using Eq. 3.10, one can write the sum of the contributions of  $N$  different irradiations to  $Yd$  as:

$$Yd = \sum_{n=1}^N p_n (yc_2 a_n + yi_2 b_n + yc_3 c_n + yi_3 d_n). \tag{3.11}$$

Here,  $p_n$  is proportional to the power of the  $n$ -th irradiation or, more precisely, to the signal of the power monitor. One can use the reactor power instead of the fission rate  $f$  because it is directly proportional to  $f$  (for a given critical core loading).

**Irradiation History Correction** The fuel in the reactor remembers not only the current irradiation, but also the past irradiations. The corrections necessary for the irradiation history strongly depend on the observed gamma line and the involved parental states of the isotope emitting the gamma rays. Particularly, the decay constants are of importance. The longer the half-life, the

larger the correction becomes since it takes about seven half-lives of an isotope for 99% of it to have decayed, and it takes ten times the half-life for 99.9% to decay. The state with the longest half-life dominates the entire chain.

A severe case is the decay of the  $^{238}\text{U}$  capture product,  $^{239}\text{Np}$ , which has a half-life of 2.36 *days*. If one does a first irradiation on Monday, and a second on Wednesday of the same duration and at the same power level, 55 % of the  $^{239}\text{Np}$  from the first irradiation will still remain. This will lead to a corresponding large correction (see Fig. 3.13). Unfortunately, the gamma lines of  $^{239}\text{Np}$  are the only possible option to measure the capture rate in  $^{238}\text{U}$ . For most of the fission products, the irradiation history corrections are much lower since the dominating half-lives are in the order of ten hours. A 48-hour cooling time between irradiations will therefore lead to corrections in the order of a few tens of percent. One other difficult case is the 1596 *keV* gamma line of  $^{140}\text{La}$ . Lanthanum-140 originates from the decay of  $^{140}\text{Ba}$  (which has a half-life of 12.75 *days*) and therefore only builds up in time. It reaches its maximum after more than four days, which would lead to an irradiation history correction for the above mentioned example of more than 100%. This is why  $^{140}\text{La}$  has not been used (see Subsec. 3.2.3.4).

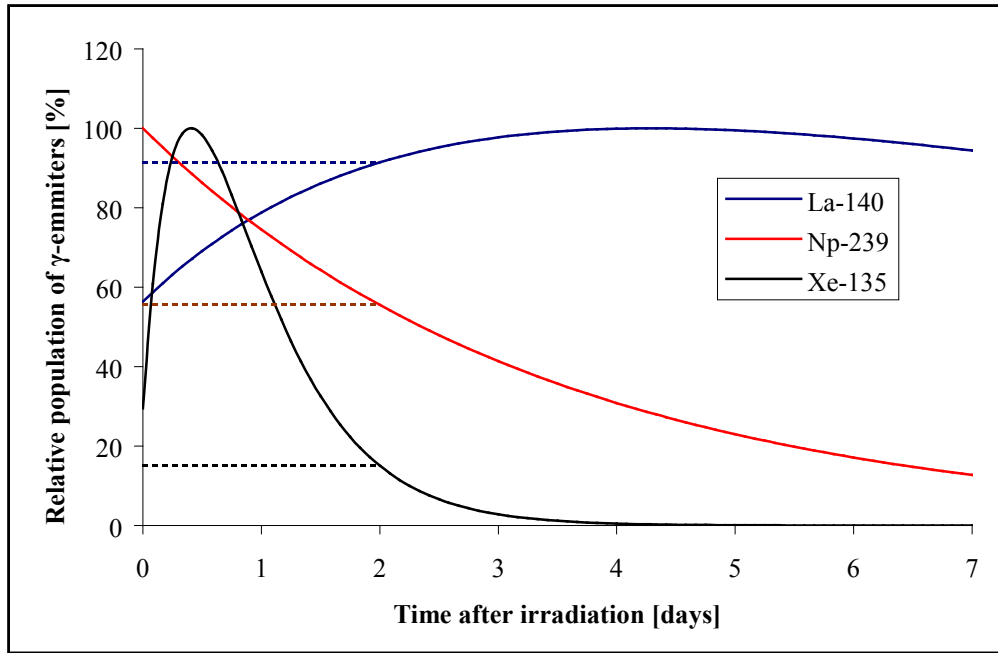


Figure 3.13: Examples of the relative populations of fission and  $^{238}\text{U}$  capture products

To account for this, a decay correction is applied for each past irradiation in the same manner as for the current irradiation (i.e. as per Eq. 3.10). The user inputs, via a text file, the current and past irradiation dates, times, and powers. The MATLAB routine then calculates the integrated activity  $z_n$  originating from each irradiation ( $n$ ) and sums them to yield the total activity as expressed by Eq. 3.11. The activity expressed by Eq. 3.11 is for a given fissile isotope ( $^{235}\text{U}$  or  $^{238}\text{U}$ ). The two activities need to be combined finally, to obtain the total fission rate in the pin using Eq. 3.1.

In deducing the total measured activity, each of the measured activities  $z_n$  due to irradiation (n) is weighted according to the reactor power ratio  $p_n$  between the irradiation (n) and the current irradiation (1). This approach works well as long as the flux shape and spectra in the different irradiations involved do not change significantly, i.e. if the core configurations are similar for all irradiations. In that case, the ratio of the measured pin power to the total reactor power - or to the signal of the reactor monitor from which the power is deduced - is constant. If the flux distribution changes (as illustrated in Fig. 3.14), this is no longer true and a new factor that takes into account the change in flux shape between the different core configurations has to be introduced for each pin.

The change of flux shape is important because the lattice configurations, detailed in Subsections 3.1.1 to 3.1.5, were quickly altered, sometimes within less than seven days. As a result, the  $^{239}\text{Np}$  activity, as  $^{238}\text{U}$  capture product with half-life of 2.36 days, depended significantly on past irradiations, in which a different relationship had existed between pin powers in the test zone and the signal of the power monitor in the graphite driver zone. To correct for the flux shape changes across the PROTEUS zones that occurred between different configurations, the power ratio  $p_n$  used in Eq. 3.11 has to be replaced, for each pin, by the pin power ratio  $f_n$  between irradiation (n) and the current irradiation (1). This can be estimated from the measured power monitor ratio  $p_n$  and an appropriate correction factor, deduced from the corresponding MCNPX whole-reactor calculation, as:

$$f_n^{exp} = p_n^{exp} * \left( \frac{f_n^{MCNPX}}{p_n^{MCNPX}} \right) \quad (3.12)$$

where the superscripts *exp* and *MCNPX* stand for measured and calculated values, respectively.

The impact of the calculated correction factor becomes smaller as more time lies between irradiations carried out in different PROTEUS configurations. For the worst case, i.e. with the largest changes in flux distribution between two configurations, the effect of this correction on the  $^{238}\text{U}$  capture rate was in the order of 1.5%. In each case, the correction factor was assessed on the basis of whole-reactor calculations with negligible statistical uncertainty. As shown in Chapter 5 and 6, excellent agreement with experiment has been obtained for the MCNPX whole-reactor modeling of both unperturbed and perturbed configurations. Thus, overall, the uncertainty on the final reaction rate results was not significantly affected by the applied corrections.

**Gamma Attenuation** Not all of the emitted gamma-rays enter the detector. In order to deduce the number of fission product decays from the gamma-ray count rate, one has to know the fraction of gamma-rays emitted inside the fuel pin that cross the detector surface behind the collimator. Photons can get “lost” in three different ways: they can either be emitted in a direction which is not covered by the detector, they can be absorbed before they exit the fuel pin, or they can be absorbed by the collimator. In order to calculate the probability of a photon born inside the fuel pin to reach the detector, one needs to know the distance it travels in each material. The



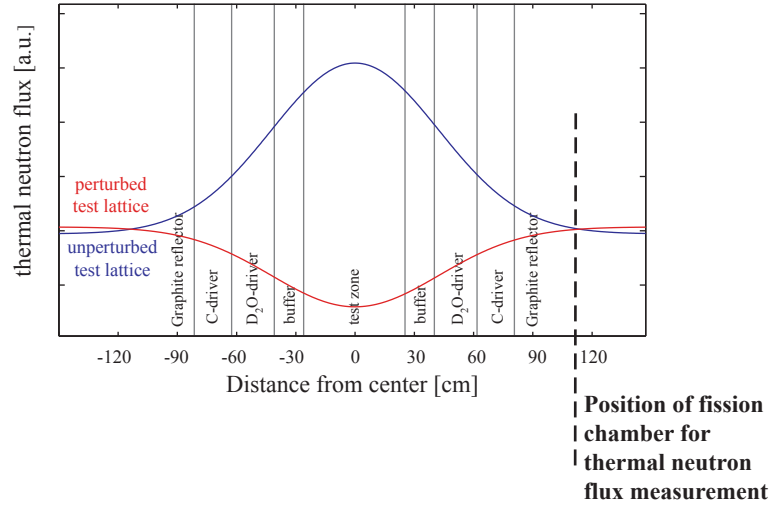


Figure 3.14: Schematic showing how the neutron flux level in the PROTEUS test zone can vary significantly between two different test zone configurations, with the reactor power being calibrated via a detector located in the graphite reflector. The sketch is qualitative, the actual variations between the various test zones investigated currently being much smaller.

first step therefore is to calculate the  $^{235}\text{U}$  and  $^{238}\text{U}$  fission and  $^{238}\text{U}$  capture distributions inside the fuel pin, which in turn give the corresponding photon source distributions. This calculation is performed with MCNPX.

The photon sources serve as input to MCNPX gamma-transport calculations, with the purpose of determining the gamma counting efficiency in the geometry of the measurement station (shown in Fig. 3.9). The photon source depends on the neutronics calculation of the individual reaction rate distributions within the pin (captures in  $^{238}\text{U}$ , fissions in  $^{235}\text{U}$  and in  $^{238}\text{U}$ ). Thus, for example, while the fissions in  $^{238}\text{U}$  are almost constant throughout the entire cross-section of the pin, fissions in  $^{235}\text{U}$  are strongly increased towards the rim of the fuel pin. This is why the photon propagation had to be performed for each reaction rate and each fuel pin inside the lattice, using photon sources distributed in fine concentric rings in order to account for the corresponding gamma self-absorption in the fuel.

**Detector Efficiency and Dead Time** The count rate has to be corrected for the detector efficiency. The EG&G Ortec germanium gamma-ray detectors have a nominal relative efficiency of 18%. The detector efficiencies for different gamma energies were measured with a  $^{152}\text{Eu}$  point source on a rotating dummy rod. In the energy range of interest ( $> 200 \text{ keV}$ ), the efficiency  $\epsilon$  can be fitted to a polynomial function of the form

$$\log(\epsilon) = \sum_{i>0} a_i \log(E)^{i-1}. \quad (3.13)$$

After the detector has recorded an incoming photon, it is inert to a second photon for a short amount of time. This period is called the detector dead time. The dead time correction is automatically done by the DSPec system. It works accurately up to a dead time of 25% to 30%. Dead times between 5% and 30% occurred in the counting of the fuel pins, depending on the reactor power during the irradiation and the cooling time between the irradiation and the gamma scan. Scans with dead times larger than 25% were not taken into account.

#### 3.2.3.2 The MATLAB Routine

The MATLAB routine used currently for analysis of the experiments is a collection of MATLAB programs that automate the evaluation of the reaction rate distributions. It takes all the necessary input files, rearranges the information in terms of suitable data, and calculates and prints out the radial distributions of normalized fission and capture rates and the unnormalized ratio of  $^{238}\text{U}$ -captures to total fissions. As a first step, the input files are read. These are:

- the measured spectra and the dates of the measurement
- the needed nuclear data
- detector efficiencies
- attenuation corrections
- irradiation history and power, and correction factors accounting for changing the configuration

The second step is to calculate the individual reaction rates ( $C_8$  and  $F_{\text{tot}}$ ) for each pin and each gamma scan as described above, employing all the necessary corrections. The measurements following a given irradiation consist of several gamma scans per pin, and two detectors are used per scan. In the third step, the results of the individual scans of the fuel pins are normalized and averaged. For the  $^{238}\text{U}$  capture and total fission rates, this is done in the following order:

1. The average is taken over the scans measured with the two detectors after a given irradiation.
2. One particular fuel pin was scanned after each irradiation (pin P19), such that small fluctuations in reactor power and irradiation duration could be taken into account. The obtained averages are normalized to the reference pin.
3. If a given pin is measured repeatedly after more than one irradiation, an average over all measurements of the campaign is taken.
4. The  $\gamma$ -ray dependent reaction rate distributions are normalized to unity on the total as-

sembly

5. The average over the gamma-lines is taken from the normalized rates obtained in the previous step
6. The results are once again normalized to an average of 1

Obtaining the reaction rate ratio  $C_8/F_{\text{tot}}$  requires a partly different approach:

1. For each pin, the  $^{238}\text{U}$  capture rate and the individual fission rate estimates from all scans and all  $\gamma$ -ray lines are gathered.
2. For each pin and each scan  $C_8/F_{\gamma_1}, C_8/F_{\gamma_2} \dots C_8/F_{\gamma_n}$  are constructed.
3. The  $C_8/F_{\gamma_i}$  are averaged over all scans.
4. Optionally, the average over all the  $\gamma$ -ray lines is taken.

The last step of the routine is to store the results and display the radial reaction rate distributions. A more detailed description of the MATLAB routine and the associated files is given in [10].

### 3.2.3.3 Uncertainties and Uncertainty Propagation

Uncertainties are fully propagated throughout the whole analysis chain in order to account for possible correlations between different measurements. When calculating a single fission rate estimate according to Eq. 3.1, the uncertainties on variables represented by non-capital letters are neglected. The uncertainty on the efficiency of the detector in Eq. 3.1 and 3.2 does not need to be considered for normalized capture and fission rate distributions as the efficiency terms cancel out. In the case of  $C_8/F_{\text{tot}}$ , the ratio is calculated pin-by-pin and the ratio of efficiencies  $e_{\text{Fiss}}/e_{\text{Capt}}$  does not cancel out. However, the detector has been calibrated with a unique  $^{152}\text{Eu}$  source, which emits  $\gamma$ -rays from 122 keV to 1408 keV, covering the entire range of energies for the measured  $\gamma$ -rays (see Subsec. 3.2.3.1 and 3.2.3.4). Therefore, the main uncertainty on the detector efficiency, which comes from the activity of the source, cancels out in Eq. 3.3. The uncertainty on the calibration process is thus negligible in comparison to uncertainties on, for example, the fission yields. The uncertainties on the ratios of fission in  $^{23x}\text{U}$  to total fissions  $r_x$  depend primarily on the composition of the fuel pins. The measured pins are fresh and their compositions well characterized, which justifies, to first approximation, neglecting these uncertainties. In addition, when considering normalized fission and capture rate distributions on similar fresh pins, the contributions of the uncertainty on  $r_x$  become entirely negligible. The irradiation, cooling, and measurement durations, as well as the half-lives are well known (usually within 0.2%) and are therefore not propagated.

To determine the uncertainty on  $F_{\text{tot}}$  for each pin, the uncertainties and covariances of the

parameters in Eq. 3.1 that are in capital letters, i.e. the branching ratio  $B$ , the count rates  $C$ , the attenuation correction factors  $A$ , and the activity of the isotope integrated during the measurement period  $Yd$ , have to be considered. For a single gamma-ray line, the branching ratios are constant and therefore completely correlated. The count rates for different measurements are assumed to be completely independent and, therefore, are uncorrelated. The radial distributions for the fission rates in  $^{235}\text{U}$  and  $^{238}\text{U}$ , as also the capture rate in  $^{238}\text{U}$ , are almost the same within each pin, which is why the gamma-attenuation correction factors can be assumed completely correlated for measurements of a given reaction rate on two different pins. The parameters  $Yd$  depend only on the uncertainties of the fission yields (see Eq. 3.11). Since the fission yields are always the same for a given gamma-ray line, they are completely correlated.

For each pair of variables  $(A, B)$  (that has non-negligible uncertainties and which are partially correlated), a correlation matrix,  $Corr(A, B)$ , is built. From this, the covariance matrix for each variable is derived as:

$$Cov(A, B) = \sigma_A * Corr(A, B) * \sigma_B, \quad (3.14)$$

where  $\sigma_X$  denotes the standard deviation of the variable  $X$ . The gamma-ray lines chosen for this study (see Subsection 3.2.3.4) are emitted by isotopes of different mass chains. Therefore, the nuclear data necessary for the different gamma-ray lines are not correlated. The count rates and the attenuation factors (calculated by MCNPX) are independent for different gamma-ray lines, which is why the covariance of the fission rates can be calculated separately for each gamma-ray line.

Once the correlation matrices for  $B$ ,  $C$ ,  $A_5$ ,  $A_8$ ,  $Yd_5$ , and  $Yd_8$  are set up, the corresponding covariance matrices can be derived according to Eq. 3.14. To simplify the propagation of the covariances throughout Eq. 3.1, an intermediate step is performed by calculating the covariance of  $AY = r_5 A_5 Yd_5 + r_8 A_8 Yd_8 = A_5 Y_5 + A_8 Y_8$ :

$$\begin{aligned} Cov(AY^1, AY^2) = & Cov(A_5^1, A_5^2)Cov(Y_5^1, Y_5^2) + Y_5^1 Y_5^2 Cov(A_5^1, A_5^2) + A_5^1 A_5^2 Cov(Y_5^1, Y_5^2) + \dots \\ & Cov(A_8^1, A_8^2)Cov(Y_8^1, Y_8^2) + Y_8^1 Y_8^2 Cov(A_8^1, A_8^2) + A_8^1 A_8^2 Cov(Y_8^1, Y_8^2) \end{aligned} \quad (3.15)$$

The covariance of the total fission rate  $F_{tot}$  can now readily be calculated, using the following formula:

$$\frac{Cov(F_{tot}^1, F_{tot}^2)}{F_{tot}^1 F_{tot}^2} + 1 = \left( \frac{Cov(C^1, C^2)}{C^1 C^2} + 1 \right) \left( \frac{Cov(B^1, B^2)}{B^1 B^2} + 1 \right) \left( \frac{Cov(AY^1, AY^2)}{AY^1 AY^2} + 1 \right) \quad (3.16)$$

The covariances are further propagated throughout the normalization and averaging process detailed in Subsection 3.2.3.2. This is done, employing the following generalized formula:

$$\text{cov}(Y^1, Y^2) = \left[ \frac{\partial Y}{\partial X} \right] \text{cov}(X^1, X^2) \left[ \frac{\partial Y}{\partial X} \right]' \quad (3.17)$$

where  $\left[ \frac{\partial Y}{\partial X} \right]$  denotes the Jacobian matrix for the operation of  $X$  to  $Y$ .

Finally, the variance of the calculated fission rate  $F_{tot}$  is extracted from the diagonal entries of the covariance matrix  $\text{cov}(F_{tot}^1, F_{tot}^2)$ .

In the case of the  $C_8$  distribution the exact same treatment of uncertainty has been applied (replacing  $AY$  by  $A$  in Eq. 3.16). In the case of the reaction rate ratio  $C_8/F_{tot}$ , the covariance matrices from the individual reaction rates are further propagated (according to Eq. 3.17) through the division:

$$\frac{\partial C_8/F_{tot}}{\partial C_8} = \frac{1}{F_{tot}} \quad (3.18)$$

$$\frac{\partial C_8/F_{tot}}{\partial F_{tot}} = \frac{-C_8}{F_{tot}^2} \quad (3.19)$$

**Uncertainties on Nuclear Data** There are considerable differences in the nuclear data of interest to this study, between the various nuclear data libraries. When using the deterministic neutronics code CASMO-4E [11], one is restricted to using one of the libraries that were processed for this code. These are JEFF-2.2 [12] and the more recent ENDF/B-VI [13], none of them being adequate to be used for the nuclear data required to analyze the experiments. For that purpose, the latest libraries available are ENDF/B-VII.0 [14] and JEFF-3.1.1 [15].

However, there are two values in ENDF/B-VII.0 which make this library a questionable choice. The first is the branching ratio of  $^{239}\text{Np}$ , which is given as  $15.20 \pm 0.15\%$  and, as such, is almost 6% higher than the value given in ENDF/B-VI.8 [13] and JEFF-3.1.1 (14.38 % in both libraries). Secondly, the uncertainty on the cumulative fission yield from  $^{235}\text{U}$ -fissions for  $^{133}\text{I}$  is claimed to be 64%, whereas the uncertainty on the same yield in JEFF-3.1.1 is given as 1.6%.

Because of the above described inconsistencies of ENDF/B-VII.0, the nuclear decay data of JEFF-3.1.1 has been used in this study. However, this library also has one peculiarity, namely the uncertainty on the branching ratio of the  $^{239}\text{Np}$  gamma-ray line at 277.6 keV, which is given at 3%. Previous libraries had lower uncertainties (1.5% in ENDF/B-VI.8 and 0.7% in the latest ENSDF evaluation [16]). A  $1\sigma$ -uncertainty of 1% seems more reasonable and was assumed in this work, as done previously [17].

### 3.2.3.4 Choosing Gamma Lines

The automatic peak analysis tool from GammaVision detects about 200 gamma peaks in a typical measured spectrum. The software subtracts the background, derives the net count rate, and identifies the corresponding precursor of the gamma-ray emitter, via comparison with a user-given library. Not all of the identified peaks are useful for the derivation of reaction rates. In fact, only a few are well suited.

To measure the capture rate in  $^{238}\text{U}$ , only the gamma lines emitted by the decay of  $^{239}\text{Np}$  are available, because  $^{239}\text{Np}$  is the only product of this reaction. Out of the 33 emitted gamma lines, the one at 277.6 keV is prominent and free from interferences with other gamma ray lines.

In order for a gamma line of a fission product to qualify as indicator for the total fission rate, it needs to fulfill a number of requirements. These are:

1. Good peak statistics. This is the case, if the cumulative fission yield of the precursor and the branching ratio of the gamma line are large. Additionally, the background needs to be low enough and the half-life of at least one step in the decay chain needs to be longer than a couple of hours. At the same time, all the half-lives of the decay chain combined can not be longer than a few days.
2. Small uncertainties on the nuclear data mentioned above, especially for the cumulative fission yield and the branching ratio.
3. Isolation of the peak from other peaks in the gamma-ray spectrum.
4. No significantly disturbing gamma source in the vicinity of the peak energy, e.g. from neutron activation of the structural material.

In addition, a peak energy which is close to the energy of the gamma line used to measure the capture rate (277.6 keV) is preferable, so that possible systematic errors which are energy dependent (e.g. in the corrections for the detector efficiency and the attenuation) cancel out in the derivation of the reaction rate ratio of captures in  $^{238}\text{U}$  to total fissions.

On the basis of the above criteria, three gamma-ray lines were selected to measure the fission rate. Their energies and some of their nuclear properties are listed in Table 3.1. The fission product  $^{140}\text{La}$ , which is usually used for such measurements, was not selected because of its long half-life (see Subsec. 3.2.3.1).

The decay schemes of  $^{135}\text{Xe}$ ,  $^{143}\text{Ce}$ , and  $^{133}\text{I}$  are shown in Figs. 3.8, 3.15, and 3.16, respectively. That of the  $^{238}\text{U}$ -capture product  $^{239}\text{Np}$  is shown in Fig. 3.17. Note that the selected gamma-rays and their decay schemes do not necessarily correspond to the standard template used for the analysis depicted in Fig 3.12. However, their nuclear properties, especially their half-lives, happen to be quite compatible so that the real decay chains can indeed be fitted into the template.

Table 3.1: Selected gamma-ray lines for the measurement of the total fission rate and the capture rate in  $^{238}\text{U}$ . Values are taken from the nuclear data library JEFF-3.1, errors are relative and given in percent (inside parentheses). The uncertainty on the branching ratio of  $^{239}\text{Np}$  was adjusted based on the ENDF/B-VI.8 value.

Precursor	$\gamma$ -energy [keV]	Half-life [hrs]	Parent half- life [hrs]	Branching ratio [%]	Cum. $^{235}\text{U}$ fiss. yield [%]
$^{135}\text{Xe}$	249.8	9.14(0.2)	6.57(0.3)	90.0(3)	6.61(3)
$^{143}\text{Ce}$	293.3	33.10(0.2)	0.236(1.11)	42.8(0.4)	5.95(1.4)
$^{133}\text{I}$	529.9	20.8(0.5)	0.208(2.4)	87.0(3)	6.59(1.6)
$^{239}\text{Np}$	277.6	56.52(0.2)	0.391(0.2)	14.38(1)	-

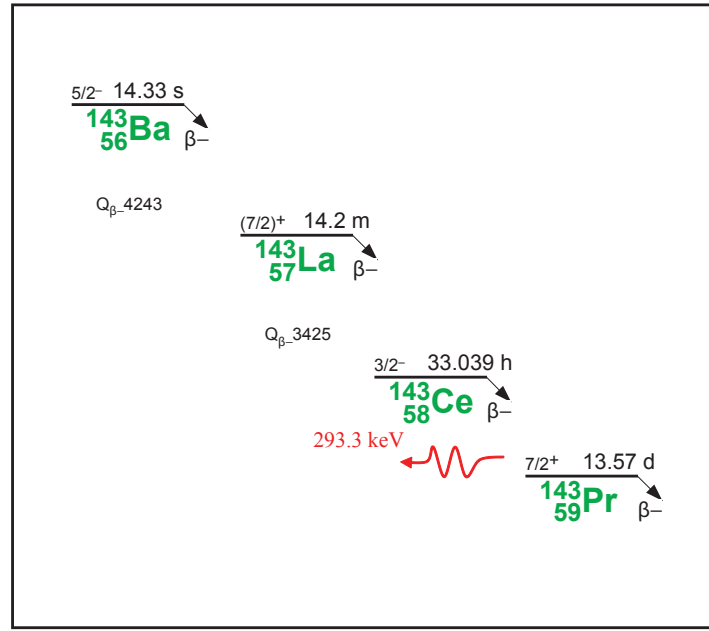


Figure 3.15: The decay scheme of  $^{143}\text{Ce}$

For the decay chain leading to  $^{135}\text{Xe}$  (see Fig. 3.8) and hence, the emission of the 249.8 keV gamma-ray line, the isomeric state  $^{135}\text{Xe}^m$  and the common parent  $^{135}\text{I}$  need to be considered.  $^{135}\text{Te}$  decays almost instantly (half-life of 19 s) into  $^{135}\text{I}$ , which is why it does not need to be considered as a separate state but can simply be included in the cumulative fission yield of  $^{135}\text{I}$ .  $^{135}\text{Xe}^m$  makes a  $\beta^-$ -decay only in 0.004% of all cases. This path is neglected because in all the remaining cases it undergoes an internal transformation (IT).  $^{135}\text{Cs}^*$  emits almost instantly the desired gamma-ray and one can therefore use the standard template for this decay chain. The corresponding states are summarized in Table 3.2.

The decay chain leading to  $^{143}\text{Ce}$  and the associated emission of the 293.3 keV gamma-ray line is rather simple.  $^{143}\text{Ba}$  decays, with a half-life of only 14.33 s, almost instantly into  $^{143}\text{La}$ , which in turn, decays to  $^{143}\text{Ce}$ . As before, the  $^{143}\text{Ba}$  state does not have to be treated individually.  $^{143}\text{Ce}$  decays solely into  $^{143}\text{Pr}^*$ , which almost immediately emits the gamma-rays of interest through de-excitation. Due to the simplicity of this decay chain, state 1 of the decay template does not have to be occupied (see Table 3.2).

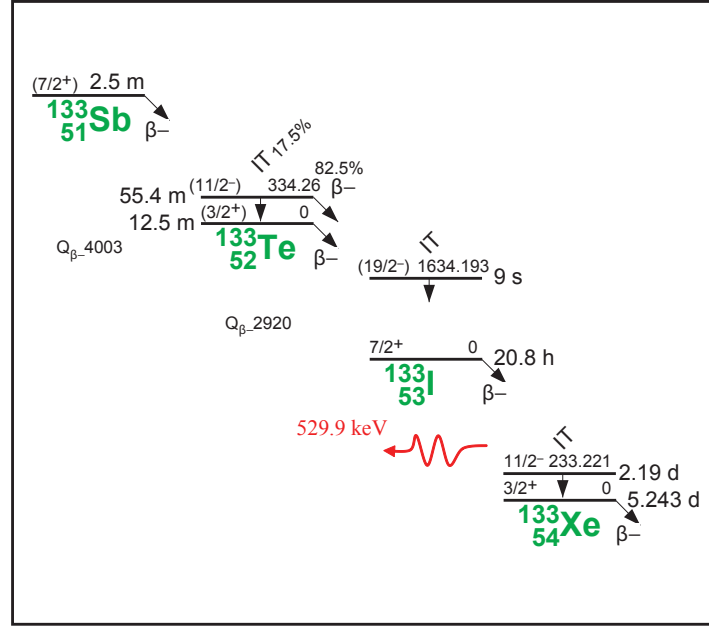

Figure 3.16: The decay scheme of  $^{133}\text{I}$ 

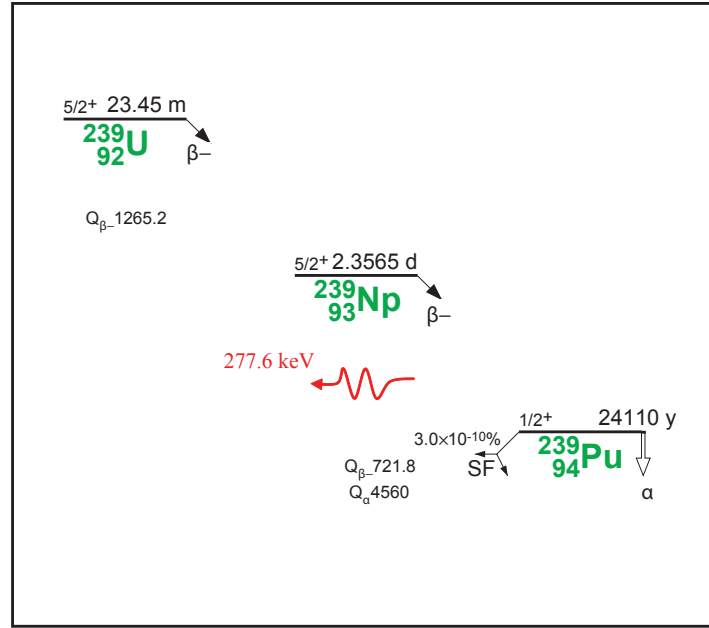
Table 3.2: Identification of the states of the decay template used in the MATLAB routine for the selected gamma ray emitters

Precursor	State 1	State 2	State 3	State 4
$^{135}\text{Xe}$	$^{135}\text{I}$	$^{135}\text{Xe}^{\text{m}}$	$^{135}\text{Xe}$	$^{135}\text{Cs}^*$
$^{143}\text{Ce}$	-	$^{143}\text{La}$	$^{143}\text{Ce}$	$^{143}\text{Pr}^*$
$^{133}\text{I}$	$^{133}\text{Te}^{\text{m}}$	$^{133}\text{Te}$	$^{133}\text{I}^{\text{m}} + ^{133}\text{I}$	$^{133}\text{Xe}^*$
$^{239}\text{Np}$	-	$^{239}\text{Np}^{\text{m}}$	$^{239}\text{Np}$	$^{239}\text{Pu}^*$

The decay chain of  $^{133}\text{I}$  is slightly more complicated. There are four states of interest:  $^{133}\text{Te}$ ,  $^{133}\text{Te}^{\text{m}}$ ,  $^{133}\text{I}$ , and  $^{133}\text{I}^{\text{m}}$ . The decay of  $^{133}\text{Sb}$  is fast enough (2.5 min) so that it can be considered as instantaneous. The metastable state  $^{133}\text{I}^{\text{m}}$  only undergoes internal transition with a very short half-life of 9 s. It can therefore (mathematically speaking) be combined with the ground state  $^{133}\text{I}$ . However,  $^{133}\text{Te}$  and  $^{133}\text{Te}^{\text{m}}$  need to be treated separately. This leads to the attribution of the states of the decay template as shown in Table 3.2.

The  $^{239}\text{Np}$  chain has an equivalent scheme to that of  $^{143}\text{Ce}$ . Here too, the scheme is simple enough so that state 1 of the template is left unoccupied. There is no fission yield to consider, and it is assumed that the production of  $^{239}\text{Np}$  is only possible through the  $(n, \gamma)$  reaction on  $^{238}\text{U}$ , i.e. the production of  $^{239}\text{U}$  followed by a  $\beta^-$ -decay to  $^{239}\text{Np}$ .



Figure 3.17: The decay scheme of  $^{239}\text{Np}$ 

### 3.3 Reactivity Measurements

Complementary to the reaction rate measurements discussed in the previous section, reactivity worths of individual fuel pins were measured. These measurements were carried out exclusively in the unperturbed configuration.

#### 3.3.1 Compensation Technique

The effects on the system reactivity of removing individual fuel pins from the reference SCWR-like test lattice have been measured using the compensation technique [18, 19]. Thereby, the PROTEUS reactivity changes are compensated by the control mechanisms of the reactor. The first of these control mechanisms corresponds to the four ZEBRA control rods (CR1 - CR4), which can be moved manually by the operator (see Sec. 2.1). Their individual worths are a few tens of cents (slight differences between them can arise due to the direct surroundings of each rod in terms of C-driver loadings). The second control mechanism is the so called autorod (AR) which has a worth of a few cents. The autorod position is adjusted automatically (via a feedback mechanism) to compensate for very small reactivity changes, originating in fluctuations and slow drifts (e.g. from the warming up of the reactor during operation).

The compensation technique works as follows. The operator stabilizes the reactor. The positions of autorod and control rods are noted and stored. The fuel pin, whose reactivity worth is to be measured, is removed while the reactor is critical. In order to re-stabilize the reactor, the operator compensates for the change in reactivity by adjusting the positions of the control rods.

Fine tuning is done automatically by the autorod. Upon stabilization of the reactor, the new positions of auto- and control rods are noted and stored once again. To obtain the reactivity change which accompanies the removal of a fuel pin, one calculates the differences in critical rod positions before and after the removal of the fuel pin.

The changes in positions of the auto- and control rods yield the reactivity effect. In order to translate this effect (expressed in terms of mm of movement of each rod type) into a reactivity worth  $\Delta\rho$ , one must calibrate the control and auto rods. This calibration is done in three steps: First, the linearity in reactivity of the autorod is checked. Then, the control rods are inter-calibrated versus the autorod and, finally, the system is calibrated absolutely.

Linearity of the autorod means that, if an inserted reactivity effect of  $\Delta\rho$  results in an autorod movement of  $x$  mm, an insertion of  $2\Delta\rho$  results in a movement of  $2x$  mm, or alternatively, the autorod movement  $x$  responding to a change in reactivity of  $\Delta\rho$  is independent of the initial position of the autorod. The linearity of the autorod can be checked using a well-defined change in reactivity at different initial AR positions. Previous measurements in the LWR-PROTEUS program have shown that the autorod is almost, but not perfectly linear. The small non-linearity, however, is configuration independent. Therefore, this measurement has not been repeated for the current series of experiments.

A polynomial of the form:

$$\left. \frac{eARU}{mm} \right|_{AR} (AR) = a + b \cdot AR + c \cdot AR^2 + d \cdot AR^3 \quad (3.20)$$

adequately models the differential worth of the autorod in terms of effective autorod units (eARU). Using this, a movement of the autorod from position  $AR_a$  to  $AR_b$  can be described as (non-linearity corrected):

$$\Delta eARU = \int_{AR_a}^{AR_b} \left. \frac{eARU}{mm} \right|_{AR} (AR) dAR. \quad (3.21)$$

The movement of the autorod, induced by the reactivity change, is expressed in eARU.

The second step of the calibration relates the movement of a control rod to that of the autorod. In other words, a movement of the control rod has to be expressed in eARU. This is necessary because of the limited worth of the autorod itself, which can only compensate very small reactivity changes (up to a few cents). Removing a fuel pin usually results in a larger  $\Delta\rho$  so that a control rod movement is necessary to reach criticality again. This calibration was done by analyzing the response of the autorod to various control rod movements, which yielded the quantity of interest, namely the number of eARU per mm of control rod movement. A fifth-order polynomial function was fitted to the recorded data points. Because of the small differences between the control rod

worths, this step was repeated for all four control rods (CR1 - CR4). A change in reactivity, induced by the removal of a fuel pin, can now be expressed in eARU by the following formula:

$$\rho[eARU] = - \left\{ \sum_{i=1}^4 \int_{CR_{i_a}}^{CR_{i_b}} \frac{eARU}{mm} \Big|_{CR_i} (CR) dCR + \int_{AR_a}^{AR_b} \frac{eARU}{mm} \Big|_{AR} (AR) dAR \right\}. \quad (3.22)$$

The final step is to relate the equivalent autorod units (eARU) to cents. This was done using alternative experimental techniques to measure the change in reactivity (stable period technique or inverse kinetics technique). When using the stable period technique, the asymptotic reactor period is measured some time after a positive reactivity step (has to be small enough for the reactor to remain in a safe operating mode). From the measured period, the magnitude of the inserted reactivity is calculated using the well-known inhour equation. This technique is described in more detail elsewhere [20, 21]. The inverse kinetics technique measures the evolution of the reactor neutron population  $P(t)$  and the reactivity, as a function of time, is derived employing the point neutrons kinetics equations in their general form [20, 22].

### 3.3.2 Measurement Procedure

Due to the symmetry of the SCWR-like reference test lattice, only three generic fuel pin positions exist: the corner pins (at the intersection of rows and columns of fuel pins), the neighbors to the corner pins, and the remote pins (that do not touch a corner pin). Therefore, the worths of only the fuel pins K11, K12, K13, and K14 (see Fig. 2.17) were measured. The measurement procedure was the same for each of these pins.

The first step of each pin removal experiment was to drive the reactor critical. Thereby, the reactor power, as well as the critical control rod and autorod positions, were chosen carefully, since these parameters have direct influence on the quality and the accuracy of the measurements. Choosing the optimal reactor power is a trade-off between low statistical fluctuations of the autorod (the AR automatically adjusts its position by a feedback circuit in which an ionization chamber is used to measure the deviation from the nominal neutron flux level) and small temperature drift effects. The higher the reactor power, the stronger are the temperature drift effects which are corrected by the autorod movement. This correction interferes with the measurement of the fuel pin worth and has to be kept to a minimum. The neutron flux level, which was set at  $5 \cdot 10^5 \text{ cm}^{-2}\text{s}^{-1}$ , is the minimal flux which still has low enough statistical fluctuations of the autorod. Once the target flux was reached, the neutron source used for starting the reactor was removed. As regards the initial control rod positions, care was taken to be within the calibrated range of the control rod system, for which conditions close to linearity had been shown to exist. One had to assure that the range of near-linearity was maintained during the course of the measurement. Therefore, the necessary control rod movements had to be anticipated correctly.

Once sufficient stabilization was achieved – indicated by a constant value of the autorod position – the pin removal experiment was started. First, the pin under investigation was withdrawn from the active zone of the reactor. This was done manually by pulling on a steel wire which was attached to the top of the fuel pin. The wire was guided through a small opening in the upper reactor shielding, via a pulley device, to a cable winch at the side of the reactor. The wire was pulled out up to a predefined position which ensured that the fuel pin in the reactor would be withdrawn from the active zone, but would remain in the upper lattice plate so that it could be brought back into its initial position without shutting the reactor down. At the same time, the operator was moving one of the control rods, CR1 (the other three control rods were kept at constant positions), to compensate the change in reactivity. Once again, stabilization of the reactor was awaited to ensure a constant position of the autorod (approximately 10 minutes). The next step was to reinsert the previously removed fuel pin while readjusting the control rod position of CR1. This procedure was repeated four times before the reactor was shut down.

Throughout the cyclic movements of the studied fuel pin, the autorod and control rod positions were recorded automatically every second. A program computed the average autorod position before every reactivity step by taking the average over the 120 seconds preceding the step. Finally, the reactivity worth of each step was computed using Eq. 3.22. The average over the four movement cycles of the fuel pin was taken. The dispersion of the individual values around the average corresponds, in first order, to the statistical experimental error. The systematic uncertainties on nuclear data and on the control rod inter-calibration have not been considered. The nuclear data that was used, was the same as in the LWR-PROTEUS program. According to Murphy and Lüthi [19], the uncertainty on the nuclear data is in the order of 3.7%, while that on the inter-calibration is around 0.5%. The systematic uncertainty, however, cancels out when a ratio of reactivity effects is taken. A typical statistical uncertainty (dispersion around the average) was found to be in the order of 0.5%.

# Bibliography

- [1] Y. Ishiwatari, Y. Oka, and S. Koshizuka. Control of a High Temperature Supercritical Pressure Light Water Cooled and Moderated Reactor with Water Rods. *Journal of Nuclear Science and Technology*, 40(5):298–306, 2003.
- [2] A. Santamarina, N. Hfaiedh, R. Letellier, V. Marotte, S. Misu, A. Sargeni, C. Vaglio, and I. Zmijarevic. Advanced neutronics tools for BWR design calculations. *Nuclear Engineering and Design*, 238:1965–1974, 2008.
- [3] F. Jatuff, K. Macku, and R. Chawla. On the accuracy of reactor physics calculations for square HPLWR fuel assemblies. *Annals of Nuclear Energy*, 33:198–207, 2006.
- [4] A. Yamaji, Y. Oka, and S. Koshizuka. Three-dimensional Core Design of High Temperature Supercritical-Pressure Light Water Reactor with Neutronic and Thermal-Hydraulic Coupling. *Journal of Nuclear Science and Technology*, 42(1):8–19, 2005.
- [5] K. Kamei, A. Yamaji, Y. Ishiwatari, Y. Oka, and J. Liu. Fuel and Core Design of Super Light Water Reactor with Low Leakage Fuel Loading Pattern. *Journal of Nuclear Science and Technology*, 43(2):129–139, 2006.
- [6] Ken Nakajima, Masanori Akai, and Takenori Suzaki. Measurement of the Modified Conversion Ratio by Gamma-Ray Spectrometry of Fuel Rods for Water-Moderated UO<sub>2</sub> Cores. *Nuclear Science and Engineering*, 116:138–146, 1994.
- [7] U.C. Bergmann, R. Chawla, F. Jatuff, and M.F. Murphy. Optimised non-invasive method to determine <sup>238</sup>U-capture-to-total-fissions in reactor fuel. *Nuclear Instruments & Methods in Physics Research, Section A*, 556:331–338, 2006.
- [8] ORTEC. *GammaVision-32, Gamma-ray Spectrum Analysis and MCA Emulator*, 2003. A66-B32 User’s Manual.
- [9] M.F. Murphy. The LWR-PROTEUS Fuel Pin  $\gamma$ -Scanning Machine. In *Proceedings of the Annual Meeting on Nuclear Technology '99, Karlsruhe, Germany*, page 425, 1999.
- [10] G. Perret. A MATLAB routine to yield measured radial and axial reaction rate distributions.

- Technical Report TM-41-07-04, Paul Scherrer Institute, 2007.
- [11] Joel Rhodes, Kord Smith, and Malte Edenius. *CASMO-4E, Extended Capability CASMO-4, User's Manual*. Studsvik Scandpower, 2004. SSP-01/401Rev2.
  - [12] C. Nordborg and M. Salvatores. Status of the JEF Evaluated Data Library. In *Proceedings of International Conference on Nuclear Data for Science and Technology, Gatlinburg, Tennessee, USA, May 9-13*, volume 2, page 680, 1994.
  - [13] P.F. Rose et al. ENDF-201, ENDF/B-VI Summary Documentation. Technical Report JBNL-NCS-17541, 4th Edition, 1991.
  - [14] M.B. Chadwick. ENDF/B-VII.0: Next Generation Evaluated Nuclear Data Library for Nuclear Science and Technology. Technical Report Nucl. Data Sheets, 102, 2931, 2006.
  - [15] A. Santamarina, D. Bernard, and Y. Rugama. The JEFF-3.1.1 Nuclear Data Library. Technical Report JEFF Report 22, 2009.
  - [16] Brookhaven National Laboratory National Nuclear Data Center. Nuclear database, Nov 2010. <http://www.nndc.bnl.gov/ensdf>.
  - [17] G. Perret, M.F. Murphy, M. Plaschy, F. Jatuff, and R. Chawla. Modified conversion ratio measurements in a SVEA-96 Optima2 BWR assembly compared with MCNPX predictions. In *First International Conference on Physics and Technology of Reactors and Applications (PHYTRA1), Marrakech, Morocco, March 14-16*, 2007.
  - [18] M.F. Murphy and A. Lüthi. LWR-PROTEUS: The results of Measurements in Configuration 7A. Technical Report TM-41-01-01, Paul Scherrer Institute, Villigen, Switzerland, March 2001.
  - [19] M.F. Murphy and A. Lüthi. LWR-PROTEUS Phase II: A Measurement plan for the determination of the reactivity effect of burnt fuel samples. Technical Report AN-41-02-04, Paul Scherrer Institute, Villigen, Switzerland, June 2002.
  - [20] M. Rosselet. *Reactivity Measurements and their Interpretation in Systems with Large Spatial Effects*. PhD thesis, École Polytechnique Fédérale de Lausanne, 1999.
  - [21] T. Williams. HTR-PROTEUS CORE 1: ZEBRA Control Rod S-Curves and Rest Worths. Technical Report TM-41-92-40, Paul Scherrer Institute, Villigen, Switzerland, February 1993.
  - [22] T. Williams et al. Current Status of Methods for Subcriticality Measurements on the PROTEUS Facility. Technical Report TM-41-95-08, Paul Scherrer Institute, Villigen, Switzerland, 1995.

## 4 Neutronics Modeling of the SCWR-Like Lattice

While the previous chapter was dedicated to the experimental methods used to obtain reaction rate distributions and fuel-pin reactivity worths in the SCWR-like test lattice, this chapter describes the computational methods tested against the integral measurements. In the chapters following, comparisons are made between calculational and experimental results for the different types of test zone configurations investigated.

Based on previous reporting of discrepancies between deterministic and probabilistic neutronics codes for the prediction of the characteristics of perturbed SCWR assemblies [1], one code of each type has been considered currently. Section 4.1 gives an introduction to the probabilistic code MCNPX [2] and to the deterministic assembly code CASMO-4E [3]. In Section 4.2, the computational models that were used for the validation of the calculational tools are introduced, and the validation strategy is discussed in Section 4.3.

### 4.1 Codes

#### 4.1.1 MCNPX

MCNPX stands for Monte Carlo N-Particle Extended and belongs to the family of probabilistic radiation transport codes. It can be used for calculating generalized charged or neutron particle transport problems (or a combination thereof). It is very versatile and can treat almost any three-dimensional geometry.

##### 4.1.1.1 Method

The Monte Carlo method obtains solutions of a problem by simulating individual particles and recording (user-specified) tracking information about the particle histories. This process is repeated many times before taking the aggregate of the recorded particle behavior. For quantities of interest (such as the volumetric flux), this measured average is normally distributed around the

real average of the entire system (according to the central limit theorem). Hence, by increasing the number of recorded particles, one can reduce the uncertainty on the recorded average.

Monte Carlo programs replicate a statistical process, i.e. a process that has a certain number of outcomes which happen with a certain probability [2]. The method does not need an analytic solution of the equations describing the problem and is therefore particularly useful in cases where these equations can not be solved analytically (which is true for the vast majority of neutron transport problems in meaningful geometries). The probabilistic events that happen during the lifetime of a particle are treated in sequence. The total phenomenon is described by statistical sampling of the probability density function describing these events (i.e. interaction cross-sections). This treatment is based on the selection of random numbers – the name Monte Carlo is a reference to the famous casino.

MCNPX follows each of many particles throughout their existence in the simulated system. Any given particle, such as a neutron, starts from its predefined source or location of production inside the system. It moves, governed by the laws of physics, through the material (hence with constant speed in a straight line) until it hits a nucleus (in the medium). The outcome of this collision is chosen randomly according to the probabilities of all possible outcomes (weights of the interaction cross-sections). If, for example, the neutron is elastically scattered, then another random number is drawn to choose the direction in which the neutron travels after the collision, weighted according to the kinematics. This process is continued until the neutron and all its daughter particles (originating from the interactions of the initial particle) are in a terminal state. This terminal state may be the absorption of the neutron, leakage out of the system boundaries, or downscattering below a set energy cutoff. This particle history is now complete and the process is repeated many more times (as defined by the user). As more and more neutron histories are tracked, the distribution of neutrons in the system becomes better known. The quantities of interest to the user are tallied and estimates on their uncertainties are calculated.

### 4.1.1.2 KCODE Option

One of the most important parameters for a nuclear system is its effective multiplication factor  $k_{\text{eff}}$ , which is a measure of the rate of change of the total number of neutrons in the system. It is defined as the number of neutrons in the  $(i + 1)^{\text{st}}$  generation divided by the number of neutrons in the  $i^{\text{th}}$  generation. A system is said to be critical if  $k_{\text{eff}} = 1$ , i.e. the total number of neutrons remains constant over time and the nuclear chain reaction sustains itself. If  $k_{\text{eff}} < 1$ , the system is subcritical and the chain reaction will discontinue. On the other hand, if  $k_{\text{eff}} > 1$ , the system is supercritical and the number of neutrons increases with every generation.

MCNPX offers a simple option for calculating the criticality of any given geometry. As input, all that is needed beyond the geometry definition, the specification of data libraries, and physics models and behaviors to be used in the calculation, is the so-called KCODE card. Source neutrons are divided into batches. Each batch of source neutrons is transported and yields the



number of neutrons produced by the system in one generation, which corresponds to the next batch of source neutrons. A neutron generation corresponds to the life of a neutron from its birth somewhere in the system until its death by parasitic absorption, induction of fission, or leakage out of the system. Therefore, one  $k_{\text{eff}}$  cycle is the computational equivalent of a neutron generation. The number of generations or cycles are specified in the KCODE card, together with the number of neutrons per cycle. The fission distribution of the  $i^{\text{th}}$  cycle serves as neutron source distribution in the  $(i + 1)^{\text{st}}$  cycle. To take delayed neutrons into account, the total average number of neutrons born per fission (including prompt and delayed neutrons),  $\bar{\nu}_{\text{tot}}$ , is considered. Obviously, the neutron source distribution for the first cycle can not come from the previous fission distribution and has to be defined by the user. It is important to let this fission source converge (over some inactive cycles) before the actual calculation begins. An additional entry in the KCODE card is required to specify how many cycles should be discarded. At the end of the calculation, an estimate of  $k_{\text{eff}}$  is given together with the corresponding confidence interval.

#### 4.1.1.3 Limitations

Monte Carlo codes have become very mature over the last two decades and they are being employed more and more for problems which used to be only possible to solve with deterministic codes. This is due not only to the rapid improvement of computers, but also to the inclusion of improved physics models and data for various particle transport problems (such as biological radiation dose calculations). Nevertheless, the limited computer power still is a big constraint for MCNPX. Calculations, especially of large systems, are very time consuming. This makes MCNPX unfeasible to use as a real-time reactor core monitoring tool, for example.

MCNPX, as do all reactor physics codes, relies on an appropriate nuclear data library as source of information about the particle interaction probability with the medium. Calculational accuracy is therefore limited by the accuracy of the provided nuclear data. Special care has to be taken when stating uncertainties with MCNPX. The confidence intervals, which are provided by MCNPX with every tallied parameter, only take the statistical error into account. In many cases, the total uncertainty of a calculated value, including statistical and systematic uncertainties as well as uncertainties due to the nuclear data, is considerably larger than the MCNPX-reported statistical uncertainty alone.

#### 4.1.2 CASMO-4E

As representative tool for deterministic analysis, the industrial LWR assembly code CASMO-4E [3] has been employed throughout this work. Its use has been in conjunction with its 70 energy-group library based on ENDF/B-VI data. CASMO-4E solves the neutron transport (or

Boltzmann) equation [4]

$$\frac{\partial n}{\partial t} + v\hat{\Omega}\nabla n + v\Sigma_t n - \int_0^\infty dE' \int_{4\pi} d\hat{\Omega}' v'\Sigma_s n - s = 0 \quad (4.1)$$

and is designed to model both boiling and pressurized water reactors (BWRs and PWRs). As a 2-D code, it cannot handle axial variations. A buckling correction is used to account for neutron leakage and obtain a critical system. Most commonly, CASMO-4E is used to model LWR fuel assemblies with reflective boundary conditions, i.e. an infinite array of identical assemblies, defined in terms of constituent pin geometries and compositions, structural materials and water gaps, assembly boundaries, etc. This approach is appropriate for modeling relatively large regions of a standard LWR core. A multi-zone system such as the PROTEUS research reactor, however, cannot be modeled in this way. Hence, unlike the case of a Monte Carlo modeling of the entire reactor, a direct comparison of CASMO-4E results with the experimental data is not feasible.

#### 4.1.2.1 Methodology

The flow diagram of CASMO-4E [5] is depicted in Fig. 4.1. For the present study, a burnup calculation is not used and the corresponding process steps are therefore not utilized.

After the input has been read, the first step is the resonance calculation. In the energy range above about 4 eV, heavy isotopes show strong variations in their cross sections. This is the so-called resonance region. In the resonances, the cross sections for a given reaction - neutron capture, for example - change by several orders of magnitude over a relatively small energy range. Due to the very large cross-section value within a resonance, the capture rate at the corresponding energy strongly depends on the concentration of the nuclide. If the nuclide is infinitely diluted in the material, the neutron flux is not affected. However, if the concentration is not negligible, the neutron flux is depressed at this energy and the effective absorption cross-section (resonance integral) is reduced. This effect is known as self-shielding.

In the case of non-resonant absorbers, macroscopic cross-sections are directly derived from the available microscopic cross-sections of the multigroup cross-section libraries (by multiplication with the number density of the nuclide). The derivation of macroscopic cross sections in the resonance region requires a more complex approach. The problem is that, for the calculation of the macroscopic absorption cross section of a spatial region (containing heavy nuclei), the neutron flux needs to be known. On the other hand, in order to solve the transport equation, the cross sections need to be calculated first. The standard approach, widely used in deterministic reactor physics codes, is to calculate case-dependent cross sections from tabulated case-independent parameters. These tabulated parameters are the resonance integrals, which have been generated for various homogeneous mixtures of the resonant absorber with hydrogen. In order to account for the heterogeneity of the geometry, the appropriate resonance integrals are combined via an equivalence theorem [6], which interpolates the tabulated resonance integrals to obtain a

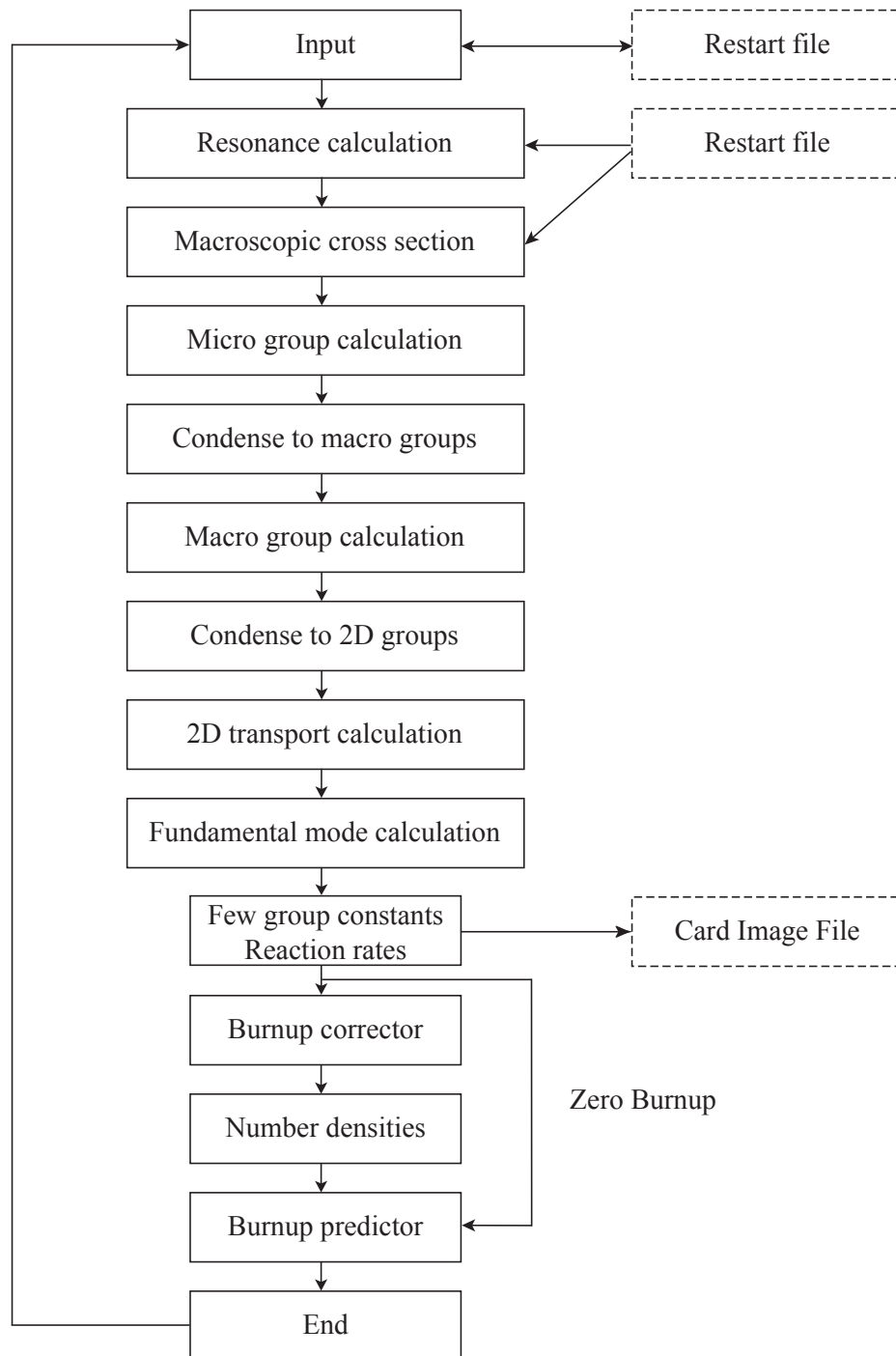


Figure 4.1: Flow diagram of the CASMO-4E code [5]

resonance integral for the particular heterogeneous problem.

Micro-group calculations are performed at the 1-D pin cell level. Each pin type, normally consisting of three or four regions, is calculated separately. At the pin cell level, the neutron flux distribution is calculated, using the maximum number of energy groups available. This is possible without using too much computing resources, because of the simple geometry. In the case of pins containing burnable absorbers like gadolinium, the fuel region is split into many annular regions to account for the strong variation in the thermal neutron flux. The calculations are done in a 70 energy-group structure. The neutron transport equation is solved in its integral form using the method of collision probabilities [7] to evaluate the spatial distribution of neutrons inside the pin cell. The collision probability method is based on the calculation of the mean distance that a neutron of a certain energy can travel in a certain material before it is scattered or absorbed. The probability that the neutron, born in one region, will escape this region before suffering a collision is then calculated.

Before one can continue the calculation and expand it to the entire assembly, the micro energy groups have to be condensed into the macro energy-group structure. The macro-group calculation is performed on the entire lattice. Again the integral transport equation is solved, but this time in 40 energy groups and with homogenized pin cells. A response matrix method [8, 9] is used to solve the equation, where the outward current becomes the inward current of the adjacent cell. For each mesh, the transport probabilities between the various surfaces are calculated. By using the current instead of the flux as boundary condition, the summation over a large portion of the cells is avoided since only neighboring cells have to be included. This strongly reduces the computation time. The macro-group calculation updates the energy distribution of neutrons in each pin cell.

After the macro-group calculation, the 40 energy groups are condensed to the 2-D energy group structure. By default there are eight energy groups in this structure, four thermal and four fast groups.

After the neutron energy distribution has been updated by the macro-group calculation, the 2-D transport calculation is performed. Since the macro-group calculation is processed with homogenized pin cells, it is not able to modify the spatial distribution of neutrons inside the pin cell. The 2-D transport calculation includes the effects of the surroundings of a pin cell on the flux and gives a detailed spatial distribution of neutrons in every pin cell with the energy distribution derived in the macro-group calculation. It is a two-dimensional calculation in the defined 2-D energy group structure. The flux distribution in the lattice is calculated by solving the neutron transport equation, utilizing the method of characteristics [10, 11]. Here, the Boltzmann equation is solved along a certain number of directions. The calculation of the angular dependence is thereby broken up into discrete directions. To account for the remaining directions, that are not covered by any characteristic, each direction is associated with a certain weight. The thus obtained average values for the angular flux in each mesh, in each discrete direction, are used to calculate the scalar flux.

So far, the results obtained do not account for the effects of leakage. A fundamental mode calculation is performed to include leakage into the infinite lattice results via a critical-buckling correction. This calculation is done in the macro-group energy structure employing diffusion theory.

Few-group constants and reaction rates in all regions of the lattice are calculated from the detailed flux distribution derived from the procedure above. These tables are printed in the output file, from where they can be taken for further analysis.

#### 4.1.2.2 Limitations

The most obvious limitation of CASMO-4E is the restriction to two dimensions. CASMO-4E is designed to solve two-dimensional problems and can therefore not handle variations along the Z-axis. As mentioned above, a buckling correction is used to account for neutron leakage along the Z-axis and to obtain a critical system.

A further limitation of the code is its energy-group structure. Only the micro-group calculations are performed with the maximum detail available in CASMO-4E, namely 70 energy groups. Clearly, even these 70 groups are a considerably condensed representation of the continuous cross-section data available in basic evaluated data files such as ENDF/B or the European version JEFF. Although the user can change some of the default settings (40 macro-groups, 8 groups for the two-dimensional transport calculation), the maximum of 70 groups can not be exceeded in CASMO-4E. The energy group structure is chosen to optimize execution time of the program with respect to the accuracy of the calculation.

CASMO-4E is explicitly written and optimized for calculations of commercial BWR and PWR fuel lattices. As it is a commercial code, the developers have focused on user-friendliness and speed. The price for this is a strong limitation on possible geometries one can calculate. The lattice has to be either cartesian or hexagonal. All pins must be constructed of concentric infinite cylinders. Up to sixteen pins (a square four-by-four lattice) may be grouped into one large unit which contains, for example, a large control rod or water channel. The input decks for the code are simple and easy to modify.

A common property of all deterministic codes is the extensive use of mathematical approximations. Among them are the interpolation of resonance integrals from tabulated values, the above mentioned collapsing of energy groups to decrease the number of times the n-group transport equation must be solved, and the homogenization of spatial regions.

## 4.2 Considered Models for the SCWR-Like Test Lattice

Use of the currently conducted experiments for the validation of a fully three-dimensional neutronics code, with which any given geometry can be modeled accurately - such as the Monte Carlo code MCNPX - is clearly quite straightforward. In this case, one can directly compare most of the measured quantities to the computational predictions. For a two-dimensional lattice code such as CASMO-4E, however, validation is not as simple, because the code is not capable of calculating the multi-zone geometry of the PROTEUS reactor. In order to overcome this problem, one has to introduce additional calculational models to represent the implemented SCWR-like test lattice, which can be computed with the two-dimensional code as well.

The standard validation scheme for deterministic codes, as employed previously in the LWR-PROTEUS program, is shown in Figure 4.2. This strategy is based on the fact that measurements in the earlier LWR-PROTEUS test zone configuration were made in a central test assembly, surrounded by a ring of eight similar assemblies. The situation with the SCWR-like test lattice is quite different, so that a new approach had to be taken for the analysis of the current experiments. A detailed discussion of this issue is presented in Sec. 4.3.

To validate MCNPX, an existing whole-reactor model [12] was adapted to the current test zone geometry and used to predict reaction rate distributions and fuel pin removal worths. This model (see Figure 4.3) includes detailed descriptions of all neutronically relevant components of the PROTEUS reactor. Depicted are the test zone containing the SCWR-like lattice in the center, the buffer zone, the D<sub>2</sub>O driver zone, and the graphite driver zone. Blue areas denote water and dark orange circles denote fuel pins. In the test zone, the light blue circles are structural support pins, the larger grey circles denoting the metal rods inserted into the central moderator regions. The LWR-PROTEUS model is based on an accurate geometrical and material data base [13, 14], and great attention has been paid to ensure precise modeling. Even the zebra control rods (see Sec. 2.1) have been modeled, and their actual position during the experiment could be explicitly represented in the calculation.

For identifying an optimal approach towards the current validation of deterministic LWR design tools such as CASMO-4E, two other models have been considered in addition to the PROTEUS whole-reactor model used by MCNPX (see Figure 4.3). These models, which can be employed by both CASMO-4E and MCNPX, focus on the experimental SCWR-like test lattice itself, and are referred to here as the “reduced geometry” and “open perimeter” models, respectively.

The reduced geometry model, shown in Figure 4.4 (left hand side), corresponds effectively to a radially infinite pattern of SCWR-like “assemblies” of the type shown in Figure 2.17 (b), i.e. the PROTEUS test lattice but with the outermost fuel-pin rows and columns added in. Once again, the blue areas denote water, dark orange circles denote fuel pins, and the larger grey circles are the metal rods inserted into the central moderator regions. The area within the yellow-bordered square corresponds to the part of the lattice actually built into the PROTEUS

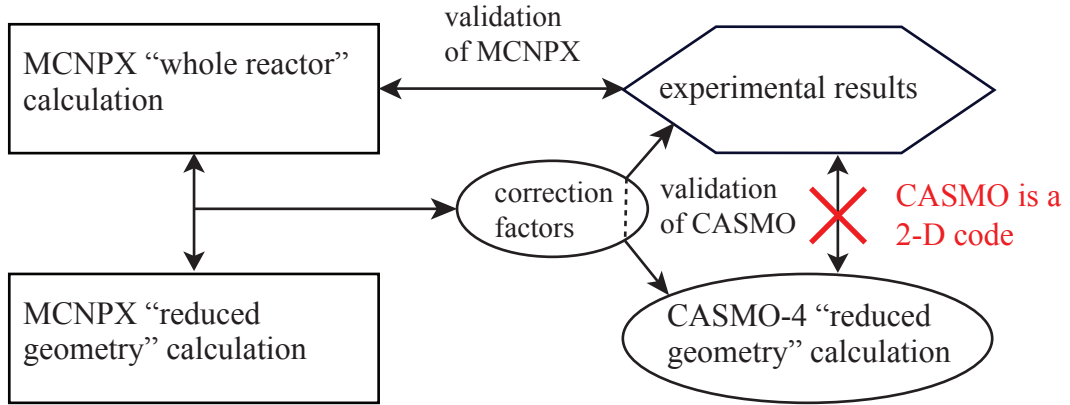


Figure 4.2: Standard scheme employed in the earlier LWR-PROTEUS experiments, for validation of neutronics codes that are limited to a two-dimensional representation of the test lattice.

test zone. The distance between the outermost pins of neighboring assemblies in the considered pattern, i.e. the in-between moderator thickness, has been set at  $4.8\text{ mm}$  (This corresponds to the up-scaled distance between fuel-pin rows at the interface of neighboring assemblies in the SCWR core design considered by Yamaji et al. [15]; the scaling factor equals the ratio of the fuel pin dimensions in the PROTEUS lattice and the Yamaji assembly). The reduced geometry model can easily be calculated by CASMO-4E employing, due to the given symmetry, a quarter-geometry representation of the assembly in conjunction with reflective boundary conditions at each boundary. Results corresponding to critical conditions can be obtained using the critical buckling search. For MCNPX, the reduced geometry model can be modeled exactly, critical conditions being established in this case via adjustment of the model height.

The second additional model which has been considered, viz. the open-perimeter model, is shown in Figure 4.4 (right hand side). As can be seen, this differs from the reduced geometry model in that the outermost fuel-pin rows and columns of the “assembly” have been replaced by moderator. Effectively, this model corresponds to a repeated pattern of the actually implemented test lattice in PROTEUS, in which the outermost fuel pins had to be omitted.

Clearly, neither the reduced geometry, nor open perimeter, model can exactly simulate the neutron conditions of the experimental lattice as done by the whole-reactor model of PROTEUS. The latter calculates the effective neutron spectrum at the different fuel pin positions in the test zone, taking full account of the influence of the outer regions (buffer, driver, etc.) of the PROTEUS reactor. Both the other models, on the other hand, omit these outer zones completely, focusing - each, in a different specific manner - on the SCWR-like lattice itself. The reaction rate distributions calculated for the SCWR-like lattice by the three different models will thus not be the same, the differences tending to decrease towards the central part where the models are identical.

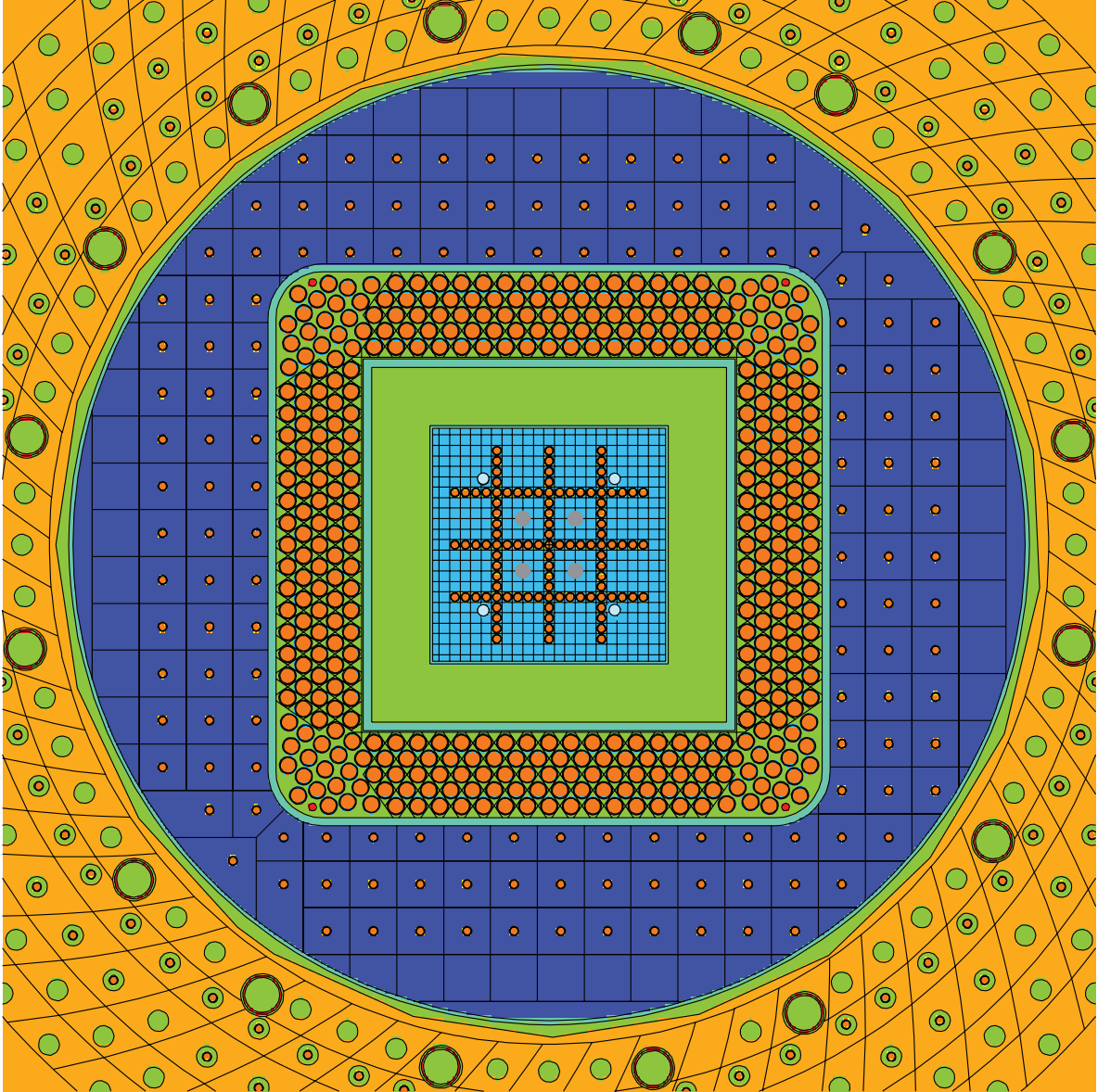


Figure 4.3: Cross-section of the MCNPX whole-reactor model of the PROTEUS reactor (in this example with the reference lattice, perturbed by four metal rods). Depicted are the test zone containing the SCWR-like lattice in the center, the buffer zone, the  $D_2O$  driver zone, and the graphite driver zone. Blue areas denote water and dark orange circles denote fuel pins. In the test zone, the light blue circles are structural support pins, the larger grey circles denoting the metal rods inserted into the central moderator regions.



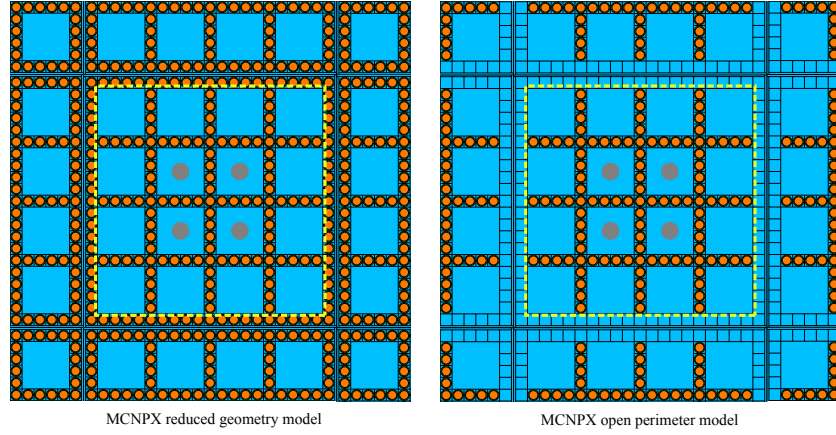


Figure 4.4: Cross-sections of the reduced geometry and open perimeter models of the SCWR-like test lattice (in this example perturbed by four metal rods). Once again, the blue areas denote water, dark orange circles denote fuel pins, and the larger grey circles are the metal rods inserted into the central moderator regions. The area within the yellow-bordered square corresponds to the part of the lattice actually built into the PROTEUS test zone. Each depicted assembly type is modeled with reflective boundary conditions at its borders in X and Y directions, which leads to an infinite system (indicated in each figure by adjoining parts of adjacent assemblies).

Figure 4.5 shows a comparison of the results obtained using MCNPX as applied to each of the three models for the unperturbed SCWR-lattice case. Shown are the total fission rate ( $F_{\text{tot}}$ ) and the  $^{238}\text{U}$ -capture rate ( $C_8$ ), as well as the ratio  $C_8/F_{\text{tot}}$ , for the various fuel pin positions along the central row of the experimental test lattice. Considering the symmetry of the configuration, results need to be given only for one-half of the lattice, and this has been done in terms of pins K11 to K20, the former being the central pin (see Figure 2.17). It should be noted that, for the case of the reduced geometry model, results are shown also for an extra pin position, viz. K21, corresponding to the outermost pins added into this model (see Figure 4.4). For  $F_{\text{tot}}$  and  $C_8$ , the results from each model have been normalized to unity at the center, i.e. to the value for K11. In the case of  $C_8/F_{\text{tot}}$  - a reaction ratio characterizing the local neutron spectrum - normalization is not necessary and the results can be compared directly.

It is seen from Figure 4.5 that, as expected, the differences between the three models remain relatively small over the central part of the SCWR-like lattice – between the positions K11 to K17 – where the measurements have been carried out. For the outer positions, the effects of the missing outermost fuel pins in the open perimeter model (as compared to the reduced geometry model) are clearly visible in terms of the higher  $F_{\text{tot}}$  values resulting from the softer neutron spectrum in this region.

The effects of the outer zones of PROTEUS in the whole-reactor model reach further towards the center of the test lattice for the  $^{238}\text{U}$ -capture rate than for the total fission rate. This is due to the fact that  $F_{\text{tot}}$  is a reaction rate sensitive to neutrons in the thermal region, where the neutron mean free path is small and the coupling between neighboring regions is much stronger than between distant regions. Conversely,  $C_8$  is more sensitive to epithermal neutrons with larger

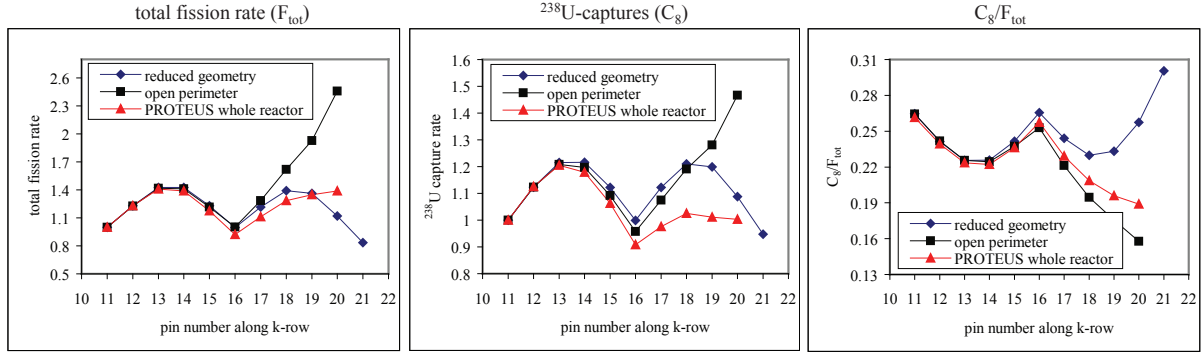


Figure 4.5: Differences between  $F_{\text{tot}}$ ,  $C_8$  and  $C_8/F_{\text{tot}}$  distributions as obtained from the three different MCNPX models for the case of the unperturbed SCWR-like lattice.

mean free paths. Hence, perturbations of  $C_8$  occur over a wider range. For pin K17 and positions further on the outside, the absence of the outermost fuel pins in the experimental lattice is clearly an important factor for making the effects of the outer PROTEUS zones considerably larger than in the test assembly of previous LWR-PROTEUS experiments, e.g. Bergmann et al.[16]. This was, of course, the basic reason for excluding pins K18 to K20 (and corresponding positions in the other directions) from the current measurement campaigns.

As mentioned earlier, and discussed in greater detail in the following section, the inability of CASMO-4E to model the complete multi-zone PROTEUS reactor, requires a clearly justified approach for achieving an indirect comparison with experimental results. The Monte Carlo modeling with MCNPX can provide the necessary “bridge”, in that calculations can be done for both the complete PROTEUS reactor and one of the two “CASMO-4E-compatible” models discussed above. For the choice to be made in the latter context, one has several arguments which favor the reduced geometry model over the open perimeter model, viz.

1. Although the results shown in Figure 4.5 for the central part of the SCWR-like lattice are of similar quality in the two cases, the shapes of  $F_{\text{tot}}$  and  $C_8$  distributions for the outer part resemble those of the whole-reactor model much more closely in the case of the reduced geometry model.
2. The outermost fuel pins in the reduced geometry model occur in a part of the SCWR-like lattice which remains unperturbed in the context of the perturbed test lattice configurations investigated currently, e.g. the control rod related investigations described in Subsection 3.1.2. As such, a normalization of results “over all pins” between MCNPX and CASMO-4E (see following section) can be expected to be much less biased by possible perturbation-related shortcomings in CASMO-4E.
3. Finally, the reduced geometry model is very close in its characteristics to the Yamaji SCWR assembly and, as such, is the more representative choice for serving as reference for

the deterministic modeling. For example, the presence of the outermost fuel pins causes the neutron spectrum in the outer part of the reduced geometry model to be much more similar to that in the inner part, providing a higher degree of symmetry across the model as compared to the situation for the open perimeter model.

For all the above reasons, the reduced geometry model has been chosen for providing the normalization basis for CASMO-4E, relative to MCNPX, as discussed in the following.

### 4.3 Validation Strategy

The standard validation methodology for a code that is not capable of calculating the complete geometry of a given experimental setup is to compare the calculated and measured values via the use of suitably developed correction factors (see Figure 4.2). In previous experiments in the LWR-PROTEUS program, for example, such correction factors were obtained for reaction rate distributions in the central test assembly by considering ratios of calculational results from appropriate Monte Carlo models. The experimental data could thus be corrected for the PROTEUS outer-zone effects and then compared directly to the results from the deterministic code in question. In this way, one effectively produced  $C'/E$  (calculation/experiment) values, where the  $C'$  indicates the use of corrected data.

The above approach clearly implies that (a) the applied corrections are small, and (b) the errors in the correction factors are much smaller than the corrections themselves. Furthermore, to obtain  $C'$ , the results of all three models - MCNPX PROTEUS whole-reactor, MCNPX reduced geometry, and CASMO-4E reduced geometry - must be normalized in the same way, i.e. the derived pin-wise results have to be divided by the average over a specific selection of fuel pins. The same is true for the comparison of  $C'$  to experimental values, which implies that the choice of the combination of fuel pins to which one needs to normalize results is limited to all or a subset of the measured pins. In the investigations of perturbations of the SCWR-like lattice, however, the pins that were measured are close to the perturbations introduced (see, for example, Figures 3.2 and 3.3), and this is where one would expect discrepancies to be found. By normalizing to a selection of pins, for many of which the results could be systematically “erroneous” with respect to experiment, one would be averaging out these potential discrepancies and the results could then appear to agree in a region of the lattice where they actually do not.

In order to avoid such possible misinterpretation, an alternative approach - essentially consisting of two separate steps - has been chosen (see Fig. 4.6). In the first step, the experimental results are compared directly to the results of the MCNPX PROTEUS whole-reactor calculation, normalization being carried out on the basis of the full set of measured pins. Contingent on obtaining good agreement (i.e. in consistency with the statistical uncertainties of the measurements), MCNPX can be considered as validated, within the experimental accuracies, for the actually implemented SCWR-like test lattice. This implies that the Monte Carlo modeling

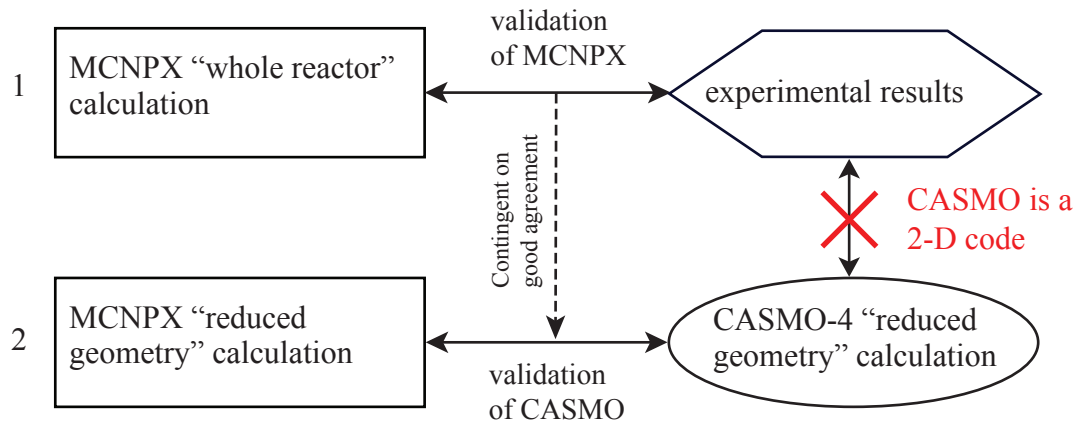


Figure 4.6: The scheme as adapted for the validation of CASMO-4E throughout this work.

is able to reproduce the physics of both the SCWR-like lattice per se and the finite effects of the outer PROTEUS reactor regions. Since it is highly unlikely that the agreement is due to a fortuitous “canceling of errors”, one can then assume that MCNPX is able to model - to an accuracy corresponding to the measurement uncertainties - the “pure” SCWR-like configuration of the reduced geometry model.

The second step uses the thus established MCNPX reduced geometry model as basis for validation of CASMO-4E. Because the Monte Carlo modeling has been experimentally validated, one can now use any set of fuel pins as basis for normalization of the results in the code-to-code comparison. The choice made currently is the complete set of pins in the reduced geometry model. Since a large number of these are relatively distant from the perturbations affected in the central moderator regions (see Figure 4.4, left hand side), the earlier mentioned possibility of a “smoothing out” of systematically discrepant predictions near the perturbations is largely reduced.

# Bibliography

- [1] F. Jatuff, K. Macku, and R. Chawla. On the accuracy of reactor physics calculations for square HPLWR fuel assemblies. *Annals of Nuclear Energy*, 33:198–207, 2006.
- [2] X-5 Monte Carlo Team. *MCNP - A General Monte Carlo N Particle Transport Code, Version 5*, 2003. LA-UR-03-1987.
- [3] Joel Rhodes, Kord Smith, and Malte Edenius. *CASMO-4E, Extended Capability CASMO-4, User's Manual*. Studsvik Scandpower, 2004. SSP-01/401Rev2.
- [4] J.J. Duderstadt and L.J. Hamilton. *Nuclear Reactor Analysis*. John Wiley & Sons, Inc., New York, USA, 1976.
- [5] D. Knott, B.H. Forssén, and M. Edenius. *CASMO-4: A Fuel Assembly Burnup Program, Methodology*. Studsvik Scandpower, 1995. SOA-95/2.
- [6] R.J.J. Stamm'ler, J. Blomstrand, and Z.J. Weiss. Equivalence Relations for Resonance Integral Calculations. *Journal of Nuclear Energy*, 27:885–888, 1973.
- [7] R.J.J. Stamm'ler and M.J. Abbate. *Methods of Steady-State Reactor Physics in Nuclear Design*. Academic Press Limited, London, UK, 1983.
- [8] Zbigniew Weiss. Some Basic Properties of the Response Matrix Equations. *Nuclear Science and Engineering*, 63:457–492, 1977.
- [9] Akinao Shimizu. Response Matrix Method. *Journal of the Atomic Energy Society of Japan*, 5:359–368, 1963.
- [10] J.R. Askew. A Characteristics Formulation of the Neutron Transport Equation in Complicated Geometries. Technical Report AEEW-M 1108, United Kingdom Atomic Energy Authority, Winfrith, 1972.
- [11] M.J. Halsall. CACTUS, A Characteristics Solution of the Neutron Transport Equations in Complicated Geometries. Technical Report AEEW-R 1291, United Kingdom Atomic Energy Authority, Winfrith, 1980.

- [12] O.P. Joneja, M. Plaschy, F. Jatuff, A. Lüthi, M.F. Murphy, R. Seiler, and R. Chawla. Validation of an MCNP4B whole-reactor model for LWR-PROTEUS using ENDF/B-V, ENDF/B-VI and JEF-2.2 cross section libraries. *Annals of Nuclear Energy*, 28:701–713, 2001.
- [13] A.K. Ziver and T. Williams. LWR-PROTEUS system component description. Technical Report TM-41-98-07, Paul Scherrer Institute, Villigen, Switzerland, 1998.
- [14] A.K. Ziver, T. Williams, P. Grimm, and R. Seiler. Description of the test zone components for the PWR phase of the LWR-PROTEUS Experiment. Technical Report TM-41-98-21, Paul Scherrer Institute, Villigen, Switzerland, 1998.
- [15] A. Yamaji, Y. Oka, and S. Koshizuka. Conceptual core design of a 1000MWe supercritical pressure light water cooled and moderated reactor. In *ANS/HPS Student Conference, Texas A&M University*, 2001.
- [16] U.C. Bergmann, P. Grimm, F. Jatuff, and M.F. Murphy. Investigations of  $^{238}\text{U}$  Captures to Total Fissions in a Westinghouse SVEA-96+ Assembly. *Nuclear Science and Engineering*, 156:86–95, 2007.

## 5 Reaction Rate Distributions: Unperturbed Lattice

The last two chapters have been dedicated largely to the experimental (Chapter 3) and calculational (Chapter 4) approaches for deriving reaction rate distributions across a given fuel configuration. In this chapter, the corresponding results obtained for the unperturbed SCWR-like test lattice implemented in PROTEUS, obtained with the two approaches, are compared with each other. The aim of this comparison is the quantification of the accuracy with which modern reactor physics codes can predict such distributions. Following this first step with the unperturbed fuel lattice, similar comparisons are made in Chapter 6 for the perturbed configurations. As per the validation strategy discussed in Sec. 4.3, the experimentally obtained reaction rate distributions are first compared to predictions from the MCNPX whole-reactor model of PROTEUS, before the calculated results from the MCNPX and CASMO-4E reduced geometry models are compared to each other.

The strong moderation heterogeneity across the investigated fuel lattice (even without inserted perturbations) renders its neutronic characteristics quite different from those of a regular lattice. Therefore, Sec. 5.1 is dedicated to the characterization of this fuel lattice, based on experimentally derived reaction rate distributions. In order to verify the experimental results, two independent tests were performed: the experiments were carried out twice to check the reproducibility of the results<sup>1</sup>, and the measured fuel pins were selected in a symmetrical manner with respect to the octagonal symmetry of PROTEUS such that this symmetry could be confirmed by the results obtained. These consistency checks are discussed in Sec. 5.2. The measurements are then compared with the predictions from the MCNPX whole-reactor model in Sec. 5.3, and the MCNPX and CASMO-4E reduced geometry calculations are compared in Sec. 5.4. The results of these two separate comparisons have been published in [1] and [2], respectively.

### 5.1 Characterization of the Test Lattice

As mentioned, an SCWR lattice is fundamentally different from a standard LWR assembly due to its heterogeneous moderation. Even though the fuel pins all have the same material

---

<sup>1</sup>During the intervening period of three years, the reactor had been reconfigured for other experiments, and the SCWR-like test lattice was re-introduced with certain modifications to allow supplementary measurements.

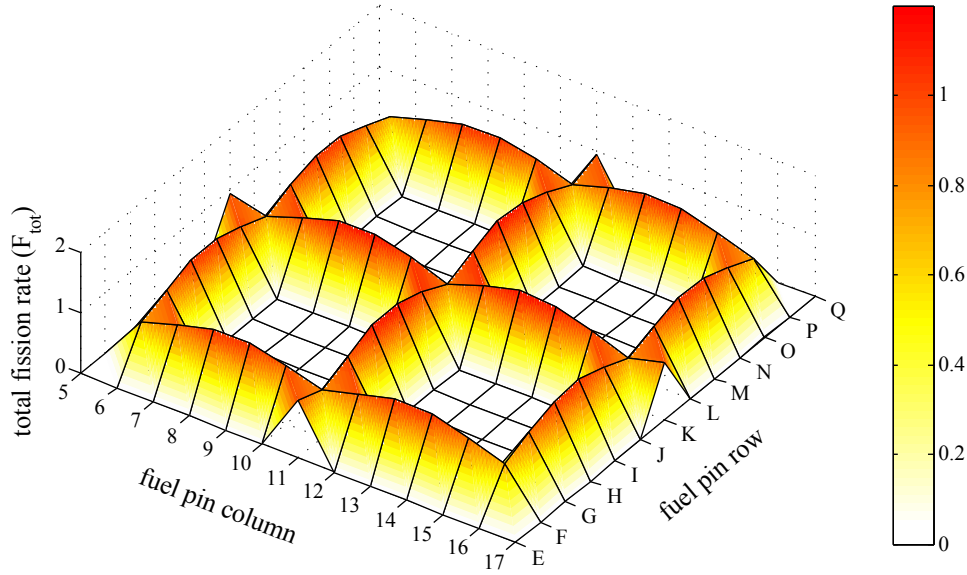


Figure 5.1: Surface plot of the experimentally derived total fission rate ( $F_{\text{tot}}$ ) distribution in the unperturbed configuration as a function of the fuel pin position.

composition, the fission rate (and hence the power) varies strongly between neighboring pins. Fig. 5.1 illustrates the total fission rate ( $F_{\text{tot}}$ ) distribution over the measured cross section of the unperturbed SCWR-like test lattice in PROTEUS. The reaction rates measured in the individual pins have been normalized to an average of unity over the lattice. Fewer fissions (about 85% of the average) are seen to take place in fuel pins at intersections of columns and rows of pins (denoted as corner pins), while more fissions (about 120% of the average) occur in the fuel pins distant from these intersections (denoted as remote pins). The fission rate in the fuel pins between the two extreme positions (denoted as neighbors) is close to unity. This is as to be expected from the different moderation conditions to which the different fuel pins are subjected. While the corner pins have four direct neighbors and therefore see little moderator, the remote pins only have two neighbors and see more moderator. Hence, more thermal neutrons enter the remote pins, inducing a higher fission rate.

An analogous surface plot of the  $^{238}\text{U}$  capture rate ( $C_8$ ) distribution is shown in Fig. 5.2. In the case of  $C_8$  as well, the reaction rate is depressed at the intersections of columns and rows of fuel pins and increased at locations away from them, although the magnitude of the difference between the two extreme positions is smaller as compared to that for  $F_{\text{tot}}$  (only about 18%, instead of 35%). This is due to the different energy regimes to which the two reaction rates are sensitive. While  $F_{\text{tot}}$  consists almost exclusively of thermal fissions (more than 95%), more than half of the neutrons captured in  $^{238}\text{U}$  have epithermal energies. Hence,  $C_8$  is correspondingly more sensitive to the epithermal energy range, where the neutrons have longer mean free paths, so that their number is less affected by local changes of the lattice geometry than in the case of thermal neutrons.

The distribution of the reaction rate ratio  $C_8/F_{\text{tot}}$  is illustrated in Fig. 5.3. Because the depression



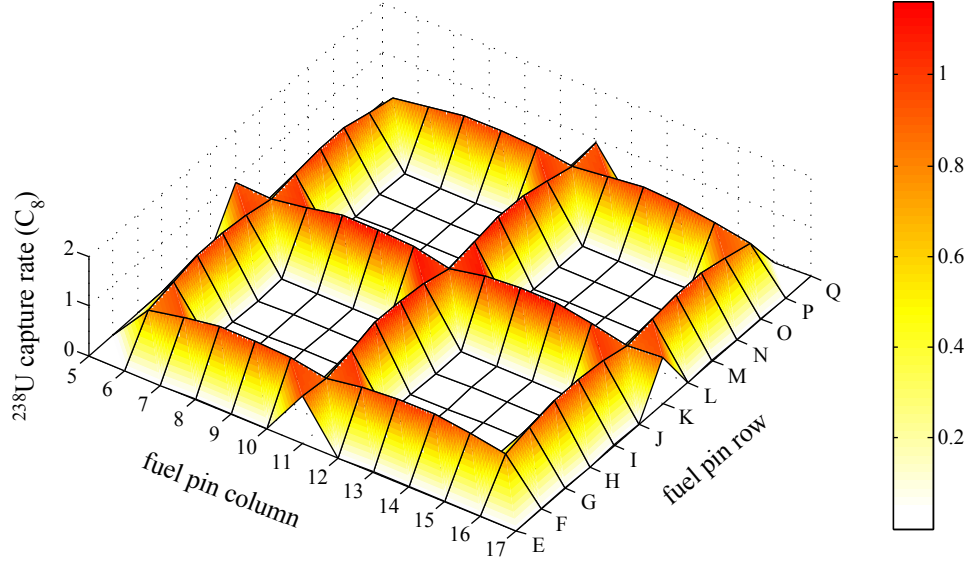


Figure 5.2: Surface plot of the experimentally derived  $^{238}\text{U}$  capture rate ( $C_8$ ) distribution in the unperturbed configuration as a function of the fuel pin position.

in the corner pins is stronger for  $F_{\text{tot}}$  than for  $C_8$ , the net effect, when considering the ratio, is an increase of the value in these fuel pins. The opposite applies to the remote pin positions. The difference between the maximum and the minimum value is 18%. The increase of  $C_8/F_{\text{tot}}$  in the corner pins indicates a local hardening of the spectrum, which can be seen more directly in Fig. 5.4, which compares the calculated spectra for the different fuel pin positions. These spectra were obtained from the MCNPX whole-reactor calculations for PROTEUS and have been normalized to an integral value of one. The Maxwellian peak becomes more pronounced as the fuel pins get better moderated, so that the spectrum seen by pin K13 is softer (i.e. the fraction of thermal neutrons is larger) than that seen by K11. Consistent with the measured value of the spectral index  $C_8/F_{\text{tot}}$ , the spectrum of pin K12, in terms of hardness, lies between the two others.

Fig. 5.5 gives a summarized overview of the spatial variations of the reaction rates along the central row of fuel pins (row K in Fig. 5.9). On the left and in the middle,  $F_{\text{tot}}$  and  $C_8$  are plotted, respectively, each normalized to an average of unity across the shown traverse. On the right,  $C_8/F_{\text{tot}}$  (which does not need any normalization) is depicted. Once again, one can see how the depressed total fission rate in the corner pins and the more weakly depressed  $^{238}\text{U}$  capture rate combine to yield an increase in  $C_8/F_{\text{tot}}$ , indicating the harder spectrum at these positions. Additionally, focusing on  $F_{\text{tot}}$ , one can see the global buckling (radial) of the reactor, when one compares the values of generically equivalent fuel pin positions, e.g. the corner pins at positions 6, 11, and 16.

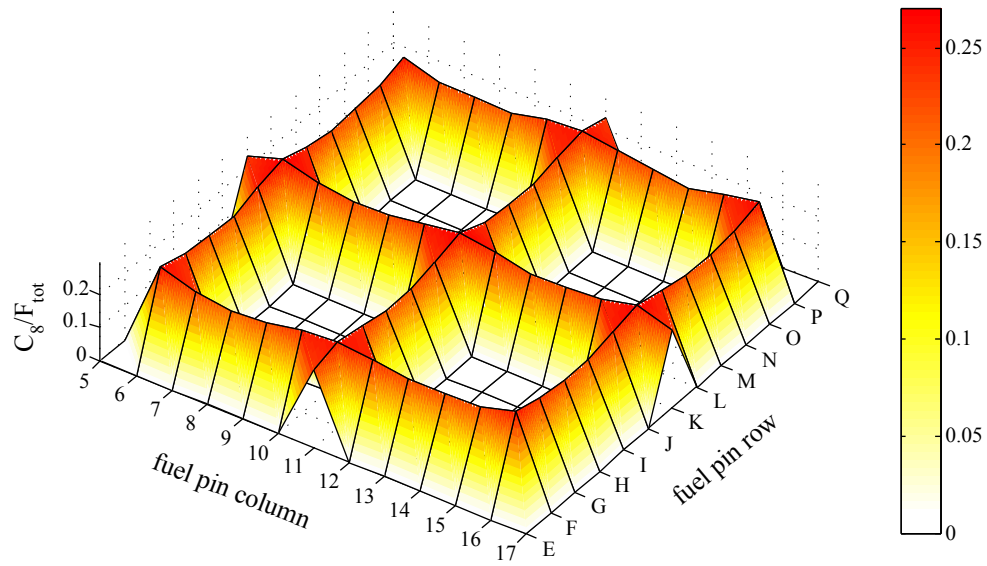


Figure 5.3: Surface plot of the experimentally derived distribution of the reaction rate ratio  $C_8/F_{\text{tot}}$  in the unperturbed configuration as a function of the fuel pin position.

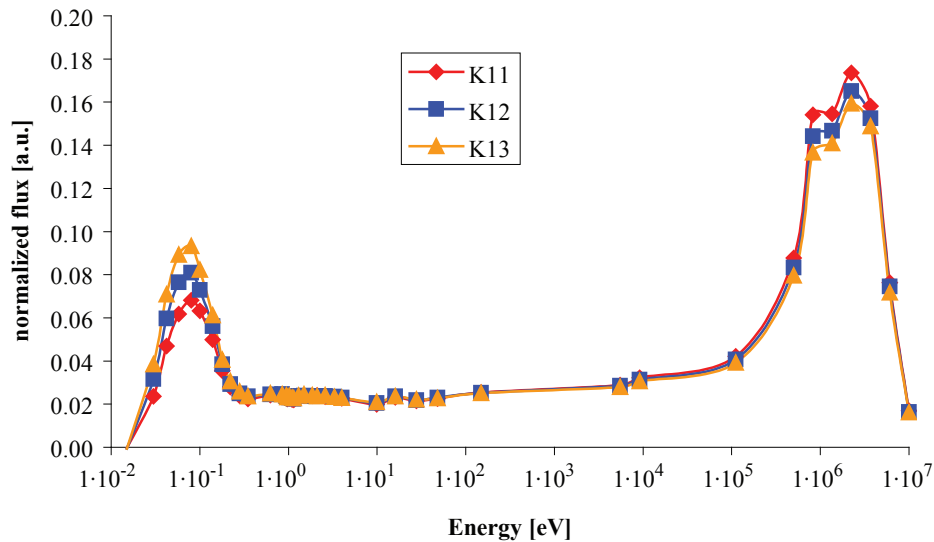


Figure 5.4: MCNPX-calculated neutron energy spectra (normalized to an integral value of one) for the three generic fuel pin positions K11 (corner), K12 (neighbor), and K13 (remote). The Maxwellian peak becomes more pronounced as the fuel pins get better moderated.

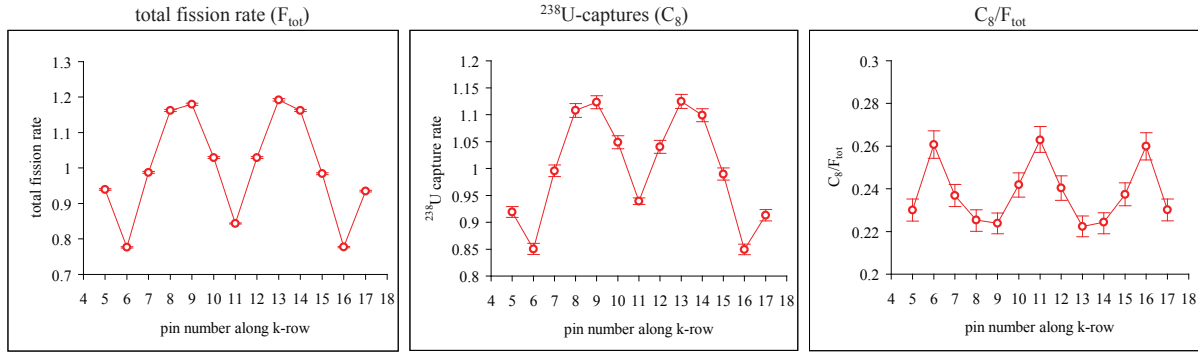


Figure 5.5: Reaction rates ( $C_8$  and  $F_{tot}$ ) and their ratio ( $C_8/F_{tot}$ ) to illustrate the characteristic variations for the central traverse (fuel pins along the K-row) of the SCWR-like test lattice (see Fig. 2.17) implemented in PROTEUS.

## 5.2 Verification of Experimental Results

### 5.2.1 Reproducibility of Measurements

The gamma-scanning measurements on the unperturbed SCWR-like lattice in PROTEUS were conducted twice to assess the reproducibility of the results. Forty-six fuel rods were measured in 2006 and sixty-one rods in 2009. The two central traverses (i.e. the row from K5 to K17 and the column from E11 to Q11 in Fig. 2.17) were part of the program in both campaigns, thus providing a basis to test the reproducibility of the measurements. As a representative sample of the rods measured in both campaigns, the horizontal traverse from K5 to K17 has been chosen. Fig. 5.6 shows the results from both campaigns: The reaction rates (total fission rate on the left, and  $^{238}\text{U}$  capture rate in the middle) are plotted against the positions of the measured rods in the lattice, each set of measurements having been normalized to the average value for the traverse. On the right hand side of Fig. 5.6, the reaction rate ratio  $C_8/F_{tot}$  is shown for the same fuel pins.

The results from the two campaigns show excellent agreement. They lie within the depicted  $1\sigma$ -uncertainties (in the order of 0.4% for  $F_{tot}$ , 0.8% for  $C_8$ , and 2.2% for  $C_8/F_{tot}$ ); the error bars on the left hand side of Fig. 5.6 are smaller than the symbols. The  $^{238}\text{U}$  capture rates for the fuel rods in positions K12 and K13 are different by slightly more than  $1\sigma$  (but less than  $2\sigma$ ), which is still consistent with statistical fluctuations and does not affect the overall excellent agreement. The corresponding fluctuation is also seen in the  $C_8/F_{tot}$  distribution. While the gamma-ray line of  $^{133}\text{I}$  at 529.9 keV has been chosen here as a representative example, results for the other fission-product gamma rays were found to be in similar agreement between the two measurement campaigns.

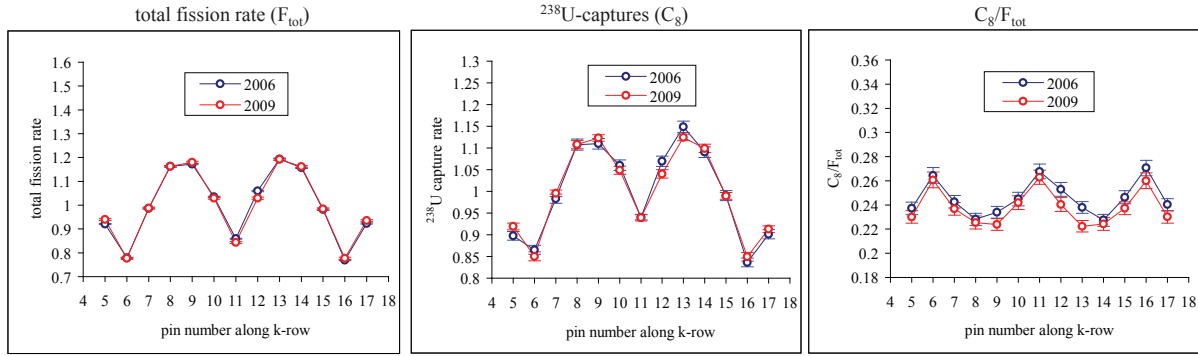


Figure 5.6: Comparison between the measurement campaigns of the years 2006 and 2009: on the left for the total fission rate measured with the gamma line of  $^{133}\text{I}$ , in the middle for the  $^{238}\text{U}$  capture rate measured with the gamma line of  $^{239}\text{Np}$ , and on the right for the  $C_8/F_{\text{tot}}$  ratio.

### 5.2.2 Symmetry Check

As described in Sec. 2.1, PROTEUS is a complex multi-zone system which has been used for various experimental programs and modified correspondingly over the years. While the SCWR-like lattice, implemented in the central test zone of the reactor, has a perfect eighth-core symmetry, this can not be assumed a priori for the entire system, even though it was laid out symmetrically (e.g. the C-driver pins were azimuthally distributed as evenly as possible). Accordingly, the fuel pins that were measured during the unperturbed configuration campaign (see Sec. 3.1.1) were chosen such as to enable a systematic check of the symmetry of the system. All pins of the four central squares (around the four central moderator channels) were measured and hence, due to the octagonal symmetry of the lattice, each unique lattice position was effectively evaluated at least four times. Thus, the symmetry of the system could be checked by comparing the measured reaction rates of several different, symmetrically located fuel pins.

Fig. 5.7 illustrates how the measured fuel pins were divided into four symmetry groups. Each group contains one or two different exponents of each unique lattice position. The pins in each group are put into a certain order, forming a “chain” that starts at the center of the assembly (pin K11) and then moves clockwise around one of the central squares. It should be noted that, since the octagonal symmetry is divided into four groups, some unique pin positions are repeated within a single group (namely, the pins that are not located on the central traverses - vertical and horizontal).

The results of the symmetry check carried out are summarized in Fig. 5.8. On the graph in the upper left corner, the total fission rate is plotted for each pin chain according to Fig. 5.7. The colors of the lines correspond to the color of the group. The symmetric fuel pin position is plotted on the X-axis. Number one corresponds to the lattice position K11, which is part of each symmetry group. From there, the sequence of pin positions moves clockwise around the central

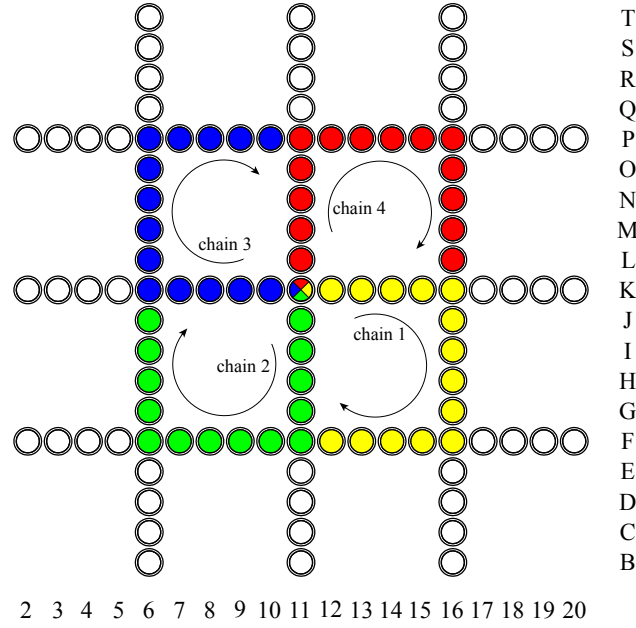


Figure 5.7: Grouping of the measured fuel pins into four symmetry groups. In each group, the pins are arranged into a “chain”, starting at the center (K11) and moving clockwise around one of the central moderator channels.

moderator channels as mentioned earlier. The agreement appears to be excellent, since the lines appear to be on top of each other. However, due to the small uncertainties on  $F_{\text{tot}}$ , a closer look is necessary to deduce the degree of symmetry of the system. On the upper right corner of Fig. 5.8, the deviation of each individual pin from the average for the corresponding symmetric pin positions is plotted. Additionally, the average (over the symmetric pins)  $1\sigma$  uncertainty interval is shaded in grey. The total fission rates of symmetric pins are seen to agree within  $1\sigma$  with their average value, indicating the high degree of symmetry over the test lattice. Eight out of fifty-six analyzed fuel pins lie outside the  $1\sigma$  uncertainty interval, which is even less than would be expected statistically.

An analogous analysis has been carried out for the  $^{238}\text{U}$  capture rate and for the reaction rate ratio  $C_8/F_{\text{tot}}$ . Their results are shown in the middle and bottom sections of Fig. 5.8, respectively. The results are similar to those for  $F_{\text{tot}}$ . However, the values of  $C_8$  are spread out further, which is due to the larger uncertainties on these measurements. The  $C_8/F_{\text{tot}}$  values also agree within the given uncertainty interval.

Effectively, the analysis of the symmetric fuel pins measured showed that the outer zones of PROTEUS do not contain asymmetries which influence the neutron distribution in the implemented SCWR-like test lattice. Thus, the entire PROTEUS reactor can be assumed to be octagonally symmetric as regards reaction rate measurements in the test zone. Accordingly, the perturbed configuration campaigns presented in Chapter 6 were carried out with a reduced number of measured pins, viz. those in the central horizontal and vertical rows, as also the remaining pins around the south-east moderator channel.

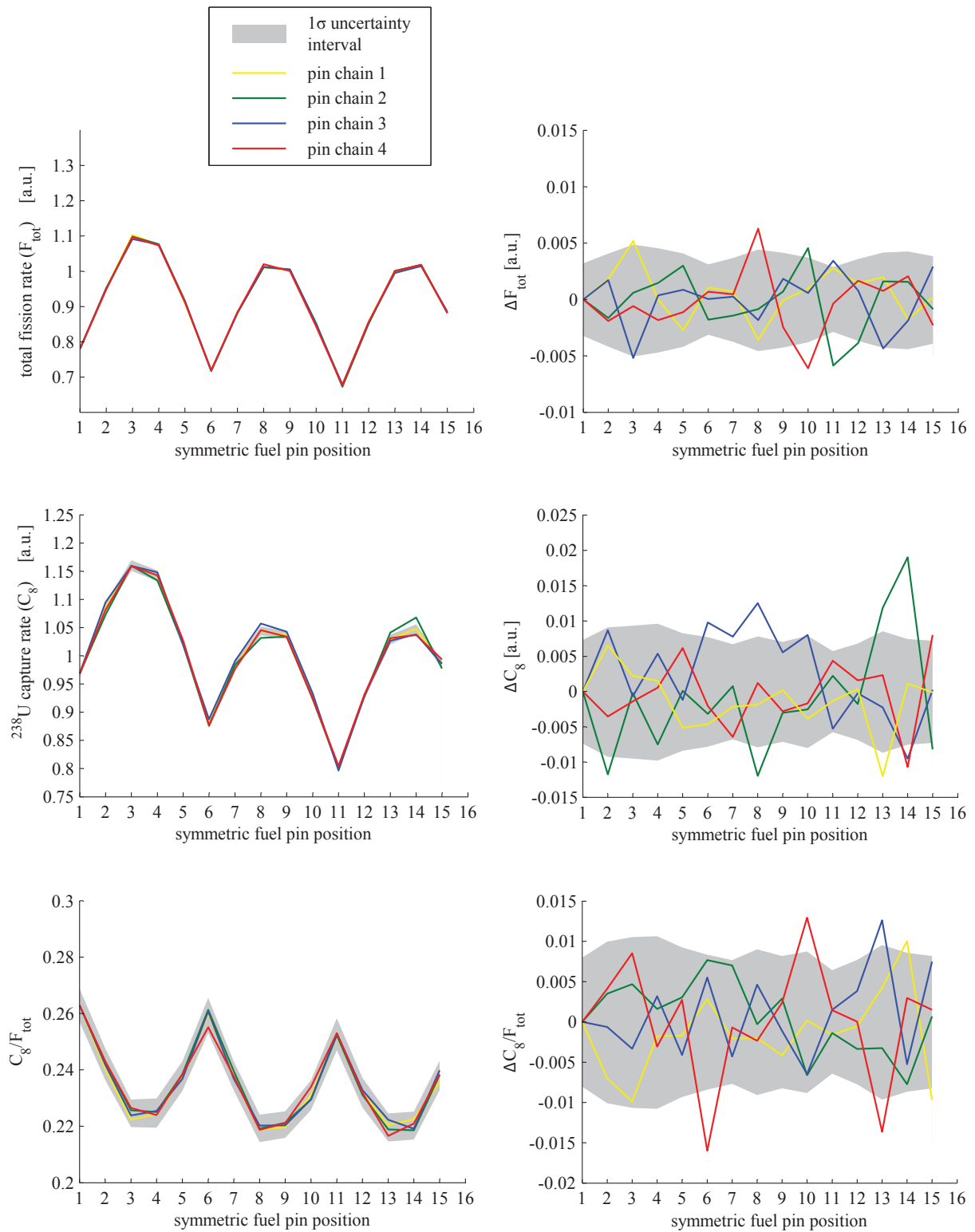


Figure 5.8: Analysis of the symmetry of the experimentally obtained results:  $F_{\text{tot}}$  (top section),  $C_8$  (middle section), and  $C_8/F_{\text{tot}}$  (bottom section). For each measurement type, the absolute values along the pin chains are plotted on the left and their deviations from the average value are plotted on the right. The  $1\sigma$  uncertainty interval is indicated in each case by the grey shaded area.

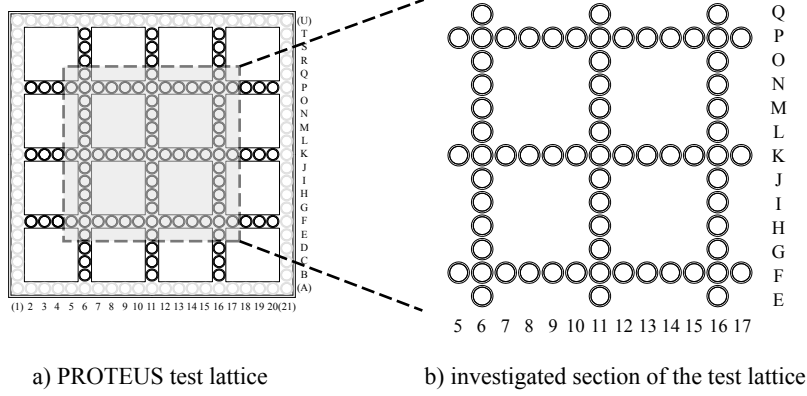


Figure 5.9: Explicitly investigated section of the PROTEUS test lattice, consisting, for the main part, of fuel pins measured in the unperturbed test lattice.

### 5.3 Comparison of MCNPX Whole-Reactor Calculation with Experiment

This section corresponds to the first step of the validation strategy described in Section 4.3, viz. comparison of the experimental results with MCNPX PROTEUS whole-reactor calculations. For the individual reaction rates ( $C_8$  and  $F_{\text{tot}}$ ), calculated and measured distributions were each normalized to an average of unity for the 61 sampled fuel pins. After that, ratios of computed and measured values were taken for each experimental position of the lattice. Since the reaction rate ratio  $C_8/F_{\text{tot}}$  does not need any further normalization, its values for the individual pins did not need to be averaged, and the corresponding comparison between experimental and computational results could be done directly (see Subsec. 5.3.2).

For the sake of clarity in the presentation of the results, only the central section of the PROTEUS experimental lattice will be shown. This section, for the main part, is constituted by the 61 pins which were part of the measurement campaign. It is depicted in Fig. 5.9, and used as basis for presenting the results for the sampled pins in Figs. 5.12, 5.10, and 5.14.

#### 5.3.1 Comparison Between Computed and Measured $F_{\text{tot}}$ and $C_8$ Distributions

Fig. 5.10 shows the calculation/experiment ( $C/E$ ) values for the total fission rate ( $F_{\text{tot}}$ ) across the SCWR-like lattice. The upper and lower values in each cell correspond to the  $C/E$  for the corresponding fuel pin and to its relative uncertainty, respectively. Nearly all the measured values agree with calculation within  $2\sigma$ , the agreement for only two measurements being slightly worse, viz. between  $2\sigma$  and  $3\sigma$  (orange marked cells). The combined uncertainty, coming from the experimental error and the statistical uncertainty of the probabilistic calculation, adds up

Map of C/E's for total fissions ( $F_{\text{tot}}$ )

Q						1.008 0.005							
P		0.995 0.005	0.997 0.004	1.010 0.004	1.001 0.004	0.997 0.004	0.998 0.005	0.999 0.004	0.994 0.004	1.003 0.004	1.008 0.005	0.997 0.005	
O		1.003 0.004					1.003 0.005					0.995 0.004	
N		0.997 0.004					1.004 0.004					1.005 0.004	
M		1.002 0.004					0.997 0.005					0.999 0.004	
L		0.999 0.004					1.005 0.004					1.002 0.005	
K	0.994 0.004	0.998 0.005	1.000 0.004	1.003 0.004	1.002 0.004	1.001 0.004	0.996 0.004	1.000 0.004	0.991 0.004	1.004 0.004	1.000 0.004	0.995 0.005	0.997 0.004
J		1.000 0.004					1.006 0.005					0.999 0.004	
I		0.996 0.004					0.997 0.005					1.003 0.005	
H		1.001 0.004					1.002 0.004					0.999 0.004	
G		0.997 0.004					0.996 0.005					1.003 0.004	
F		1.003 0.004	0.998 0.004	0.998 0.004	1.002 0.004	0.999 0.004	1.000 0.005	1.000 0.004	1.001 0.004	1.002 0.004	0.996 0.004	0.995 0.005	
E							1.000 0.005						
	5	6	7	8	9	10	11	12	13	14	15	16	17

Figure 5.10: Calculation/experiment (C/E) values for the normalized distribution of the total fission rate (upper value in each cell), along with the corresponding  $\sigma$  uncertainty (lower value in each cell); the orange values represent deviations between calculation and experiment of  $2\sigma$  to  $3\sigma$ .

to about 0.4%. The statistical uncertainty from the Monte Carlo calculation is about 4 times smaller than the experimental uncertainty.

Fig. 5.11 shows a frequency plot of the deviations from unity of the individual C/E's. Each bin has a width of  $\sigma/2$  and its y-value represents the relative frequency of measurements with the corresponding deviation from unity (i.e. the fraction of the measured pins, for which calculated and experimental results agree within the given range of standard deviations). The black line shows a Gaussian distribution centered at 0 with the variance equal to the square of the average uncertainty of the C/E values. A  $\chi^2$ -goodness-of-fit test was performed and yielded a satisfactory p-value of 0.74. (The p-value is the probability of measuring a set of data with worse agreement than the present sample, under the assumption that the true underlying distribution is the above-mentioned Gaussian; if the p-value were below 0.05, the tested Gaussian would be rejected).



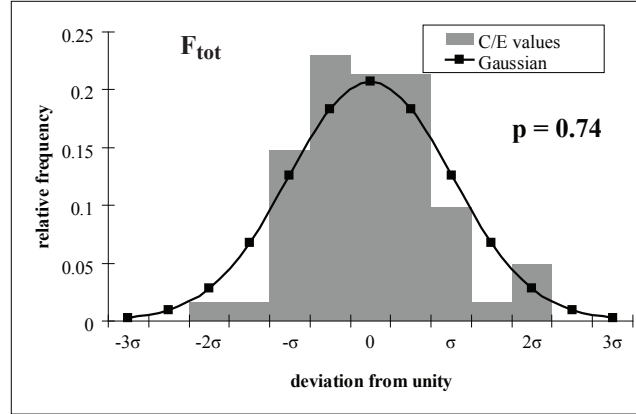


Figure 5.11: Frequency of deviations from unity for C/E values of  $F_{tot}$ . The  $\chi^2$ -test yielded a p-value of 0.74.

In Fig. 5.12, the ratio between calculated and measured values is depicted for the  $^{238}\text{U}$  capture rate ( $C_8$ ). In each cell, the ratio (upper value) is given, along with its uncertainty (lower value). All but four C/E's are seen to be equal to unity within  $2\sigma$ , the  $1\sigma$  uncertainties being between 0.7 and 1.0%.

Fig. 5.13 shows the frequency plot for the  $C_8$  C/E map. The distribution follows nicely the Gaussian distribution centered at 0 with the variance equal to the square of the average uncertainty of the results. In this case, the  $\chi^2$ -test yielded a p-value of 0.55. Experiment and calculation are thus confirmed to agree well according to the given uncertainties on the C/E values for  $C_8$ , which are higher than those for the total fission rate. This is due to the considerably better statistical accuracy obtained for both the experimental (gamma counting) and calculated (MCNPX tallies) results for total fissions. Here again, uncertainties on the calculated values are much smaller than on the experimental values.

### 5.3.2 Comparison Between Computed and Measured $C_8/F_{tot}$ Values

As mentioned before, the reaction rate ratio  $C_8/F_{tot}$  - apart from representing an important neutron balance component in the SCWR-like lattice - is useful as a spectral index characterizing the individual fuel pin positions. Fig. 5.14 gives the pin-specific C/E's for this ratio, the upper value in each cell being the C/E and the lower value its  $1\sigma$  uncertainty. Calculation and experiment agree within  $2\sigma$  in each case, the  $1\sigma$  level for each individual value being in the order of 2.2%. These errors are much larger than those indicated in the  $C_8$  and  $F_{tot}$  maps since, as discussed earlier, there is no normalization carried out between the individual spectral-index values. As such, systematic errors (i.e. uncertainties in branching ratios, fission yields, etc.) do not cancel out.

In this case, however - with the calculation and experimental results for the individual pins not having been normalized to unity before the comparisons - the mean of the C/E values may be

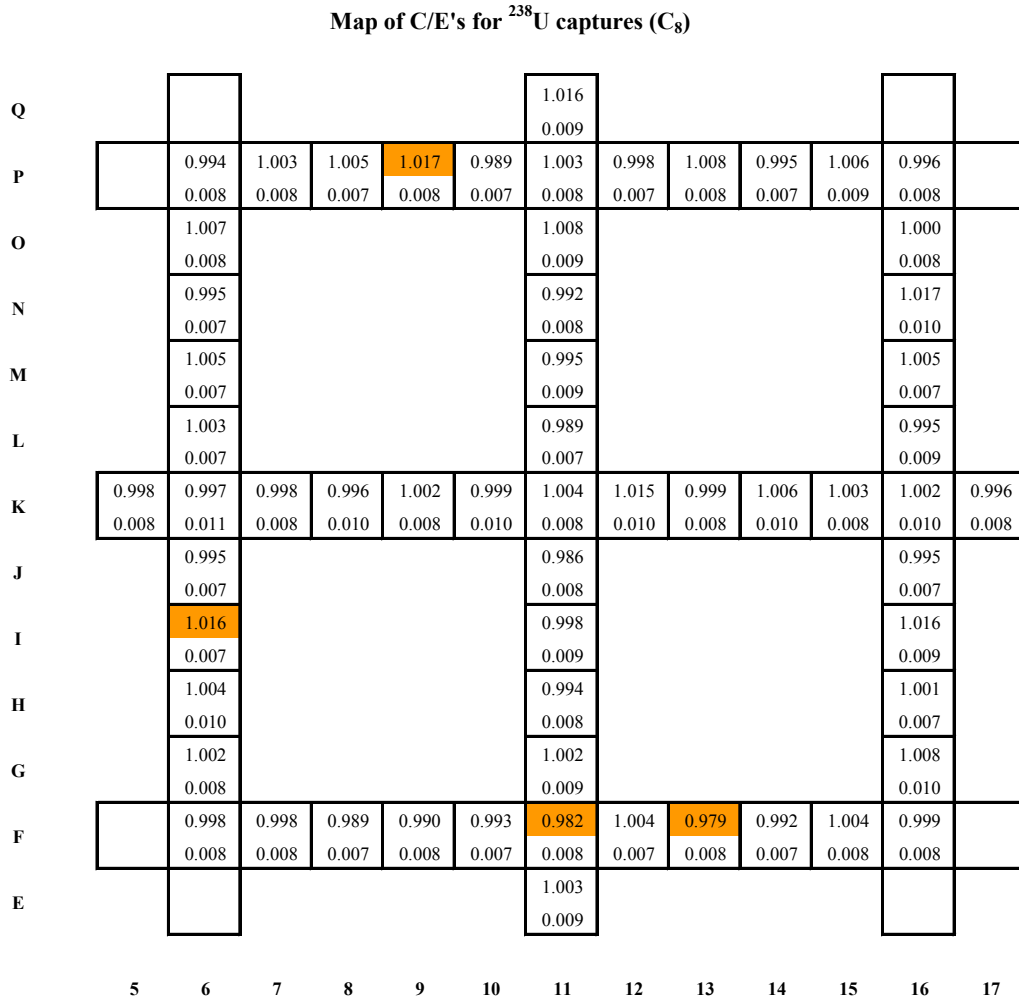


Figure 5.12: Calculation/experiment (C/E) values for the normalized distribution of the  $^{238}\text{U}$  capture rate (upper value in each cell), along with the corresponding  $1\sigma$  uncertainty (lower value in each cell); the orange values represent deviations between calculation and experiment of  $2\sigma$  to  $3\sigma$ .

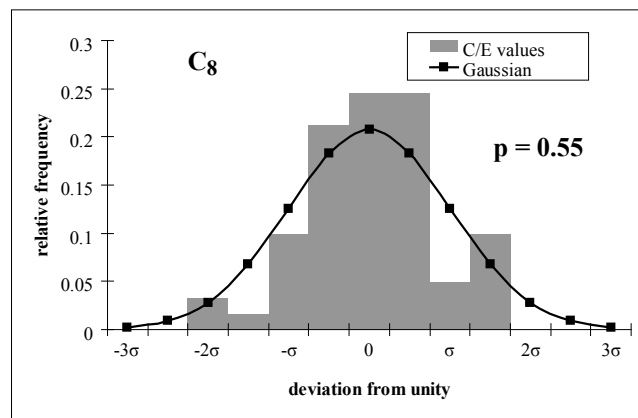


Figure 5.13: Frequency of deviations from unity for C/E values of  $C_8$ . The  $\chi^2$ -test yielded a p-value of 0.55.

**Map of C/E's for the ratio of  $^{238}\text{U}$  captures to total fissions ( $C_8/F_{\text{tot}}$ )**

Q							0.988 0.023						
P		0.987 0.023	0.989 0.023	0.976 0.021	0.998 0.023	0.977 0.021	1.009 0.023	0.983 0.022	0.996 0.023	0.979 0.021	0.982 0.022	0.984 0.022	
O		1.003 0.022					0.988 0.022					0.990 0.023	
N		0.981 0.021					0.989 0.022					1.000 0.024	
M		0.990 0.022					0.984 0.022					0.987 0.023	
L		0.987 0.022					0.981 0.022					0.981 0.022	
K	1.002 0.023	0.985 0.025	0.997 0.022	0.985 0.024	0.998 0.022	0.986 0.024	1.002 0.023	1.001 0.024	1.003 0.022	0.991 0.024	0.997 0.022	0.993 0.025	0.994 0.023
J		0.983 0.022					0.980 0.023					0.984 0.022	
I		1.001 0.022					0.986 0.021					0.995 0.022	
H		0.989 0.024					0.989 0.023					0.990 0.022	
G		0.999 0.023					0.989 0.022					0.996 0.024	
F		0.984 0.023	1.005 0.023	0.980 0.022	0.991 0.023	0.982 0.022	0.979 0.024	0.992 0.023	0.975 0.023	0.982 0.022	0.992 0.023	0.993 0.023	
E							0.984 0.023						
	5	6	7	8	9	10	11	12	13	14	15	16	17

Figure 5.14: Calculation/experiment (C/E) values for the reaction rate ratio  $C_8/F_{\text{tot}}$  at the individual fuel rod positions of the SCWR-like lattice (upper value in each cell), along with the corresponding  $1\sigma$  uncertainty (lower value in each cell); in each case calculation and experiment agree well within  $2\sigma$ .

different from 1.0. The mean over all C/E values is found to be 0.989, i.e. considering the total uncertainty ( $\sim 2.2\%$ ), the calculated result agrees with experiment within  $1\sigma$ .

As regards the distribution of the C/E deviations from unity in this case, it is clear that the Gaussian distribution underlying the derived values must be centered at -1.1% and that the variance to be ascribed to it should be the square of the purely statistical errors. As before, the latter come from the measurement counting uncertainty and the Monte Carlo uncertainty and sum up to 0.9%. It is this value (denoted by  $\sigma'$ ) which is used as the standard deviation in the frequency plot shown in Fig. 5.15, the p-value of the  $\chi^2$ -test for the Gaussian fit being found to be 0.79. This underlines the agreement of the MCNPX-calculated and measured variations of the neutron spectrum across the SCWR-like lattice, consistent with the findings for the individual reaction rates as discussed in the previous subsection.

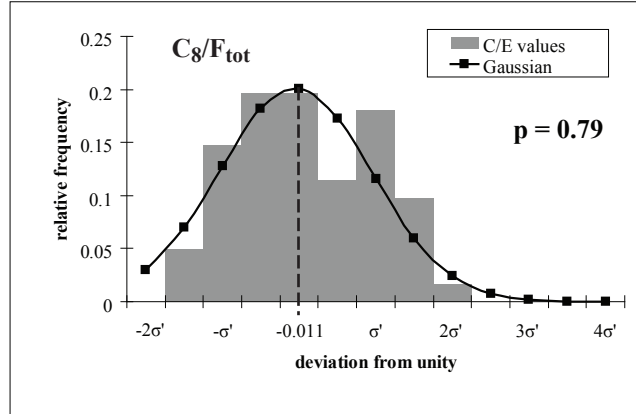


Figure 5.15: Frequency of deviations from unity for C/E values of  $C_8/F_{tot}$ . The  $\chi^2$ -test for the Gaussian fit with  $\sigma' = 0.9\%$  (statistical error) yielded a p-value of 0.79.

## 5.4 Comparison Between CASMO-4E and MCNPX

The Monte Carlo modeling of the PROTEUS whole-reactor results in excellent agreement between calculated and measured reaction rate distributions in the unperturbed SCWR-lattice. Step 1 of the validation strategy sketched in Sec. 4.3 for deterministic codes is thus seen to be fulfilled. With MCNPX effectively validated for the SCWR-specific physics represented in the experiments, validation of the CASMO-4E reduced geometry model (Fig. 4.4) can be accomplished in Step 2, via an inter-code comparison based on reduced geometry modeling. The corresponding results obtained are reported in this section.

Before comparing the distributions for the individual reaction rates ( $C_8$  and  $F_{tot}$ ), as calculated by the two codes, each reaction rate was first normalized to an average of unity over all pins in the reduced geometry model. As discussed earlier, the spectral index  $C_8/F_{tot}$  does not need to be normalized. In this case, the individual pin values have been compared directly and the average  $C/C'$  value, where  $C$  and  $C'$  denote results from the CASMO-4E and MCNPX reduced geometry calculations, is given separately.

Fig. 5.16 summarizes the results of the comparison of CASMO-4E and MCNPX calculated distributions of the individual reaction rates and their ratio. In each case, the results are given in terms of  $C/C'$  values for pin positions corresponding to the lower right quadrant of the SCWR-like “assembly” represented on the left hand side of Fig. 4.4. Cells highlighted in yellow indicate differences of 1 to 2%, with respect to the pin average. The statistical uncertainty of the MCNPX calculation was below 0.1% for  $C_8$  and  $F_{tot}$ , and around 0.1% for  $C_8/F_{tot}$ . Therefore, the presented differences are numerically significant.

In general, the codes are seen to agree well; the largest discrepancy is 1.1% for the total fission rate of pin A21. However, certain minor trends can be observed when comparing the  $C/C'$  of the intrinsically different fuel pin positions in the lattice. Thus, while the pins at the intersections

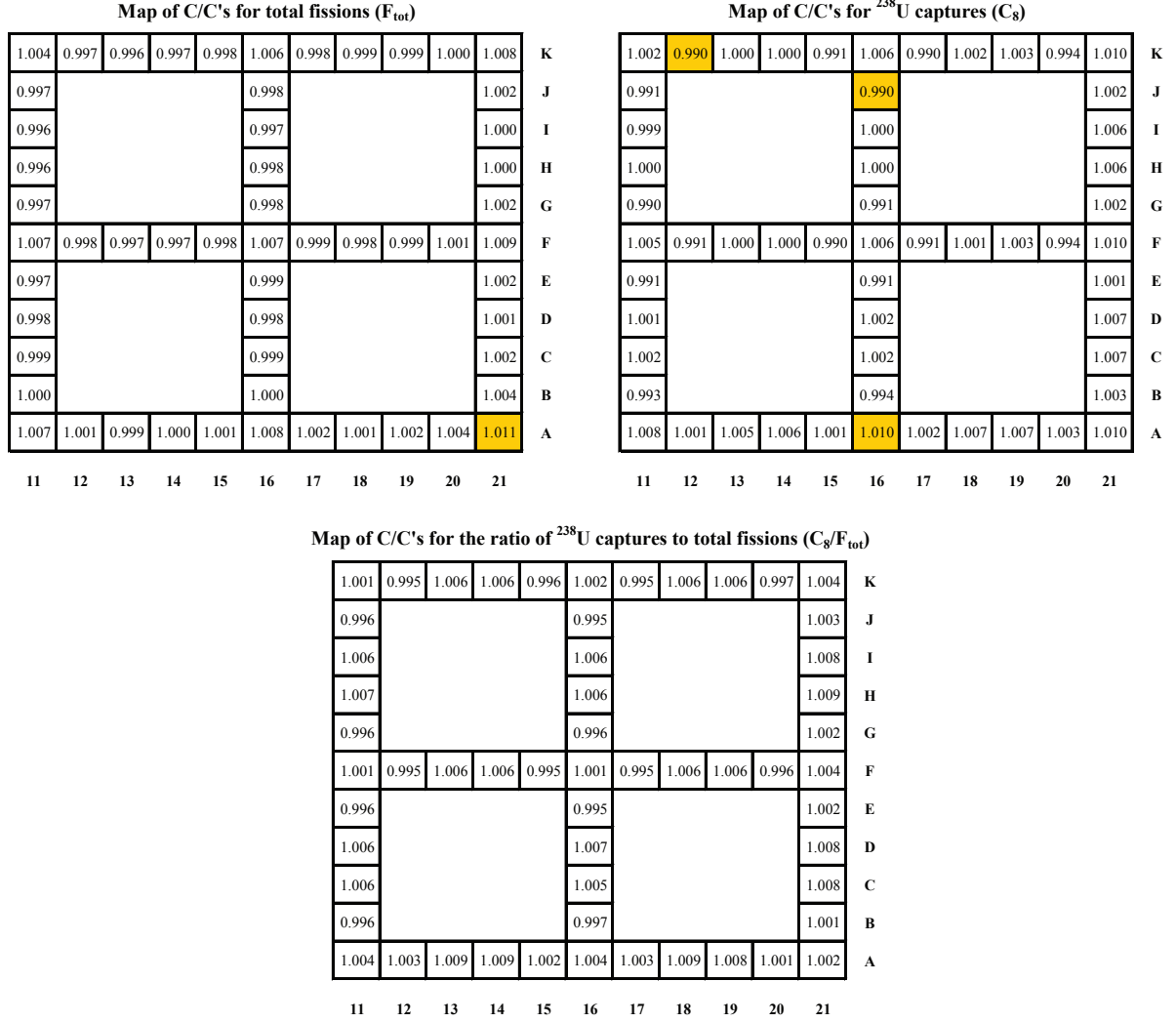


Figure 5.16: Lower right quadrant of the unperturbed reduced geometry “assembly” (see left hand side of Fig. 4.4): Comparison between CASMO-4E (C) and MCNPX (C') calculations of the individual reaction rates ( $F_{\text{tot}}$  and  $C_8$ ) and their ratio ( $C_8/F_{\text{tot}}$ ). The pin average C/C' value is 1.0 for  $F_{\text{tot}}$  and  $C_8$  (due to the normalization) and 1.002 in the case of  $C_8/F_{\text{tot}}$ . Values that differ more than 1% from the pin average are highlighted in yellow.

of fuel rows and columns are slightly overestimated by CASMO-4E (approximately 0.7% for  $F_{\text{tot}}$  and 0.6% for  $C_8$ ), they are just as slightly underestimated in the other positions (i.e. neighbors to intersections and pins remote from intersections). While the underestimation for  $F_{\text{tot}}$  is nearly constant for these other pins, it varies between “neighbors” and “remotes” for  $C_8$ . These small trends are also reflected in the  $C/C'$  distribution for  $C_8/F_{\text{tot}}$ .

Additionally, there is a weak trend over the entire “assembly”. While CASMO-4E tends to underestimate reaction rates towards the center (pin K11), it tends to overestimate them at the periphery (row A and column 21). Because the direction of this trend is the same, and its magnitude is comparable for  $F_{\text{tot}}$  and  $C_8$ , the  $C_8/F_{\text{tot}}$  comparison does not show the effect.

Finally, it is worth noting the excellent agreement between CASMO-4E and MCNPX for the absolute value of the reaction rate ratio  $C_8/F_{\text{tot}}$  (pin average  $C/C'$  of 1.002).

# Bibliography

- [1] D. Rätz, K.A. Jordan, M.F. Murphy, G. Perret, and R. Chawla. Comparison of Measured and Calculated Reaction Rate Distributions in an SCWR-like Test Lattice. *Annals of Nuclear Energy*, 38:794–801, 2011.
- [2] D. Rätz, K.A. Jordan, G. Perret, and R. Chawla. Experimental Validation of Control Rod Related Perturbations of Moderator Regions in an SCWR-like Fuel Lattice. *Annals of Nuclear Energy*, 38:2319–2332, 2011.





## 6 Reaction Rate Distributions: Perturbed Lattices

The previous chapter characterized the unperturbed SCWR-like configuration implemented in the experimental test zone of PROTEUS. The whole-reactor model of MCNPX was validated against the experiments via the comparison of calculated and measured reaction rate distributions. The reduced geometry models of CASMO-4E and MCNPX were compared in terms of predicted reaction rate distributions as well. The obtained results of both comparisons yielded excellent agreement. It was shown that both codes can predict these reaction rate distributions within the stated uncertainties for the unperturbed SCWR-like lattice, which features highly heterogeneous moderation conditions of the individual fuel pins across the assembly.

In this chapter, other types of heterogeneities, representative of different kinds of perturbations encountered in practical SCWR assembly designs, have been investigated. The goal, in each case, is to validate MCNPX and CASMO-4E on the basis of measurements made in the corresponding PROTEUS test zone configuration. The same parameters are compared and the same methodology is applied as in the previous chapter.

In Sec. 6.1, the codes are validated for the case with control rod related perturbations of the four central moderation channels (see Subsec. 3.1.2). Sec. 6.2 validates the codes for the configurations with inserted water tanks in the four central moderator channels to simulate the variation of water density between moderator and coolant regions of an SCWR assembly (see Subsec. 3.1.3). Finally, in Sec. 6.3, measured and calculated reaction rate distributions are compared for the configurations where the central fuel pin (K11) was removed (Subsec. 3.1.4) and replaced by gadolinium-poisoned fuel (Subsec. 3.1.5).

### 6.1 Control Rod Related Perturbations

Results corresponding to the two-step validation strategy outlined in Sec. 4.3 are presented. The comparison of MCNPX whole-reactor calculations with experiment is discussed in Subsec. 6.1.2, while the code-to-code reduced geometry model comparisons between MCNPX and CASMO-4E [1] are made in Subsec. 6.1.3. Before presenting these validation results, however, it is useful to compare the calculated values of certain integral parameters characterizing the three

different “SCWR assembly states” represented in the current experiments. The considered states are the two different perturbed SCWR-like lattices, as well as the corresponding unperturbed configuration. It is clearly adequate, for this purpose, to simply consider the reduced geometry model, and this has been done in Subsec. 6.1.1 on the basis of CASMO-4E calculations.

### 6.1.1 Comparison of the Perturbed and Unperturbed Lattices (Reduced Geometry Model Results)

The integral parameters currently chosen for the comparison of lattice characteristics as obtained from the corresponding CASMO-4E reduced model calculations are:

- the infinite multiplication factor  $k_\infty$  (i.e. productions/absorptions in the zero leakage spectrum)
- the critical axial buckling  $B_c^2$  (i.e. the applied axial buckling for obtaining  $k_{\text{eff}} = 1.0$ )
- the migration area, calculated from  $M^2 = (k_\infty - 1)/B_c^2$
- the reaction rate ratios  $C_8/F_{\text{tot}}$ ,  $F_8/F_{\text{tot}}$ ,  $\text{Abs}_{\text{tot}}/F_{\text{tot}}$ , and  $\text{Prod}_{\text{tot}}/F_{\text{tot}}$  for the full assembly, calculated in the fundamental mode (i.e.  $k_{\text{eff}} = 1$ ) spectrum;  $C_8$  stands for captures in  $^{238}\text{U}$ ,  $F_8$  for fissions in  $^{238}\text{U}$ ,  $F_{\text{tot}}$  for total fissions (i.e. fissions in  $^{235}\text{U}$  and  $^{238}\text{U}$ ),  $\text{Abs}_{\text{tot}}$  for total absorptions, and  $\text{Prod}_{\text{tot}}$  for total productions, the first two reaction rate ratios serving here primarily as spectral indices and the latter two as overall neutron balance components
- $(k_\infty)_{\text{FM}}$ , i.e. productions/absorptions in the fundamental mode (i.e.  $k_{\text{eff}} = 1$ ) spectrum

Table 6.1 presents the comparison of calculated results for the three different reduced geometry model cases. These are the two perturbed assemblies (with aluminum and steel rods inserted into the central moderator regions to simulate moderator displacement and neutron absorption effects, respectively), along with the unperturbed configuration. The infinite multiplication factor  $k_\infty$  of the assembly is seen to be high for each of the three configurations. This explains the large critical buckling values, which correspond to extrapolated axial heights as little as 31 to 33 *cm*. All three configurations thus effectively represent high leakage systems.

The aluminum configuration is seen to have a 2% higher migration area than the unperturbed assembly. This can be ascribed to the low absorption cross-section of aluminum and is in line with its functioning as “moderator displacer” (see Subsec. 3.1.2). Effects on the reaction rate ratios, however, are more significant for the steel configuration. The steel rods, as expected from their “absorber” role, affect  $\text{Abs}_{\text{tot}}/F_{\text{tot}}$  by  $\sim 3\%$ , and this is directly reflected in the 3% decrease in  $k_\infty$  for the assembly. The corresponding changes are negligible for the aluminum case. As regards the spectrum hardening effects of the two types of perturbations, these may be assessed qualitatively from the corresponding changes in  $C_8/F_{\text{tot}}$  and  $F_8/F_{\text{tot}}$ . These changes

Table 6.1: CASMO-4E reduced geometry model results for integral parameters characterizing the unperturbed SCWR-like lattice, and the two perturbed configurations with inserted aluminum and steel rods, respectively.

Parameter	Unperturbed	Al. rods	St. rods
$k_{\infty}$ (zero leakage spectrum)	1.476	1.476	1.432
$B_c^2$ [ $cm^{-2}$ ]	$9.84 \cdot 10^{-3}$	$9.63 \cdot 10^{-3}$	$9.00 \cdot 10^{-3}$
$M^2$ [ $cm^2$ ]	48.35	49.41	47.95
$C_8/F_{tot}$	0.2547	0.2580	0.2618
$F_8/F_{tot}$	0.0352	0.0356	0.0360
$Abs_{tot}/F_{tot}$	1.670	1.670	1.721
$Prod_{tot}/F_{tot}$	2.451	2.451	2.451
$k_{\infty}$ (fundamental mode spectrum)	1.467	1.467	1.424

are more than twice as large for the steel configuration (i.e. combined moderator-displacement and absorption effects) as for the aluminum case (moderator displacement only).

The graphs on the left and in the middle of Fig. 6.1 show the effects of the two types of perturbations on the pin-wise reaction rate profiles  $F_{tot}$  and  $C_8$ , as calculated by CASMO-4E. Depicted is the central row of pins in the reduced geometry model, i.e. for the positions K11 to K21 (see Fig. 2.17). In each case - i.e. unperturbed, aluminum and steel - the individual reaction rate values have been normalized to an average value of unity over all pins in the reduced geometry model. The aluminum rods are seen to have an effect on the total fission rate of at most 7.5% (3% for the  $^{238}U$  capture rate). The steel rods lower the total fission rate by up to 18% (9% for the  $^{238}U$  capture rate). As to be expected, the pins close to the perturbations are affected more strongly, especially those pins that, in the unperturbed case, have a locally higher reaction rate relative to their neighbors (pins K13 and K14). For both perturbation types, the general double-humped shape of the reaction rate distributions remains the same. However, the ratios of average reaction rate values between the central perturbed region of the assembly (i.e. pins K11 to K16; see Fig. 3.2) and the outer region (K16 to K21) change significantly. The central region loses importance, relative to the outer region, the changes being - as expected - considerably stronger for the steel case.

The right hand side of Fig. 6.1 shows the pin-wise variation of the reaction rate ratio  $C_8/F_{tot}$  for the three lattice configurations. Relative to the unperturbed case, the aluminum rods are seen to harden the neutron spectrum in the central region (K11-K14), such that the spectral index is increased by  $\sim 5\%$ . The effect gets weaker in the outer region and is below 1% already at pin K17. The steel rods harden the spectrum even more ( $C_8/F_{tot}$  is 10-14% higher in the central region). This effect too, disappears towards K17.

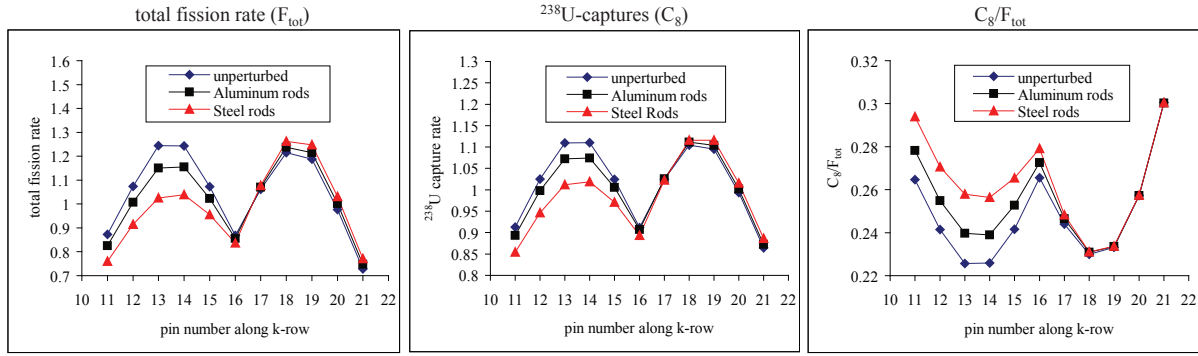


Figure 6.1: Effects of the control rod related perturbations on distributions of the total fission rate (left), of the  $^{238}\text{U}$  capture rate (middle), as also of the ratio  $C_8/F_{\text{tot}}$  (right), as calculated using the CASMO-4E reduced geometry model.

### 6.1.2 Comparison of MCNPX Whole-Reactor Calculations with Experiments

The study of the unperturbed SCWR-like test lattice reported in Chapter 5 demonstrated excellent agreement between measurements and results from the MCNPX PROTEUS whole-reactor calculation. In this section, findings are presented from the corresponding analysis for each of the two differently perturbed test zone configurations.

#### 6.1.2.1 Aluminum Rods in the Central Moderator Regions

The top and middle parts of Fig. 6.2 show - for the case with inserted aluminum rods - the comparison of MCNPX calculated (C) and experimental (E) results for the distribution of the individual reaction rates, total fissions ( $F_{\text{tot}}$ ) and  $^{238}\text{U}$  captures ( $C_8$ ), respectively. For each reaction rate, the reported fuel-pin specific C/E values are based on an initial normalization of both calculated and experimental results to an average value of 1.0 for the 34 measured fuel pin positions. The average  $1\sigma$  uncertainty on each C/E is 0.4% in the case of  $F_{\text{tot}}$  and 0.8% in the case of  $C_8$ . As in the case of the unperturbed test lattice, these uncertainties are mainly due to the experimental statistical accuracies achieved in the counting of the corresponding gamma rays, the statistical uncertainty on the MCNPX tallies being much lower. It is seen that the agreement between the MCNPX PROTEUS whole-reactor calculation and experiment is excellent for both the  $F_{\text{tot}}$  and  $C_8$  reaction rate distributions across the perturbed test lattice. For each pin position, the calculated and experimental results agree within  $2\sigma$ .

The bottom part of Fig. 6.2 shows the C/E values for the reaction rate ratio  $C_8/F_{\text{tot}}$ . Once again, unlike the case of the individual reaction rates, these distributions did not have to be normalized, and a direct comparison of experimental and calculational results could be performed. As mentioned earlier,  $C_8/F_{\text{tot}}$  is a useful spectral index characterizing the individual fuel pin positions in the SCWR-like lattice. However, with normalization not being necessary, the sys-

tematic errors in the measurement of the reaction rate ratio (such as uncertainties on nuclear data, detector efficiencies, etc.) do not cancel out and remain in the final overall uncertainty on each experimental result. As in the case of the unperturbed test lattice, the average total  $1\sigma$  uncertainty on the C/E values for this spectral index is much larger, viz. 2.2%. The average C/E value for  $C_8/F_{\text{tot}}$  in the 34 measured fuel pin positions is found to be 0.980, which can be regarded as unity within  $1\sigma$ . As before, the relative spread of the individual C/E values around this average, however, is governed only by the statistical uncertainties ( $\sigma'$ ) in the reaction rate measurements and in the MCNPX tallies, and these sum up to 0.9%. Indeed, the individual C/E results for  $C_8/F_{\text{tot}}$  in the 34 measured fuel pin positions are all seen to agree within  $2\sigma'$  with the mean value of 0.980. In other words, there is a bias of about 2% on each C/E value (within the 2.2%  $1\sigma$  uncertainty on the absolute reaction rate ratio value), but the relative variation of the spectral index across the perturbed test lattice is reproduced well by the MCNPX calculation, viz. within the 0.9% statistical accuracy.

In brief, the agreement between measured distributions of the individual reaction rates - as also of  $C_8/F_{\text{tot}}$  - with calculational results from the MCNPX PROTEUS whole-reactor modeling is seen to be of the same quality as reported earlier for the unperturbed SCWR-like test lattice (Chapter 5).

#### 6.1.2.2 Steel Rods in the Central Moderator Regions

Fig. 6.3 gives the comparison of MCNPX calculated results with the measured  $F_{\text{tot}}$ ,  $C_8$ , and  $C_8/F_{\text{tot}}$  distributions in the test lattice perturbed by steel rods in the four central moderator regions; this is analogous to the Fig. 6.2 presentation of C/E values for the aluminum configuration. The same 34 fuel pin positions were measured in this campaign. Once again, the top part of the figure depicts the C/E values for  $F_{\text{tot}}$ , and the average  $1\sigma$  uncertainty on an individual value is 0.4%. It is seen that there are only 4 fuel pins for which the deviation between calculation and experiment lies between 2 and  $3\sigma$ . From the middle part of Fig. 6.3, depicting the C/E values for the  $^{238}\text{U}$  capture rate (average  $1\sigma$  of 0.8%), one sees that the calculated and measured results agree within  $2\sigma$  for all but one fuel pin position.

In the case of the C/E values for the spectral index  $C_8/F_{\text{tot}}$ , presented in the bottom part of Fig. 6.3, the mean value is 0.978, which again can be regarded as unity considering the 2.2% experimental uncertainty ( $1\sigma$ ) on the non-normalized reaction rate ratio values. The statistical component ( $\sigma'$ ) of this total uncertainty is once again just 0.9%. The agreement between the individual C/E values and the mean value of 0.978 is seen to be within  $2\sigma'$  for all 34 fuel pin positions.

These results show that - as with the aluminum “moderator displacer” configuration - MCNPX is also capable of correctly predicting reaction rate distributions in the perturbed SCWR-like test lattice with inserted steel “absorber” rods.

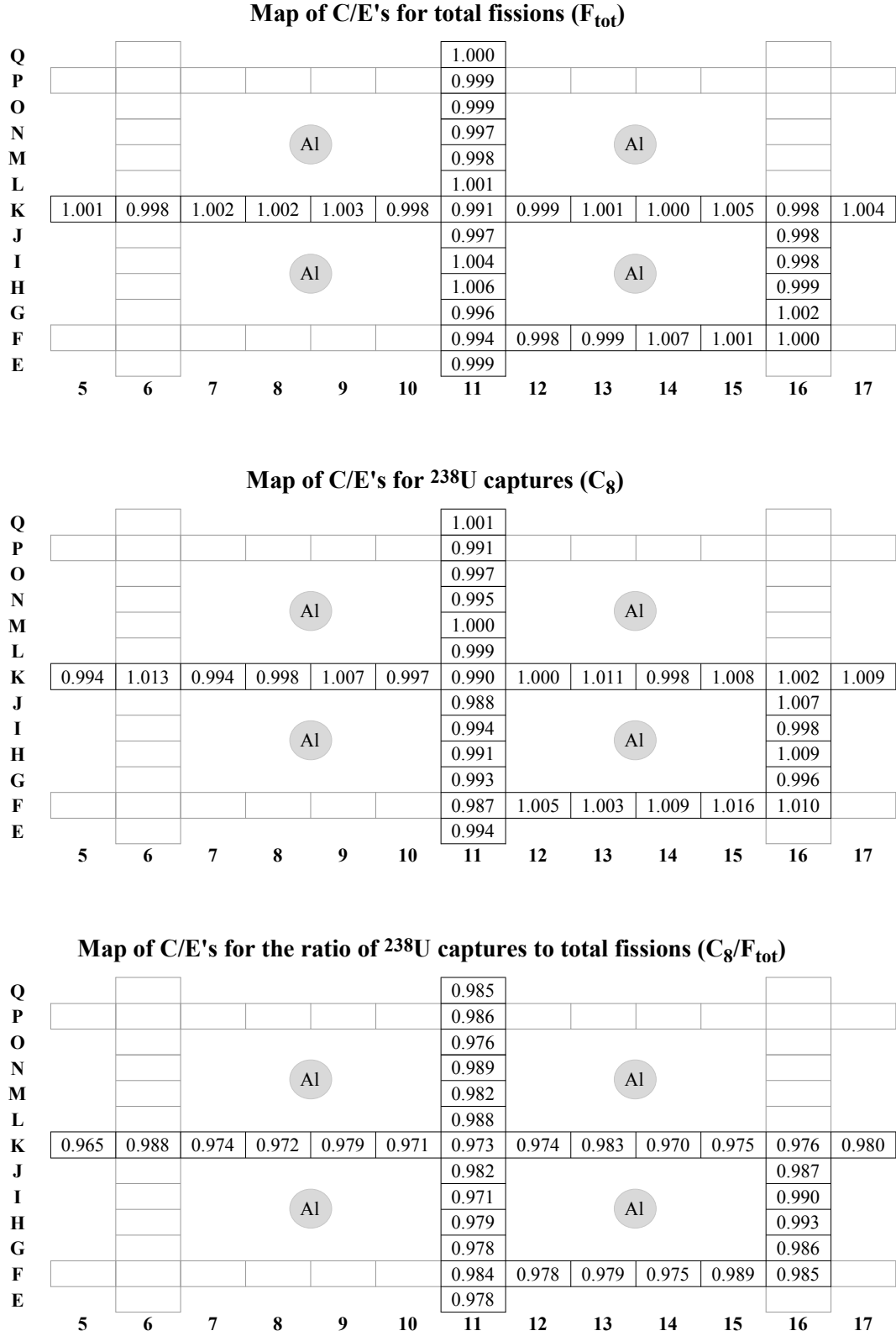


Figure 6.2: Pin-wise maps of calculation/experiment (C/E) values for  $F_{\text{tot}}$  (top part of figure),  $C_8$  (middle) and  $C_8/F_{\text{tot}}$  (bottom) for the test lattice with four inserted aluminum rods, the calculational results being based on MCNPX modeling of the whole PROTEUS reactor. In each map, the C/E value for each of the 34 measured pin positions is consistent with the mean value (1.0 for  $F_{\text{tot}}$  and  $C_8$ , 0.980 for  $C_8/F_{\text{tot}}$ ) within twice the corresponding statistical uncertainty.

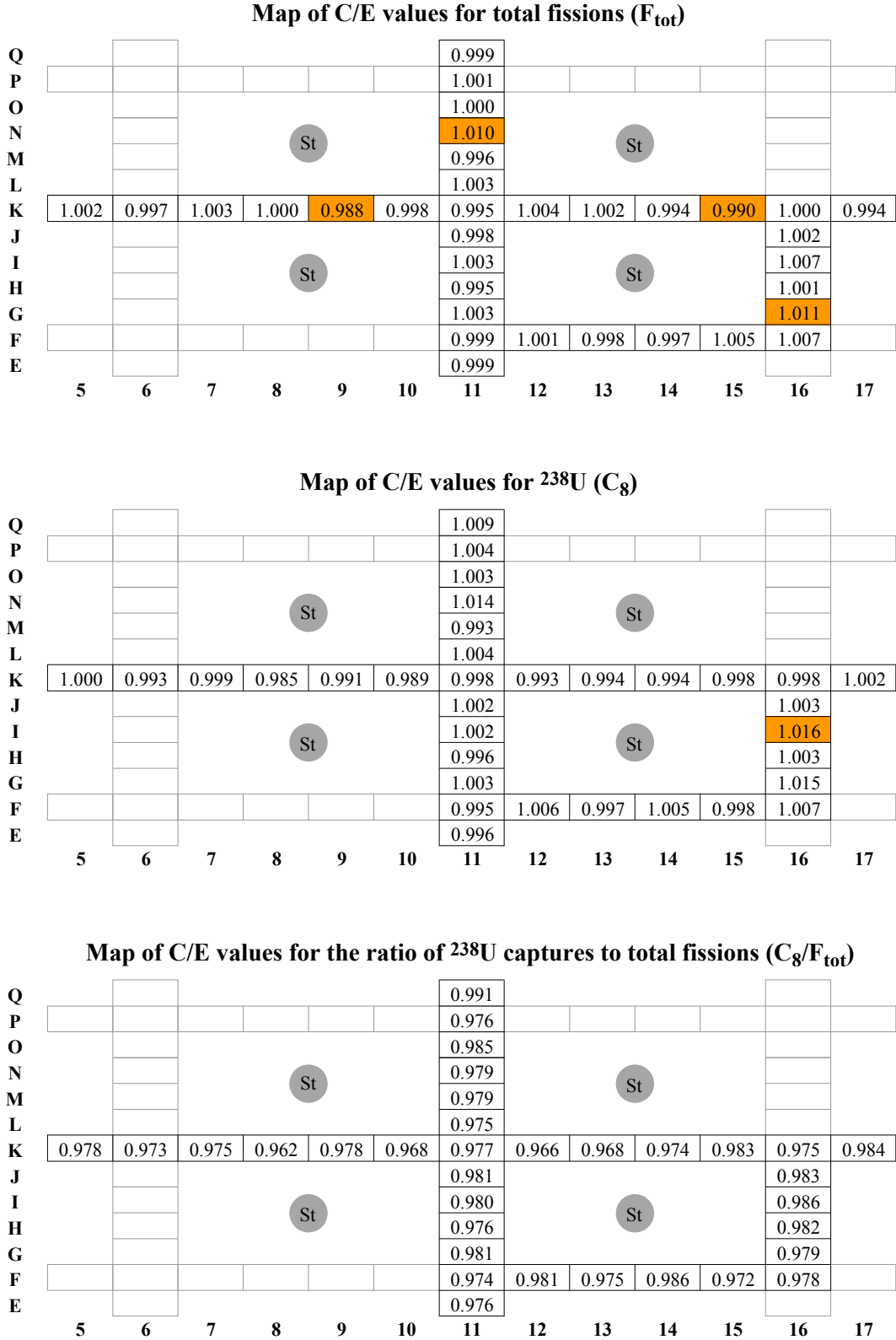


Figure 6.3: Pin-wise maps of calculation/experiment (C/E) values for  $F_{\text{tot}}$  (top part of figure),  $C_8$  (middle) and  $C_8/F_{\text{tot}}$  (bottom) for the test lattice with four inserted steel rods, the calculational results being based on MCNPX modeling of the whole PROTEUS reactor. The C/E values marked in orange are the only ones which deviate from the mean value (1.0 for  $F_{\text{tot}}$  and  $C_8$ , 0.978 for  $C_8/F_{\text{tot}}$ ) by between 2 and 3 times the corresponding statistical uncertainty.

### 6.1.3 Comparison of CASMO-4E and MCNPX Reduced Geometry Models

The Monte Carlo modeling of the PROTEUS whole-reactor has been shown - as for the unperturbed case - to agree with measured reaction rate distributions in each of the test lattices corresponding to the studied perturbations. This fulfills Step 1 of the validation strategy sketched in Sec. 4.3 for deterministic codes. With MCNPX effectively validated for the SCWR-specific physics represented in the experiments, validation of the CASMO-4E reduced geometry model (Fig. 4.4) can be accomplished in Step 2. This, as before, is done via inter-code comparisons based on reduced geometry modeling. The corresponding results obtained, for each of the control rod related perturbations studied, are reported in this subsection.

Before comparing the distributions for the individual reaction rates ( $C_8$  and  $F_{\text{tot}}$ ), as calculated by the two codes, each reaction rate was first normalized to an average of unity over all pins in the reduced geometry model. As discussed earlier, the spectral index  $C_8/F_{\text{tot}}$  does not need to be normalized. In this case, the individual pin values have been compared directly, the average  $C/C'$  value being given separately. ( $C$  and  $C'$  denote results from the CASMO-4E and MCNPX reduced geometry calculations, respectively.)

#### 6.1.3.1 Aluminum Rods in Central Moderator Regions

The inter-code comparison, for the reduced geometry model corresponding to the lattice with aluminum rods inserted into the central water regions, has been made analogously to the unperturbed case. As before, CASMO-4E was run in quarter geometry with reflected boundary conditions and standard input options. One of the latter is that critical conditions are achieved via a homogeneously applied, fundamental mode buckling in the axial direction, which modifies the infinite lattice results obtained from the transport calculation.

Fig. 6.4 presents the three different sets of  $C/C'$  values, viz. for  $C_8$ ,  $F_{\text{tot}}$ , and  $C_8/F_{\text{tot}}$ . Values in yellow and orange indicate discrepancies of more than 1 and 2%, respectively. It is seen that the pins in the upper left corner of the figure - i.e. the ones located in the center of the assembly, in between the four aluminum rods - have fission rates that are systematically overestimated by CASMO-4E (up to as much as 2.6%). A similar overall trend is observed for the  $^{238}\text{U}$ -capture rate, although the pattern of discrepancies is slightly more scattered due to the differences between the intrinsically distinct fuel pin positions discussed earlier for the unperturbed core.

The  $C_8/F_{\text{tot}}$  comparison gives satisfactory results despite the discrepancies in the individual reaction rates. All pins agree within  $\sim 1\%$  of the pin average  $C/C'$  value of 1.002 (which again, as for the unperturbed lattice shows excellent agreement between the two codes as regards the absolute reaction rate value).



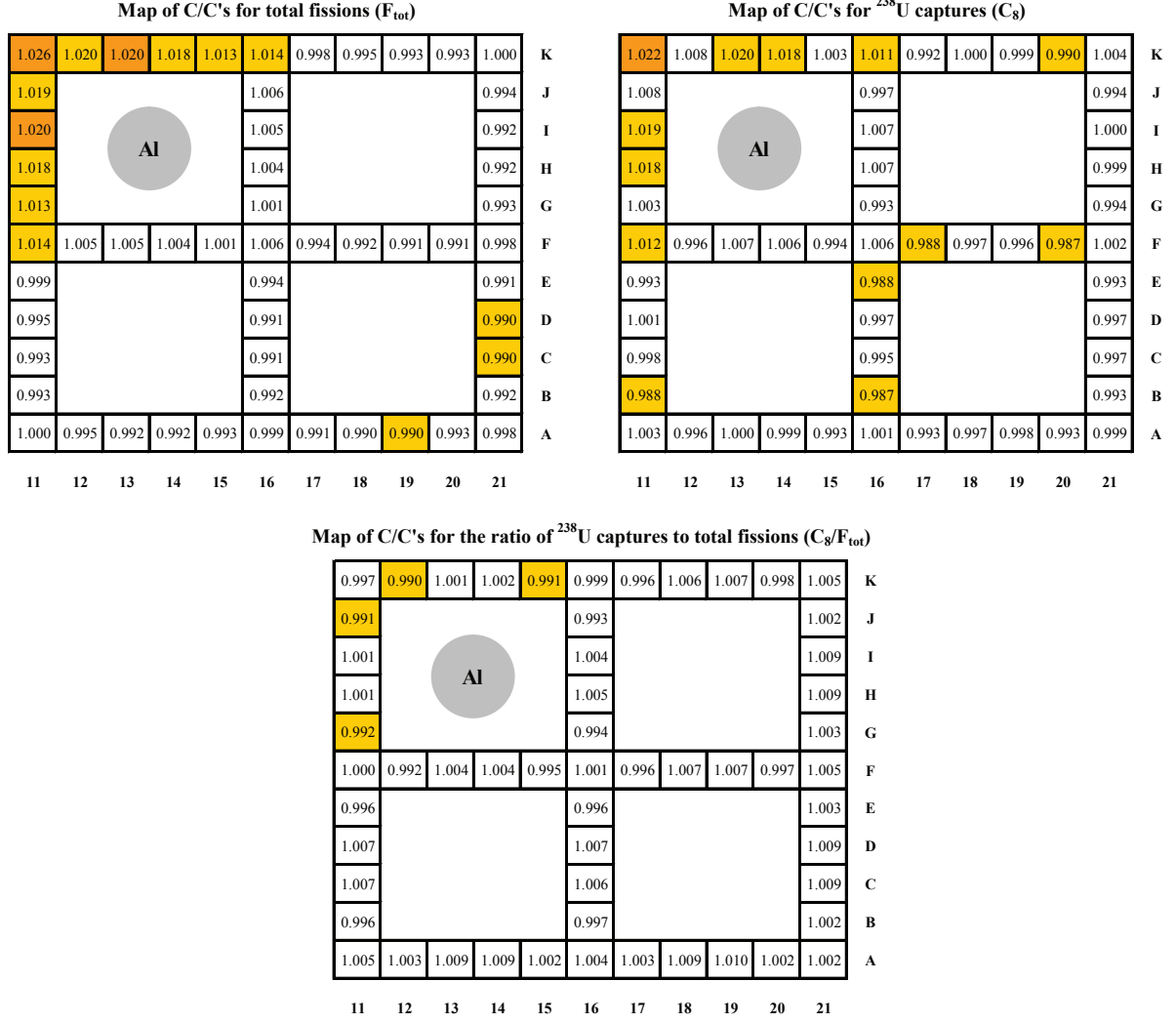


Figure 6.4: Lower right quadrant of the reduced geometry “assembly” with aluminum rods (see left hand side of Fig. 4.4): Comparison between CASMO-4E (C) and MCNPX (C’) calculations of the individual reaction rates ( $F_{\text{tot}}$  and  $C_8$ ) and their ratio ( $C_8/F_{\text{tot}}$ ). The pin average C/C’ value is 1.0 for  $F_{\text{tot}}$  and  $C_8$  (due to the normalization) and 1.002 in the case of  $C_8/F_{\text{tot}}$ . Values that differ more than 1% from the pin average are highlighted in yellow, those differing by more than 2% are in orange.

### 6.1.3.2 Steel Rods in Central Moderator Regions

Fig. 6.5 illustrates the reduced geometry model comparison between the codes for the lattice with inserted steel rods. In contrast to the “moderator-displacement-only” case of the aluminum configuration, excellent agreement is observed between the codes, the CASMO-4E and MCNPX calculated values all agreeing within  $\sim 1\%$ , for both reaction rates, as also for their ratio. This was initially a surprising finding, considering that the steel rods perturb the thermal flux and the spectrum much stronger than the aluminum rods (see Fig. 6.1), so that greater discrepancies between the codes were expected. It was felt that a more detailed look needed to be taken into the “standard” input options for CASMO-4E, and the corresponding investigation is discussed in the following subsection.

### 6.1.4 Investigation of Discrepancies

As mentioned earlier, the main motivation for the two separate measurement campaigns on control rod related perturbations of the SCWR-like lattice has been to enable the distinction between the effects of neutron absorption of the inserted rods and those of moderator displacement. Aluminum was chosen for the first campaign because of its low neutron absorption cross-section. To first order, it can thus be regarded as pure moderator displacer. Steel, on the other hand, is a much stronger neutron absorber, but does at the same time displace moderator. Since the dimensions of the rods were the same, the displacement effect is equal in the two cases.

The results obtained show that CASMO-4E, with its standard input options, has problems predicting the reaction rate distribution near the perturbing aluminum rods. It underestimates the negative effect of the moderator displacement on the neutron flux (both thermal and epithermal). The underestimation seems to be nearly the same for thermal and epithermal neutrons since the spectral index is calculated correctly. This consideration should also apply for the lattice with inserted steel rods, but here CASMO-4E performed satisfactorily. An effect related to the higher degree of “transparency” induced by the aluminum in the moderator seems to be implied, and it is this feature which has led to a closer examination of the leakage treatment.

To start with, an infinitely large reduced geometry system (hence, without leakage) was modeled with both MCNPX and CASMO-4E. In the former case, reflected boundary conditions were applied in all directions while, in the case of CASMO-4E, the calculation was repeated but with zero axial buckling. It was found that the inter-code discrepancies for the lattice with aluminum rods disappeared.

The explanation for the finite system is indeed to be found in the leakage treatment and the larger migration area induced by the inserted aluminum rods. To calculate the leakage for the critical configuration, the standard procedure in CASMO-4E is to homogenize the entire lattice and use spatially averaged group constants. If there is a global leakage gradient across the lattice - as in the case with aluminum rods inserted in the central moderator regions of the SCWR-like lattice

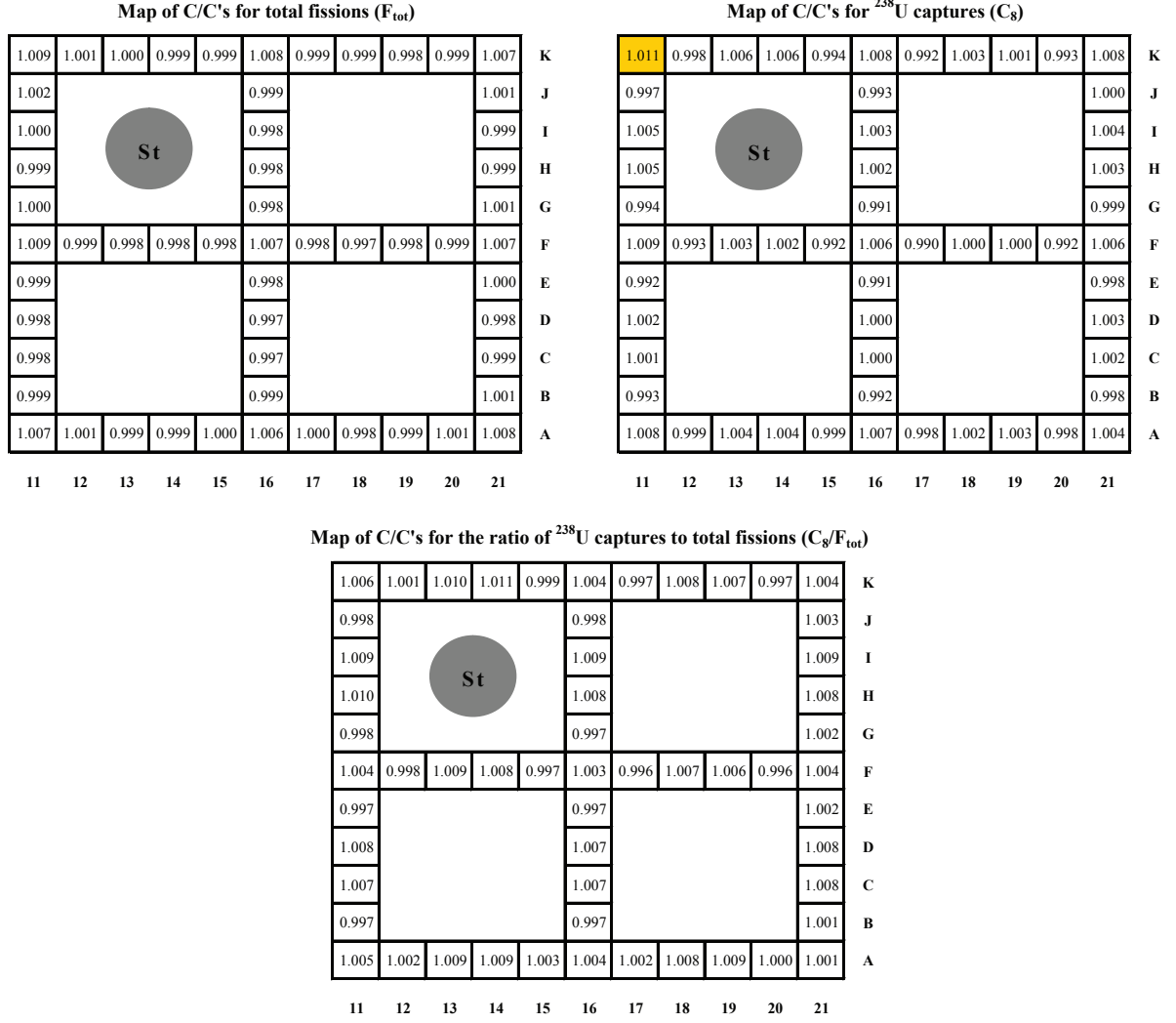


Figure 6.5: Lower right quadrant of the reduced geometry “assembly” with steel rods (see left hand side of Fig. 4.4): Comparison between CASMO-4E (C) and MCNPX (C’) calculations of the individual reaction rates ( $F_{\text{tot}}$  and  $C_8$ ) and their ratio ( $C_8/F_{\text{tot}}$ ). The pin average C/C’ value is 1.0 for  $F_{\text{tot}}$  and  $C_8$  (due to the normalization) and 1.004 in the case of  $C_8/F_{\text{tot}}$ . Values that differ more than 1% from the pin average are highlighted in yellow.

- CASMO-4E underestimates the leakage of fast neutrons in the region where it is highest, and the flux at all energies and hence the reaction rates are locally overestimated as a consequence.

There is, however, an optional input card in CASMO-4E called BZ2 (recommended for the calculation of critical experiments only), with which one can force the addition of a  $DB^2$  term to the absorption of each individual region, rather than to that of the homogenized assembly. A unique critical buckling estimated during an earlier fundamental mode calculation is used to modify the total cross section of each region by a  $DB^2$  term, where  $D$  is region dependent, before performing the 2D transport calculation. This procedure was used for a second, reduced geometry calculation for the configuration with inserted aluminum rods, the results obtained being compared with MCNPX (see Fig. 6.6). The CASMO-4E agreement with MCNPX is now within  $\sim 1\%$  for all pins, with only very slight trends ( $\sim 0.4\%$ ) visible for the reaction rates across the lattice. The earlier observed, inter-code discrepancies for the critical case are thus seen to disappear almost completely.

## 6.2 Moderation Density Variations

As discussed in Subsec. 3.1.3, an important aspect of the SCWR is that considerable differences can occur in the densities of moderator and coolant (both are light water). This follows from the fact that proposed fuel assembly designs tend to separate high density water in the moderator channels and low density water in the cooling channels (around the fuel pins) using appropriate structural materials, in order that greater effectiveness can be achieved for the moderator regions. To investigate the capability of the codes to correctly predict reaction rate distributions in assemblies with separated coolant and moderator, “water-tanks” were inserted into the four central moderator channels of the SCWR-like test lattice. These could be filled with different mixtures of  $H_2O$  and  $D_2O$  in order to simulate different water densities.

### 6.2.1 Characterization of the Perturbed Lattices (Reduced Geometry Model Results)

For characterization of the two different perturbed lattices considered (see Subsec. 3.1.3), Table 6.2 compares the CASMO-4E reduced geometry results for the various integral parameters considered earlier with those of the unperturbed test lattice. The case in which the water-tanks were filled with pure  $H_2O$  is denoted as “ $H_2O$  tanks (100%)”, whereas “ $D_2O$  tanks (66%)” denotes the case where the water-tanks were filled with a mixture of 66%  $D_2O$  and 34%  $H_2O$ . The  $k_\infty$  of all three cases are rather high, which explains the large critical buckling values that correspond to extrapolated heights of only 31 to 32 *cm*.

The migration area of case  $H_2O$  tanks (100%) is smaller than in the unperturbed case. This comes from the stronger slowing down power (relative to the reference mixture of 67%  $H_2O$  and

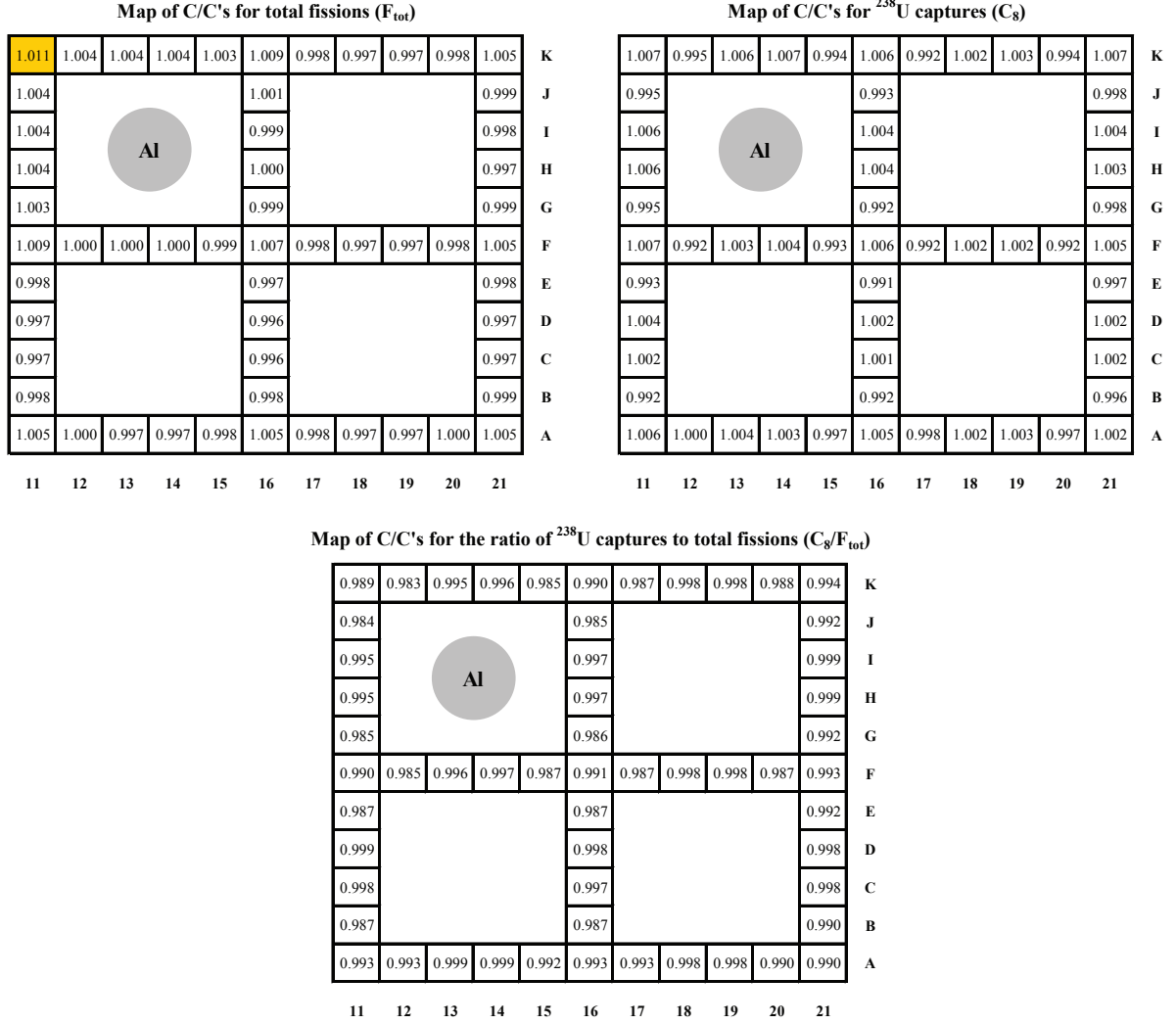


Figure 6.6: Lower right quadrant of the reduced geometry “assembly” with aluminum rods (see left hand side of Fig. 4.4): Comparison between BZ2-treated CASMO-4E (C) and MCNPX (C’) calculations of the individual reaction rates ( $F_{\text{tot}}$  and  $C_8$ ) and their ratio ( $C_8/F_{\text{tot}}$ ). The pin average C/C’ value is 1.0 for  $F_{\text{tot}}$  and  $C_8$  (due to the normalization) and 0.992 in the case of  $C_8/F_{\text{tot}}$ . Values that differ more than 1% from the pin average are highlighted in yellow.

Table 6.2: CASMO-4E reduced geometry model results for integral parameters characterizing the unperturbed SCWR-like lattice, and the two perturbed configurations with inserted water tanks containing 100% H<sub>2</sub>O, and a mixture of 66% D<sub>2</sub>O and 34% H<sub>2</sub>O, respectively.

Parameter	Unperturbed	H <sub>2</sub> O tanks (100%)	D <sub>2</sub> O tanks (66%)
$k_{\infty}$ (zero leakage spectrum)	1.476	1.461	1.485
$B_c^2$ [ $cm^{-2}$ ]	$9.84 \cdot 10^{-3}$	$9.78 \cdot 10^{-3}$	$9.67 \cdot 10^{-3}$
$M^2$ [ $cm^2$ ]	48.35	47.10	50.20
$C_8/F_{tot}$	0.2547	0.2494	0.2618
$F_8/F_{tot}$	0.0352	0.0359	0.0356
$Abs_{tot}/F_{tot}$	1.670	1.684	1.661
$Prod_{tot}/F_{tot}$	2.451	2.451	2.451
$k_{\infty}$ (fundamental mode spectrum)	1.467	1.456	1.476

33% D<sub>2</sub>O), as also the higher absorption rate in the moderator; the latter is reflected in the higher  $Abs_{tot}/F_{tot}$  value and the corresponding reduction of  $k_{\infty}$ . The opposite is true for the case D<sub>2</sub>O tanks (66%), where the migration area is increased by 4% and  $k_{\infty}$  is increased. The better moderation of H<sub>2</sub>O is seen in the  $C_8/F_{tot}$  ratio, which is smaller - i.e. there are more thermal neutrons in the system - when the fraction of light water in the mixture is increased.

Fig. 6.7 illustrates the effect of the perturbing water-tanks on the reaction rate distributions. The graphs on the left and in the middle show, respectively, the individual reaction rate distributions for  $F_{tot}$  and  $C_8$  as calculated by CASMO-4E. Shown is half of the central traverse across the test lattice (fuel pins K11, at the center of the assembly, to K21, at the periphery; see Fig. 2.17). In each case - i.e. unperturbed, H<sub>2</sub>O tanks (100%), and D<sub>2</sub>O tanks (66%) - the individual reaction rate values have been normalized to an average value of unity over all pins in the reduced geometry model. The insertion of water tanks filled with pure H<sub>2</sub>O increases the local fission rate  $F_{tot}$  by about 5% at most (1% for  $C_8$ ). This occurs in the pins that are closest to the perturbations (see Fig. 3.3). The effect is reversed when the water tanks are filled with 66% D<sub>2</sub>O. In this case, the total fission rate in the pins near the perturbations is reduced by 13% at most (5% for  $C_8$ ). Both effects fade out towards the periphery of the core, as the distance to the perturbing water tanks increases.

On the right hand side of Fig. 6.7, the pin-wise reaction rate ratio  $C_8/F_{tot}$  is plotted for the unperturbed and the two perturbed configurations. Again, the most significant changes occur in the direct vicinity of the water tanks and fade out towards the periphery of the assembly (the effects are below 1% for pins K18 to K21). Case H<sub>2</sub>O tanks (100%), as expected, is seen to soften the spectrum, which is indicated by the decrease of  $C_8/F_{tot}$  by about 8%. For case D<sub>2</sub>O tanks (66%), the spectral index is increased by up to 14% in the region of the water tanks.

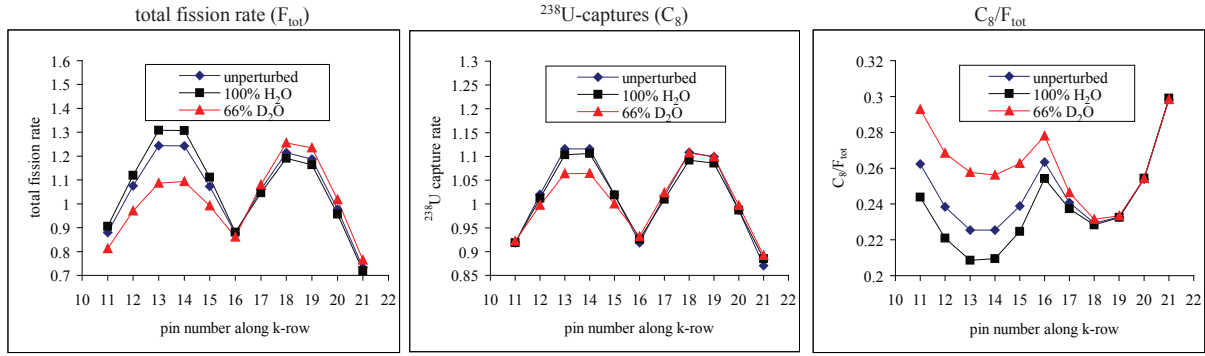


Figure 6.7: Effects of the water tank perturbations on distributions of the total fission rate (left), of the  $^{238}\text{U}$  capture rate (middle), as also of the ratio  $C_8/F_{\text{tot}}$  (right), as calculated using the CASMO-4E reduced geometry model.

### 6.2.2 Comparison of MCNPX Whole-Reactor Calculations with Experiments

Fig. 6.8 shows the comparison of experimentally derived values (E) and calculations (C) with MCNPX in terms of C/E values for the 34 measured fuel pin positions of the configuration in which the water tanks were filled with pure  $\text{H}_2\text{O}$  (configuration  $\text{H}_2\text{O}$  tanks (100%)). The upper-most plot of Fig. 6.8 depicts the C/E values for the total fission rate. The pin-wise distribution of the reaction rates - measured and calculated - was normalized to an average of unity over all measured pins before taking the ratio. The average  $1\sigma$  uncertainty of each value is 0.4%, which, once again, mainly consists of the gamma-ray counting uncertainty of the experiment. Orange shaded cells represent a  $2\sigma$  -  $3\sigma$  deviation between measurement and calculation. The plot in the middle of Fig. 6.8 shows the analogous C/E values for the  $C_8$  rate. Here, the average  $1\sigma$  uncertainty is 0.8%. The calculated and measured values agree for each fuel pin position within  $2\sigma$ .

The plot at the bottom of Fig. 6.8 shows the C/E values for the reaction rate ratio  $C_8/F_{\text{tot}}$ . As discussed for the other test zone configurations, the average  $1\sigma$  uncertainty of the C/E values for this spectral index is much larger than for the individual reaction rates, namely 2.2% (because the uncertainties on nuclear data, such as the fission yields and the branching ratios do not cancel out during the normalization). The average C/E value is found to be 0.989, which can be regarded as unity within  $1\sigma$ . In other words, there is a 1.1% bias on each C/E value. The statistical uncertainties  $\sigma'$  of both the measurements and MCNPX calculations govern the spread of values around the C/E. These uncertainties, as earlier, sum up to 0.9%. All but one of the pin-wise C/E values agree within  $2\sigma'$  with the mean C/E, emphasizing the consistency of experiment and calculation as regards the local spectral variations.

Fig. 6.9 illustrates the analogous results for the case in which the water tanks were filled with a mixture of 66%  $\text{D}_2\text{O}$  and 34%  $\text{H}_2\text{O}$ . The uncertainties are the same as for the previous configuration, namely 0.4%, 0.8%, and 2.2% for  $F_{\text{tot}}$ ,  $C_8$ , and  $C_8/F_{\text{tot}}$  respectively. Values that

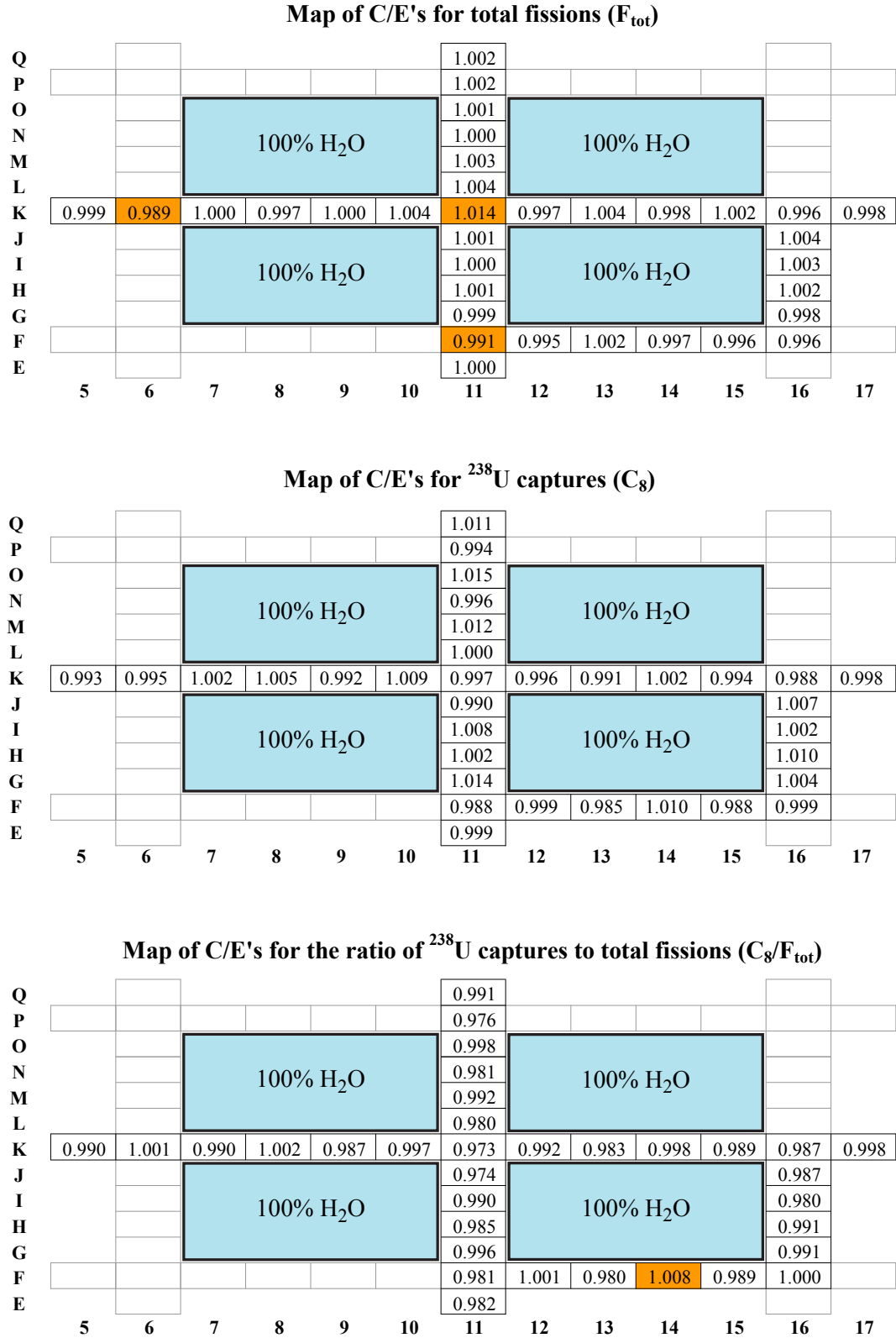


Figure 6.8: Pin-wise maps of calculation/experiment (C/E) values for  $F_{\text{tot}}$  (top part of figure),  $C_8$  (middle) and  $C_8/F_{\text{tot}}$  (bottom) for the test lattice with four inserted water tanks containing 100%  $\text{H}_2\text{O}$ , the calculational results being based on MCNPX modeling of the whole PROTEUS reactor. The C/E values marked in orange are the only ones which deviate from the mean value (1.0 for  $F_{\text{tot}}$  and  $C_8$ , 0.989 for  $C_8/F_{\text{tot}}$ ) by between 2 and 3 times the corresponding statistical uncertainty.



disagree between  $2\sigma$  and  $3\sigma$  ( $2\sigma'$  and  $3\sigma'$  in the case of  $C_8/F_{\text{tot}}$ ) are highlighted in orange. The average C/E value for  $C_8/F_{\text{tot}}$  is 0.982 and agrees with unity, given the stated absolute uncertainty on the ratio. These results confirm one more time the outstanding agreement between measurements and MCNPX calculations.

### 6.2.3 Comparison of CASMO-4E and MCNPX Reduced Geometry Models

Fig. 6.10 and 6.11 show the results of the comparison between the reduced geometry models of MCNPX and CASMO-4E for the configuration with water tanks filled with pure  $\text{H}_2\text{O}$ , and a mixture of 66%  $\text{D}_2\text{O}$  and 34%  $\text{H}_2\text{O}$ , respectively. As in the case of analogous comparisons made earlier, there are no statistical uncertainties in the results obtained with the deterministic code and the statistics on the MCNPX calculations were good enough to achieve uncertainties of less than 0.1%. Consequently, the discrepancies can be regarded as coming from true methods differences between the codes, as also from differences in the nuclear data libraries. Cells highlighted in orange indicate here that the disagreement between the codes is between 1% and 2%.

As discussed in Subsec. 6.1.4 for the configuration with aluminum rods, an optional card had to be inserted into the CASMO-4E input file to calculate leakage effects correctly: the BZ2 card. This is necessary in the present configurations because of the leakage gradient caused by the inserted water tanks, which have different migration areas. As mentioned, the BZ2 card forces the addition of a  $\text{DB}^2$  term to the absorption of each individual region, rather than to that of the homogenized assembly. An earlier estimated critical buckling value is used to modify the total cross section of each region by a  $\text{DB}^2$  term, where D is region dependent, before performing the 2D transport calculation. The treatment of the leakage in this way is seen, from Figs. 6.10 and 6.11, to lead to a good overall agreement between the two codes.

There are only a few fuel pin positions where discrepancies of more than 1% can be observed. For the individual reaction rates ( $C_8$  and  $F_{\text{tot}}$ ) the pins at intersections of fuel pin columns and rows show the largest deviation (up to 1.8%). If the leakage were to be calculated by the standard method in CASMO-4E, the discrepancies in the total fission rate in certain fuel pins would reach as high as 4.6%<sup>1</sup>. The remaining higher predictions for  $F_{\text{tot}}$  and  $C_8$  of CASMO-4E (in lattice positions K11, K16, and F11) are qualitatively consistent with the comparisons made for the unperturbed lattice, where the deterministic code was observed to slightly overestimate the reaction rates at the intersections of pin rows and columns and, moreover, a slight gradient could be observed across the modeled configuration when comparing K11, F16, and A21 (see Sec. 5.4).

<sup>1</sup>This was the maximal discrepancy for the  $\text{D}_2\text{O}$  tanks 66% case, the corresponding maximal effect for the  $\text{H}_2\text{O}$  tanks 100% case being 3.0%.

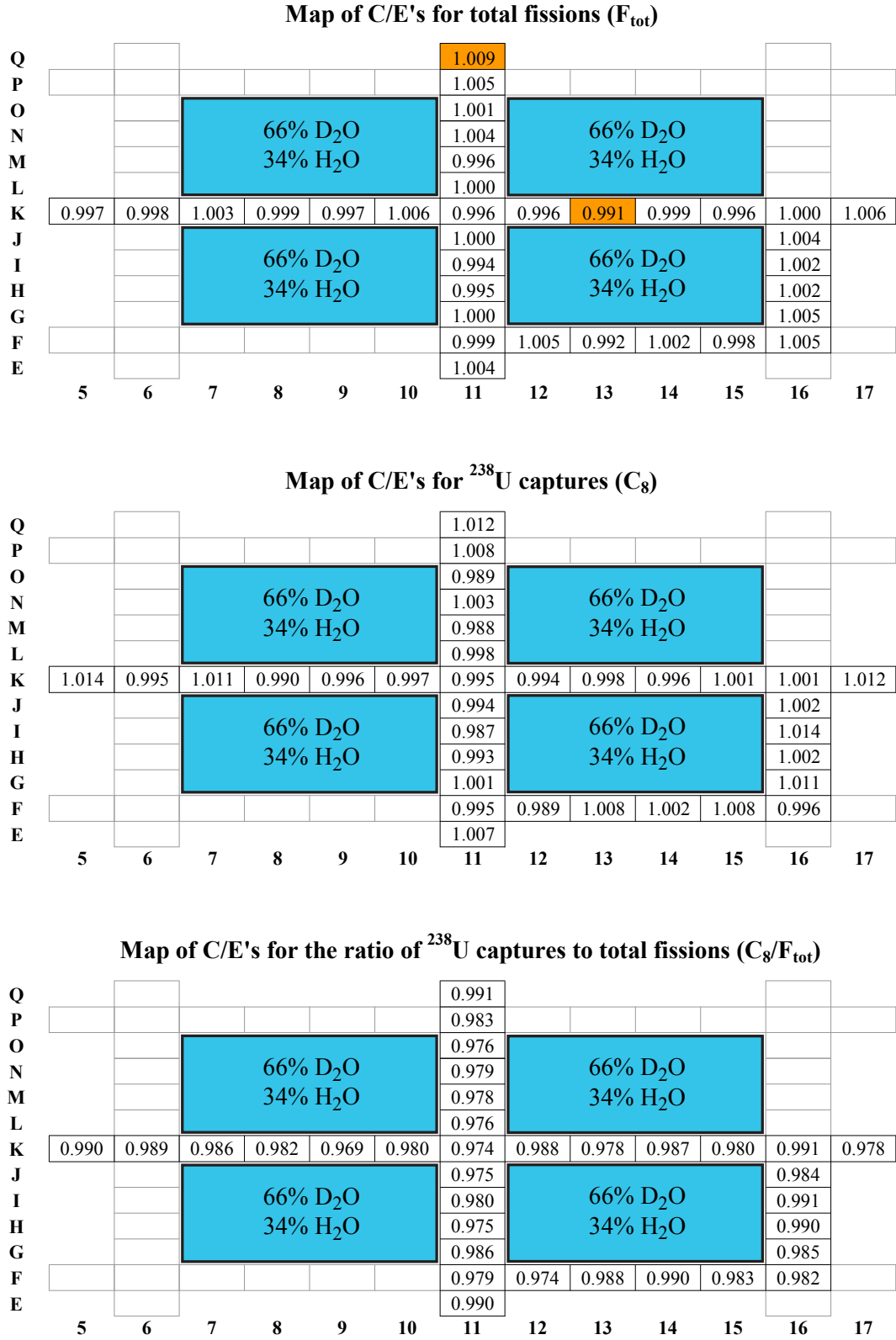


Figure 6.9: Pin-wise maps of calculation/experiment (C/E) values for  $F_{\text{tot}}$  (top part of figure),  $C_8$  (middle) and  $C_8/F_{\text{tot}}$  (bottom) for the test lattice with four inserted water tanks containing a mixture of 66%  $\text{D}_2\text{O}$  and 34%  $\text{H}_2\text{O}$ , the calculational results being based on MCNPX modeling of the whole PROTEUS reactor. The C/E values marked in orange are the only ones which deviate from the mean value (1.0 for  $F_{\text{tot}}$  and  $C_8$ , 0.982 for  $C_8/F_{\text{tot}}$ ) by between 2 and 3 times the corresponding statistical uncertainty.

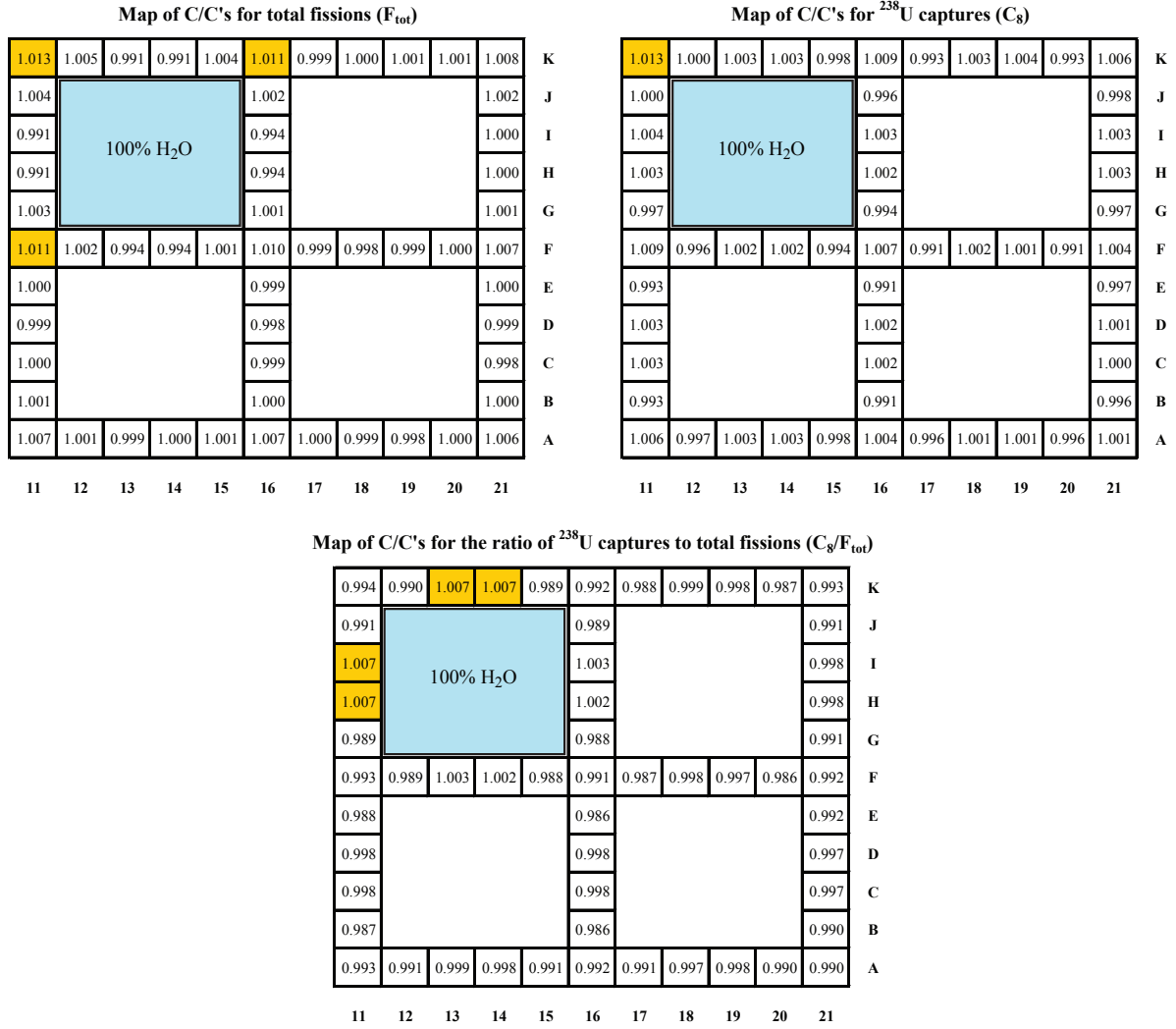


Figure 6.10: Lower right quadrant of the reduced geometry “assembly” with inserted water tanks containing 100% H<sub>2</sub>O: Comparison between CASMO-4E (C) and MCNPX (C') calculations of the individual reaction rates ( $F_{\text{tot}}$  and  $C_8$ ) and their ratio ( $C_8/F_{\text{tot}}$ ). The pin average C/C' value is 1.0 for  $F_{\text{tot}}$  and  $C_8$  (due to the normalization) and 0.994 in the case of  $C_8/F_{\text{tot}}$ . Values that differ between 1% and 2% from the pin average are highlighted in yellow.

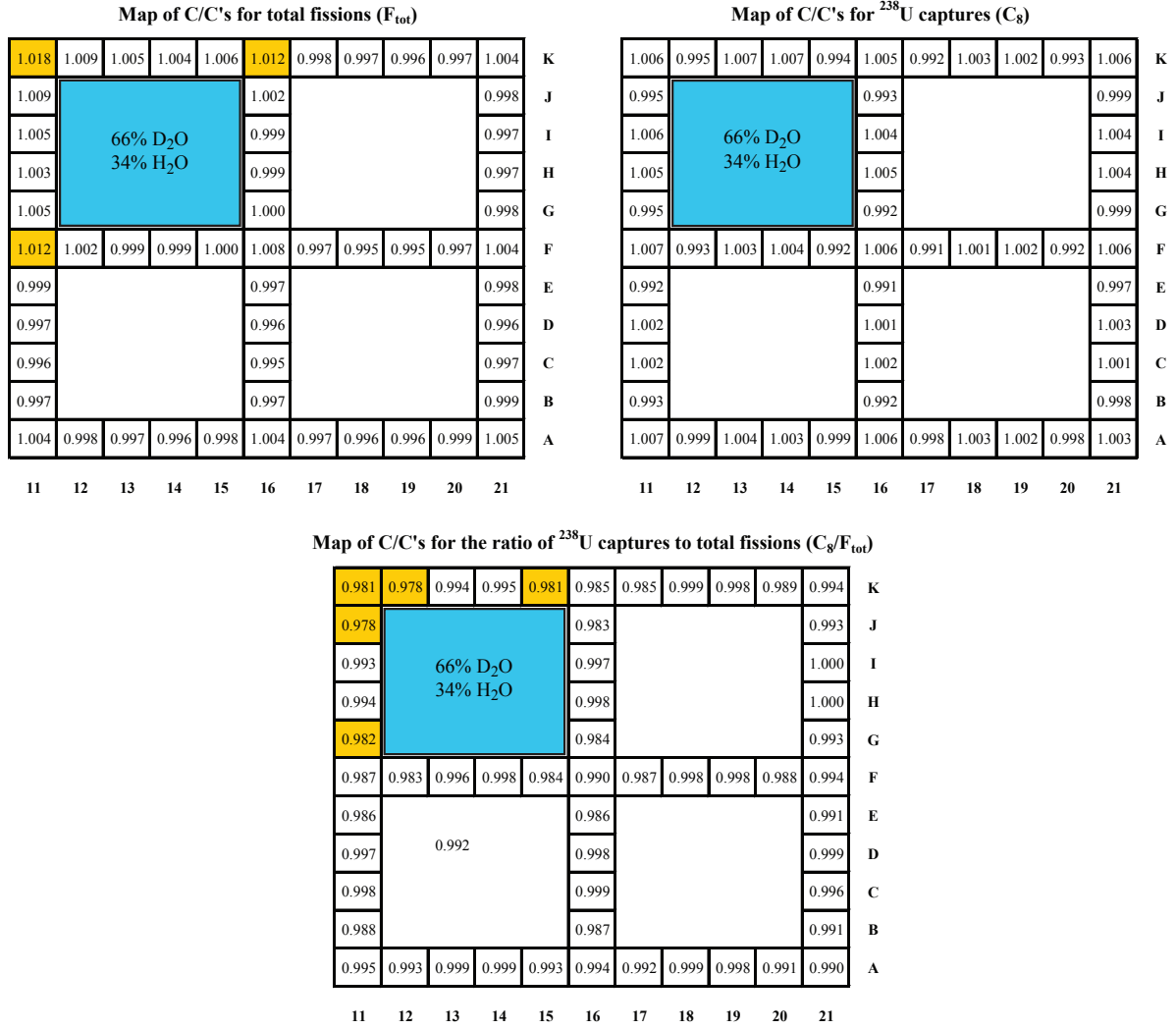


Figure 6.11: Lower right quadrant of the reduced geometry “assembly” with inserted water tanks containing a mixture of 66% D<sub>2</sub>O and 34% H<sub>2</sub>O: Comparison between CASMO-4E (C) and MCNPX (C’) calculations of the individual reaction rates ( $F_{\text{tot}}$  and  $C_8$ ) and their ratio ( $C_8/F_{\text{tot}}$ ). The pin average C/C’ value is 1.0 for  $F_{\text{tot}}$  and  $C_8$  (due to the normalization) and 0.992 in the case of  $C_8/F_{\text{tot}}$ . Values that differ between 1% and 2% from the pin average are highlighted in yellow.

## 6.3 Removing the Central Pin and Replacing it with Gadolinium-Poisoned Fuel

As discussed in Subsec. 3.1.5, the introduction of gadolinium-poisoned fuel pins into the SCWR assembly has been proposed to compensate for the excess reactivity at the beginning of cycle (BOC) [2, 3]. Gadolinium, being a strong neutron absorber, disturbs the local neutron flux considerably. This section investigates the codes' abilities to correctly predict reaction rate distributions in an SCWR-like fuel lattice with an inserted Gd-poisoned fuel pin at the center.

For the sake of completeness, analogous studies for the lattice in which the central fuel pin (K11) has been removed (see Subsec 3.1.4) are also presented. This configuration is an intermediate step between the unperturbed and the Gd-poisoned configuration. As before, the perturbations are first studied in terms of their characterization on the basis of CASMO-4E reduced geometry calculations. Thereafter, the predictions from the MCNPX whole-reactor model are compared to the measurements. Finally, the reduced geometry calculations with CASMO-4E and MCNPX are compared.

### 6.3.1 Characterization of the Perturbed Lattices (Reduced Geometry Model Results)

As in the previous sections, the basic characteristics of the configurations are compared to each other by means of CASMO-4E reduced geometry calculations. Table 6.3 shows the considered integral parameters for the two perturbed configurations, as also for the unperturbed case. The case in which the central fuel pin is removed is denoted as “K11 removed”, and the configuration with the inserted Gd-poisoned fuel pin as “K11 Gd-poisoned”. Comparing the unperturbed and the K11 removed configurations, one sees that the effect on the “assembly”-averaged parameters are indeed quite small. The  $k_{\infty}$  value, calculated in the zero leakage spectrum remains unchanged, even though a fuel pin has been removed from the lattice. In the fundamental mode spectrum, the  $k_{\infty}$  actually increases slightly ( $\approx 0.3\%$ ), reflecting the positive pin-removal reactivity effect mentioned in Subsec. 3.1.4.

The insertion of the Gd-poisoned fuel pin has a clearly stronger effect on the neutron balance. The infinite multiplication factor  $k_{\infty}$  is reduced by 0.7%, which comes mainly from the associated increase in the  $Abs_{tot}/F_{tot}$  ratio. The critical buckling changes by almost 3%, while the migration area remains practically unchanged. The spectral indices  $C_8/F_{tot}$  and  $F_8/F_{tot}$  change only marginally by 0.3% each, i.e. even less than in the K11 removed configuration. The effect of the perturbing Gd-poisoned fuel pin can thus be summarized as increasing the absorptions without changing the neutron energy spectrum.

The effects of the two perturbations on the reaction rate distributions of  $F_{tot}$  and  $C_8$ , as well as on their ratio  $C_8/F_{tot}$  are depicted in Fig. 6.12. Since K11 is missing in the “K11 removed”

Table 6.3: CASMO-4E reduced geometry model results for integral parameters characterizing the unperturbed SCWR-like lattice, and the two perturbed configurations with fuel pin K11 first removed, and then replaced by a Gd-poisoned fuel pin.

Parameter	Unperturbed	K11 re- moved	K11 Gd- poisoned
$k_{\infty}$ (zero leakage spectrum)	1.476	1.476	1.466
$B_c^2$ [ $cm^{-2}$ ]	$9.84 \cdot 10^{-3}$	$9.85 \cdot 10^{-3}$	$9.66 \cdot 10^{-3}$
$M^2$ [ $cm^2$ ]	48.35	48.31	48.25
$C_8/F_{tot}$	0.2547	0.2525	0.2555
$F_8/F_{tot}$	0.0352	0.0356	0.0353
$Abs_{tot}/F_{tot}$	1.670	1.667	1.681
$Prod_{tot}/F_{tot}$	2.451	2.451	2.451
$k_{\infty}$ (fundamental mode spectrum)	1.467	1.471	1.458

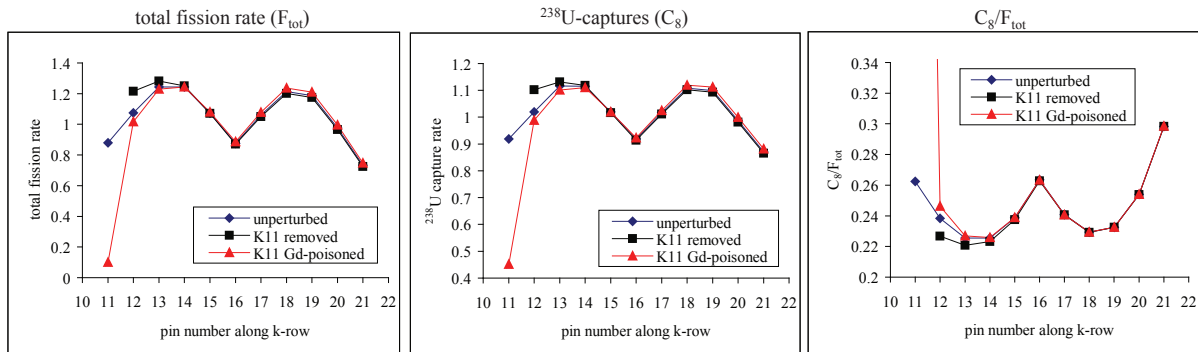


Figure 6.12: Effects of the perturbations induced by first removing fuel pin K11, and then replacing it by a Gd-poisoned pin, on distributions of the total fission rate (left), of the  $^{238}U$  capture rate (middle), as also of the ratio  $C_8/F_{tot}$  (right), as calculated using the CASMO-4E reduced geometry model.

configuration, both reaction rates are “reduced to zero” at this position. However, the reaction rates are also increased in the vicinity of K11. Due to the flooding of the cell K11 with water, the neighboring pins are suddenly better moderated which increases their total fission rate. The same effect, but to a lesser extent, is observed for the  $C_8$  rate. The spectrum in these pins therefore gets softer which can be seen from the  $C_8/F_{\text{tot}}$  values. These effects are discussed in greater detail in Chapter 7.

For the K11 Gd-poisoned configuration, the reaction rates are - as to be expected - strongly reduced at the central pin position itself (K11). While the total fission rate is reduced by 89% (as compared to the K11 value in the unperturbed configuration), the  $C_8$  rate is only reduced by 50%. With the very strong thermal neutron absorption in the gadolinium, the spectrum at K11 is clearly much harder,  $C_8/F_{\text{tot}}$  becoming as high as 435% of the unperturbed value.

These effects, although strong, are only felt over a limited area. The reaction rate differences between the unperturbed and the K11 Gd-poisoned configuration are reduced to 1% already for the lattice position K13, i.e. only two pins away from K11. The local nature of the Gd fuel pin effect, as compared to the weak effect of removing K11 that was spread out over a larger area, is partly because the moderation conditions of the fuel pins do not change across the “assembly”, the Gd pin having the same outer clad diameter as the other  $\text{UO}_2$  pins.

### 6.3.2 Comparison of MCNPX Whole-Reactor Calculations with Experiments

Fig. 6.13 shows the comparison of experimentally derived reaction rate values (E) and whole-reactor calculation results from MCNPX (C), in terms of C/E values for the 33 measured fuel pin positions of the configuration with fuel pin K11 removed. As before, maps of  $F_{\text{tot}}$ ,  $C_8$ , and  $C_8/F_{\text{tot}}$  are plotted over the region in which the reaction rates had been measured during the experimental campaign. As expected, the findings do not differ from those for the unperturbed configuration discussed in Chapter 5. MCNPX correctly predicts the effects of the enhanced moderation on the fuel pins in the neighborhood of the central “waterhole” (see Subsec. 6.3.1 above). For both reaction rate distributions, as well as for their ratio, the calculation results for all pins agree within  $2\sigma$  with the experiment, the  $1\sigma$  level being, as before, 0.4%, 0.8%, and 0.9% ( $\sigma'$ ) for  $F_{\text{tot}}$ ,  $C_8$ , and  $C_8/F_{\text{tot}}$ , respectively. The assembly averaged C/E values were 1 for  $F_{\text{tot}}$  and  $C_8$  (due to normalization), and 0.986 for  $C_8/F_{\text{tot}}$ .

The results of the comparison between measured and MCNPX whole-reactor calculated reaction rate distributions for the K11 Gd-poisoned configuration are shown in Fig. 6.14. Only two values were slightly outside the  $2\sigma$  confidence interval (the uncertainties being the same as before), underlying the excellent agreement between MCNPX and the experiments. Even the reaction rates of the Gd-poisoned fuel pin itself - a pin type for which discrepant results have been reported in earlier experiments with BWR assemblies [4, 5, 6, 7] - agree within uncertainties.

The discrepant results for Gd fuel pins reported from earlier studies were recalculated by the

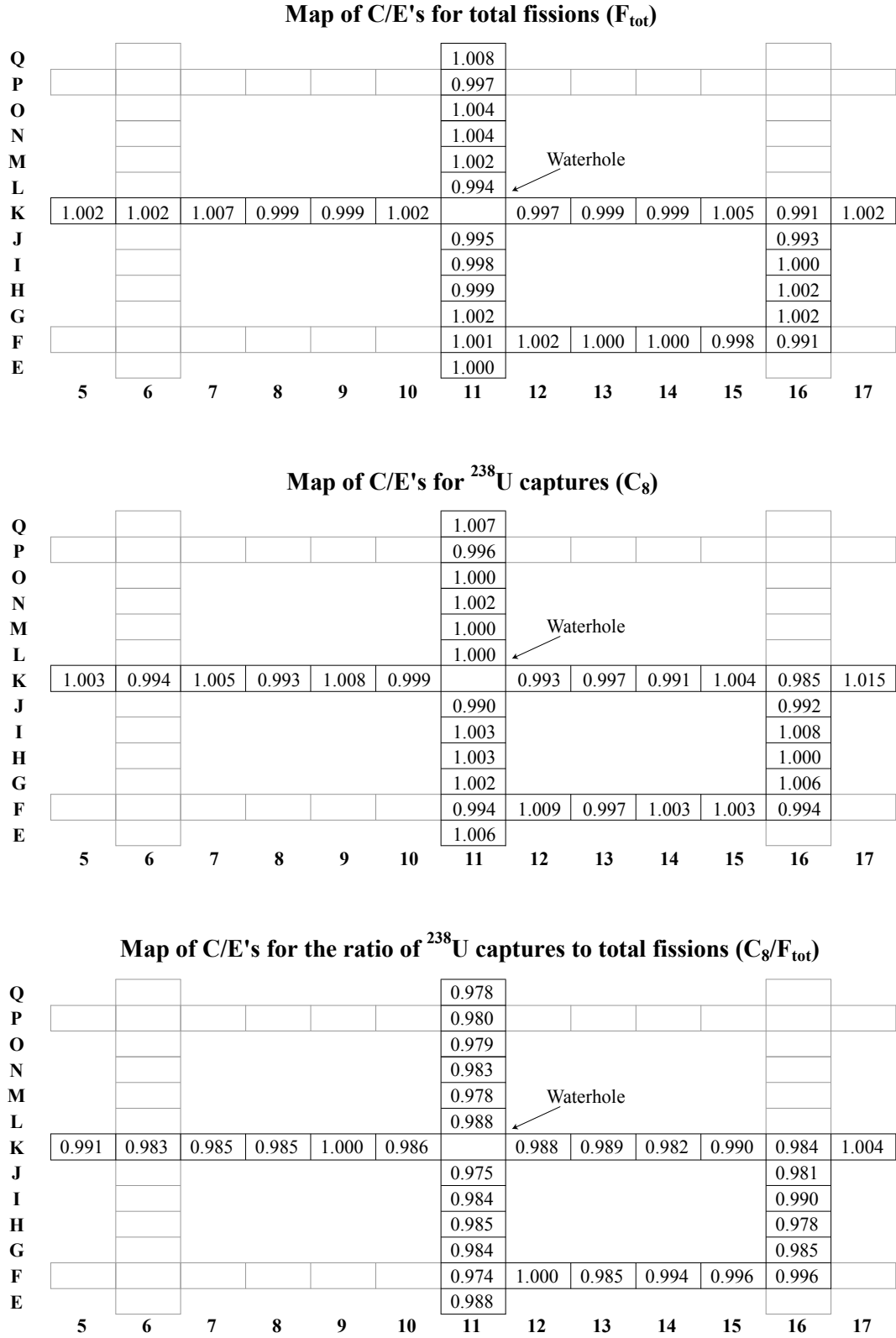


Figure 6.13: Pin-wise maps of calculation/experiment (C/E) values for  $F_{\text{tot}}$  (top part of figure),  $C_8$  (middle) and  $C_8/F_{\text{tot}}$  (bottom) for the test lattice with fuel pin K11 removed, the calculational results being based on MCNPX modeling of the whole PROTEUS reactor. In each map, the C/E value for each of the 33 measured pin positions is consistent with the mean value (1.0 for  $F_{\text{tot}}$  and  $C_8$ , 0.986 for  $C_8/F_{\text{tot}}$ ) within twice the corresponding statistical uncertainty.



authors, using newly measured gadolinium capture and total cross sections, as well as resonance parameters in the range of 1 to 300 eV, from the Rensselaer Polytechnic Institute (RPI)[8]. The findings of this study are discussed by Perret et al. [9] and indicate that the usage of the new cross section data, along with JEFF-3.1 [10] data for the other materials, improves the agreement between measured and calculated total fission rates in Gd-poisoned fuel pins. The  $C_8$  rate did not change significantly due to the limited epithermal flux change in the Gd-poisoned pins.

As a part of the present study, the MCNPX calculation for the K11 Gd-poisoned configuration has been repeated using different nuclear data libraries. A total of three calculations were performed, one using the ENDF/B-VII.0 [11] nuclear data library (which was used throughout this thesis for the MCNPX calculations), one employing the JEFF-3.1.1 library [12], and one using the ENDF/B-VII.0 library with the RPI-updated gadolinium cross sections. The original ENDF/B-VII.0 and the JEFF-3.1.1 library both gave well-agreeing results, the differences between the two libraries being in the order of 0.1% to 0.2% for the C/E values of the Gd-poisoned fuel pin at lattice position K11.

If the gadolinium data from RPI is implemented into the ENDF/B-VII.0 library, the total fission rate of the Gd-poisoned pin is increased by 2.1%. This is consistent with the findings of Perret et al., who reported an increase of 1.4% to 1.8% depending on the elevation at which the SVEA-96 Optima2 BWR assemblies were measured. The even stronger effect in the present K11 Gd-poisoned configuration is due to the spectrum being more thermal in this lattice, as compared to the BWR experiments. (The effects of the RPI data are stronger in the thermal energy range.) However, by using the RPI data, the C/E value for  $F_{\text{tot}}$  in the Gd pin at K11 is increased from  $0.997 \pm 0.005$  to  $1.018 \pm 0.006$ , thus disagreeing by  $3\sigma$  and contradicting the findings of Perret et al. The C/E for the  $C_8$  rate changes from  $0.989 \pm 0.007$  to  $0.996 \pm 0.013$ , an agreement within the given uncertainties. This is also consistent with the earlier observations. The C/E value for  $C_8/F_{\text{tot}}$  is reduced from  $0.979 \pm 0.009$  to  $0.965 \pm 0.014$ , which is also consistent with Perret et al. In conclusion, the relative trends observed in both studies agree well, but the RPI gadolinium data is found to worsen the absolute C/E value for the total fission rate in the K11 Gd-poisoned lattice. This result is in contradiction to the improvements reported for the BWR experiments performed at PROTEUS.

### 6.3.3 Comparison of CASMO-4E and MCNPX Reduced Geometry Models

Fig. 6.15 shows the comparison between the reduced geometry models of CASMO-4E and MCNPX for the “K11 removed” configuration. All values, for both reaction rates and for their ratio, agree within 1% of the assembly average (the average being 1 for  $F_{\text{tot}}$  and  $C_8$ , and 0.993 for  $C_8/F_{\text{tot}}$ ). The agreement is, in fact, even better than that obtained for the unperturbed configuration (see Sec. 5.4). Especially for the  $F_{\text{tot}}$  rate in the pins close to the center (i.e. K12 - K14 and G11 - J11), MCNPX and CASMO-4E predict the distribution more closely. This is due to the fact that removing K11 enhances the moderation of the pins surrounding the waterhole and brings them, in terms of spectral and moderation conditions, closer to their neighboring pins

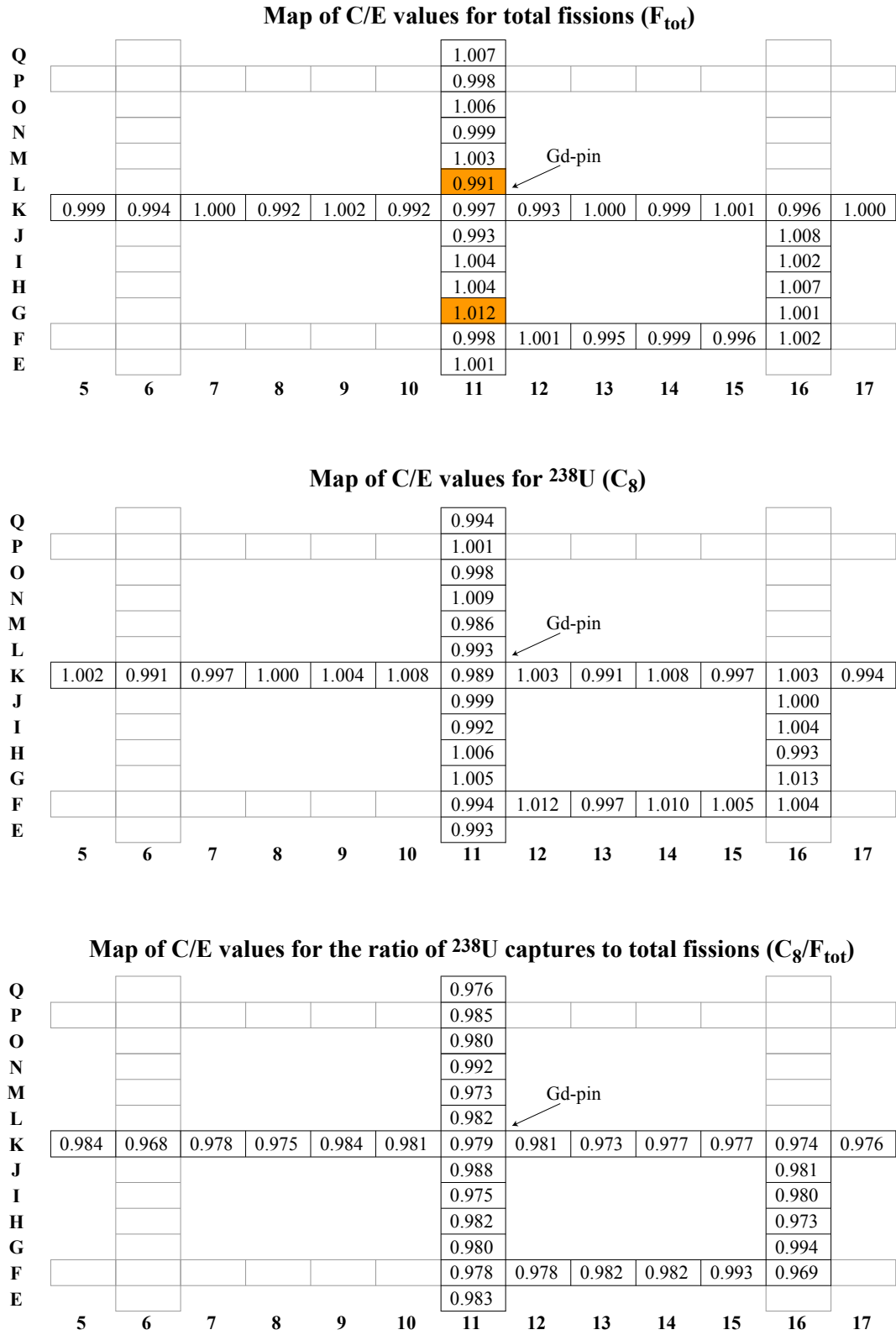


Figure 6.14: Pin-wise maps of calculation/experiment (C/E) values for  $F_{\text{tot}}$  (top part of figure),  $C_8$  (middle) and  $C_8/F_{\text{tot}}$  (bottom) for the test lattice with fuel pin K11 replaced by a Gd-poisoned fuel pin, the calculational results being based on MCNPX modeling of the whole PROTEUS reactor. The C/E values marked in orange are the only ones which deviate from the mean value (1.0 for  $F_{\text{tot}}$  and  $C_8$ , 0.980 for  $C_8/F_{\text{tot}}$ ) by between 2 and 3 times the corresponding statistical uncertainty.

(see Fig. 6.12). The moderation heterogeneity of the central section is therefore reduced, which leads to an even better agreement between the codes.

The results of the reduced geometry comparison between CASMO-4E and MCNPX for the K11 Gd-poisoned configuration are depicted in Fig. 6.16. The total fission rate distribution shows excellent agreement between the two codes, with all the values agreeing within 1%. Even for the Gd-poisoned fuel pin itself, the agreement is well within  $1\sigma$  ( $C/C' = 1.002$ ). For the  $C_8$  rate, however, the value in this pin disagrees by 3% and, consequently, the disagreement for  $C_8/F_{\text{tot}}$  is similar (2.8%), considering that the average value is 0.994. The ratio  $C_8/F_{\text{tot}}$  disagrees by 1.2% for the two neighboring pins (K12 and J11), which is similar to what was observed in other configurations. For the present calculations, the BZ2 card was implemented in the CASMO-4E input. The discrepancies for  $C_8$  in K11 become even larger (4%), if this card is taken out.

The observed discrepancy could come from several sources. The Gd-poisoned fuel pin inserted into the SCWR-like test lattice differed from the standard PROTEUS driver fuel (used for constructing the test zone), not only in terms of its gadolinium content but also in terms of its  $^{235}\text{U}$  enrichment, pellet radius and total fuel height. The Gd-pin also had two clads, the outermost being the same as for the driver fuel pins in order to keep the associated moderator volume constant (see Subsec. 3.1.5). In the following, an attempt has been made to narrow down the number of possible sources of the observed discrepancy by separately examining certain individual effects. For each of these effects, special CASMO-4E and MCNPX inputs were created, and the corresponding cases run, in order to see how the change influenced the  $C/C'$  value for  $C_8$  in the Gd-pin. In order to check the consistency of the results, the  $C/C'$  values for  $F_{\text{tot}}$  were also looked at. Unless stated otherwise, for all the cases discussed below, the agreement between CASMO-4E and MCNPX was within 1% for the total fission rate in the Gd-poisoned pin.

- Changing the  $^{235}\text{U}$  enrichment of the pin did not have an effect on the discrepancy between the codes.
- Altering the Gd content of the pin had a linear effect on the magnitude of the discrepancy. Setting the Gd content to zero gave consistent results.
- Changing the neutron cross section data library with which the MCNPX calculations were performed changed the  $C/C'$  value of  $C_8$  by up to 1%. However, it also changed the  $C/C'$  value for  $F_{\text{tot}}$ , leaving the difference ( $C/C'(C_8) - C/C'(F_{\text{tot}})$ ) almost constant (within 0.6%). The neutron library effect thus seems to invoke a shift of both reaction rates and is thus unable to resolve the observed, energy dependent discrepancy.
- Changing the position in the lattice where the Gd-poisoned pin was inserted (K11, K12, K13, F13, or F16) reduced the discrepancy by up to 1.6%.
- Switching from a quarter-assembly calculation to a full-assembly calculation had no effect on the results.

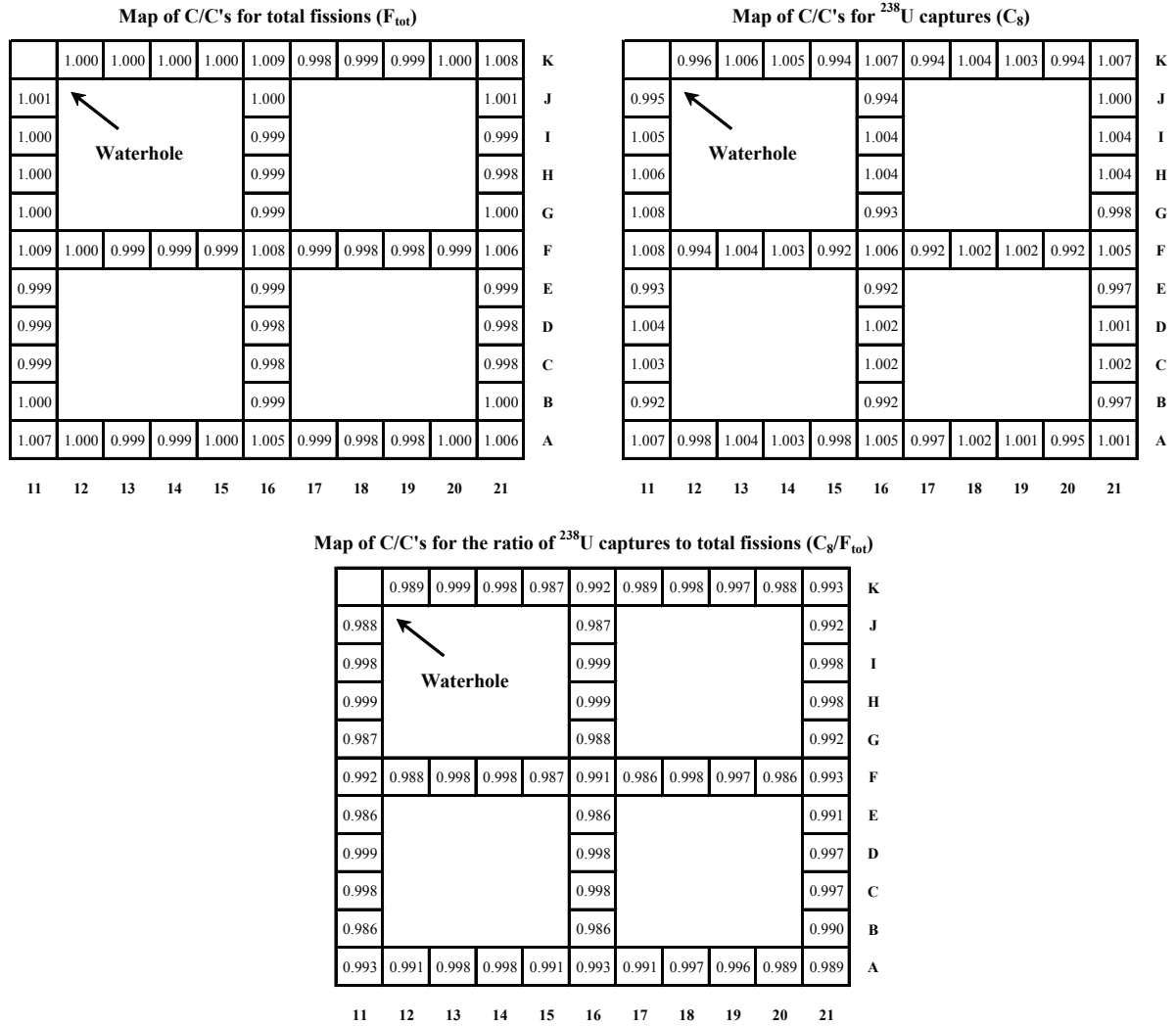


Figure 6.15: Lower right quadrant of the reduced geometry “assembly” with fuel pin K11 removed (see left hand side of Fig. 4.4): Comparison between BZ2-treated CASMO-4E (C) and MCNPX (C’) calculations of the individual reaction rates ( $F_{\text{tot}}$  and  $C_8$ ) and their ratio ( $C_8/F_{\text{tot}}$ ). The pin average C/C’ value is 1.0 for  $F_{\text{tot}}$  and  $C_8$  (due to the normalization) and 0.993 in the case of  $C_8/F_{\text{tot}}$ . Values that differ more than 1% from the pin average would have been highlighted in yellow, but there are none.

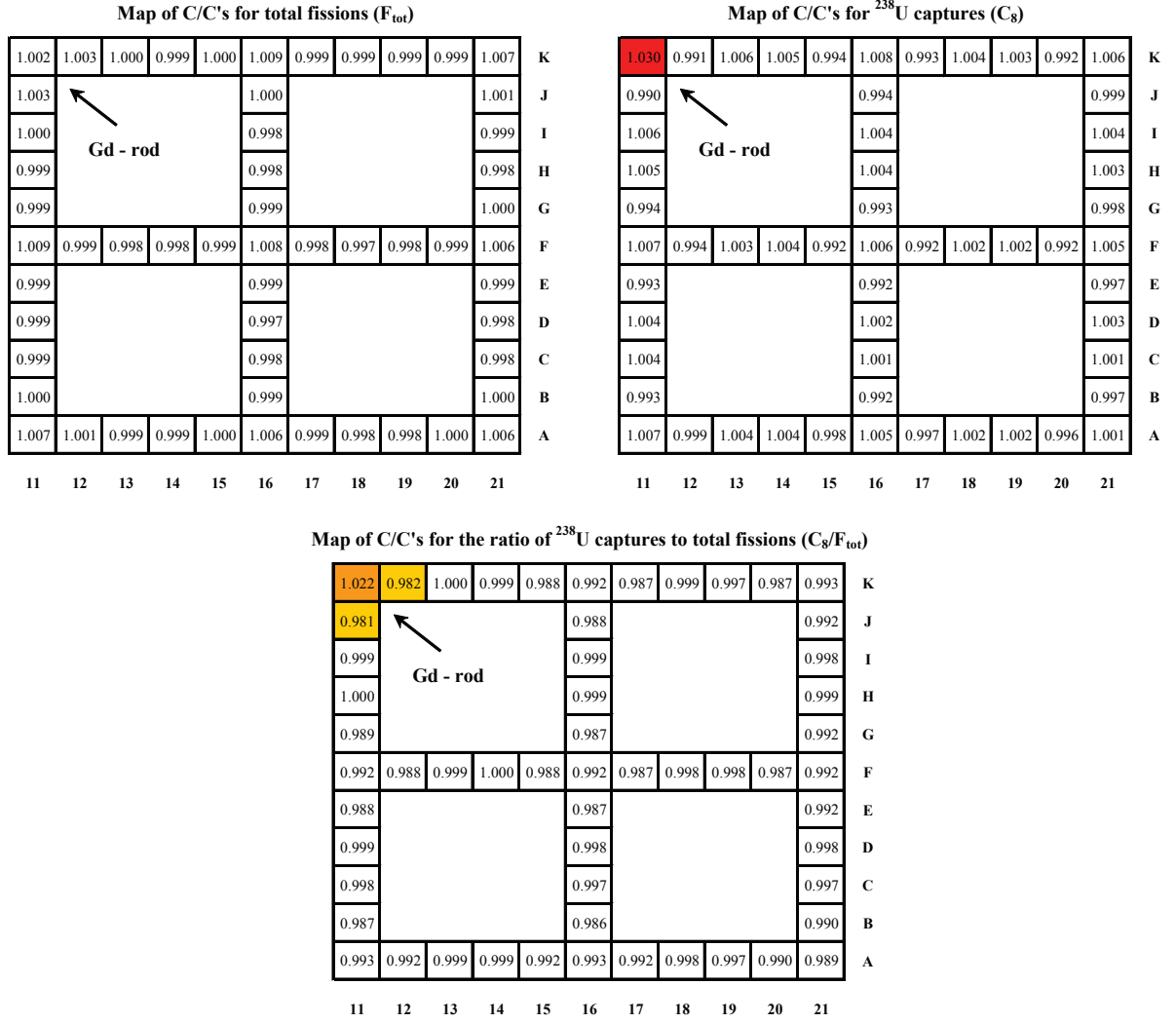


Figure 6.16: Lower right quadrant of the reduced geometry “assembly” with fuel pin K11 replaced by a Gd-poisoned fuel pin (see left hand side of Fig. 4.4): Comparison between BZ2-treated CASMO-4E (C) and MCNPX (C’) calculations of the individual reaction rates ( $F_{\text{tot}}$  and  $C_8$ ) and their ratio ( $C_8/F_{\text{tot}}$ ). The pin average C/C’ value is 1.0 for  $F_{\text{tot}}$  and  $C_8$  (due to the normalization) and 0.994 in the case of  $C_8/F_{\text{tot}}$ . Values that differ more than 1% from the pin average are highlighted in yellow (more than 2% is in orange, and more than 3% is in red).

- Further reducing the dimension of the Gd-poisoned pin had a strong worsening effect on the  $C/C'$  of  $C_8$ . When setting the radius of the Gd-containing fuel to 1 mm, the  $C/C'$  of  $F_{\text{tot}}$  started to worsen as well (1.9% for the BZ2 treated case and 1.1% for the case without the BZ2 card). This discrepancy, however, is still much smaller than the 18% overestimation of  $C_8$  by CASMO-4E for the same case. Increasing the radius of the pellet had the opposite effect and when the radius was chosen to be equal to that of the non-poisoned fuel, the discrepancy in  $C_8$  was reduced to 1.3%.

In conclusion, the  $C_8$  discrepancy for the inserted Gd-pin does not appear to come from nuclear data, nor from the available CASMO-4E input choices, but is probably due to an erroneous treatment by the code's routines of this particular test lattice configuration. Thereby, several effects seem to be contributing, one being the earlier observed, systematic overestimation of reaction rates in fuel pins at intersections of columns and rows of pins (corner pins). The important specific effect in this case seems to be the reduced size of the Gd-pin, relative to the non-poisoned fuel (pellet diameter of 8.19 mm, instead of 10.18 mm).

It should be mentioned that using the CASMO-4E default value for the lattice quadrature caused  $F_{\text{tot}}$ , as well as  $C_8$ , to be calculated wrongly in the Gd-pin. However, refining the mesh of characteristics along which the neutron transport equation is solved, eliminated the problem for  $F_{\text{tot}}$ . The number of characteristics, or rather the spacing between them, is of particular importance for fuel pins containing burnable absorbers because their macro-region is split up by CASMO-4E into 10 annular rings, each covering one tenth of the volume of the pin. The thicknesses of the outer annuli are thus quite small and, if the characteristics are spaced too far apart, it becomes possible that they are not intersected by enough characteristics. This feature is intensified by the fact that, due to the very high capture cross section of gadolinium, most of the neutron absorptions in these pins take place close to the surface. Refining the mesh of characteristics in all energy groups to a very large number, however, did not resolve the problem in the  $C_8$  rate.

The above mentioned division of the Gd-poisoned fuel region in CASMO-4E allows for a closer study of the within-pin reaction rate distribution. Fig. 6.17 shows the radial distributions for  $F_{\text{tot}}$  and  $C_8$  as calculated by CASMO-4E and MCNPX (annuli 1 and 10 are at the center and at the edge of the fuel pellet, respectively). They were both normalized such that the summation of the 10 annuli equaled the corresponding total value used for deriving the  $C/C'$  for the pin. As for the integral values, the radial distribution of the total fission rate is in good agreement. For the  $C_8$  rate, a systematic overestimation of the inner nine annuli is observed, which gets partly compensated by an underestimation of the outermost annulus.

A final answer on the origin of the discrepant  $C/C'$  value for  $C_8$  in the Gd-pin could not be found. However, it is likely that the effect is a combination of two different factors, the first being the generic CASMO-4E overprediction of reaction rates at pin row/column intersections and the second being more specific, viz. the smaller pellet diameter of the Gd-pin relative to the other fuel pins. Since the discrepancy is only observed for the  $C_8$  rate and not for the  $F_{\text{tot}}$

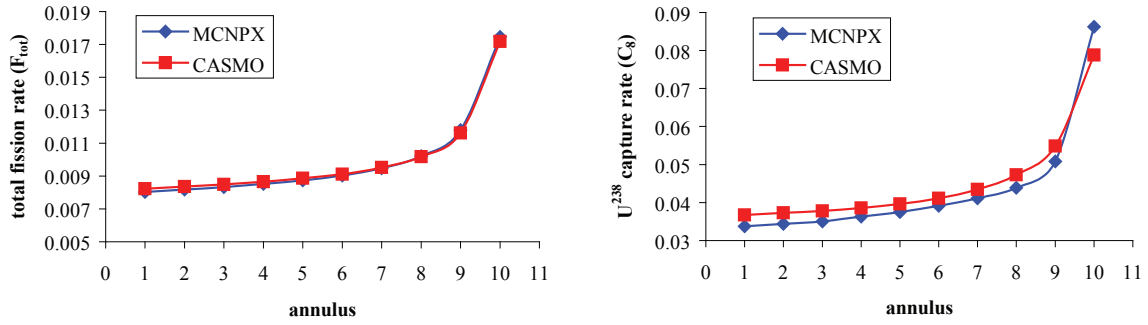


Figure 6.17: Radial distribution of  $F_{tot}$  (left hand side) and  $C_8$  (right hand side) within the gadolinium-poisoned fuel pin as calculated by CASMO-4E and MCNPX. On the X-axis, the annulus number is indicated, starting from the center of the pin. The annuli all have the same volume.

rate, the problem can be assumed to lie in the epithermal energy region. A likely origin of the discrepancy could thus be the CASMO-4E resonance treatment of the Gd-poisoned fuel pin in this particular test lattice.

## 6.4 Chapter Summary

In the present chapter, the validation of MCNPX and CASMO-4E, based on pin-wise reaction rate (and ratio) distributions, has been carried out for perturbed SCWR-like test lattices. As in the case of the reference unperturbed configuration, a two-step validation approach has been employed, the steps being the direct comparison of the measured values to whole-reactor MCNPX calculations, followed by a code-to-code comparison of reduced geometry calculations. The six investigated perturbations have been arranged in three groups, according to their neutronics effects on the test lattice.

The first group of perturbations has been related to control rod effects. Four aluminum and four steel rods were inserted, in two different configurations, into the four central moderator channels of the SCWR-like test lattice. Moderator displacement and absorption effects could thus be studied separately. In each case, the agreement for the distributions of  $F_{tot}$  and  $C_8$ , as well as of their ratio,  $C_8/F_{tot}$ , between experiment and whole-reactor MCNPX calculations, has been found to be within the combined uncertainties (the  $1\sigma$ -level being 0.4%, 0.8%, and 2.2%, respectively). The comparison between reduced geometry calculations with CASMO-4E and MCNPX yielded diverse results. While the pin-wise reaction rates for the steel rod case agreed within 1%, the aluminum rod case showed discrepancies of up to 2.6% in individual fuel pins. These were identified as being due to an erroneous treatment of the neutron leakage with the standard CASMO-4E input. Employing the optional input card BZ2, with which a region-wise, rather than an average, leakage correction is applied, has resolved these discrepancies such that the codes once again agree within 1%.

Moderation density variations have been investigated in the second group of perturbations. Water tanks were filled with two different mixtures of  $\text{H}_2\text{O}$  and  $\text{D}_2\text{O}$ , simulating different water densities. These were inserted, in two separate configurations, into the four central moderator channels of the test lattice. As before, the MCNPX whole-reactor calculations have shown excellent agreement with the experimentally derived results. The code-to-code comparison, however, yielded discrepancies of up to 4.6% for some individual fuel pin reaction rates, which could be reduced to 1.8% by employing the BZ2 card in CASMO-4E. This maximal value has been found to occur at the intersection of rows and columns of fuel pins, the cause being a combination of the slight overprediction of these fuel pins in the unperturbed lattice and a residual error in the leakage treatment.

The last group of perturbations investigated correspond to the removal of the central fuel pin and its subsequent replacement with gadolinium-poisoned fuel. Once again, the MCNPX whole-reactor calculations have been found to agree with the experiments well within uncertainties. In the case of the code-to-code comparisons, CASMO-4E and MCNPX agree equally well for the removed pin configuration as for the unperturbed reference lattice, which is to be expected, considering the relatively minor perturbation caused by the removal of a single fuel pin. Inserting a gadolinium-poisoned fuel pin, however, significantly changed the neutron flux. While the total fission rate in the Gd-pin is calculated correctly by CASMO-4E, the  $C_8$  rate has been found to be overestimated by about 3%. The origin of this overestimation has been narrowed down to a likely shortcoming in the CASMO-4E treatment of the specific experimental setup (a smaller-diameter Gd-pin at the center of the SCWR-like lattice).



# Bibliography

- [1] D. Rätz, K.A. Jordan, G. Perret, and R. Chawla. Experimental Validation of Control Rod Related Perturbations of Moderator Regions in an SCWR-like Fuel Lattice. *Annals of Nuclear Energy*, 38:2319–2332, 2011.
- [2] A. Yamaji, Y. Oka, and S. Koshizuka. Three-dimensional Core Design of High Temperature Supercritical-Pressure Light Water Reactor with Neutronic and Thermal-Hydraulic Coupling. *Journal of Nuclear Science and Technology*, 42(1):8–19, 2005.
- [3] K. Kamei, A. Yamaji, Y. Ishiwatari, Y. Oka, and J. Liu. Fuel and Core Design of Super Light Water Reactor with Low Leakage Fuel Loading Pattern. *Journal of Nuclear Science and Technology*, 43(2):129–139, 2006.
- [4] U.C. Bergmann, P. Grimm, F. Jatuff, and M.F. Murphy. Investigations of  $^{238}\text{U}$  Captures to Total Fissions in a Westinghouse SVEA-96+ Assembly. *Nuclear Science and Engineering*, 156:86–95, 2007.
- [5] G. Perret, M.F. Murphy, M. Plaschy, F. Jatuff, and R. Chawla. Modified conversion ratio measurements in a SVEA-96 Optima2 BWR assembly compared with MCNPX predictions. In *First International Conference on Physics and Technology of Reactors and Applications (PHYTRA1)*, Marrakech, Morocco, March 14-16, 2007.
- [6] G. Perret, M. Plaschy, M.F. Murphy, F. Jatuff, and R. Chawla. Characterisation of Radial Reaction Rate Distributions Across the 92-Pin Section of a SVEA-96 Optima2 Assembly. *Annals of Nuclear Energy*, 35:478–484, 2008.
- [7] M.F. Murphy, F. Jatuff, G. Perret, M. Plaschy, U. Bergmann, and R. Chawla. Comparison of 3D Reaction Rate Distributions Measured in an Optima2 BWR Assembly with MCNPX Predictions. *Annals of Nuclear Energy*, 35:2042–2050, 2008.
- [8] G. Leinweber, D.P. Barry, M.J. Trbovich, J.A. Burke, N.J. Drindak, H.D. Knox, and R.V. Ballad. Neutron Capture and Total Cross-Section Measurements and Resonance Parameters of Gadolinium. *Nuclear Science and Engineering*, 154:261–279, 2006.
- [9] G. Perret, M.F. Murphy, F. Jatuff, J.C. Sublet, O. Bouland, and R. Chawla. Impact of New

- Gadolinium Cross Sections on Reaction Rate Distributions in 10 x 10 BWR Assemblies. *Nuclear Science and Engineering*, 163:17–25, 2009.
- [10] A. Koning, R. Forrest, M. Kellett, R. Mills, H. Henriksson, and Y. Rugama. The JEFF-3.1 Nuclear Data Library. Technical Report JEFF Report 21, 2006.
- [11] M.B. Chadwick. ENDF/B-VII.0: Next Generation Evaluated Nuclear Data Library for Nuclear Science and Technology. Technical Report Nucl. Data Sheets, 102, 2931, 2006.
- [12] A. Santamarina, D. Bernard, and Y. Rugama. The JEFF-3.1.1 Nuclear Data Library. Technical Report JEFF Report 22, 2009.

## 7 Reactivity Effects

The previous two chapters have been dedicated to the validation of CASMO-4E and MCNPX via the comparison of measured and calculated pin-wise reaction rate distributions across the SCWR-like test lattice under a variety of conditions. It has been seen how, in each case, this type of integral data accurately represents the specific SCWR-related neutronics effects under study. Thus, the distributions of  $F_{\text{tot}}$  and  $C_8$  as also of the ratio  $C_8/F_{\text{tot}}$ , have served as valuable checks on the codes' abilities to model the spectral variations between the individual fuel pins in the various SCWR-like situations simulated.

The present chapter investigates the use of reactivity based information from the PROTEUS experiments to provide a further validation basis for CASMO-4E and MCNPX. Clearly, the criticality, i.e.  $k_{\text{eff}}$ , of the complete multi-zone PROTEUS reactor can reflect the neutronics of the test zone only in an indirect manner. This follows from the fact that the PROTEUS  $k_{\text{eff}}$  value also depends on the nature of the coupling between the test zone and the outer reactor regions (buffer, driver, etc.). The situation is different for the case of reactivity effect ratios, if the effects studied are perturbations affected only in the central region of the test zone [1]. In this case, the coupling between the test zone and the outer PROTEUS reactor regions can be assumed to remain largely unchanged, such that the ratio of two different reactivity changes of this type can be viewed as an item of integral data truly representative of the test lattice under study.

This chapter is split up into two main sections. In Sec. 7.1, measured and calculated reactivity effects due to the removal of single fuel pins from the central part of the unperturbed SCWR-like lattice are studied. For the values calculated using the reduced geometry model with CASMO-4E and MCNPX, the origin of the reactivity change is investigated in each case via its decomposition into contributions from individual neutron balance changes. Sec. 7.2 addresses the more challenging task of interpreting changes in the PROTEUS  $k_{\text{eff}}$  value as function of the different test zone configurations studied in this thesis. Here, the consideration of changes in the coupling between test zone and outer reactor regions is clearly much more important.

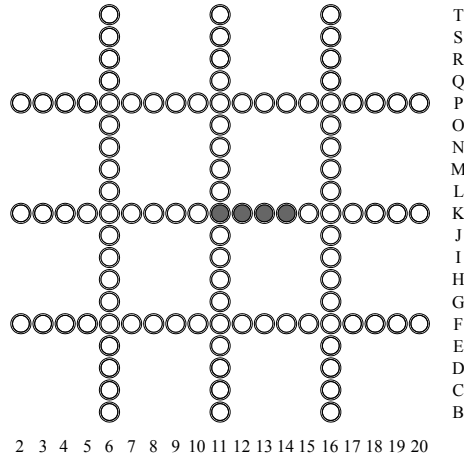


Figure 7.1: The unperturbed SCWR-like lattice as implemented in the test zone of PROTEUS. The dark shaded areas indicate fuel pins that were measured (one at a time) during the pin-removal worth experiments.

## 7.1 Pin Removal Worths in the Unperturbed Configuration

As indicated above, measuring the reactivity change induced by the removal of a fuel pin from the central part of a test lattice is an integral experiment, which is well suited for code validation. In the case of the SCWR-like lattice, when a fuel pin is removed, the area is filled with moderator. The removal of a fuel pin and its substitution with moderator have competing effects on the reactivity of the system. On one hand, removing fissile material eliminates fissions in the channel where the fuel pin was located and lowers the reactivity. On the other hand, the introduction of moderator at this particular location improves the neutron moderation locally. Therefore, the neighboring fuel pins, which were previously undermoderated, see more thermal neutrons, and this results in an increase in their fission rate and hence, of the reactivity. These two effects can be of similar magnitude, which challenges the computer codes since they must predict a small net effect.

The unperturbed SCWR-like test lattice in PROTEUS is symmetrical. If one ignores boundary effects, there are only three generic fuel pin positions in the lattice. These are the corner pins (at intersections of rows and columns of fuel pins), the neighbors (of the corner pins), and the remotes (which are not neighboring a corner pin). Therefore, it was sufficient to measure the pin worth of just three fuel pins (see Fig. 7.1). The selected pins were as close to the center of the test zone as possible, in order to minimize the effect of the outer PROTEUS reactor regions. This selection had also the advantage to limit the bias induced by the reflective radial boundary of the reduced geometry calculations. Therefore, the corner pin K11, the neighboring pin K12, and the remote pin K13 were measured. Pin K14, which is similar to K13, was also measured in order to investigate the degree of independence with respect to the PROTEUS outer zones.

### 7.1.1 Measurements and Calculations

The measurement of pin reactivity worths in PROTEUS is usually conducted employing a compensation technique, where the operator compensates the change of reactivity (induced by the withdrawal or the re-introduction of the fuel pin) with control rods. These control rods are calibrated in advance and their movements are recorded for later analysis. More details on the compensation technique employed at PROTEUS are given in Section 3.3.1.

To assess the fuel pin worths with the whole-reactor model of MCNPX, the input was changed accordingly. Due to the large size of the whole-reactor model, it took substantial computing resources to obtain accurate estimates for  $k_{\text{eff}}$ . Each calculation was performed on a computer cluster with almost 500 CPU's and took 24 hours to accomplish. The  $1\sigma$  uncertainty that could be achieved in these computations was 2 pcm, corresponding to 0.002%, which is close to the lower limit of accuracy (0.001% or 1 pcm) with which MCNPX calculations can predict tallied parameters and  $k_{\text{eff}}$ .

The procedure to obtain the reactivity worths in the reduced geometry model of MCNPX was similar. There was one important difference, however: the two-dimensional input was not generally a critical system, yielding a  $k_{\text{eff}}$  value of one. Reactivity effects have to be measured in a critical system, which is why one is forced to adjust the model until  $k_{\text{eff}} = 1$ . In MCNPX, this is done by ensuring radial reflection boundaries and adjusting the axial height of the model. Unfortunately, there is no routine to determine this height. It needs to be found via trial and error. Accordingly, a calculation was performed with an initial guess to estimate  $k_{\text{eff}}$ . If the obtained  $k_{\text{eff}}$  was below 1, the system height was increased in order to reduce the buckling, which decreased the leakage of the system and increased the reactivity. If  $k_{\text{eff}}$  was greater than one, the system height was reduced and the reactivity lowered. This process was rather time consuming, since between every iteration a  $k_{\text{eff}}$  estimate with small uncertainty had to be calculated. Due to the large  $k_{\infty}$  of the system (in the order of 1.4 to 1.5), the leakage term had to be large in order to get  $k_{\text{eff}} = 1$ , so that the system height was quite small. In fact, the total height of the critical system was only about 30 cm while it was infinitely large in the radial direction, so that one can effectively speak in terms of a “pancake” model.

After the critical height of the unperturbed configuration (i.e. with no fuel pins removed) had been found, the final pin-removal worth calculations were performed. The height of the system was kept constant, so that the reactivity worth of the removed fuel pin could be calculated by subtracting  $k_{\text{eff}}$  of the perturbed configuration from  $k_{\text{eff}}$  of the unperturbed configuration.

The reduced geometry model with CASMO-4E was very similar to that of MCNPX. However, one did not specify a system height. CASMO-4E achieves a critical system, i.e.  $k_{\text{eff}} = 1$ , via a critical buckling search. This is equivalent to setting the height in MCNPX, since here too, the leakage is used to lower the overall system reactivity. Once the critical buckling was found for the unperturbed assembly, the same buckling value was inserted into the inputs for the perturbed configurations. This forced CASMO-4E to use this buckling and to deduce a  $k_{\text{eff}}$  which was not

equal to one. Once again, the reactivity worth of the removed fuel pin was calculated from the difference between the  $k_{\text{eff}}$ 's of the perturbed and unperturbed calculations.

### 7.1.2 Results

The results of the experiments and the calculations are summarized in Table. 7.1. Shown are the pin removal worths for the investigated lattice locations which, in each case, equals the change in  $k_{\text{eff}}$  of the entire system. This change,  $\Delta\rho$ , is given in pcm (percent millirho,  $1 \text{ pcm} = 1 \cdot 10^{-5} \rho$ ) along with the  $1\sigma$ -uncertainty (also in pcm). Focusing on the experimental values provides insight into the peculiarities of this SCWR-like test lattice (configuration III.4, to use the LWR-PROTEUS configuration numbering). The reactivity in the case of the unperturbed SCWR-like test lattice has been taken as reference, from which the reactivities of the perturbed configurations are subtracted. Therefore, the first experimental value in the table,  $\Delta\rho$  for configuration III.4, is zero. The other cases are the changes in reactivity when removing fuel pin K11, K12, K13, and K14, respectively.

#### 7.1.2.1 Experimental Values

As described in Subsec. 3.3.1, the effect of removing individual fuel pins on the system reactivity has been measured using the compensation technique [2, 3]. Reactivity changes in the test zone of PROTEUS are compensated by the control mechanisms of the reactor. In order to relate the movement of these control mechanisms to absolute reactivity changes, other techniques need to be used to calibrate the control rods (stable period technique or inverse kinetics technique). These techniques, which require a calculated value for the delayed neutron fraction  $\beta_{\text{eff}}$ , are described in more detail elsewhere [4, 5].

The largest source of uncertainty is the systematic error on the nuclear data used for calculating  $\beta_{\text{eff}}$ , which is in the order of 3.7% [3]. Other uncertainties on the measurement come from counting statistics (0.5%) and from the inter-calibration between control rods and autorod (see Subsection 3.3.1), which also contributes to approximately 0.5% [3]. The non-linearity correction for the autorod is a third systematic uncertainty, but this is only about 0.2% and thus of little importance. The total uncertainty on a measured reactivity worth is about 4%. When taking the ratio of reactivity effects, however, the systematic uncertainties cancel out and the total uncertainty is only about 0.5%.

When removing fuel pin K11, the net effect on the reactivity is 19.9 pcm. This is a positive  $\Delta\rho$ , i.e. the reactivity of the system with the pin removed is larger than with the pin inserted. One has the unusual situation of being able to increase reactivity by removing fuel. In this case, the enhanced moderation and the increased fission rate of the neighboring fuel pins overcompensate for the fission rate in the withdrawn fuel pin. This is possible due to the strong undermoderation of the corner pins.

Table 7.1: Measured and calculated values of pin-removal reactivity worths in the central part of the unperturbed SCWR-like test lattice.

Case	Experiment		MCNPX whole reactor model		MCNPX reduced geometry model		CASMO reduced geometry model		CASMO - MCNPX	
	$\Delta\rho$ [pcm]	$1\sigma$ [pcm]	$\Delta\rho$ [pcm]	$1\sigma$ [pcm]	$\Delta\rho$ [pcm]	$1\sigma$ [pcm]	$\Delta\rho$ [pcm]	$1\sigma$ [pcm]	$\Delta\Delta\rho$ [pcm]	$\Delta\Delta\rho$ [ $\sigma$ 's]
<b>III.4</b>	0		0		0		0			
<b>III.4-K11</b>	19.9	0.8	17	3	28	3	34.9	-	7	2.4
<b>III.4-K12</b>	-7.2	0.3	-11	3	-14	3	-4.0	-	10	3.5
<b>III.4-K13</b>	-38.2	1.5	-37	3	-49	3	-39.0	-	10	3.5
<b>III.4-K14</b>	-38.4	1.5	-41	3	-51	3	-38.8	-	12	4.3

The removal of pin K12 leads to a negative reactivity effect. However, at  $-7.2$  pcm, which corresponds to less than one cent, the net effect is rather small; the two competing effects are similar in magnitude and nearly cancel out. From the excellent agreement between the  $\Delta\rho$ -values for the removals of fuel pins K13 and K14, one can observe that the outer PROTEUS zone effects are relatively insignificant in the central region of the test zone.

#### 7.1.2.2 MCNPX Whole-Reactor Calculations

The second set of numbers in Table 7.1 gives the pin removal worths and their statistical uncertainties, as calculated using the MCNPX whole-reactor model of PROTEUS. Within the stated uncertainties, the calculated values agree well with the experimental results. The largest discrepancy - slightly more than  $1\sigma$  - occurs for the case where pin K12 was removed. The relatively large uncertainties on the MCNPX calculations (compared to the experimental uncertainties) are due to the lower limit on the accuracy of an MCNPX tallied parameter and the consistent propagation thereof. One can conclude, from the comparison made in Table 7.1, that MCNPX is validated for the calculation of pin removal worths in the present unperturbed SCWR-like fuel lattice, to the extent of the achievable statistical accuracy.

#### 7.1.2.3 Reduced Geometry Calculations

As in the case of the reaction rate distributions, a direct comparison with the experimental results is not possible for CASMO-4E. Resort has accordingly been made to the use of the reduced geometry model (see Sec. 4.2). It clearly needs to be borne in mind that the relative importance of the removed fuel pin is different in the reduced geometry model than in the real experiment. Due to the reflective boundary conditions along the X- and Y-axes, removing a fuel pin in the modeled assembly automatically removes a fuel pin in each of the surrounding assemblies as well. Furthermore, the multi-zone nature of the PROTEUS reactor, with the outer regions “driving” the test zone critical, is completely absent in the reduced geometry model. Therefore, the reduced geometry worths and the experimentally obtained worths can not be

Table 7.2: CASMO-4E and MCNPX reactivity worth predictions for the removal of a fuel pin and its replacement with void. The reduced geometry model has been used in each case.

Case	MCNPX reduced geometry model		CASMO reduced geometry model		CASMO - MCNPX	
	$\Delta\rho$ [pcm]	$1\sigma$ [pcm]	$\Delta\rho$ [pcm]	$1\sigma$ [pcm]	$\Delta\Delta\rho$ [pcm]	$\Delta\Delta\rho$ [ $\sigma$ 's]
<b>III.4</b>	0		0			
<b>III.4-K11</b>	-86	3	-84.9	-	1	0.4
<b>III.4-K12</b>	-114	3	-109.8	-	4	1.4
<b>III.4-K13</b>	-153	3	-140.0	-	13	4.3
<b>III.4-K14</b>	-151	3	-140.0	-	11	3.7

expected to be the same.

When comparing the  $\Delta\rho$ -values obtained from the whole-reactor model and the reduced geometry model of MCNPX, the worths are generally larger (positive and negative) in the reduced geometry case (see Table 7.1). This corresponds to the fact that the relative importance of the SCWR-like test lattice - from the  $k_{\text{eff}}$  viewpoint - is higher in the reduced geometry model. Due to symmetry and reflective boundary conditions in this case, every SCWR-like fuel assembly has the same relative importance, and the radial net leakage is zero. In the whole-reactor model - as in reality - the PROTEUS test zone is subcritical on its own, and there is a net current of neutrons directed towards it from the outer driver / buffer regions. The SCWR-like test lattice, as such, contributes considerably less to the  $k_{\text{eff}}$  of the complete system. This basic characteristic of the driven system is clearly reflected in its smaller pin removal worths.

Again as in the case of reaction rate distributions, the CASMO-4E pin removal worths from usage of the reduced geometry model may be “validated” via comparison with the corresponding MCNPX results. This is done in Table 7.1 with the data block on the right showing the differences in fuel pin worth predictions between MCNPX and CASMO-4E, in units of pcm and of standard deviations ( $\sigma$ ). It is seen that there are notable discrepancies between the two codes, on the order of 7 – 12 pcm (or 2.4 – 4.3  $\sigma$ ). CASMO-4E systematically calculates the net effects of the pin removals as less negative (more positive in the case of K11). The discrepancies are in the order of 20% of the net effect, which seems rather high. However, one needs to remember that the net effect is the sum of two competing effects, viz. increased moderation and the removal of fissile material.

To give an idea on the magnitude of these effects, Table 7.2 shows the calculated change in reactivity of the system if the fuel pin is replaced by void, which does not improve neutron moderation. The difference between the net effect and the isolated fissile material effect is seen to be approximately 100 pcm for cases K12 - K14 and about 120 pcm for case K11 (reflecting the stronger undermoderation of this fuel pin). This difference, to first order, corresponds to the positive reactivity effect of the locally enhanced moderation which overcompensates (case K11), almost zeros out (case K12), or partly compensates (cases K13 and K14) the negative effect



Table 7.3: Measured and calculated fuel pin reactivity worth ratios.

Ratio	Experiment		MCNPX whole reactor model		MCNPX reduced geometry model		CASMO reduced geometry model	
	$\Delta\rho$ [pcm]	$1\sigma$ [pcm]	$\Delta\rho$ [pcm]	$1\sigma$ [pcm]	$\Delta\rho$ [pcm]	$1\sigma$ [pcm]	$\Delta\rho$ [pcm]	$1\sigma$ [pcm]
<b>ave(K13,K14)</b>	-38.3	0.2	-39	2	-50	2	-38.9	-
<b>K11/ave(K13,K14)</b>	-0.52	0.01	-0.44	0.08	-0.56	0.06	-0.90	-
<b>K12/ave(K13,K14)</b>	0.19	0.01	0.28	0.07	0.28	0.06	0.10	-

of removing fissile material. When comparing the CASMO-4E and MCNPX differences in  $\Delta\rho$ , for the net effect and for the isolated effect of removing fissile material, one observes that the discrepancies between the codes remain almost unchanged for cases K13 and K14. On the other hand, the discrepancies seem to disappear almost completely when one looks at the isolated effect for cases K11 and K12. Although one needs to keep the MCNPX statistical uncertainties in mind, it does seem that the CASMO-4E modeling deficiencies for the more strongly undermoderated fuel pin positions are linked to calculation of the additional moderator effect.

#### 7.1.2.4 Comparison of Reactivity Worth Ratios

As discussed earlier, pin removal worths as calculated in the reduced geometry model can not be compared directly to the experimentally obtained values. Besides employing the validation strategy of comparing CASMO-4E against MCNPX on reduced-geometry basis, there is another approach possible in the case of reactivity worths measured in the central part of the test zone. This follows from the fact that, when taking a ratio between two pin worths, the first-order outer zone effects of PROTEUS cancel out. The experimentally determined ratios of pin removal worths are thus, to a good approximation, characteristics of the SCWR-like test lattice. As such, their calculation should be relatively independent of the modeling, and a direct comparison of the measured ratios becomes justified, not only with a whole-reactor model, but with reduced geometry models as well.

A disadvantage of this approach is that one loses a data point, since one fuel pin worth has to be selected as reference, to serve as denominator for the other worths. This is of particular importance in the present test lattice, since there are only three generic fuel pin positions, which results in only two ratios that can be compared. Table 7.3 summarizes the results of this comparison. The average of the pin worth of the symmetric lattice positions K13 and K14 was chosen as denominator for forming the ratios. This reduced the uncertainty on the final results, since the statistical uncertainty on the average is  $\sqrt{2}$  times less than that for a single value. This average is shown in the line “ave(K13,K14)” of Table 7.3, for the experiments as well as for the three computational models. The reactivity ratios of K11 and K12, with respect to “ave(K13,K14)”, are given in the last two lines, respectively.

The comparison of the experiments to the MCNPX whole-reactor model confirms the good agreement, which was observed earlier for the individual pin worths. Unfortunately, the uncertainties on the ratios are quite large for the MCNPX calculation. They result from the consequent propagation of the uncertainties on the tallied  $k_{\text{eff}}$  values (which have been minimized to the achievable limit in MCNPX). The comparison between the reduced geometry model of MCNPX and the experiments also shows agreement within the stated uncertainties. This confirms the earlier statement that the reactivity worth ratios are, to a good approximation, characteristics of the SCWR-like test lattice and, as such, relatively independent of the modeling.

Comparing the experimental ratios to those obtained using the CASMO-4E reduced geometry model, one sees some clear discrepancies. The effect of withdrawing the fuel pin K11 (compared to the effect of removing K13 or K14) is strongly overestimated by CASMO-4E. On the other hand, the effect of removing K12 is underestimated (it needs to be kept in mind, however, that the net effect of removing K12 is close to zero, which makes the ratio considered here quite sensitive).

### 7.1.3 Decomposition of Reactivity Effects

The previous subsection has shown notable discrepancies between the pin removal worths predicted with the reduced geometry models of CASMO-4E and MCNPX. In order to identify the sources of these discrepancies, a decomposition of the reactivity effects in the reduced geometry model has been made for both codes. This subsection presents the chosen approach and the analysis conducted.

The applied reactivity decomposition methodology [1, 6] was developed at PSI to allow the breakdown of a given reactivity effect into individual contributions in terms of space, energy and process (e.g. absorption, leakage, production ...). This technique, which was applied in the context of pin removal experiments conducted on heterogeneous BWR fuel assemblies in the LWR-PROTEUS Phase I program, is essentially based on the consideration of detailed neutron balances drawn up for the unperturbed and perturbed system. Although, as such, different in approach from perturbation theory based methods, which have also been applied in the past at PROTEUS (e.g. [7]), the currently applied methodology does represent an extension in the degree of detail possible for the reactivity decomposition in a relatively small system such as a single fuel assembly.

Because the investigation of individual fuel pin removals from the SCWR-like “assembly” of the reduced geometry model is of primary interest currently, the reactivity decomposition has been carried out in terms of process type and space variable. Energy dependence of the neutron balance was not studied, i.e. the analysis was performed in a single energy group.

The individual processes that have been tracked in each pin cell are the standard ones, viz. neutron absorptions, captures, fissions, productions, and leakage. As indicated above, it is

possible to study all these processes because of the small number of cases which have to be calculated (only four fuel pins were removed) and the relatively simple geometry of the model (only a single assembly needs to be represented in the reduced geometry model). In addition, the fission source (FSC), was studied; this is defined as

$$\text{FSC} = \frac{\text{RIF} \cdot \nu \cdot \Sigma_f}{k_{\text{eff}}} = \frac{\text{neutron productions}}{k_{\text{eff}}}, \quad (7.1)$$

where RIF stands for region integrated flux and  $\Sigma_f$  is the macroscopic fission cross section.

In order to enable a consistent comparison between the decomposition of CASMO-4E and MCNPX results, the corresponding neutron balances had to be normalized appropriately. For this, the neutron production over all pin cells -  $\sum \text{fissions}(i) \cdot \bar{\nu}(i)$  - is kept constant for the unperturbed and perturbed cases. Because of this normalization, the fission source FSC summed over all regions of the system is proportional to the inverse of the multiplication factor  $k_{\text{eff}}$ . Hence, the comparison of the integrated fission sources between the unperturbed and perturbed configuration (in either code) will give the net reactivity effect of removing the fuel pin. By choosing the total neutron production to be normalized to 100'000, the net reactivity effect will be expressed in percent mille (pcm). Finally, subtracting the net reactivity effects predicted by CASMO-4E and MCNPX yields the discrepancy in  $\Delta\rho$  between the two codes.

### 7.1.3.1 Pin-Wise Decomposition

Fig. 7.2 illustrates the pin-wise contributions of the fission source predicted with MCNPX for the unperturbed (top) and perturbed (middle) configurations, and their differences (bottom). The fission sources are calculated according to Eq. 7.1 and both calculations are normalized to 100'000 produced neutrons. In this example, the fuel pin at the center of the assembly (position K11, i.e. a corner pin) was removed, which is reflected by the fission source in the perturbed configuration at position K11 being zero.

With the chosen normalization, the pin-wise distribution of the fission source differences between the perturbed and the unperturbed system (shown at the bottom of Fig. 7.2) clearly represents the spatial decomposition of the pin removal worth. While the local FSC is seen to be strongly reduced in the removed pin cell, it is increased in the neighboring positions. In fact, the net effect on the fission source of K11 and the 12 fuel pins closest to it is positive. By looking at the color pattern, one can see that the pins in the central part of the assembly see a strong positive effect, while those at the periphery see a small negative effect. As to be expected, the relative importance of the central zone of the assembly is much higher.

The same analysis procedure has been applied to the results of the CASMO-4E reduced geometry calculations and, as a last step, the differences between the pin-wise fission source distributions from the two codes have been taken. This yields the pin-wise decomposition of the discrepancy in

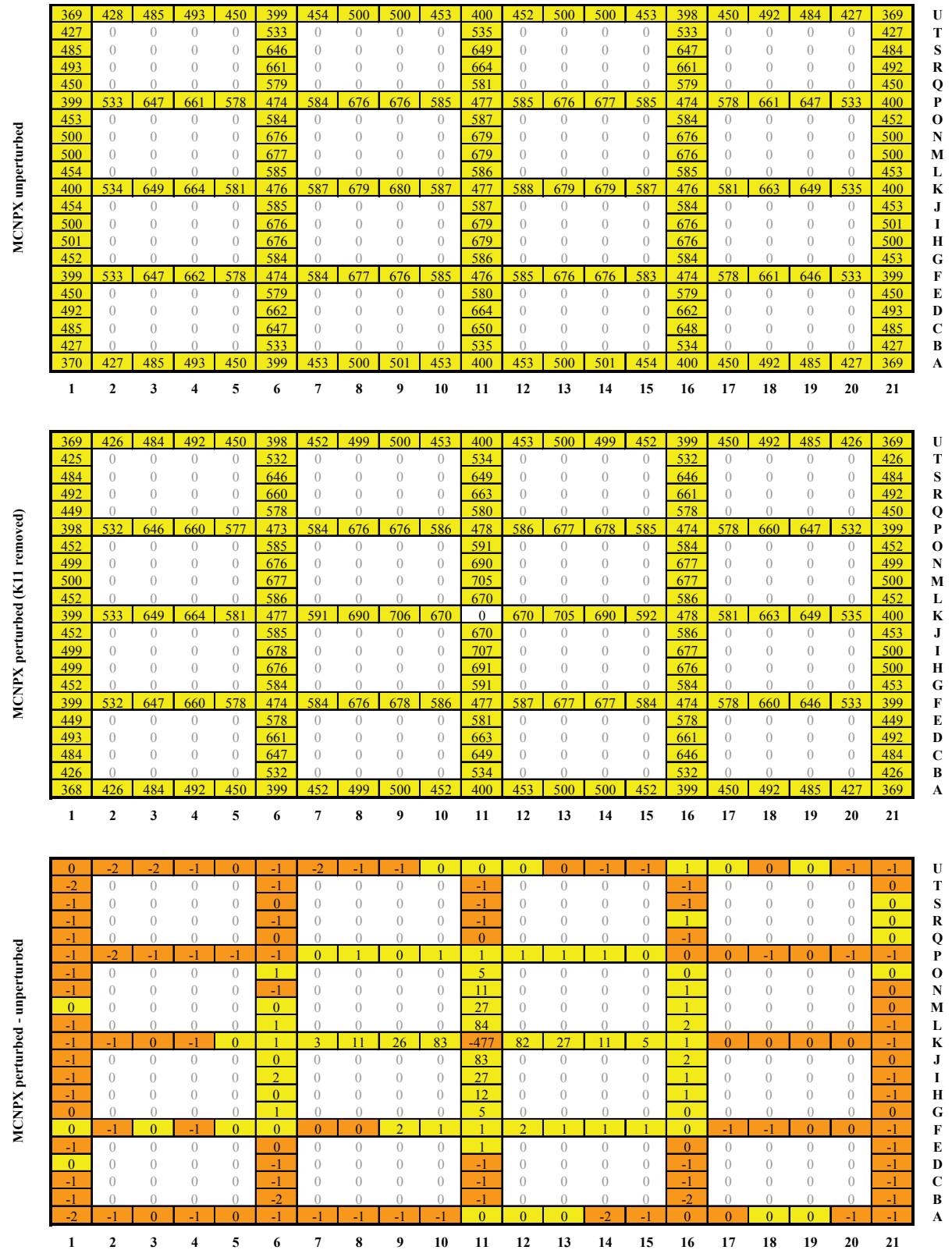


Figure 7.2: Pin-wise fission source distributions predicted with MCNPX for the unperturbed and the perturbed configuration where the pin K11 was removed. Yellow colored cells indicate a positive value, orange colored cells indicate a negative value.

0	1	1	0	0	1	1	0	0	-1	-1	-1	0	0	1	-1	-1	-1	-1	0	0	U
1	0	0	0	0	0	0	0	0	0	1	0	0	0	0	0	0	0	0	0	0	T
1	0	0	0	0	0	0	0	0	0	0	0	0	0	0	0	0	0	0	0	0	S
0	0	0	0	0	0	0	0	0	0	1	0	0	0	0	0	-1	0	0	0	0	R
0	0	0	0	0	0	0	0	0	0	0	0	0	0	0	0	0	0	0	0	0	Q
0	1	1	0	1	1	0	0	1	0	0	0	0	0	0	0	0	0	1	0	0	P
0	0	0	0	0	-1	0	0	0	0	-1	0	0	0	0	0	0	0	0	0	0	O
0	0	0	0	0	1	0	0	0	0	0	0	0	0	0	-1	0	0	0	0	0	N
-1	0	0	0	0	1	0	0	0	0	0	0	0	0	0	0	0	0	0	0	0	M
1	0	0	0	0	0	0	0	0	0	-2	0	0	0	0	-1	0	0	0	0	0	L
0	1	-1	0	0	0	1	-1	0	-1	-3	0	0	0	-1	0	0	0	0	0	0	K
1	0	0	0	0	1	0	0	0	0	-1	0	0	0	0	-1	0	0	0	0	0	J
0	0	0	0	0	-1	0	0	0	0	-1	0	0	0	0	0	0	0	0	0	0	I
1	0	0	0	0	0	0	0	0	0	-1	0	0	0	0	0	0	0	0	0	0	H
0	0	0	0	0	-1	0	0	0	0	-1	0	0	0	0	0	0	0	0	0	0	G
-1	0	-1	1	-1	-1	0	1	-1	0	0	-1	0	-1	-1	-1	0	0	-1	-1	0	F
0	0	0	0	0	0	0	0	0	0	-1	0	0	0	0	0	0	0	0	0	0	E
-1	0	0	0	0	0	0	0	0	0	1	0	0	0	0	0	0	0	0	0	1	D
0	0	0	0	0	0	0	0	0	0	0	0	0	0	0	1	0	0	0	0	0	C
1	0	0	0	0	1	0	0	0	0	1	0	0	0	0	1	0	0	0	0	0	B
1	1	0	0	0	0	1	1	1	1	0	-1	-1	1	1	0	0	-1	-1	0	0	A
1	2	3	4	5	6	7	8	9	10	11	12	13	14	15	16	17	18	19	20	21	

Figure 7.3: Discrepancies between CASMO-4E and MCNPX for the pin-wise decomposition of the reactivity effect of removing pin K11. Yellow colored cells indicate a positive value, orange colored cell indicate a negative value.

the predicted reactivity change. Fig. 7.3 shows this pin-wise decomposition for the removal of pin K11. Most of the pin cells are seen to either agree or to show a difference of just 1 neutron. The largest discrepancy is in the removed pin itself which is due to the difference in the fission source of the unperturbed configurations. The sum over all pin cells yields the observed difference in the total reactivity effect predictions of CASMO-4E and MCNPX, viz.  $-7 pcm$ , the value indicated previously in the second-to-last column of Table 7.1. Apart from that, there is no trend visible in the pin-wise decomposition. The color pattern is random and completely explained by the statistical uncertainties of the MCNPX results. The uncertainty propagation yields an absolute error of  $\pm 1$  neutron on each individual value in Fig. 7.3.

The spatial decomposition of the reactivity effects for the removal of fuel pins K12 and K13 has been analyzed analogously. The pin-wise contributions to the fission source differences between CASMO-4E and MCNPX are shown in Fig. 7.4 and 7.5, respectively. Once again, the local discrepancies are small and within the statistical uncertainty of MCNPX.

### 7.1.3.2 Decomposition in Terms of Pin Types

The pin-wise decomposition of the reactivity effects has not led to an explanation of the observed discrepancies between CASMO-4E and MCNPX. The distribution of positive and negative contributions appears to be arbitrary. This is due to the statistical nature of the uncertainties of MCNPX. The systematic discrepancies between the codes are too small to be resolved with this approach. Therefore, another attempt has been made by grouping similar fuel pins together. For each generic pin position, a group has been formed. Additionally, a group containing all the water regions (including the water gap between assemblies) has been considered. Fig. 7.6

-1	1	0	0	0	1	2	0	0	0	-1	-1	0	0	0	-1	0	0	-1	0	0	U
1	0	0	0	0	0	0	0	0	0	0	0	0	0	0	0	0	0	0	0	0	T
0	0	0	0	0	0	0	0	0	0	-1	0	0	0	0	0	0	0	0	0	0	S
0	0	0	0	0	0	0	0	0	0	-1	0	0	0	0	0	-1	0	0	0	0	R
0	0	0	0	0	0	0	0	0	0	0	0	0	0	0	0	-1	0	0	0	0	Q
0	0	1	0	0	0	-1	0	0	0	0	0	0	1	0	0	-1	-1	1	0	0	P
-1	0	0	0	0	0	0	0	0	0	0	0	0	0	0	-1	0	0	0	0	-2	O
0	0	0	0	0	1	0	0	0	0	0	0	0	0	0	0	0	0	0	0	-1	N
0	0	0	0	0	0	0	0	0	0	-1	0	0	0	0	-1	0	0	0	0	0	M
1	0	0	0	0	1	0	0	0	0	0	0	0	0	0	0	0	0	0	0	-1	L
0	0	0	0	0	0	1	-1	1	-1	-2	1	-3	-1	-1	0	0	-1	-1	0	0	K
1	0	0	0	0	0	0	0	0	0	0	0	0	0	0	-2	0	0	0	0	-1	J
0	0	0	0	0	-1	0	0	0	0	1	0	0	0	0	-1	0	0	0	0	0	I
0	0	0	0	0	0	0	0	0	0	0	0	0	0	0	-1	0	0	0	0	0	H
0	0	0	0	0	-1	0	0	0	0	0	0	0	0	0	-1	0	0	0	0	0	G
0	-1	0	0	-1	-1	0	0	1	0	0	0	0	0	-1	-1	0	0	-1	-1	0	F
0	0	0	0	0	-1	0	0	0	0	0	0	0	0	0	0	0	0	0	0	0	E
0	0	0	0	0	0	0	0	0	0	0	0	0	0	0	0	0	0	0	0	0	D
0	0	0	0	0	1	0	0	0	0	1	0	0	0	0	0	0	0	0	0	1	C
0	0	0	0	0	1	0	0	0	0	0	0	0	0	0	1	0	0	0	0	0	B
1	0	0	1	1	0	1	0	1	0	0	0	0	1	1	0	1	-1	0	1	0	A
1	2	3	4	5	6	7	8	9	10	11	12	13	14	15	16	17	18	19	20	21	

Figure 7.4: Discrepancies between CASMO-4E and MCNPX for the pin-wise decomposition of the reactivity effect of removing pin K12.

0	1	0	0	0	1	2	0	0	-1	-1	-1	0	-1	0	-1	0	0	-1	0	0	U
1	0	0	0	0	0	0	0	0	0	0	0	0	0	0	0	0	0	0	0	0	T
1	0	0	0	0	0	0	0	0	0	0	0	0	0	0	0	0	0	0	-1	0	S
0	0	0	0	0	0	0	0	0	0	0	0	0	0	0	-1	0	0	0	0	0	R
0	0	0	0	0	-1	0	0	0	0	0	0	0	0	0	-1	0	0	0	0	-1	Q
0	0	1	0	0	0	0	-1	0	0	1	0	-1	1	1	0	0	0	0	0	0	P
0	0	0	0	0	0	0	0	0	0	0	0	0	0	0	0	0	0	0	-1	0	O
1	0	0	0	0	0	0	0	0	0	0	0	0	0	0	1	0	0	0	0	-1	N
0	0	0	0	0	1	0	0	0	0	0	0	0	0	0	0	0	0	0	0	-1	M
1	0	0	0	0	0	0	0	0	0	0	0	0	0	0	1	0	0	0	0	-1	L
-1	0	0	1	0	0	1	-1	-1	-1	-1	-1	1	-1	0	0	0	0	-1	-1	0	K
0	0	0	0	0	0	0	0	0	0	0	0	0	0	0	-1	0	0	0	0	0	J
0	0	0	0	0	-1	0	0	0	0	0	0	0	0	0	0	0	0	0	0	0	I
0	0	0	0	0	0	0	0	0	0	0	0	0	0	0	0	0	0	0	0	0	H
0	0	0	0	0	-1	0	0	0	0	0	0	0	0	0	0	0	0	0	0	0	G
0	-1	0	0	-1	0	0	0	0	-1	0	1	1	0	0	0	0	0	-1	-1	0	F
0	0	0	0	0	0	0	0	0	0	-1	0	0	0	0	0	0	0	0	0	0	E
-1	0	0	0	0	0	0	0	0	0	0	0	0	0	0	0	0	0	0	0	1	D
0	0	0	0	0	0	0	0	0	0	-1	0	0	0	0	0	0	0	0	0	0	C
1	0	0	0	0	0	0	0	0	0	0	0	0	0	0	1	0	0	0	0	0	B
2	1	0	-1	0	0	0	0	2	1	0	0	0	1	1	0	0	-2	0	1	0	A
1	2	3	4	5	6	7	8	9	10	11	12	13	14	15	16	17	18	19	20	21	

Figure 7.5: Discrepancies between CASMO-4E and MCNPX for the pin-wise decomposition of the reactivity effect of removing pin K13.

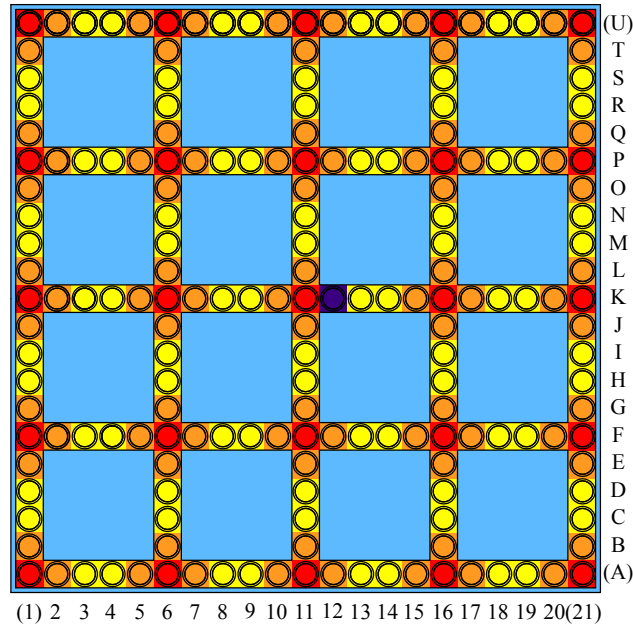


Figure 7.6: Grouping of the pins used for the group-wise decomposition of reactivity effects. Each generic fuel pin position is its own group (corner pins are red, neighbors orange, and remotes yellow). The water areas are also put into one group (blue). The removed fuel pin is a separate group.

illustrates the grouping, where the group of the corner pins (at intersections of columns and rows of fuel pins) is colored in red, that of the neighbors (adjacent to corner pins) is in orange, and the group of the remotes (not directly neighboring a corner pin) is in yellow. The removed pin (in this example K12) is considered as a separate group and is shown colored in dark blue. The water regions are shown in light blue. It is important to note that the decomposition is done with respect to fuel pin cells, i.e. the fuel pin, its cladding and the surrounding water.

In analyzing the reduced geometry model calculations, the neutron balance components which have been considered for each of the above defined, subregion “groups” are absorptions (ABS), captures (CAP), fissions (FIS), productions (fissions  $\cdot \nu$ , NU-FIS), fission source (FSC), and leakage (LEAK). It is also useful, in this context, to consider the group-specific neutron multiplicities within the system. This can be done in terms of the group-specific “ $k_\infty$ ”, i.e. the corresponding ratio of neutron productions to absorptions.

Fig. 7.7 summarizes the reactivity effect decomposition carried out in this manner for the case of removing the fuel pin K11. Thereby, each process detailed above was assessed on the basis of both CASMO-4E and MCNPX calculations for the unperturbed and perturbed configurations. The data block on the upper left side contains the neutron balance for the unperturbed configuration as calculated by CASMO-4E. Each column represents one of the subregion groups and each row is one process. The last column shows the total of all groups, i.e. the neutron balance for the entire SCWR-like assembly. As before, the decomposition was normalized to 100'000 produced

Figure 7.7: Group-wise decomposition of reactivity effects when removing pin K11



neutrons, which is why the NU-FIS values always sum up to this amount.

As mentioned, the group-specific  $k_\infty$  values, which are also indicated in each data block, are useful indices for the different multiplicities of the different generic pin types, viz. corner, neighbor and remote. The better moderated a fuel pin is, the higher is its  $k_\infty$ . The difference between the corner pins and the remote pins  $k_\infty$  is about 5,900 pcm.

The data block in the center of the upper row in Fig. 7.7 shows the CASMO-4E neutron balance for the perturbed configuration, where K11 was removed. While NU-FIS is still normalized to 100'000, the fission source has now changed due to the difference in  $k_{\text{eff}}$ , which is also seen in the group-wise entries of  $k_{\text{eff}}$ . The data block on the upper right shows the difference between perturbed and unperturbed configuration, as calculated by CASMO-4E. The biggest change happens in the pin cell with the removed fuel pin itself. The water which replaced the fuel only captures a few neutrons, while the fissions are reduced to zero. Most of the differences appearing in the removed fuel pin cell are compensated by the changes in the neighbor group, which contains the four pins adjacent to K11. This confirms what was observed in the pin-wise decomposition. The total difference in FSC, summed over all groups, equals the calculated  $\Delta\rho$  induced by the removal of fuel pin K11, which is the same as the value shown in the CASMO-4E column of Table 7.1.

The middle row of data blocks in Fig. 7.7 shows the analogous results for the MCNPX calculations. On the left is the unperturbed configuration, also normalized to 100'000 produced neutrons. The neutron balance for the perturbed configuration is shown in the middle, and the difference between perturbed and unperturbed calculations is on the right hand side. Once again, the total difference in FSC is equal to the change in reactivity due to the removal of fuel pin K11 and is the same as the value shown in the MCNPX reduced geometry column of Table 7.1.

In the bottom row of data blocks in Fig. 7.7, the differences between CASMO-4E and MCNPX are given for each state, i.e. the unperturbed and perturbed configurations, as also for the changes between the two states. It is seen that there are significant differences between the two codes for the unperturbed SCWR-like assembly itself. Looking first at the different pin-type multiplicities (group-specific  $k_\infty$  values), the CASMO-4E values are between 0.5% and 0.7% lower than for the MCNPX case for each of the three pin groups - corner, neighbor and remote. The fact that the assembly  $k_\infty$  value difference between the codes is only about -0.3% is largely explained by the significantly lower (by 2.4%) neutron absorptions in the “water” group with CASMO-4E.

Of clear interest are the code differences in computing the fission source distribution across the unperturbed configuration. It is seen that while, for the corner pins, CASMO-4E calculates an FSC value about 0.5% higher than MCNPX, its results for the fission source terms in the neighbor and remote pin groups are slightly (about 0.1%) lower.

The above relative trends for the two codes - in terms of differences in their group-specific values of both  $k_\infty$  and fission source - are very similar also for the perturbed configuration. This can

be seen from the middle data block at the bottom of Fig. 7.7.

The bottom data block on the right in Fig. 7.7 shows the decomposition of the differences between CASMO-4E and MCNPX when calculating the reactivity effect of removing the fuel pin K11. The summation of the differences in the fission source changes across the entire assembly (given in the column on the right and highlighted) corresponds to the discrepancy in the  $\Delta\rho$ -calculation between the two codes, i.e. is the same value (7 pcm) as given in the last column of numbers in Table 7.1. It is seen that all the FSC entries in the bottom data block on the right in Fig. 7.7 are small and, in fact, not very significantly outside the MCNPX statistical uncertainties. The changes in the neutron balance between the perturbed and unperturbed configuration are calculated with a remarkable degree of consistency between the two codes. Even though the net reactivity effect of removing pin K11 is - as in the BWR studies reported in [1, 6] - the sum of large compensating contributions (see FSC entries in the top and middle data blocks on the right hand side of Fig. 7.7), the CASMO-4E and MCNPX results are very similar.

The above described analysis has been repeated for the group-wise decomposition of the reactivity effect of removing the fuel pin K12 (neighbor pin). The results are given in Fig. 7.8. They are qualitatively quite similar to those obtained when removing pin K11, although clear differences are to be seen in the detailed neutron balance changes with respect to the unperturbed configuration. Thus, with the removed pin being a neighbor, rather than a corner pin - and hence better moderated - the fission source contribution of the pin itself to the total reactivity effect is significantly larger (588 pcm with MCNPX, instead of 477 pcm in the case of K11). The compensating fission source contributions (due to the enhanced moderation in the surrounding pins) are also correspondingly larger. The relative importance of the three generic pin types is, however, quite different (compare the FSC entries in the middle data block on the right in Fig. 7.8 with the corresponding entries in Fig. 7.7). As regards the bottom data block on the right in Fig. 7.8, the FSC entries once again show a remarkable consistency between the CASMO-4E and MCNPX calculations. The larger compensation, between the competing reactivity contributions of the removed pin itself and of its surroundings, is assessed in very similar fashion by the two codes.

Fig. 7.9 gives the analogous results obtained for the removal of the fuel pin K13 (remote). The findings are, once again, qualitatively consistent with those for the pins K11 and K12, although the individual competing reactivity contributions (see FSC entries in the middle data block on the right) are even larger in magnitude than in the previous two cases. Once again, the consistency between the two codes in predicting the net reactivity effect is excellent.

In view of the qualitative similarity between the above findings for the decomposition of the three different pin removals, it is useful to compare the individual cases directly in a summarized manner. This has been done in Table 7.4, which shows the distribution of the MCNPX calculated fission source changes (i.e. reactivity effect contributions) across the assembly, for each of the three cases. Given below each FSC entry is the corresponding difference between the CASMO-4E and MCNPX results.

Pin K12 CASMO-4	UNPERT	PIN	CORNER	NEIGHB.	REMOTE	WATER	ALL
	PERT	PIN	CORNER	NEIGHB.	REMOTE	WATER	ALL
MCNPX	UNPERT	PIN	CORNER	NEIGHB.	REMOTE	WATER	ALL
	PERT	PIN	CORNER	NEIGHB.	REMOTE	WATER	ALL
CS-MC	UNPERT	PIN	CORNER	NEIGHB.	REMOTE	WATER	ALL
	PERT	PIN	CORNER	NEIGHB.	REMOTE	WATER	ALL

Figure 7.8: Group-wise decomposition of reactivity effects when removing pin K12

Pin K13 CASMO-4	UNPERT	PIN	CORNER	NEIGHB.	REMOTE	WATER	ALL
		ABS	403	6630	25410	28401	7090
	CAP	126	2305	8416	9176	7090	27113
		FIS	277	4325	16994	19225	0
	NUL-FIS	678	10611	41639	47072	0	100000
		FSC	678	10611	41639	47072	0
	LEAK	275	3981	16229	18672	-7090	32066
		k <sub>inf</sub>	1.681	1.600	1.639	1.657	0.000
	Nu-Bar	2.447	2.453	2.450	2.449	0.000	2.450
		k <sub>eff</sub>	1.00000	1.00000	1.00000	0.00000	1.00000
	UNP-P	PIN	CORNER	NEIGHB.	REMOTE	WATER	ALL
		ABS	375	-32	-178	-152	-54
	CAP	98	-7	-42	-36	-54	-40
		FIS	277	-24	-137	-117	0
	NUL-FIS	678	-59	-334	-285	0	0
		FSC	678	-63	-350	-304	0
	LEAK	302	-28	-155	-133	54	-41
		k <sub>inf</sub>	1.681	-0.001	-0.002	-0.001	0.000
	Nu-Bar	2.447	0.000	0.000	0.000	0.000	0.000
		k <sub>eff</sub>	1.00000	0.00039	0.00039	0.00000	0.00039
MCNPX	UNPERT	PIN	CORNER	NEIGHB.	REMOTE	WATER	ALL
		ABS	373	-32	-177	-153	-55
	CAP	96	-7	-41	-36	-55	-43
		FIS	277	-25	-136	-117	0
	NUL-FIS	679	-60	-333	-286	0	0
		FSC	679	-65	-353	-309	0
	LEAK	305	-28	-156	-133	55	-44
		k <sub>inf</sub>	1.690	-0.001	-0.002	-0.001	0.000
	Nu-Bar	2.449	0.000	0.000	0.000	0.000	0.000
		k <sub>eff</sub>	0.99994	0.00049	0.00049	0.00000	0.00049
	UNP-P	PIN	CORNER	NEIGHB.	REMOTE	WATER	ALL
		ABS	2	1	-1	0	1
	CAP	2	0	-1	0	1	3
		FIS	0	0	0	0	0
	NUL-FIS	-1	1	-1	0	0	0
		FSC	-1	2	3	5	0
	LEAK	-3	1	1	0	-1	-3
		k <sub>inf</sub>	-0.009	0.000	0.000	0.000	0.000
	Nu-Bar	-0.002	0.000	0.000	0.000	0.000	0.000
		k <sub>eff</sub>	0.00006	-0.00010	-0.00010	-0.00010	-0.00010
CS-MC	UNPERT	PIN	CORNER	NEIGHB.	REMOTE	WATER	ALL
		ABS	2	82	109	145	-172
	CAP	2	53	104	145	-172	133
		FIS	0	29	5	0	34
	NUL-FIS	-1	61	-24	-36	0	0
		FSC	-1	60	-26	-39	0
	LEAK	-2	-22	-133	-181	172	-166
		k <sub>inf</sub>	-0.009	-0.011	-0.008	-0.010	0.000
	Nu-Bar	-0.002	-0.003	-0.002	-0.002	0.000	-0.002
		k <sub>eff</sub>	0.00006	0.00006	0.00006	0.00006	0.00006

Figure 7.9: Group-wise decomposition of reactivity effects when removing pin K13

Table 7.4: Distribution of the fission source changes ( $pcm$ ) across the SCWR-like assembly, as calculated by MCNPX, for the removal of fuel pins K11, K12, and K13, along with the corresponding differences in CASMO-4E and MCNPX results.

Removed pin (type)	Calculation	Pin	Corner	Neighb.	Remote	Water	All
<b>K11 (corner)</b>	MCNPX	477	4	-324	-129	0	<b>28</b>
	CS - MC	3	0	0	4	0	<b>7</b>
<b>K12 (neighbor)</b>	MCNPX	588	-107	-201	-294	0	<b>-14</b>
	CS - MC	-1	4	4	3	0	<b>10</b>
<b>K13 (remote)</b>	MCNPX	679	-65	-353	-309	0	<b>-49</b>
	CS - MC	-1	2	3	5	0	<b>10</b>

Some of the observations made earlier in the context of the comparisons of Figs. 7.7, 7.8, and 7.9 are of course also deducible from Table 7.4. There is, however, one specific trend which is clearer to see here. This is that - in the case of the removal of the better moderated pins in particular, viz. neighbor and remote - the negative fission source changes in the surroundings of the removed pin, as calculated by CASMO-4E, are systematically smaller in magnitude than the corresponding MCNPX values. This is essentially what leads to the less negative (or more positive, in the case of K11) net reactivity worths with CASMO-4E (tabulated also in Table 7.1). The effects are small, but nevertheless larger than the statistical uncertainties of the MCNPX results. Furthermore, they are consistent with the observation made in the context of the comparison of Tables 7.1 and 7.2 (see Subsec. 7.1.2.3), viz. that the CASMO-4E deficiencies, especially for the better moderated pin positions, appear to be linked to calculation of the additional moderator effect.

There is a further correlation, which can be made with respect to the results shown in Table 7.4. Thus, in relation to the data sets for the neutron balance in the unperturbed configuration, it was pointed that the multiplicity (local  $k_{\infty}$  value) was between 0.5% and 0.7% lower with CASMO-4E than with MCNPX, for each of the three pin groups (corner, neighbor and remote). It appears that the lower reactivity contribution - upon pin removal - of increased moderation in the surrounding pins is related to this fact.

## 7.2 PROTEUS Whole-Reactor $k_{\text{eff}}$ Values for the Different Configurations

As mentioned in the introduction to this chapter, the  $k_{\text{eff}}$  of the complete PROTEUS reactor reflects the neutronics of the test zone only in an indirect manner. It has been seen in the previous section that the relative changes in  $k_{\text{eff}}$  due to perturbations in the central part of the test zone can be viewed as test-lattice specific characteristics. The larger  $k_{\text{eff}}$  changes associated with modifications of the entire test zone, however, are more complex, since they involve changes in the coupling between the inner and outer regions of the multi-zone reactor. Nevertheless,

an attempt has been made currently to interpret the PROTEUS whole-reactor  $k_{\text{eff}}$  values for the different test zone configurations investigated, in order to assess the degree to which the neutronics of the SCWR-like test lattice is reflected therein.

In Subsec. 7.2.1,  $k_{\text{eff}}$  values of all configurations, calculated with the whole-reactor model of MCNPX, are compared to experiment. In Subsec. 7.2.2, the change in  $k_{\text{eff}}$  when going from the reference (unperturbed) configuration to each of the perturbed configurations is calculated and compared between the MCNPX whole-reactor and MCNPX reduced geometry models.

Throughout this section, the different measured configurations, introduced in Sec. 3.1, are denoted with individual names to simplify their identification. Henceforth, the reference PROTEUS configuration with the unperturbed SCWR-like lattice in the test zone (see Subsec. 3.1.1) will be denoted *Unperturbed*. The configuration in which the central fuel pin at position K11 is removed (see Subsec. 3.1.4) is denoted *Waterhole*, and the one with an inserted Gd-poisoned fuel pin at the same position (Subsec. 3.1.5) *Gd-pin*. The two configurations investigating control rod related effects (Subsec. 3.1.2) are denoted *Al-rods* and *St-rods*, for the cases with inserted aluminum and steel rods, respectively. Finally, the configurations with inserted water tanks (Subsec. 3.1.3) that were filled with pure  $\text{H}_2\text{O}$  and a mixture of 66%  $\text{D}_2\text{O}$  and 34%  $\text{H}_2\text{O}$  are referred to as  *$\text{H}_2\text{O}$  tanks (100%)* and  *$\text{D}_2\text{O}$  tanks (66%)*, respectively.

### 7.2.1 MCNPX Whole-Reactor $k_{\text{eff}}$ Values for the Critical Configurations

The experimental value of  $k_{\text{eff}}$  for each of the critical PROTEUS configurations is clearly unity, considering that the reactor was stable in each case and the intrinsic source was negligible (start-up sources removed from the reactor). In order to obtain the corresponding calculational result for each configuration, the MCNPX whole-reactor model was set up to resemble the experiment as much as possible. This means that the exact number of C-driver pins that were loaded in the graphite region in each case, was explicitly considered in the model. In addition, the control rod positions, recorded during the irradiations, and the water levels in the  $\text{D}_2\text{O}$ -driver and the test tank were also modeled exactly.

Table 7.5 summarizes the calculated  $k_{\text{eff}}$  value for each of the critical configurations. The statistical uncertainty on each MCNPX calculated value in the table is 2 *pcm*. One can see that MCNPX, in conjunction with the ENDF/B-VII.0 continuous-energy neutron data library, systematically overestimates  $k_{\text{eff}}$ . In most of the cases, this overestimation is between 300 and 400 *pcm*, which corresponds to about 40 to 50 *cents*, assuming a  $\beta_{\text{eff}}$  value of 734 *pcm* [8]. In the case of the configuration with four inserted stainless steel rods (denoted *St-rods*), however, the overestimation is considerably higher, viz. as much as about 800 *pcm*.

The uncertainties on the calculations, stated in Table 7.5, are of purely statistical nature and do not contain systematic uncertainties coming from either the model or the nuclear data library. One would thus clearly not expect the calculations to agree with the experimental value of

Table 7.5:  $k_{\text{eff}}$  values for the different critical PROTEUS configurations as predicted with the whole-reactor MCNPX model. The experimental  $k_{\text{eff}}$  is always 1. The difference of the calculated  $k_{\text{eff}}$  value with respect to “Unperturbed” ( $\Delta k_{\text{eff}}$ ) is shown in the right data block for each of the perturbed configurations.

Configuration	Experiment		MCNPX whole - reactor model			
	$k_{\text{eff}}$	$1\sigma$	$k_{\text{eff}}$	$1\sigma$	$\Delta k_{\text{eff}}$ [pcm]	$1\sigma$ [pcm]
<b>Unperturbed</b>	1.00000	-	1.00290	0.00002	-	-
<b>Waterhole</b>	1.00000	-	1.00287	0.00002	-3	3
<b>Gd-pin</b>	1.00000	-	1.00414	0.00002	124	3
<b>Al-rods</b>	1.00000	-	1.00403	0.00002	113	3
<b>St-rods</b>	1.00000	-	1.00787	0.00002	497	3
<b>H<sub>2</sub>O tanks (100%)</b>	1.00000	-	1.00392	0.00002	102	3
<b>D<sub>2</sub>O tanks (66%)</b>	1.00000	-	1.00353	0.00002	63	3

unity within the statistical uncertainty. The calculated  $k_{\text{eff}}$  value for the reference configuration (Unperturbed) is actually in good agreement with experiment, considering that  $k_{\text{eff}}$  can easily vary by about 500 *pcm* depending on which data library is used [9]. The bias coming from the nuclear data library, however, should be more or less constant for all configurations (because most of the nuclear data effect originates in the unperturbed system and the introduction of perturbations is only to second order dependent on the library). In order to focus on the model uncertainties, it is useful to eliminate the systematic library bias by considering the difference,  $\Delta k_{\text{eff}}$ , in calculated  $k_{\text{eff}}$  values between the Unperturbed and each of the perturbed configurations (shown in the data block on the right in Table 7.5).

If the various  $\Delta k_{\text{eff}}$  values in Table 7.5 were all zero (within the statistical uncertainty of  $\pm 3$  *pcm*), this would imply that the MCNPX whole-reactor model accurately captures both the SCWR-specific perturbation studied and the changed coupling between test zone and outer reactor regions. What one sees, however, is that - except for the Waterhole configuration, which had a very small effect on the whole-reactor  $k_{\text{eff}}$  - all the calculated values of the perturbed configurations are systematically too high. In the St-rods case, an overestimation of almost 500 *pcm* is observed for the perturbed configuration (relative to the Unperturbed  $k_{\text{eff}}$  calculation). Insertion of the steel absorber rods constitutes the largest perturbation of the PROTEUS reactor in terms of  $k_{\text{eff}}$  change (in the order of \$2.5). Hence, in order to compensate for the negative reactivity insertion in the experimental zone, the number of C-driver fuel pins that had to be loaded into the graphite driver region of PROTEUS was the highest. In fact, when plotting the  $\Delta k_{\text{eff}}$  of the various configurations against the number of C-driver fuel pins that had to be added to compensate for the negative reactivity effect of perturbing the test zone, a linear trend is observed (see Fig. 7.10).

The fact that the overestimation of the  $k_{\text{eff}}$  change depends linearly on the number of additional C-driver pins that were inserted into the graphite region suggests that the C-driver worth (change in reactivity when a single C-driver fuel pin is added) is overestimated in the whole-reactor

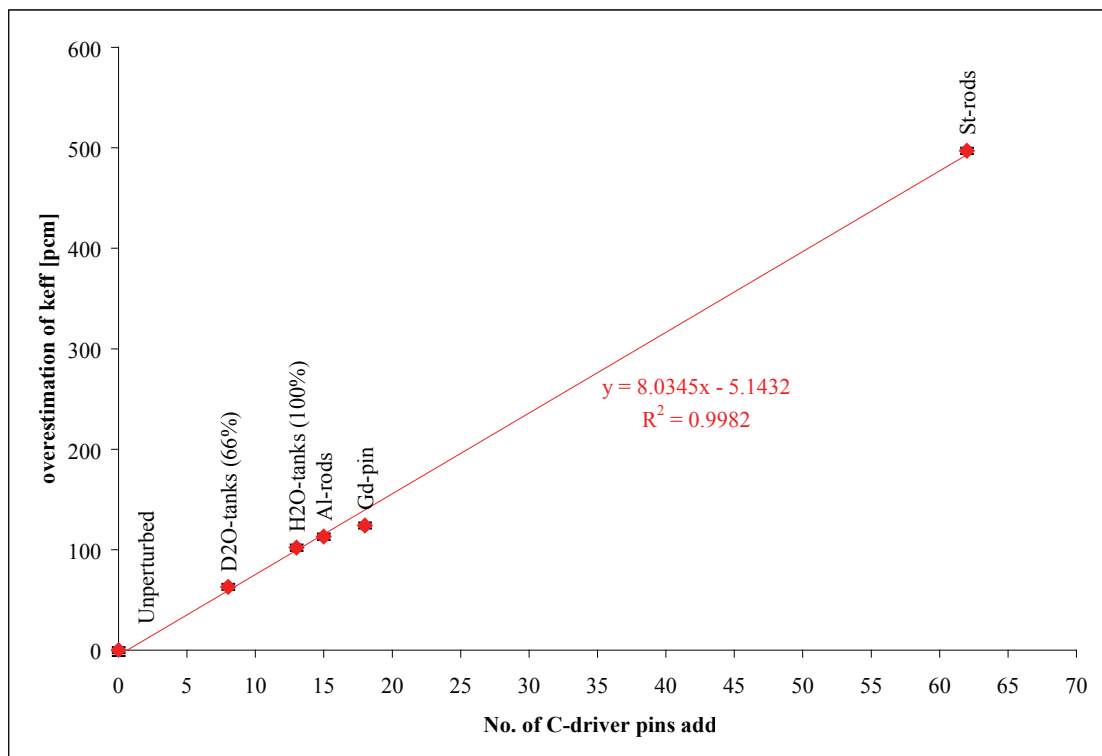


Figure 7.10: Plot of  $\Delta k_{\text{eff}}$  for the various configurations, against the number of C-driver fuel pins that had to be added to compensate for the negative reactivity effect of the perturbation.



MCNPX model. The C-driver fuel pins are exactly the same type as the fuel pins constituting the SCWR-like test lattice, and it has been seen from the various MCNPX analyses conducted in the context of the latter that excellent agreement is obtained with experiment. The discrepancy in C-driver loading has thus little to do with the composition and dimensions of the fuel pins, which are well known. As such, the source of error can be expected to lie in the uncertainties associated with their moderation in the C-driver region, i.e. in the graphite composition.

The graphite structure in PROTEUS, i.e. the C-driver and reflector zones, can be described as an annular region with 22-sided polygons as inner and outer boundaries. It consists of graphite of various ages and from several different sources [10]. Important parameters for the neutronics calculations, such as the density, the water content, and the material impurities, differ from graphite block to graphite block [11, 12]. Moreover, the graphite blocks have been frequently “man-handled” and rearranged. No detailed, space-dependent specifications for the graphite structure are available. Instead, an artificial boron content is assumed to be smeared uniformly into the graphite to account for the combined neutronics effects (in terms of an effective neutron absorption cross section). Clearly, unlike the case of the C-driver fuel pins themselves, it is likely that the graphite modeling in MCNPX has certain deficiencies.

In order to confirm the above, the dependence of the MCNPX calculated  $k_{\text{eff}}$  for the Unperturbed and the St-rods configurations on the assumed boron content was studied. As mentioned earlier, if the whole-reactor modeling - both in terms of the test zone and of its coupling with the outer regions - were correct, the predicted  $k_{\text{eff}}$  values would be equal for the two configurations. Fig. 7.11 shows the calculated  $k_{\text{eff}}$  values as a function of the modeled  $^{10}\text{B}$  content. Each set of data has been fitted to a linear equation, which is also shown on the graph. By increasing the  $^{10}\text{B}$  content, the reactivity of the system is reduced for both configurations. However, the gradient, with which it is reduced, is steeper for the St-rods configuration which leads to an intersection of the two fitted linear equations at approximately 1,040 ppb of  $^{10}\text{B}$  in graphite. Due to the large amount of computing resources, necessary to obtain an accurate  $k_{\text{eff}}$  estimate with the whole-reactor model of MCNPX, it was not possible to derive a more precise value. However, at 1,040 ppb of  $^{10}\text{B}$ , the obtained  $k_{\text{eff}}$  values for the Unperturbed and the St-rods configuration are 0.99340 and 0.99328 respectively, thus differing only by 12 pcm.

The whole-reactor  $k_{\text{eff}}$  calculations were repeated for all the configurations with the  $^{10}\text{B}$  content set to the optimized value mentioned above (1,040 ppb). This concentration is significantly different from what was used before, viz. 270 ppb [12]. The results of both calculation batches are shown in Table 7.6. By increasing the  $^{10}\text{B}$  content, the calculated  $k_{\text{eff}}$  value of the unperturbed configuration has been decreased by 950 pcm to a value of 0.99340. This is still in reasonable agreement with the experiments, considering the before mentioned dependency on nuclear data. Overall, the agreement between the calculated  $k_{\text{eff}}$  values for the various configurations is seen to improve markedly through the adjustment of the graphite region. The final results all agree within 34 pcm (approximately 5 cents), the largest difference coming once again from the St-rods case.

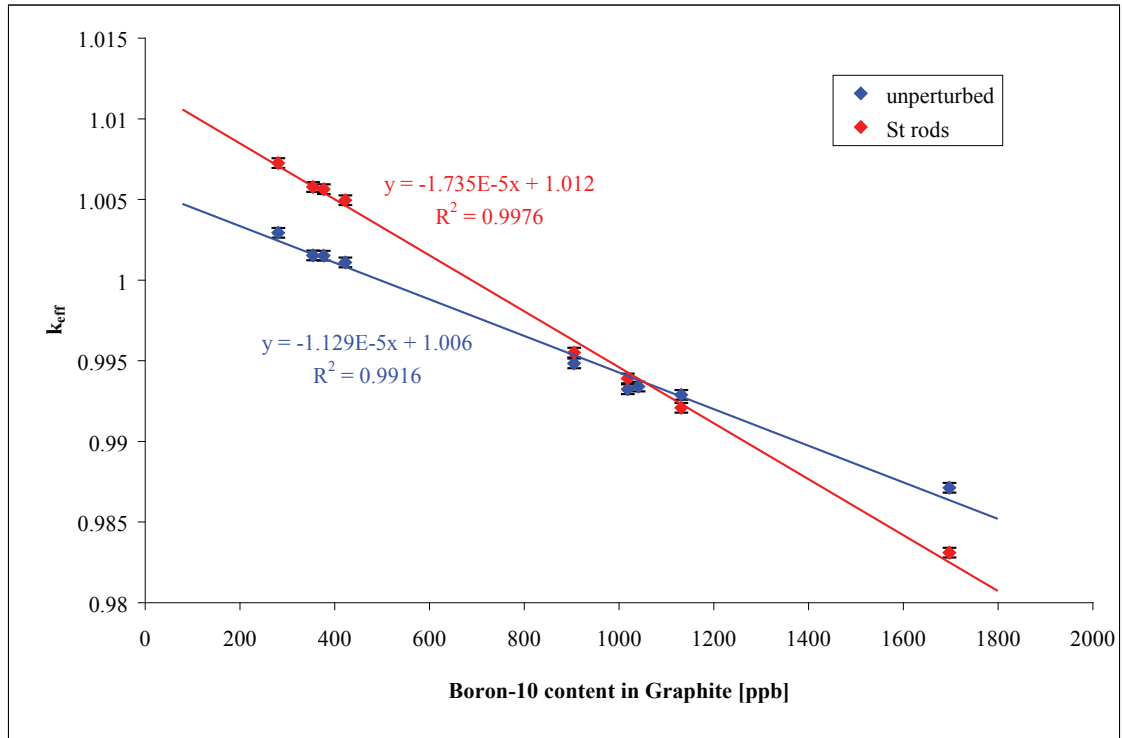


Figure 7.11: Calculated  $k_{eff}$  values for the Unperturbed and the St-rods configuration as a function of the modeled  $^{10}\text{B}$  content.

Table 7.6: Multiplication factor changes induced by an increased  $^{10}\text{B}$  content of the graphite blocks in the whole-reactor MCNPX model. For the sake of comparison, the results from the standard MCNPX model ( $^{10}\text{B}$  content of 270 *ppb*) are repeated on the left hand side. On the right, the analogous calculations are shown with the  $^{10}\text{B}$  content set to 1040 *ppb*.

Configuration	MCNPX model base case				MCNPX model optimized B-10 content			
	$k_{eff}$	$1\sigma$	$\Delta k_{eff}$ [pcm]	$1\sigma$ [pcm]	$k_{eff}$	$1\sigma$	$\Delta k_{eff}$ [pcm]	$1\sigma$ [pcm]
Unperturbed	1.00290	0.00002	0	3	0.99340	0.00002	0	3
Waterhole	1.00287	0.00002	-3	3	0.99345	0.00004	5	5
Gd-pin	1.00414	0.00002	124	3	0.99335	0.00004	-5	5
Al-rods	1.00403	0.00002	113	3	0.99334	0.00002	-6	3
St-rods	1.00787	0.00002	497	3	0.99306	0.00002	-34	3
H <sub>2</sub> O tanks (100%)	1.00392	0.00002	102	3	0.99357	0.00002	17	3
D <sub>2</sub> O tanks (66%)	1.00353	0.00002	63	3	0.99328	0.00002	-12	3

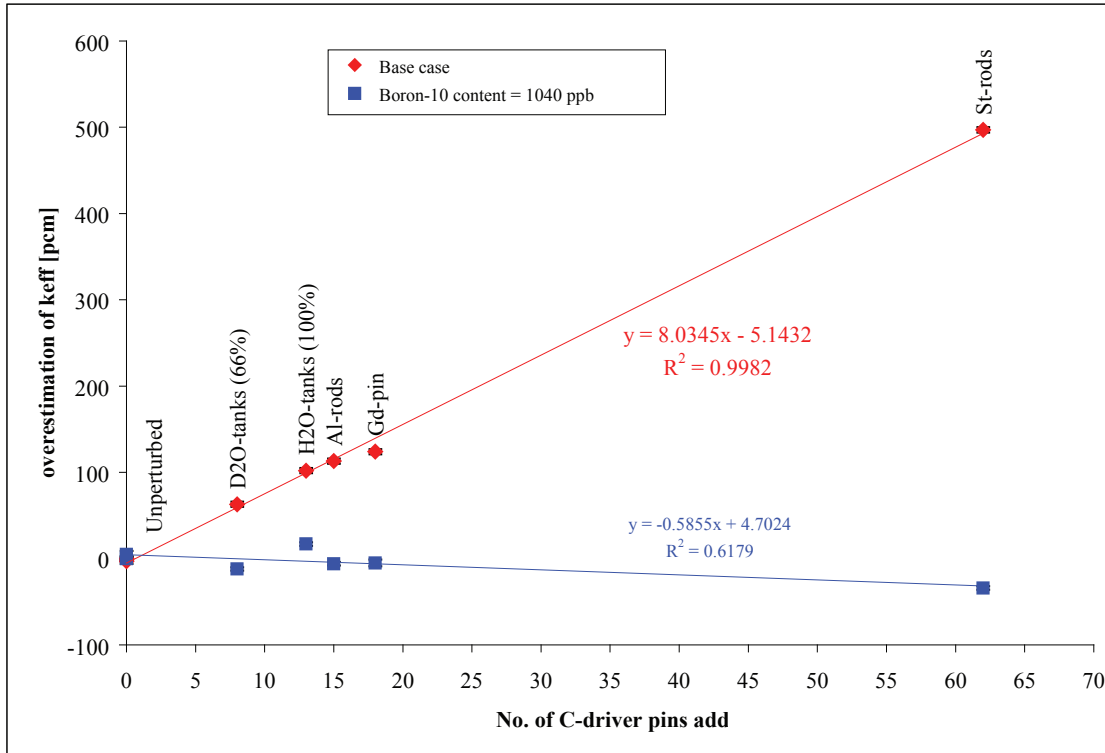


Figure 7.12: Overestimation of  $k_{\text{eff}}$  as a function of C-driver pins that had to be added to compensate for the negative reactivity effect of the introduced perturbation, for the base case calculations (red curve) and for those using the adjusted  $^{10}\text{B}$  content (blue curve).

Fig. 7.12 shows, once again, the overestimation of  $k_{\text{eff}}$  as a function of C-driver rods that had to be inserted in the graphite region to compensate for the negative reactivity effect of the introduced perturbation. This time, the results of both calculation batches, the base case and the case with adjusted  $^{10}\text{B}$  content, are plotted. As mentioned above, the agreement of the whole-reactor  $k_{\text{eff}}$  values is much better, which is expressed in the graph through a much flatter trend line. However, the slope is now negative, indicating that the C-driver worth is slightly underestimated and that the chosen effective  $^{10}\text{B}$  content seems to be marginally too large. In quantitative terms, the magnitude of the trend line slope is 14 times smaller than before (corresponding to an underestimation of the C-driver worth per fuel pin of 0.57 *pcm*, instead of the previous overestimation of 8.03 *pcm*).

The linear fit is not as good as before ( $R^2 = 0.62$ ), indicating that now other configuration-specific effects come into play that were earlier hidden by the strong overestimation of the C-driver worth. What is, however, quite apparent is that the differences in MCNPX whole-reactor  $k_{\text{eff}}$  values, between the different PROTEUS test zone configurations, depend strongly on the modeling of the outer reactor regions, i.e. on the accuracy of their technical description and, hence, of their coupling with the test zone.

Analogous to the case of pin removal worths from the central region of the test zone, as discussed

in Subsec. 7.1.2, there is an alternative approach to studying the test-lattice specificity of the whole-reactor  $k_{\text{eff}}$  changes. This is based on the fact that the ratio of the  $k_{\text{eff}}$  changes for two different test zone configurations should be quite similar when considering whole-reactor and reduced geometry models for the two configurations (see Subsec. 7.1.2.4). This aspect is treated in the following subsection.

### 7.2.2 Inter-Model Comparison of Relative Whole-Reactor $k_{\text{eff}}$ Changes

In order to carry out the above mentioned study, another batch of whole-reactor calculations was performed to derive the reactivity changes upon implementing the different test zones, while keeping the PROTEUS outer zones unchanged. Clearly, the calculated PROTEUS  $k_{\text{eff}}$  values will no longer be unity, but will still reflect the change in reactivity due to the modified test zone via:

$$k'_{\text{eff}}(\text{Perturbed}) = k_{\text{eff}}(\text{Unperturbed}) - \Delta k'_{\text{eff}}(\text{Perturbation}). \quad (7.2)$$

Unfortunately, this approach of assessing the reactivity effect of a relative large perturbation cannot be compared with experiments, as no sub-critical measurements were performed before modifying the loading of the C-Driver region. It can however, be used to compare the predictions of different codes and models. It is in this light that the two MCNPX models are being compared to each other in this subsection.

The  $k_{\text{eff}}$  change due to the perturbation of the SCWR-like test lattice is clearly not the same in the whole-reactor model and in the reduced geometry model, since the relative importance of the perturbed region is quite different (see Subsec. 7.1.2). Due to the reflective boundary conditions of the reduced geometry model, perturbing one assembly is effectively perturbing all the assemblies in the infinitely large (in X- and Y-directions) system. Therefore, the  $\Delta k'_{\text{eff}}$  values can be expected to be significantly larger in the reduced geometry calculation. This can be seen in Table 7.7, which compares the  $\Delta k'_{\text{eff}}$  values for the various perturbed test zone cases.

As discussed earlier, the meaningful comparison to be made here is in terms of  $\Delta k'_{\text{eff}}$  ratios, i.e. one of the  $\Delta k'_{\text{eff}}$  values in each of the models needs to be taken as reference, to which all the others are compared. To minimize the statistical uncertainties on the resulting ratios the largest  $\Delta k'_{\text{eff}}$  has been chosen as denominator. Thus, the calculated  $k_{\text{eff}}$  changes have all been normalized to the change in going from the Unperturbed to the St-rods configuration:

$$\frac{\Delta k'_{\text{eff}}}{\Delta k'_{\text{eff}}(St)} = \frac{k'_{\text{eff}}(\text{Perturbed}) - k_{\text{eff}}(\text{Unperturbed})}{k'_{\text{eff}}(St\text{-rods}) - k_{\text{eff}}(\text{Unperturbed})} \quad (7.3)$$

By considering such ratios, one eliminates (to first order) the differences in the relative importance

Table 7.7: Comparison of the reactivity changes calculated by the whole-reactor model and the reduced geometry model of MCNPX. The  $\Delta k'_{\text{eff}}$  values are not expected to be the same, due to the differences in the relative importance of the investigated assembly. When compared to a reference reactivity change however, the two models should yield the same answer as long as the coupling between the regions doesn't change upon perturbation of the system.

Configuration	MCNPX whole reactor model				MCNPX reduced geometry model				Difference	
	$k_{\text{eff}}$	$\Delta k'_{\text{eff}}$ [pcm]	$\Delta k'_{\text{eff}}/\Delta k'_{\text{eff}}(\text{St})$	$1\sigma$	$k_{\text{eff}}$	$\Delta k'_{\text{eff}}$ [pcm]	$\Delta k'_{\text{eff}}/\Delta k'_{\text{eff}}(\text{St})$	$1\sigma$	$1\sigma$	
<b>Unperturbed</b>	1.00290				0.99996					
<b>Waterhole</b>	1.00307	17	-0.009	0.002	1.00024	28	-0.009	0.001	0.000	0.002
<b>Gd-pin</b>	0.99813	-477	0.253	0.002	0.99338	-658	0.217	0.001	0.037	0.002
<b>Al-rods</b>	0.99901	-389	0.206	0.002	0.99141	-855	0.282	0.001	-0.075	0.002
<b>St-rods</b>	0.98406	-1884	1.000	0.002	0.96959	-3037	1.000	0.001	0.000	0.002
<b>H<sub>2</sub>O tanks (100%)</b>	0.99960	-330	0.175	0.002	0.99711	-285	0.094	0.001	0.081	0.002
<b>D<sub>2</sub>O tanks (66%)</b>	1.00063	-227	0.120	0.002	0.99296	-700	0.230	0.001	-0.110	0.002

of the test zone representation in the two different models - whole-reactor and reduced geometry. However, one feature which is treated very differently is the coupling between the test zone and the outer reactor regions. While the reduced geometry model does not represent the outer PROTEUS regions in any way, the whole-reactor model takes explicit consideration of the changes in the coupling of the test zone when going from one configuration to another. Clearly, for configurations in which the coupling remains unchanged, one can expect to obtain  $\Delta k'_{\text{eff}}$  ratios which are very similar between the whole-reactor and the reduced geometry models, i.e. the ratios represent integral parameters which are SCWR-specific.

Table 7.7 also shows, for each of the models, the results obtained for the above defined  $\Delta k'_{\text{eff}}$  ratios. Because the Unperturbed configuration was used as basis for calculating each  $\Delta k'_{\text{eff}}$  and the St-rods configuration has served as denominator, there are only five values that can be compared. From these five ratios, it is seen that four ratios differ clearly between the two models, indicating that the coupling between the test zone and the outer regions is different and that the PROTEUS outer zone effects are too large for meaningful conclusions to be drawn about the SCWR-specific neutronics. The one ratio that agrees between the models is the Waterhole configuration, which is not surprising since the same number of C-driver fuel pins were necessary in the graphite region to make the reactor critical as for the unperturbed configuration. The coupling between the regions is therefore very similar for these two cases, which is why the results agree.

In brief, the consideration of the  $\Delta k'_{\text{eff}}$  ratios between the MCNPX whole-reactor and reduced geometry models has confirmed the conclusion drawn in the previous subsection, viz. the dependency of the whole-reactor  $k_{\text{eff}}$  value on the accuracy of the description of the outer regions - and hence of the test zone coupling - is too high. This largely limits the interpretability of reactivity effects in the current PROTEUS experiments to changes made in the central region of the SCWR-like lattice, in which the C-driver loading was not changed. The latter conditions

are clearly met in the case of the individual pin removal experiments discussed in Sec 7.1.

# Bibliography

- [1] F. Tani. *Decomposition Analysis of Reactivity Effect Predictions for Modern LWR Fuel*. PhD thesis, École Polytechnique Fédérale de Lausanne, 2006.
- [2] M.F. Murphy and A. Lüthi. LWR-PROTEUS: The results of Measurements in Configuration 7A. Technical Report TM-41-01-01, Paul Scherrer Institute, Villigen, Switzerland, March 2001.
- [3] M.F. Murphy and A. Lüthi. LWR-PROTEUS Phase II: A Measurement plan for the determination of the reactivity effect of burnt fuel samples. Technical Report AN-41-02-04, Paul Scherrer Institute, Villigen, Switzerland, June 2002.
- [4] M. Rosselet. *Reactivity Measurements and their Interpretation in Systems with Large Spatial Effects*. PhD thesis, École Polytechnique Fédérale de Lausanne, 1999.
- [5] T. Williams. HTR-PROTEUS CORE 1: ZEBRA Control Rod S-Curves and Rest Worths. Technical Report TM-41-92-40, Paul Scherrer Institute, Villigen, Switzerland, February 1993.
- [6] R. Chawla, F. Jatuff, and F. Tani. Diagnostic Analysis of Pin-Removal Reactivity Worth Experiments in a SVEA-96+ Test Lattice. *Annals of Nuclear Energy*, 35:495–502, 2008.
- [7] R. van Geemert, F. Jatuff, P. Grimm, and R. Chawla. Assessment of Reactivity Effects due to Localised Perturbations in BWR Lattices. *Nuclear Science and Engineering*, 142:96–106, 2002.
- [8] K.A. Jordan. MCNPX  $\beta_{eff}$ , an MCNPX Code Extension for Calculation of Effective Delayed Neutron Fractions. Technical Report TM-41-08-04, Paul Scherrer Institute, Villigen, Switzerland, August 2008.
- [9] M. Plaschy, M. Murphy, F. Jatuff, G. Perret, R. Seiler, and R. Chawla. Validation of Monte Carlo Predictions of LWR-PROTEUS Safety Parameters Using an Improved Whole-Reactor Model. *Annals of Nuclear Energy*, 39:1536–1543, 2009.
- [10] A.K. Ziver and T. Williams. LWR-PROTEUS system component description. Technical

- Report TM-41-98-07, Paul Scherrer Institute, Villigen, Switzerland, 1998.
- [11] D. Mathews and T. Williams. LEU-HTR PROTEUS System Component Description. Technical Report TM-41-93-43 Rev. 2, Paul Scherrer Institute, Villigen, Switzerland, 1996.
- [12] F.C. Difilippo. Monte Carlo Calculations of Pebble Bed Benchmark Configurations of the PROTEUS Facility. *Nuclear Science and Engineering*, 143:240–253, 2003.



## 8 Transferability of the PROTEUS Experiments to SCWR Design

The experiments and analysis conducted in the present research are largely of generic relevance to the study of LWR lattices with strong moderation heterogeneity. In the present chapter, an assessment is made of their representativeness with respect to SCWR assembly designs under power reactor conditions (from the viewpoint of moderator/coolant densities). This, in turn, implies an evaluation of the transferability of the conclusions drawn in relation to the code validation carried out for MCNPX and CASMO-4E.

As described in Sec. 2.1, R&D on the SCWR has been ongoing since the early 1990's [1]. Nevertheless, a consensus has not yet been established on important design features, such as the assembly layout or representative average values for the moderator and coolant densities. The two thermal SCWR design concepts developed furthest are that of the EU-project (HPLWR 2 - High Performance Light Water Reactor 2) led by the Karlsruhe Institute of Technology [2] and a Japanese design called the Super Light Water Reactor (Super LWR) led by the University of Tokyo [3]. The assembly layouts of both concepts are shown in Fig. 8.1, along with the reduced geometry model of the SCWR-like test lattice implemented in PROTEUS.

The transferability of the PROTEUS experiments has been assessed by comparing integral neutronics parameters, such as spectral indices and neutron balance components. The parameters chosen for the comparison of unperturbed assembly characteristics, as obtained from the corresponding CASMO-4E and MCNPX calculations, are  $C_8/F_{\text{tot}}$ ,  $F_8/F_{\text{tot}}$ ,  $\text{Abs}_{\text{tot}}/F_{\text{tot}}$ ,  $\text{Prod}_{\text{tot}}/F_{\text{tot}}$ , and  $k_{\infty}$ , where Abs and Prod denote neutron absorption and production, respectively (see Subsec. 6.1.1). The ratio of total absorptions to total fissions has also been divided into the contributions from absorptions in fuel ( $\text{Abs}_{\text{fuel}}$ ), water ( $\text{Abs}_{\text{water}}$ ), and structural material ( $\text{Abs}_{\text{struc}}$ ). Furthermore, an additional spectral index  $\Psi$  has been used. This is defined simply as the ratio of the neutron flux below 4 eV (i.e. thermal neutron flux) to the total neutron flux. The neutron spectra have also been investigated, using both CASMO-4E and MCNPX in the 40-group energy structure of CASMO-4E.

Due to the neutronics differences between the PROTEUS test lattice and the assembly level calculations carried out in reactor design studies, the first step of the transferability analysis has been to make a comparison of integral parameters between the experimental lattice and the reduced geometry model. This is done on the basis of MCNPX calculations in Sec. 8.1. Once

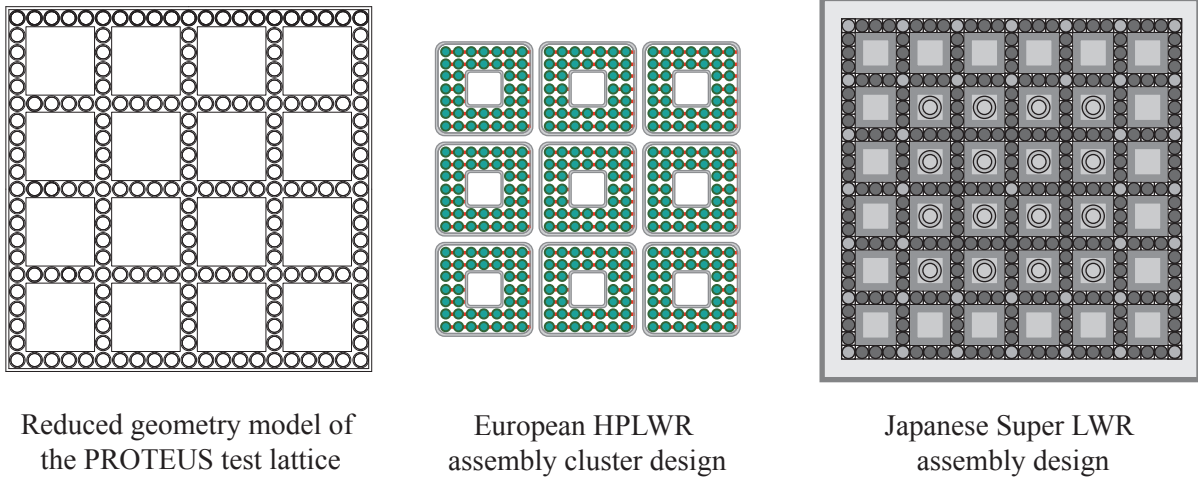


Figure 8.1: “SCWR assembly” models considered for the transferability analysis: PROTEUS test lattice (left hand side) and the two furthest advanced SCWR design concepts, viz. those from Europe (middle) [2] and Japan (right hand side) [3].

the similarity of results for the SCWR-lattice, as obtained from the whole-reactor and reduced geometry calculations, has been demonstrated, the analysis of the transferability at the assembly level is conducted in Sec. 8.2. Here, comparisons of integral parameters are made between the reduced geometry model and each of the two reference SCWR assembly designs. A significant part of these comparisons were made as part of a recently completed Master’s project, conducted under the author’s guidance [4].

Throughout this chapter, uncertainties of the calculated values have been omitted. The integral data are considered in terms of the entire assembly, so that the number of events that are tallied in the MCNPX calculations is very large. This results in very low statistical uncertainties, and is true for both the whole-reactor and the reduced geometry calculations. For the latter, pin-wise comparisons have also been made, which also have very good statistics, leading to statistical uncertainties that are below the experimental accuracy of the reported values. Finally, as previously discussed, the deterministic CASMO-4E results can be considered as exact, with the proviso that systematic uncertainties (arising from methods, modeling, or nuclear data) are not included.

## 8.1 Transferability to Reduced Geometry Calculations

The PROTEUS outer regions influence the neutronics of the experimental zone. The closer a fuel pin of the test lattice is to the outer zones, the stronger is the spectral distortion of the SCWR-specific neutron flux at that location. This was the primary reason why not all of the fuel pins constituting the test zone were measured during the gamma-scanning experiments (see Sec. 3.1). Consequently, the area over which the integral parameters of the whole-reactor model are assessed is limited to that corresponding to the experimentally investigated fuel pins, viz.

Table 8.1: Integral parameters calculated with the MCNPX whole-reactor and reduced geometry models.

Parameter	Whole reactor model	Reduced geometry model
$C_8/F_{\text{tot}}$	0.228	0.254
$F_8/F_{\text{tot}}$	0.032	0.036
$\text{Abs}_{\text{tot}}/F_{\text{tot}}$	1.624	1.669
$\text{Prod}_{\text{tot}}/F_{\text{tot}}$	2.449	2.451
$(k_\infty)_{\text{crit}}$	1.508	1.469

those in columns 5 through 17 and in rows E through Q (see Fig. 3.1).

Due to the nature of the MCNPX whole-reactor model - viz. with the considered part of the test lattice forming part of a much larger system - it was not possible to obtain  $k_\infty$  values in the zero buckling spectrum. The parameters that could be compared are  $C_8/F_{\text{tot}}$ ,  $F_8/F_{\text{tot}}$ ,  $\text{Abs}_{\text{tot}}/F_{\text{tot}}$ ,  $\text{Prod}_{\text{tot}}/F_{\text{tot}}$ , and the quotient of the last two, which is effectively  $k_\infty$  in the critical spectrum. The obtained values are shown in Table 8.1, along with the corresponding results from the MCNPX reduced geometry model calculation. For the reduced geometry, the integral parameters are evaluated as average values over the entire fuel assembly.

As can be seen from Table 8.1, the results obtained are quite similar in the whole-reactor and the reduced geometry models. The neutron balance component (and spectral index)  $C_8/F_{\text{tot}}$ , which is sensitive to the epithermal region of the neutron energy spectrum, differs by 11.4%, while the fast fission index  $F_8/F_{\text{tot}}$  differs by 12.5%. These indicate a slightly harder neutron spectrum in the reduced geometry case, which is confirmed by the comparison of the two MCNPX calculated spectra in Fig. 8.2. The neutron spectra were averaged over the same areas as used for the integral parameters. They were obtained in the 40-group energy structure of CASMO-4E by dividing the tallied neutron flux by the width (in lethargy) of the bin. In Fig. 8.2, the Maxwellian peak is less pronounced for the reduced geometry model, and the flux is constantly higher in the epithermal and fast regions.

Due to the higher  $C_8$  in the reduced geometry model, the total absorptions per fission are also higher. With an almost constant  $\text{Prod}_{\text{tot}}/F_{\text{tot}}$  ratio (the average number of emitted neutrons per fission,  $\bar{\nu}$ , only changes marginally for the slightly harder spectrum in the reduced geometry model), this leads to a lower  $k_\infty$  value in the reduced geometry case (by  $\approx 2.5\%$ ). However, the differences in the spectral and neutron balance components are rather small, indicating that the reduced geometry model is a good representation (in terms of neutronics) of the situation present in the measured area of the SCWR-like test lattice inside PROTEUS. The transferability of the experimental results to the reduced geometry model can thus be considered high.

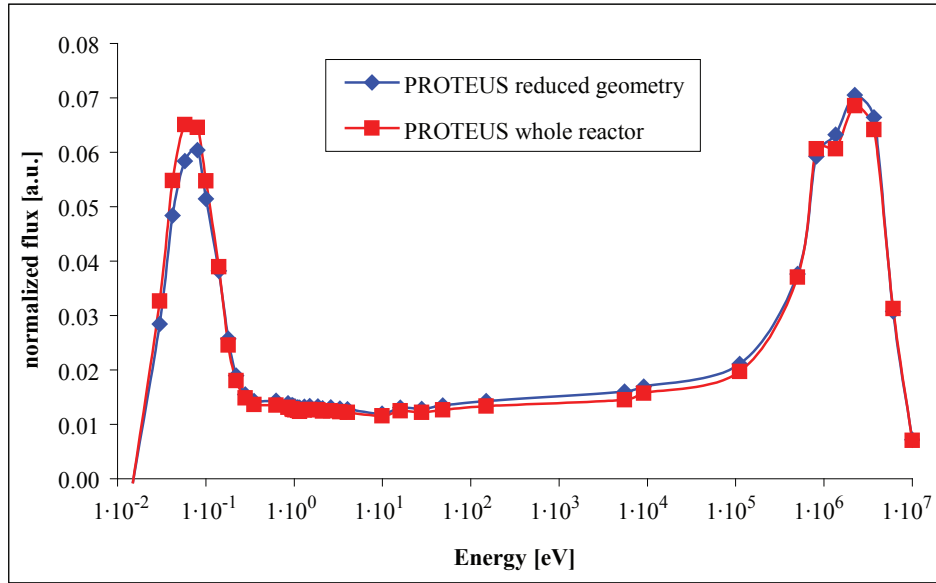


Figure 8.2: Average neutron spectrum (MCNPX calculations) in the fuel assembly of the reduced geometry model and in the measured section of the SCWR-like test lattice implemented in PROTEUS.

## 8.2 Transferability to Different SCWR Assembly Designs

The European assembly cluster design is shown in the middle of Fig. 8.1. Each assembly consists of 40 fuel pins (with 8 mm outer cladding diameter and 5% enriched  $\text{UO}_2$ ) that are arranged around a central moderator channel, which replaces nine fuel pins in the center of the 7x7 array. The assembly box wall is made of stainless steel. As indicated, nine assemblies are mounted together to form an assembly cluster, which serves as a single mechanical unit for refueling purposes. Between assemblies, there is a 10 mm gap to enhance the moderation of the outer pins of the fuel assembly. A more detailed discussion of this assembly design is given in Subsec. 2.2.2.2.

The Japanese design, shown on the right hand side of Fig. 8.1, is a further development of the assembly proposal of Yamaji et al. in 2001 [5], which is the basis upon which the PROTEUS test lattice was constructed (see Fig. 2.17). As such, its geometry is similar to the investigated test lattice. Nevertheless, there are several differences, the most significant being the size of the assembly (array of 25x25 fuel pins that contain 6.2% enriched  $\text{UO}_2$ ) with 36 moderator channels, each replacing a 3x3 array of pins. Additionally, gadolinium-poisoned fuel pins have been inserted into forty corner positions (pin column-row intersections) of the assembly. These are indicated in the figure by the light-grey pin positions. Control-rod guide tubes, which are also indicated, are installed in the 16 central moderator channels. More details on the latest Japanese thermal SCWR design are given in Subsec. 2.2.2.1.

The most significant difference between the PROTEUS test lattice and the SCWR design proposals is the water density. The PROTEUS reference lattice has no structural material (i.e.

no moderator box walls and no assembly box walls). Hence, there is only one nominal water density, namely that of an LWR at operating temperature ( $670 \text{ kg/m}^3$ , simulated by an appropriate mixture of  $\text{H}_2\text{O}$  and  $\text{D}_2\text{O}$ ). On the other hand, the European and the Japanese design distinguish between moderator and coolant. The moderator usually flows in the opposite direction of the coolant and, under full power conditions, is much more dense than the coolant. As a result, the radially averaged hydrogen density is considerably lower over a large part of an operating SCWR than in the PROTEUS test lattice. Although both moderator and coolant densities vary over the axial position considered in the core (especially in the complex European three-pass core arrangement), representative average values have been chosen for making the present comparisons.

According to Hofmeister et al. [6], the European design proposes a moderator density of  $620 \text{ kg/m}^3$  and a coolant density of  $170 \text{ kg/m}^3$  at the core mid-plane. These values have been chosen for both the European and Japanese assemblies since, in the case of the latter, they lie within the range calculated by Yamaji et al. [7]. In the European design (see middle of Fig. 8.1), moderator flows through the central channel in each assembly, as well as the space between neighboring assemblies, while coolant flows around the fuel pins. In the Japanese design (right hand side of Fig. 8.1), moderator flows through the channels between fuel pin rows and columns (each replacing a  $3 \times 3$  array of fuel pins), while coolant, as before, flows around the fuel pins. The difference in average water density has strong effects on the neutron spectrum, which are shown in Fig. 8.3. The Maxwellian peak in the sub-eV range is much more pronounced in the spectrum of the PROTEUS lattice than in the two SCWR assemblies. This is a direct consequence of the higher average  $\text{H}_2\text{O}$  density in the PROTEUS case. It should be noted that, in order to simplify the comparison between the three different assemblies, all calculations have been performed at room temperature (in spite of using, in the case of the two SCWR power reactor designs, moderator and coolant densities representative of full power operation).

### 8.2.1 Integral Parameter Comparison

The first step in assessing the transferability between the PROTEUS reduced geometry model and the assembly designs from Europe and Japan has been to compare the integral parameters of each assembly.

The results, obtained from the three models, are compared in Table 8.2. Focusing first on the CASMO-4E values, the two main deviations of the PROTEUS test lattice from a power reactor SCWR assembly, viz. the average  $\text{H}_2\text{O}$  density and the absence of structural material, is reflected in almost every parameter. While the fraction of neutrons with energies of less than 4 eV ( $\Psi$  value) is 30.3% in the PROTEUS lattice, it is only 15.0% in the European and Japanese designs. This indicates that the spectrum in PROTEUS is much softer. This is also observed when comparing other spectral indices such as  $\text{C8}/\text{F}_{\text{tot}}$  and  $\text{F8}/\text{F}_{\text{tot}}$ .

The number of absorbed neutrons in water per total fission is 2.7 times higher in the PROTEUS

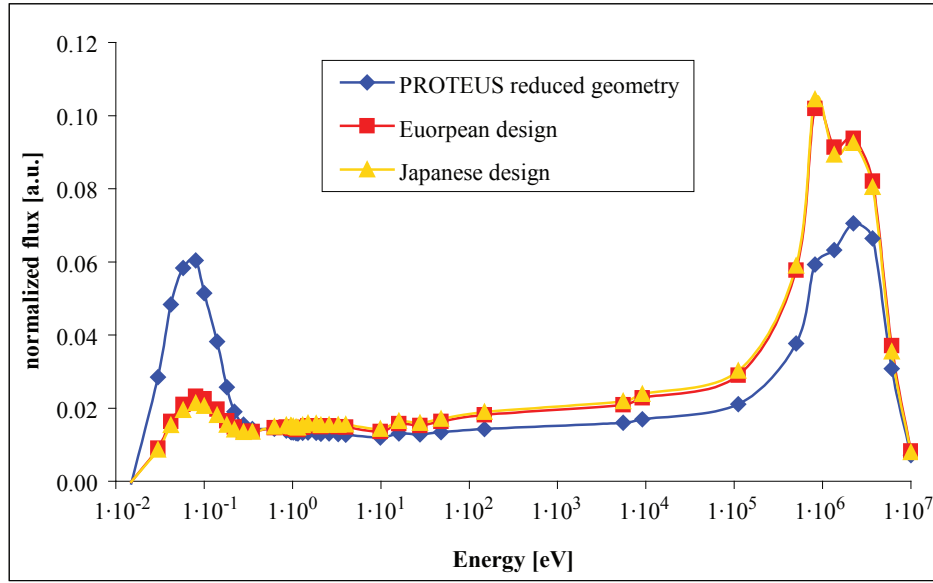


Figure 8.3: Neutron spectra in the PROTEUS reduced geometry model and in the two most advanced SCWR designs. The spectra have been obtained with CASMO-4E.

Table 8.2: Integral parameters for the PROTEUS test lattice (reduced geometry model) and the two proposed SCWR designs, as calculated by CASMO-4E and MCNPX.

Parameter	PROTEUS lattice		European assembly design		Japanese assembly design	
	CASMO	MCNPX	CASMO	MCNPX	CASMO	MCNPX
$(k_{\infty})_{B2=0}$	1.476	1.479	1.243	1.246	1.100	1.106
$B_C^2$ [cm <sup>-2</sup> ]	$9.84 \cdot 10^{-3}$		$2.59 \cdot 10^{-3}$		$1.235 \cdot 10^{-3}$	
$M^2$ [cm <sup>2</sup> ]	48.35		93.95		80.76	
$C_g/F_{tot}$	0.255	0.254	0.420	0.429	0.421	0.416
$F_g/F_{tot}$	0.035	0.036	0.064	0.063	0.062	0.060
$\Psi$	0.303	0.300	0.150	0.150	0.150	0.150
$Abs_{tot}/F_{tot}$	1.670	1.669	1.983	1.981	2.238	2.228
$Abs_{fuel}/F_{tot}$	1.458	1.451	1.656	1.656	1.965	1.953
$Abs_{water}/F_{tot}$	0.204	0.210	0.076	0.076	0.078	0.080
$Abs_{struc}/F_{tot}$	0.008	0.008	0.250	0.249	0.196	0.195
$Prod_{tot}/F_{tot}$	2.451	2.451	2.461	2.462	2.461	2.461
$(k_{\infty})_{FM}$	1.467	1.469	1.241	1.243	1.100	1.105

case, which is due to the differences in water density and the moderator-to-fuel ratio (also higher in PROTEUS). On the other hand, the number of absorbed neutrons in structural material is much higher in the European and Japanese SCWR designs. Due to the harder spectrum, the number of absorbed neutrons in the fuel is also higher in these two models. The sum of these contributions, i.e.  $Abs_{tot}$ , is larger in the European and Japanese design, which leads to a lower  $k_{\infty}$  than in the PROTEUS model (since  $Prod_{tot}/F_{tot}$  - the average number of emitted neutrons per fission,  $\bar{\nu}$  - is almost constant). A direct consequence of the lower  $k_{\infty}$  is the smaller buckling ( $B^2$ ) necessary to get a critical configuration, i.e. the extrapolated height is larger, corresponding to the lower leakage. Finally, the difference in moderation conditions is reflected in the migration area  $M^2$ .

In quantitative terms, the integral parameters shown in Table 8.2 differ quite strongly between the PROTEUS test lattice and the two SCWR design proposals.  $C_8/F_{tot}$ , for example, is 64% higher in the European design (65% in the Japanese design) than in the PROTEUS case, while  $\Psi$  is 50% lower in both designs. The infinite multiplication factor  $k_{\infty}$  is 15% (25%) lower in the European (Japanese) design than in PROTEUS. These differences come from the different  $Abs_{tot}/F_{tot}$  ratios of the configurations. There are various, partly compensating contributions in this context. Due to the absence of assembly and channel boxes in the PROTEUS test lattice, the absorptions in structural material - coming only from absorptions in the aluminum cladding - are much lower. On the other hand, the average water density is higher in the PROTEUS assembly, which leads to more parasitic absorptions. Finally, the harder spectrum in the European and Japanese designs leads to more captures in the fuel (already seen in the  $C_8/F_{tot}$  ratio). The  $Abs_{fuel}/F_{tot}$  ratio of the Japanese design is especially large due to the introduced gadolinium poisoned fuel pins, which are present in neither the European design nor in the PROTEUS lattice.

Comparing the calculated integral values between CASMO-4E and MCNPX for the individual assemblies yields good agreement in all cases. Most of the values agree within 1%. The ratio which gives the biggest discrepancies is  $C_8/F_{tot}$  (2.1% for the European design and 1.2% for the Japanese design). However, compared to the magnitude of the differences in the integral parameters when going from the PROTEUS lattice to one of the power reactor SCWR designs, this agreement is quite satisfactory. Agreement between the codes, however, does not necessarily assure the transferability of the PROTEUS experiments. Due to the considerable differences in neutron balance components and energy spectra, further studies are clearly necessary.

### 8.2.2 Pin-wise Comparisons of Reaction Rates

To further investigate the questions on the transferability raised in the previous section, additional comparisons have been carried out between CASMO-4E and MCNPX for the European and Japanese assembly designs. While good agreement has already been shown for the integral parameters, the following studies are focused on the pin-wise comparisons of reaction rate distributions, as was done during the analysis of the experiments on the basis of reduced geometry

model comparisons (see Chapters 5 and 6).

The comparison of CASMO-4E and MCNPX calculated reaction rate distributions across the Japanese SCWR assembly yielded a satisfactory degree of agreement, comparable to that achieved for the PROTEUS test lattice; the discrepancies were only slightly higher, viz. 1.0% and 1.7% for  $F_{\text{tot}}$  and  $C_8$ , respectively. Analysis of the same reaction rates across the European HPLWR assembly, however, showed more severe deviations. Fig. 8.4 illustrates the comparison between CASMO-4E (C) and MCNPX (C'), in terms of C/C' values. The total fission rate distribution, shown in the upper left plot of Fig. 8.4, is very similarly predicted by the two codes (agreement within 0.4%). However, the  $C_8$  distribution, illustrated in the upper right plot, shows discrepancies of up to 4.1%, which are, due to the good agreement in  $F_{\text{tot}}$ , directly projected into the comparison of  $C_8/F_{\text{tot}}$ , shown at the bottom.

The significant discrepancies in  $C_8$  arise exclusively in the corner pins of the assembly (A1, A7, G1, and G7, henceforth denoted as outer corners) and in the pins at the corners of the central moderator box (B2, B6, F2, and F6, henceforth denoted as inner corners). CASMO-4E predicts the  $C_8$  in the inner corners 4.1% lower than MCNPX and that in the outer corners 2.4% higher. The  $C_8$  values for all the other pins of the assembly agree within 0.8%, which is similar to what was observed for the PROTEUS test lattice. The  $C_8/F_{\text{tot}}$  map shows the same trends. The inner corner pins are underestimated by CASMO-4E by 3.7% and the outer corners overestimated by 2.4%, when considering deviations from the assembly average of 0.978. A slight overestimation of  $C_8/F_{\text{tot}}$  (in the order of 1.3%) is also seen for the pins at the centers of the sides of the moderator channel (B4, D2, D6, and F4). This comes from a slight underestimation of the local  $F_{\text{tot}}$  rate and a simultaneous overestimation of the  $C_8$  rate.

### 8.2.3 Investigation of Reaction Rate Distributions as Calculated by MCNPX

In order to better understand the observed discrepancies, one needs to look at the peculiarities of the lattice itself, which are not visible in a C/C' comparison. Therefore, the reaction rate maps, as calculated by MCNPX, are depicted in Fig. 8.5. The  $F_{\text{tot}}$  distribution (shown in the upper left plot) shows a strong increase of fissions in the outer corner pins (approximately 20%) and, on the other hand, a reduction of almost 10% in the inner corners. These are the two extreme values, originating in the unique lattice positions that they represent. The assembly was designed to optimize the power distribution and to reduce the radial power peaking factors. However, the outer corner pins are adjacent on two sides to the 1 cm wide inter-assembly gaps, located in between any two neighboring assemblies, which are filled with high density moderator. This leads to a peak in the thermal neutron flux in these pins.

The enhanced moderation can also be observed in the  $C_8/F_{\text{tot}}$  map, shown in the bottom plot of Fig. 8.5. The ratio has a minimum at the outer corners, where it is about 5% lower than the assembly average of 0.429. The  $^{238}\text{U}$  capture rate is also increased in the outer corners ( $\approx 15\%$ ), as can be seen in the upper right plot.  $C_8$  and  $F_{\text{tot}}$  rates in the inner corner pins



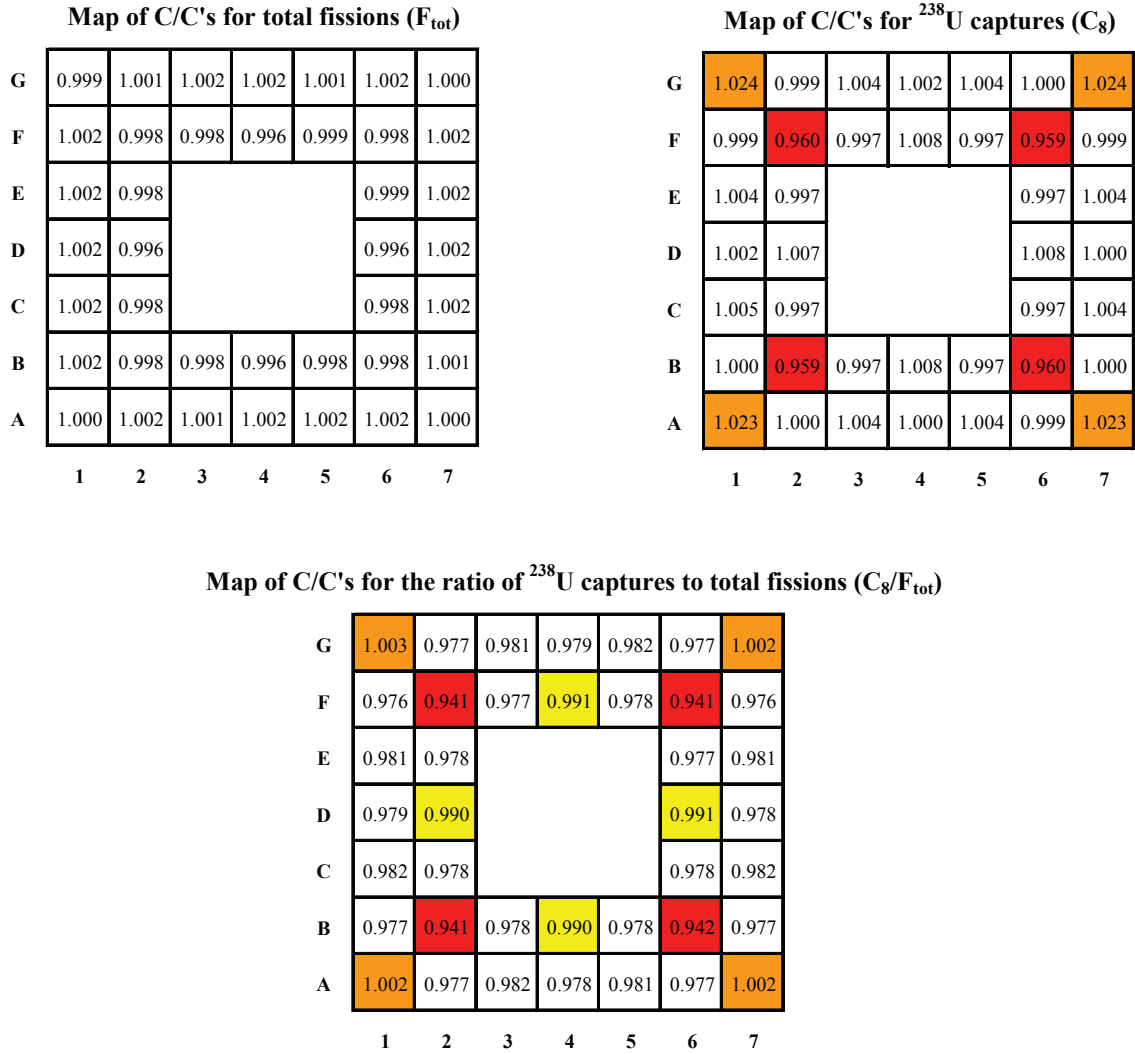


Figure 8.4: Comparison between CASMO-4E (C) and MCNPX (C') predictions in terms of C/C' values for the reaction rate (and ratio) distributions across the European HPLWR assembly. Deviations from the average value for the assembly that are between 1% and 2% are indicated by yellow coloring of the cell, those between 2% and 3% by orange, and those above 3% by red. The average values for the assembly are 1.0 for  $F_{\text{tot}}$  and  $C_8$  (due to normalization of the maps), and 0.978 for  $C_8/F_{\text{tot}}$ .

are reduced by almost the same amount, which results in  $C_8/F_{\text{tot}}$  values close to the assembly average (0.430). The inner corner pins have the least direct contact with the moderator, because they are surrounded on all four sides by neighboring fuel pins. Both the thermal flux and the effective  $^{238}\text{U}$  resonance cross section (due to shielding effects) are reduced, depressing the  $F_{\text{tot}}$  and  $C_8$  values. As for the remaining fuel pins, the distributions are rather flat. The total fission rate varies only between 0.942 and 1.036, hence within 9%, when the inner and outer corner pins are not considered. For the  $C_8$  rate, the distribution is flatter yet, the corresponding variation being between 0.955 and 1.023.

From the above, and while considering the  $C/C'$  values of Fig. 8.4, one may conclude that CASMO-4E predicts the reduction of  $^{238}\text{U}$  resonance captures in the inner corner pins as significantly more severe than MCNPX, and it also predicts the increase in the outer corner pins as higher - all of this, while the thermal flux (reflected largely by the  $F_{\text{tot}}$  distribution) is calculated very similarly by the two codes.

## 8.2.4 Further Studies for the Transferability to the European HPLWR Design

### 8.2.4.1 Integral Parameter Comparison

The investigations in the previous subsections have uncovered certain discrepancies in the pin-wise reaction rate estimations between CASMO-4E and MCNPX. The observed discrepancies are limited to the European design, since similar comparisons for the Japanese design yielded satisfactory agreement. In order to investigate the origin of the discrepancies, two hypothetical cases are considered in this subsection. To check whether the deviations come from the harder neutron spectrum in the European assembly, the first hypothetical case is that of the PROTEUS test lattice with a decreased  $\text{H}_2\text{O}$  density, the reduction being such that the spectral index  $\Psi$ , as calculated with CASMO-4E, is equal to that of the HPLWR assembly, viz. 0.150. In the following, this configuration is denoted as *PROTEUS lattice with HPLWR moderator conditions*.

The change considered for the second hypothetical configuration goes in the opposite direction. Instead of hardening the spectrum of the PROTEUS test lattice, the spectrum of the HPLWR assembly is softened. The water density of both the moderator and coolant is increased to approximately the water density of an operating PWR ( $0.705 \text{ g/cm}^3$ ). Clearly, this corresponds to a spectrum which is much softer than that envisaged for the HPLWR. This configuration is denoted as *European design with PWR moderator conditions*. By raising the water density, the  $\Psi$  value increases to 0.195. The spectra of the two hypothetical configurations are shown in Fig. 8.6, along with the spectrum of the original PROTEUS lattice (tallied, in each case, over the entire assembly).

As seen in the figure, the spectrum of the adjusted PROTEUS configuration (with HPLWR moderator conditions) resembles that of the original HPLWR and Japanese configurations (see Fig. 8.3). The spectral indices,  $C_8/F_{\text{tot}}$ ,  $F_8/F_{\text{tot}}$ , and  $\Psi$  confirm this qualitative observation (see

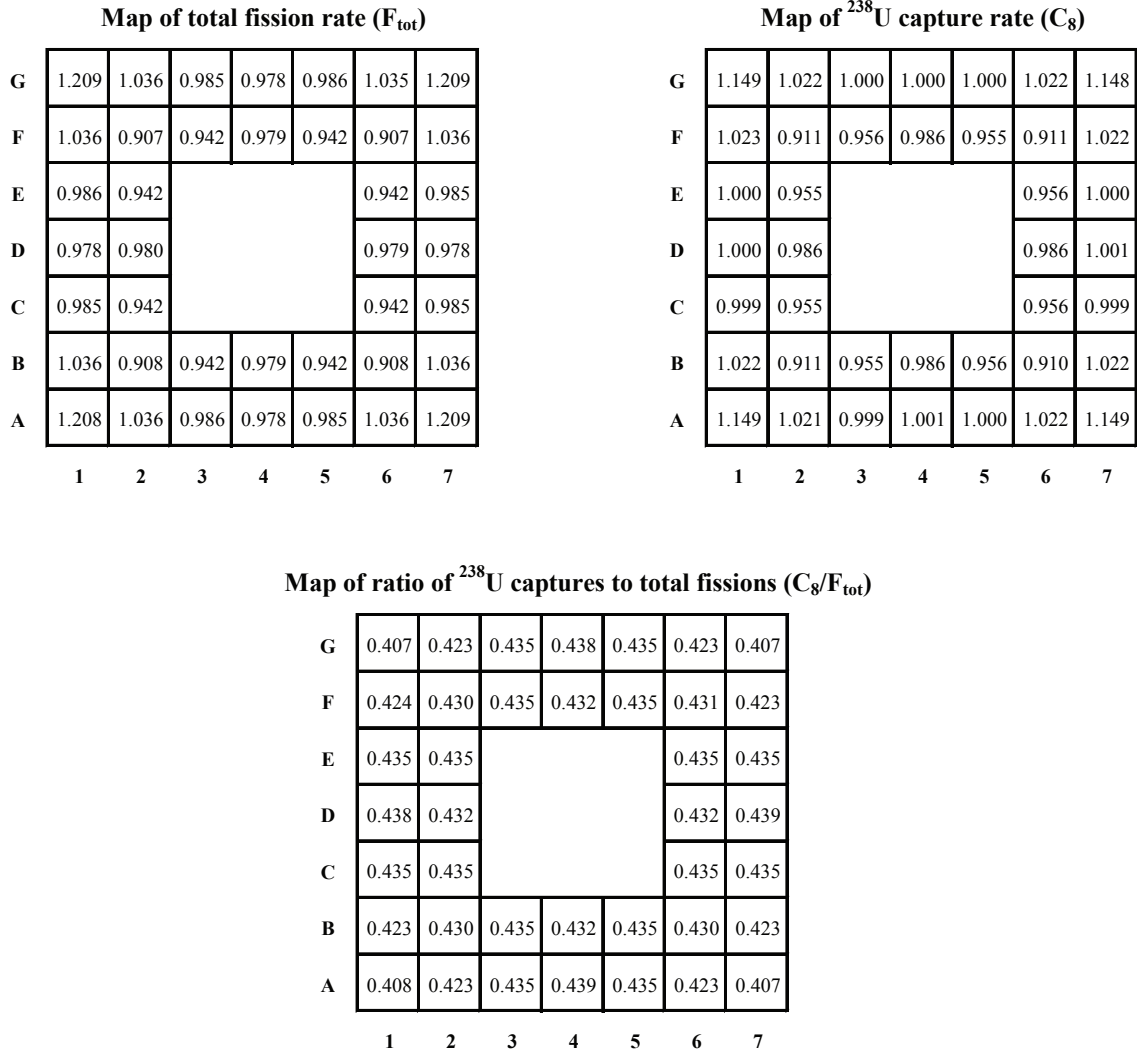


Figure 8.5: Reaction rate (and ratio) distributions across the European HPLWR assembly, as calculated by MCNPX. The average values are 1.0 for the  $F_{\text{tot}}$  and  $C_8$  rates (due to normalization), and 0.429 for the  $C_8/F_{\text{tot}}$  rate.

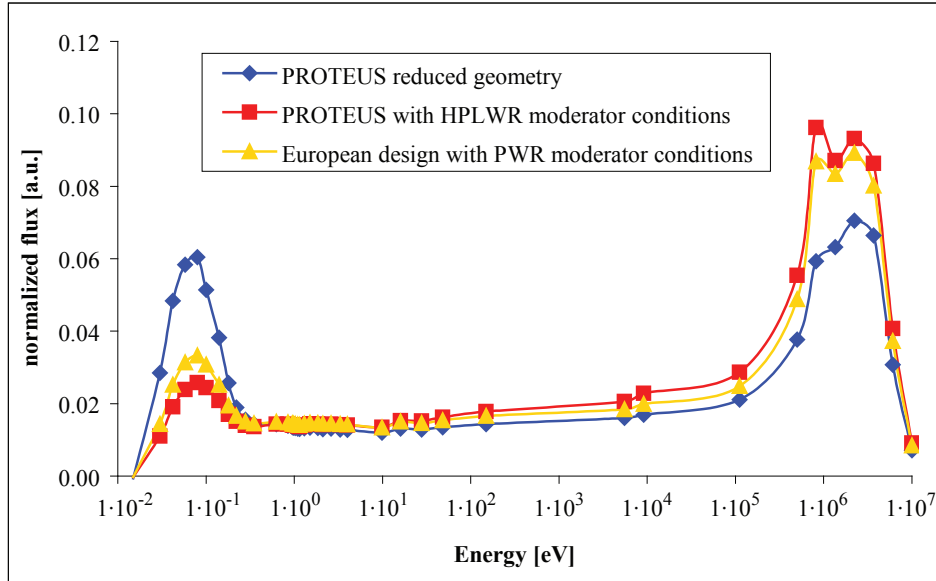


Figure 8.6: Neutron spectra in the PROTEUS reduced geometry model and in the two hypothetical configurations. In the *PROTEUS lattice with HPLWR moderator conditions* configuration, the density of the water was reduced until the spectral index  $\Psi$  was equal to that of the HPLWR assembly. In the *European assembly design with PWR moderator conditions* configuration, the density of the moderator was increased to approximately that of a PWR. The spectra have been obtained with CASMO-4E and were normalized individually.

Table 8.3 and compare with Table 8.2). On the other hand, the softening of the spectrum in the European design (by setting the moderator density to that of a PWR) yields a spectrum which is far from that of the original PROTEUS configuration. The moderator-to-fuel volume ratio is much larger in the PROTEUS lattice than in the HPLWR assembly. Nevertheless, a significant softening effect is achieved.

The integral parameters for the two hypothetical configurations, as calculated by CASMO-4E and MCNPX, are listed in Table 8.3, along with the results for the original PROTEUS lattice. The codes agree to the same degree as before, for both hypothetical configurations. While for the *PROTEUS lattice with HPLWR moderator conditions* configuration, the spectral indices differ quite strongly from the original PROTEUS case, the neutron balance in terms of total absorptions and productions does not seem to be significantly affected. The  $\text{Abs}_{\text{tot}}/\text{F}_{\text{tot}}$  ratio changes only by 2.8% and the  $\text{Prod}_{\text{tot}}/\text{F}_{\text{tot}}$  ratio by 0.5%. Because they are both increased slightly, these changes imply a change of  $k_{\infty}$ , calculated in the fundamental mode spectrum, of 2.2%. The change in  $\text{Abs}_{\text{tot}}/\text{F}_{\text{tot}}$  is the net effect of two considerably larger individual effects that compensate each other. Through the reduced water density, the parasitic absorptions in water (relative to  $\text{F}_{\text{tot}}$ ) are reduced from about 20% to less than 7%. At the same time, due to the harder spectrum, the absorptions in the fuel (relative to  $\text{F}_{\text{tot}}$ ) are increased from about 146% to 164%. This is largely due to the increased importance of  $^{238}\text{U}$  resonance captures. The absorptions in the structural material remain marginal.

Table 8.3: Comparison of integral parameters for the PROTEUS reduced geometry model and the two hypothetical configurations, as calculated by CASMO-4E and MCNPX.

Parameter	PROTEUS lattice		PROTEUS lattice with HPLWR moderator conditions		European assembly design with PWR moderator conditions	
	CASMO	MCNPX	CASMO	MCNPX	CASMO	MCNPX
$(k_{\infty})_{B2=0}$	1.476	1.479	1.442	1.453	1.266	1.269
$B_C^2 [\text{cm}^{-2}]$	$9.84 \cdot 10^{-3}$		$2.05 \cdot 10^{-3}$		$4.764 \cdot 10^{-3}$	
$M^2 [\text{cm}^2]$	48.35		215.92		55.80	
$C_8/F_{\text{tot}}$	0.255	0.254	0.410	0.407	0.349	0.354
$F_8/F_{\text{tot}}$	0.035	0.036	0.067	0.068	0.049	0.049
$\Psi$	0.303	0.300	0.150	0.151	0.195	0.194
$\text{Abs}_{\text{tot}}/F_{\text{tot}}$	1.670	1.669	1.717	1.703	1.943	1.932
$\text{Abs}_{\text{fuel}}/F_{\text{tot}}$	1.458	1.451	1.644	1.630	1.568	1.557
$\text{Abs}_{\text{water}}/F_{\text{tot}}$	0.204	0.210	0.065	0.065	0.113	0.113
$\text{Abs}_{\text{struc}}/F_{\text{tot}}$	0.008	0.008	0.008	0.008	0.262	0.262
$\text{Prod}_{\text{tot}}/F_{\text{tot}}$	2.451	2.451	2.463	2.464	2.456	2.456
$(k_{\infty})_{\text{FM}}$	1.467	1.469	1.434	1.447	1.264	1.271

Analogous observations can be made for the other hypothetical configuration, the HPLWR assembly with moderator density of a PWR. Comparing the results with those of the original HPLWR assembly (see Table 8.2), the spectral indices change notably, but not as strongly as in the previous case. Once again, the  $\text{Abs}_{\text{tot}}/F_{\text{tot}}$  changes only marginally. This time, this is due to the compensation of an increase in parasitic absorptions in the water and a reduction of the absorption in the fuel.

#### 8.2.4.2 Pin-Wise Comparison of Reaction Rates

In comparing CASMO-4E and MCNPX results for the pin-wise reaction rate distributions for the two hypothetical cases, it was found that the reduction of the moderator density in the PROTEUS test lattice did not significantly change the excellent pin-wise agreement between the codes. In fact, the maximal discrepancies that were found in a single pin were 0.7% for  $F_{\text{tot}}$  and 1.3% for  $C_8$  (previously 1.1% and 1.0% for  $F_{\text{tot}}$  and  $C_8$  respectively, as shown in Sec. 5.4). However, the increased water density in the European HPLWR assembly was found to considerably improve the  $C_8$  discrepancies found for the corner pins in the original case (see Subsec. 8.2.2).

Fig. 8.7 shows the CASMO-4E, MCNPX comparisons for the European HPLWR assembly with PWR moderator conditions. On the upper left of the figure, the  $C/C'$  map for the total fission rate is plotted, showing excellent agreement between the codes, the largest deviation being 0.3% (0.4% for the standard HPLWR configuration). As stated above, the increased moderation results in much better agreement in the pin-wise  $C_8$  distribution, which is shown on the upper right of

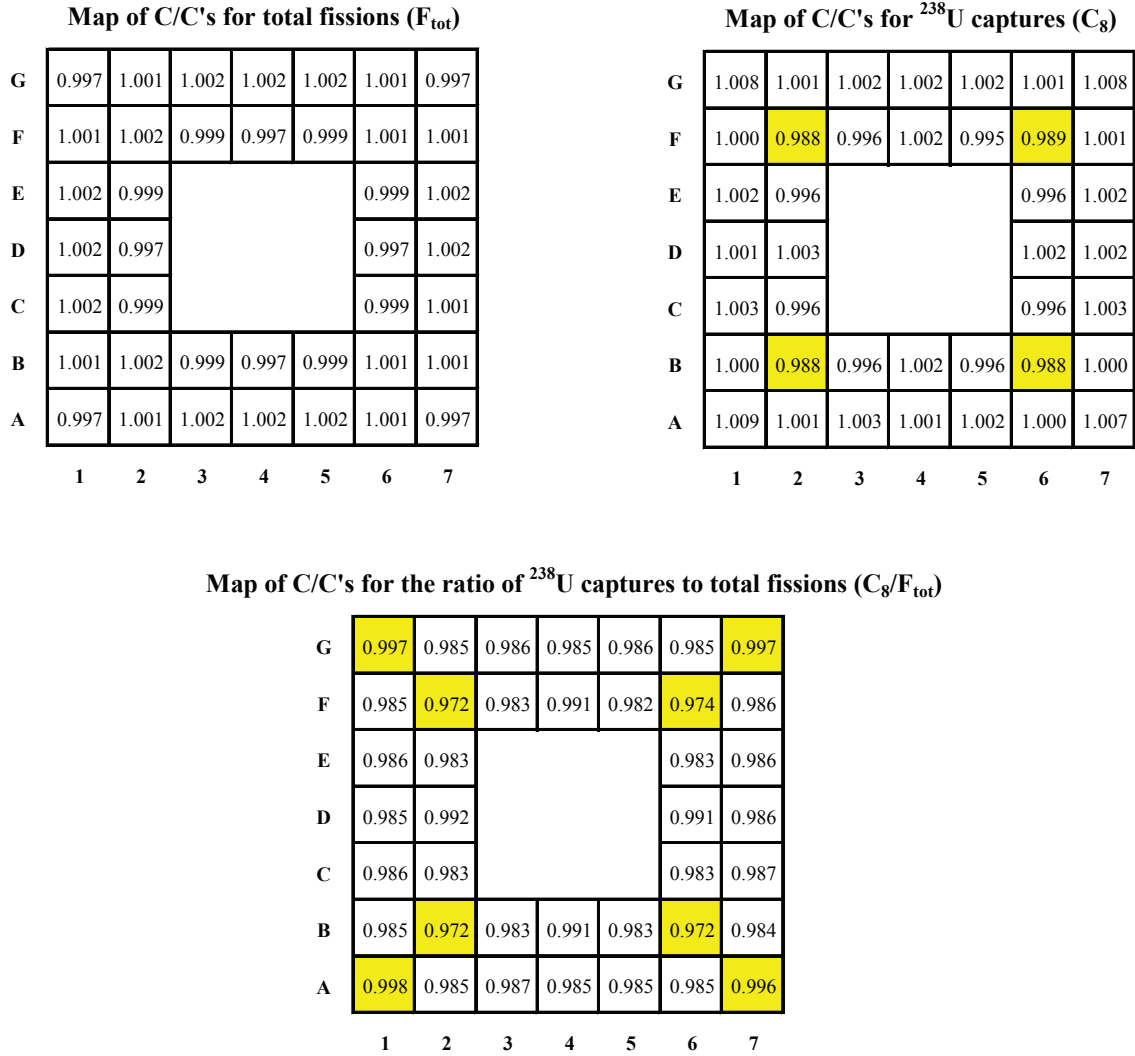


Figure 8.7: Comparison between CASMO-4E (C) and MCNPX (C') predictions in terms of C/C' values for the reaction rate (and ratio) distributions across the European HPLWR assembly with PWR moderator conditions. Deviations from the average value for the assembly that are between 1% and 2% are indicated by yellow coloring of the cell. The average values for the assembly are 1.0 for  $F_{\text{tot}}$  and  $C_8$  (due to normalization of the maps), and 0.985 for  $C_8/F_{\text{tot}}$ .

Fig. 8.7. The outer corners agree now within 0.8% (before it was 2.4%) and the inner corners remain the only pins that have discrepancies of more than 1%, namely 1.2% (before it was 4.1%). The previous 0.8% overestimation of CASMO-4E for the pins at the center of the lines adjacent to the moderator channel (B4, D2, D6, and F4) has also improved to 0.3%. Thus, overall, CASMO-4E and MCNPX agree rather well for the HPLWR lattice with increased moderator and coolant density (to an extent which is similar to that observed for the well moderated PROTEUS test lattice configuration). The trend previously observed for the original HPLWR assembly, however, is still visible:  $C_8$  in the outer corner pins is estimated to be higher with CASMO-4E than with MCNPX, and lower in the case of the inner corner pins.

The pin-wise comparison of the  $C_8/F_{\text{tot}}$  ratio, which is depicted in the bottom plot of Fig. 8.8, shows a pattern which is quite similar to that of the  $C_8$  map. This is not surprising since the  $C/C'$  values for  $F_{\text{tot}}$  are very close to 1 for all pins. Thus, the results for the outer corner pins are overestimated by CASMO-4E, while those for the inner corner pins are underestimated, when considering the deviations from the assembly average which, in this case, is 0.985. The discrepancies are also of similar magnitude, the largest being 1.3%.

#### 8.2.4.3 Investigation of Reaction Rate Distributions as Calculated by MCNPX

To better understand the differences between the original HPLWR assembly, which had yielded discrepancies between the codes, and the HPLWR assembly with increased moderator and coolant density, which has yielded much better agreement, the MCNPX results for the modified assembly are depicted in Fig. 8.8. Coupling the results with those shown for the original assembly in Fig. 8.5, it is seen - from the  $F_{\text{tot}}$  map in the upper left plot - that the heterogeneity of the thermal flux distribution is slightly increased. Thus,  $F_{\text{tot}}$  in the outer corner pins is slightly more peaked (22.1% above the assembly average, as compared to 20.9% in the original setup) and the depression at the inner corner pins is 11.0% (before it was 9.3%). The total fission distribution in the other pins remains the same within 0.4%.

Contrary to the change for  $F_{\text{tot}}$ , the  $C_8$  distribution becomes flatter for the increased moderation conditions. The peaking in the outer corner pins is reduced from 14.9% to 12.2%, and the depression in the inner corner pins is reduced from 8.9% to 7.7%, all relative to the respective assembly average. The pattern for the remaining pins is also flatter than before, the maximum deviation from unity now being 3.1% (as compared to 4.5% in the original HPLWR assembly). As regards the  $C_8/F_{\text{tot}}$  distribution, this is somewhat more pronounced. Due to the increase in moderator density, the spectrum is softer in all pins, but the deviation of  $C_8/F_{\text{tot}}$  in the outer corner pins (from the assembly average, which is 0.355 in this case) is larger (0.030) than in the case for the original assembly (deviation of 0.022 from the average value of 0.429).

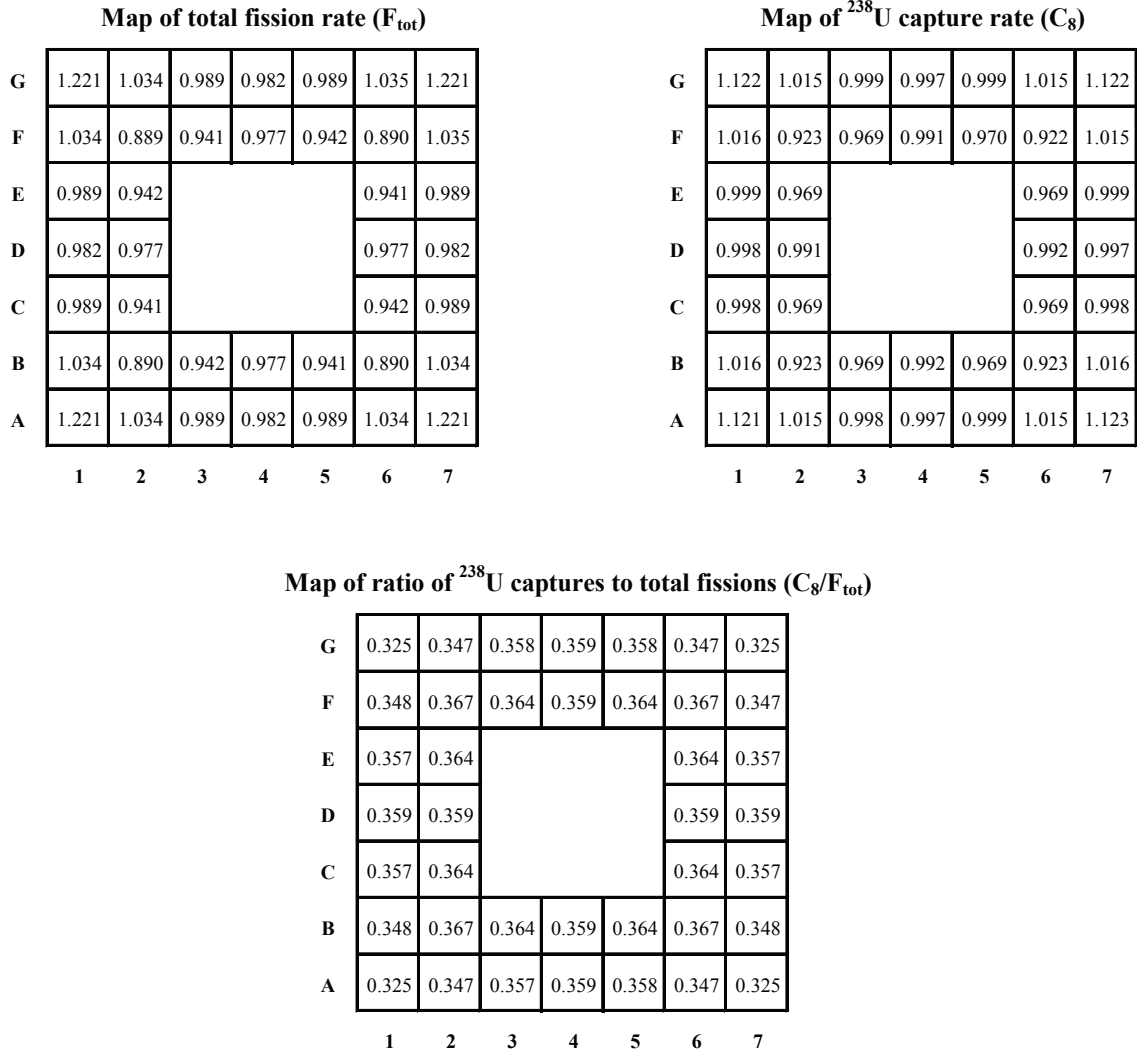


Figure 8.8: Reaction rate (and ratio) distributions across the European HPLWR assembly with PWR moderator conditions, as calculated by MCNPX. The average values are 1.0 for the  $F_{\text{tot}}$  and  $C_8$  rates (due to normalization), and 0.355 for the  $C_8/F_{\text{tot}}$  rate.



### 8.2.5 Chapter Summary

It has been seen that, although the PROTEUS experiments are of generic relevance to the study of LWR lattices with strong moderation heterogeneity, the direct transferability of the carried out code validation to the most recent SCWR concepts under power reactor conditions is somewhat limited. This follows from the considerable neutronics differences between the investigated power reactor designs and the experimental SCWR-like test lattice, the main cause being the higher water density in the PROTEUS experiments, which results in a considerably softer neutron spectrum.

Comparisons between CASMO-4E and MCNPX calculations for the two reference SCWR assemblies - corresponding to the European and the Japanese concept designs, respectively - show a degree of agreement in predicted integral parameters which is almost as good as for the PROTEUS test lattice. This provides some indication that the accuracy of the deterministic calculations does not deteriorate markedly when considering the power reactor situation.

In considering pin-wise reaction rate distributions, the consistency in CASMO-4E and MCNPX results remains satisfactory for  $F_{\text{tot}}$  for both the SCWR power reactor assemblies, in spite of their much harder neutron spectra relative to the experimental test lattice. Results for the pin-wise  $C_8$  distribution - which is sensitive to treatment of the resonance capture in  $^{238}\text{U}$  - is also satisfactory in the case of the Japanese assembly design. For the European HPLWR case, however, discrepancies of up to about 4% occur between CASMO-4E and MCNPX. These appear to be related to a combination of factors, viz. the harder neutron spectrum and the characteristic geometry of the HPLWR assembly which has, as opposed to the Japanese assembly and the PROTEUS test lattice, double rows and columns of fuel pins.

Overall, CASMO-4E and MCNPX have been found to yield - as in the case of the experimental SCWR-like lattice - very satisfactory agreement in the prediction of integral and pin-wise reaction rate distributions for the two SCWR power reactor fuel assembly designs. Nevertheless it is important to remain cautious when using CASMO-4E under spectral conditions, and for assembly geometries, that differ considerably from those investigated in the present experiments. Although less expected, it is also possible that MCNPX results are significantly erroneous in such cases. Clearly, a wider range of experiments - covering also harder neutron spectra, as well as lattice geometries with features such as the double pin rows and columns of the European HPLWR design - are needed for providing a sufficiently broad integral database.

# Bibliography

- [1] Y. Oka, S. Koshizuka, and T. Yamasaki. Direct Cycle Light Water Reactor Operating at Supercritical Pressure. *Journal of Nuclear Science and Technology*, 29(6):585–588, 1992.
- [2] K. Fischer, T. Schulenberg, and E. Laurien. Design of a Supercritical Water-Cooled Reactor with a Three-Pass Core Arrangement. *Nuclear Engineering and Design*, 239:800–812, 2009.
- [3] K. Kamei, A. Yamaji, Y. Ishiwatari, Y. Oka, and J. Liu. Fuel and Core Design of Super Light Water Reactor with Low Leakage Fuel Loading Pattern. *Journal of Nuclear Science and Technology*, 43(2):129–139, 2006.
- [4] A.-S. Bayard. Transferability of Measurements in the PROTEUS SCWR-like Test Lattice to the Validation of Alternative SCWR Assembly Designs. Master’s thesis, École Polytechnique Fédérale de Lausanne, Lausanne, Switzerland, 2011.
- [5] A. Yamaji, Y. Oka, and S. Koshizuka. Conceptual core design of a 1000MWe supercritical pressure light water cooled and moderated reactor. In *ANS/HPS Student Conference, Texas A&M University*, 2001.
- [6] J. Hofmeister, C. Waata, J. Starflinger, T. Schulenberg, and E. Laurien. Fuel assembly design study for a reactor with supercritical water. *Nuclear Engineering and Design*, 237:1513–1521, 2007.
- [7] A. Yamaji, Y. Oka, and S. Koshizuka. Three-dimensional Core Design of High Temperature Supercritical-Pressure Light Water Reactor with Neutronic and Thermal-Hydraulic Coupling. *Journal of Nuclear Science and Technology*, 42(1):8–19, 2005.

## 9 Conclusions and Recommendations for Future Work

The presented research has focused on the creation of an experimental neutronics database for SCWR-like fuel assemblies with large moderation heterogeneities, and on its utilization to validate Monte-Carlo and production neutronics codes. The database resulted from an extensive experimental campaign conducted at the PROTEUS zero-power research reactor of the Paul Scherrer Institute. An SCWR-like lattice was loaded in the central test zone of PROTEUS and studied under various conditions - unperturbed and perturbed corresponding to control rod related effects, the variation of moderation conditions, and the presence of a gadolinium absorber pin. The lattice was characterized by measuring pin-by-pin radial distributions of fission and  $^{238}\text{U}$  capture rates, as well as the reactivity worths of individual fuel pins.

The thesis, apart from these concluding pages, has been divided into eight chapters. Chapters 1 and 2 gave an introduction to the subject, and some background information on Supercritical-Water-Cooled Reactors (SCWRs) and the zero-power research facility PROTEUS in which the experimental part of this thesis had been carried out. Chapters 3 and 4 introduced, respectively, the experimental and calculational tools used for the code validation. Chapters 5 and 6 discussed the validation of the codes via reaction rate distributions across unperturbed and perturbed SCWR-like lattices, respectively. In total, six perturbed configurations were investigated. Chapter 7 reported on the code validation via reactivity worth predictions of single fuel pins, and also considered the accuracy of the whole-reactor  $k_{\text{eff}}$  calculations for the various PROTEUS configurations. Finally, Chapter 8 assessed the transferability of the PROTEUS experiments to current SCWR assembly design proposals.

Section 9.1 of this final chapter summarizes the thesis in terms of the main results and the corresponding conclusions. Recommendations for future work are given in Sec. 9.2.

### 9.1 Main Results

The SCWR - the Generation-IV reactor concept most closely related to today's LWRs - offers the possibility of an energy conversion efficiency of up to 45%. To achieve this increase, the coolant outlet temperature is raised to approximately 500 °C. This implies that the coolant (light

water) is in a supercritical state, with a much lower average density (in the order of  $0.2 \text{ g/cm}^3$ ) than the coolant in LWRs. In order to establish a thermal neutron spectrum, relatively large moderator regions have to be implemented into the fuel assembly. Consequently, there are strong heterogeneities in the moderation conditions, resulting in non-uniform power generation in the individual fuel pins. The power may differ by up to 25% between directly neighboring fuel pins (if constant material densities and homogeneous enrichment are assumed).

Modern nuclear design codes, such as the probabilistic MCNPX and the deterministic CASMO-4E, accurately predict neutronics parameters for current-day LWRs. However, the heterogeneous moderation conditions of an SCWR are outside the validation domain of these codes. Representative experimental data, which is necessary to validate the codes, is scarce, so that the availability of appropriate integral measurements is of considerable importance for the further development of design tools and the reactor concept. In addition, recent calculations of advanced LWR configurations with large heterogeneities in fuel/moderation conditions indicated considerable differences between deterministic and probabilistic codes [1].

Strongly heterogeneous moderation conditions across the fuel assembly influence the basic neutronics and safety-related parameters of an LWR. This doctoral thesis has presented experiments that were designed to study these effects. The accompanying analytical analysis has provided insight into the modeling of such assemblies. As presented below, this has been achieved largely in the context of investigating the corresponding predictive performance of CASMO-4E and MCNPX.

### 9.1.1 Reaction Rate Distributions in the Unperturbed SCWR-like Lattice

The unperturbed SCWR-like lattice loaded in PROTEUS has first been characterized by measuring the pin-by-pin radial distributions of total fission and  $^{238}\text{U}$  capture rates by gamma spectroscopy. Sixty-one of the 105 fuel pins were measured to fully characterize the reference lattice, and the reproducibility of the measurements was checked via two independent measurement campaigns. The experimental results were used to validate the predictions obtained with a PROTEUS whole-reactor model, set up using MCNPX in conjunction with its ENDF/B-VII.0 data library. The MCNPX predictions for the  $F_{\text{tot}}$  and  $C_8$  radial maps have been found to be in agreement with the measurements within  $2\sigma$ . The  $1\sigma$  uncertainty on the calculation-to-experimental ratios ( $C/E_s$ ) is lower than 1% for both the  $F_{\text{tot}}$  and  $C_8$  reaction rate distributions, because the normalization process reduces the impact of the uncertainty on the nuclear data. MCNPX predictions and measurements agree within  $1\sigma$  (2.2%) for the pin-by-pin values of the modified conversion ratio ( $C_8/F_{\text{tot}}$ ). The uncertainty is larger than for the  $F_{\text{tot}}$  and  $C_8$  distributions because the systematic errors on the nuclear data (e.g. branching ratio, fission yields) do not cancel out. The good agreement for  $F_{\text{tot}}$ ,  $C_8$  and  $C_8/F_{\text{tot}}$  maps confirms that MCNPX correctly captures the variation of the neutron spectrum across the SCWR lattice and can thus be considered as successfully validated for these heterogeneous moderation conditions.

A basic aim of this doctoral research has been the validation of not only Monte Carlo methods, but also of deterministic assembly codes used routinely for analyzing present-day LWRs. In considering certain specific characteristics of the test lattice configuration, it has been found advantageous to apply a 2-step validation strategy for the deterministic code studied, viz. CASMO-4E. The first step is essentially that described above, viz. the demonstration that a Monte Carlo modeling of the full PROTEUS reactor using MCNPX yields very good agreement with the experimental results. Since MCNPX can well predict the reaction rate distributions in the SCWR-like test lattice while considering the multi-zone nature of the PROTEUS reactor, one can assume that it is able to do so for the corresponding, reflected SCWR-like assembly model. In the second step, this so-called reduced geometry model is used for validating CASMO-4E.

Comparison between the reaction rate distributions predicted for the reduced geometry model by CASMO-4E (C) and MCNPX (C') yielded satisfactory results. The data library used with CASMO-4E is a proprietary library based on ENDF/B-VI. The calculated distributions of  $F_{\text{tot}}$  and  $C_8$ , as well as their ratio  $C_8/F_{\text{tot}}$ , have all been found to agree within  $\sim 1\%$ . Only a minor trend can be observed when comparing the C/C' values of the intrinsically different fuel pin positions in the lattice. CASMO-4E slightly overestimates the pins at intersections of rows and columns (0.7% for  $F_{\text{tot}}$  and 0.6% for  $C_8$ ), while underestimating just as slightly the other pin positions.

In conclusion, both the MCNPX and CASMO-4E codes can be considered as successfully validated for the unperturbed SCWR-like fuel lattice.

### 9.1.2 Reaction Rate Distributions in the Perturbed SCWR-like Lattices

Following the validation of CASMO-4E and MCNPX for the unperturbed SCWR-like test lattice, a number of perturbed lattices were investigated in much the same way. In each case, measured reaction rate distributions across the test lattice were compared with the code predictions. As before, the 2-step validation approach has been used to validate, in turn, MCNPX and CASMO-4E.

The investigated configurations can be considered in three groups. The first group is concerned with studying effects related to the insertion of control rods into the four central moderator channels of the SCWR-like lattice. In order to separate the effects of moderator displacement and neutron absorption, aluminum and stainless steel rods were inserted in turn. The second group of perturbed configurations investigates the effects of moderation density changes in the SCWR-like lattice. Water tanks filled with two different mixtures of  $\text{H}_2\text{O}$  and  $\text{D}_2\text{O}$  were inserted, in turn, into the four central moderator channels to simulate different hydrogen densities. The third group of configurations investigates the effect of removing the central fuel pin and replacing it with gadolinium-poisoned fuel. In total, reaction rate distributions were measured and analyzed in six different perturbed configurations.

**MCNPX Validation** The agreement between the whole-reactor model of MCNPX and the experiments has been found to be satisfactory for all six perturbed configurations. Most of the pins agree within  $2\sigma$ , there being no discrepancy above  $3\sigma$ . The uncertainties on the C/E values include the uncertainty of the probabilistic calculation, the counting uncertainties of the experiments and the uncertainties on the nuclear data. The nuclear data uncertainties play a significant role only for the unnormalized pin-by-pin  $C_8/F_{\text{tot}}$  distributions. The  $1\sigma$  level of the combined uncertainties are in the order of 0.4%, 0.8%, and 2.2% for  $F_{\text{tot}}$ ,  $C_8$ , and  $C_8/F_{\text{tot}}$ , respectively. MCNPX can thus be considered as validated for all the perturbed configurations.

**CASMO-4E Validation** To validate CASMO-4E, the  $F_{\text{tot}}$ ,  $C_8$ , and  $C_8/F_{\text{tot}}$  radial distributions predicted with CASMO-4E and MCNPX were compared using the reduced geometry model. This was done for each of the six perturbed configurations, and the corresponding findings are summarized below.

For the configuration with inserted steel rods, the MCNPX and CASMO-4E predictions are consistent within the uncertainties. Thus, as for the unperturbed case, calculated distributions of  $F_{\text{tot}}$  and  $C_8$ , as well as their ratio  $C_8/F_{\text{tot}}$ , all agree within  $\sim 1\%$ . For the configuration with inserted aluminum rods, however, discrepancies of up to 2.6% were found between the codes, CASMO-4E overestimating both fission and  $^{238}\text{U}$  capture rates in pins located near the perturbation. This was surprising initially, since the steel rods perturbed the system in a stronger way than the aluminum rods did. The underestimation was found to be a consequence of the default leakage treatment in CASMO-4E, which is carried out in the usual homogenized sense across the lattice. As such, the global leakage gradient across the “moderator displacement” configuration with the aluminum rods was not captured properly. The optional input card BZ2 solves this problem by allowing a region-specific treatment of the axial leakage effects. The CASMO-4E and MCNPX reaction rate results then agree well, also for the configuration with aluminum rods.

For both the configurations with perturbed moderator density, CASMO-4E and MCNPX reduced geometry model results have been found to agree generally within 1%. The fuel pins at the intersections of rows and columns have shown slightly greater disagreement (up to 1.8%). Since the water tanks introduce a global leakage gradient across the assembly, the optional CASMO-4E input card BZ2 needed to be used. Without this correction, the predictions of the total fission rate disagreed by up to 4.6%. As such, the large discrepancies between CASMO-4 and MCNP4C calculations that were reported by Jatuff et al. [1] in the case of a moderator density reduction in the central channels of an SCWR-like assembly may be ascribed to the inadequate leakage treatment provided by the default option in CASMO-4.

Since the removal of the central fuel pin only amounted to being a local perturbation of the SCWR-like lattice, it was expected that similar agreement would be found between the codes as for the unperturbed configuration. This has indeed been the case, the results for each investigated reaction rate distribution agreeing within 1%. Inserting a gadolinium-poisoned fuel pin into the

central lattice position, on the other hand, affects the neutron flux more globally. In the absorber pin itself, the total fission rate is calculated correctly by CASMO-4E, but the  $^{238}\text{U}$  capture rate is overestimated by 3.0%. Consequently, the  $C_8/F_{\text{tot}}$  rate is also overestimated (by 2.8%). It is likely that the origin of this discrepancy lies in the CASMO-4E resonance treatment of the particular setup (smaller-diameter Gd-poisoned pin at the center of the assembly).

In brief, following the successful validation of MCNPX for all investigated configurations, CASMO-4E has been shown to correctly predict reaction rate distributions in each of the perturbed cases, with the exception of the  $C_8$  and  $C_8/F_{\text{tot}}$  values measured in the Gd-poisoned fuel pin at the center of the SCWR-like lattice. It is crucial, however, to include the BZ2 card in the CASMO-4E input, in order to correctly treat the axial leakage in situations with a significant leakage gradient across the lattice.

### 9.1.3 Fuel Pin Removal Worths in the Unperturbed Lattice

To provide integral data complementary to the reaction rate distributions, reactivity worth measurements were carried out for four fuel pins in the unperturbed configuration. (Due to the highly symmetrical geometry of the SCWR-like test lattice, there are in fact only three generic fuel pin positions: corners, neighbors, and remotes). In a first step, MCNPX was validated by comparing the reactivity worth predictions using the whole-reactor model. Results agreed within the combined uncertainties of the measurements and the probabilistic calculations, typically  $\sim 10\%$  ( $1\sigma$ ) and mainly due to the relatively large statistical uncertainty on the Monte Carlo results. The latter results from the smallness of the pin removal worths ( $\sim 7$  to  $40$  pcm).

CASMO-4E could not be validated as easily, because the reactivity effect of removing a pin is different in the reduced geometry model and in the experimental situation (or in the whole-reactor model). The approach taken has been to consider the ratio of two pin removal worths. Thus, it could be shown that the results for such reactivity worth ratios obtained with the whole-reactor and reduced geometry MCNPX models agreed within the uncertainties. This, in turn, has justified the direct comparison of pin removal worths derived from the reduced geometry models of CASMO-4E and MCNPX. This comparison yielded differences of 7 to 12 pcm, corresponding to 2.4 to 4.3 standard deviations.

To identify the sources of these differences, a decomposition of the reactivity effects was carried out, using the basic approach followed by Tani [2]. The neutron balances for each fuel pin cell and water region were assessed for the MCNPX and CASMO-4E reduced geometry models, the agreement between the codes being found to lie within the statistical uncertainties of MCNPX. In order to improve the statistical accuracy of the code comparisons, the individual pin cells were grouped according to their position in the lattice (corner, neighbor and remote pins). A consistent trend could then be observed for all the considered pin worths. This is that the discrepancies between CASMO-4E and MCNPX, especially for the better moderated pin positions (neighbor and remote), appear to be linked to the calculation of the additional moderator effect caused by

the pin removal.

#### 9.1.4 PROTEUS $k_{\text{eff}}$ Changes for the Different Configurations

While the fuel pin removal worths discussed above can be viewed as test-lattice specific characteristics, the larger PROTEUS  $k_{\text{eff}}$  changes associated with modifications of the entire test zone are much more complex. This follows from the fact that they involve changes in the coupling between the inner and outer regions of the multi-zone reactor. Nevertheless, the critical conditions of the reactor for the unperturbed and the six perturbed core configurations can be considered as a useful check on the whole-reactor model of MCNPX.

Each PROTEUS configuration was modeled in as much detail as possible to reproduce the critical conditions, and the calculated  $k_{\text{eff}}$  value was compared to the experimental value of unity. It was found that  $k_{\text{eff}}$  is overpredicted from about 300 pcm in the unperturbed configuration to about 800 pcm in the configuration with stainless steel rods inserted.

Besides the bias coming from the uncertainties in nuclear data, the  $k_{\text{eff}}$  overpredictions were shown to be a linear function of the number of fuel pins present in the C-driver in the given configuration. By adjusting the artificial boron-10 content in the graphite of the PROTEUS C-driver and reflector regions - which accounts for the combined neutronics effects of the material irregularities (density variation, water content, impurities) - the predictions for all configurations could be made consistent with a  $k_{\text{eff}}$  value of about 0.99350; the remaining bias could be assumed to be coming mainly from nuclear data.

The approach of considering the ratio of the  $k_{\text{eff}}$  changes for two different PROTEUS configurations (relative to the unperturbed case) was tried out in an attempt to extract information pertaining to the studied perturbations of the SCWR-like lattice. However, the earlier drawn conclusion could be confirmed, namely that the dependency of the whole-reactor  $k_{\text{eff}}$  value on an accurate description of the outer regions, and thereby of the test zone coupling, is too high. This limits the interpretability of SCWR-specific reactivity effects between different PROTEUS configurations to such cases, in which the C-driver loading was not changed.

#### 9.1.5 Transferability of the PROTEUS Experiments to SCWR Design

The transferability of the code validation carried out for the experimental conditions of PROTEUS, to the neutronics conditions of the most recently proposed SCWR power reactor assembly designs has been assessed. The considered assemblies were developed in Japan [3] and in the European Union [4]. The Japanese lattice layout has large moderator channels, which replace an array of 3-by-3 fuel pins and are surrounded by a single row of pins. This is similar to the PROTEUS test lattice. The European layout consists of moderator channels that also replace a 3-by-3 array of fuel pins, but are surrounded by a double row of pins. The other differences



which have been considered for the SCWR assemblies, with respect to the PROTEUS test lattice, include the fact that the water densities in the moderator and coolant channels of the SCWR assemblies are considerably lower under power-reactor conditions. This results in neutron spectra which are much harder than in the PROTEUS test-lattice. Thus, in comparison to the reduced geometry model results for the reference PROTEUS lattice, the values of the integral parameters  $C_8/F_{\text{tot}}$  and  $F_8/F_{\text{tot}}$  were found to be as much as 65% and 80% higher, respectively. This limits the direct transferability of the carried out code validation to the most recent SCWR concepts, when considered under power reactor conditions.

Another point of interest has been to investigate how well CASMO-4E and MCNPX results agree for the two selected SCWR assembly designs. It has been found that the degree of agreement in predicted integral parameters is almost as good as for the PROTEUS test lattice. This provides some indication that the accuracy of the deterministic calculations does not deteriorate markedly when considering power reactor conditions. The predicted  $F_{\text{tot}}$ ,  $C_8$  and  $C_8/F_{\text{tot}}$  pin-wise radial distributions across the European and Japanese SCWR assemblies were also compared between the two codes. For the Japanese assembly design, all the considered distributions agreed within the uncertainties. For the European lattice, the fission distribution agreed very well between the two codes but discrepancies of up to  $\sim 4\%$  were observed for the  $^{238}\text{U}$  capture rate. This difference may be ascribed to the greater sensitivity to the treatment of  $^{238}\text{U}$  resonance capture, when considering the characteristic geometry of the European design with its double rows and columns of fuel pins.

Clearly, the PROTEUS experiments are of generic relevance to the study of LWR lattices with strong moderation heterogeneity. Overall, CASMO-4E and MCNPX have yielded satisfactory agreement not only for the prediction of integral parameters, but also for most of the pin-wise reaction rate distributions in the various SCWR-like configurations investigated. Nevertheless, it is important to remain cautious when using CASMO-4E under spectral conditions, and for SCWR assembly geometries, that differ considerably from those covered by the PROTEUS experiments.

## 9.2 Recommendations for Future Work

In all research, for every question answered, several new questions appear. This has also been the case for the currently presented thesis, and this section gives certain recommendations on possible further research in relation to the conducted experiments, as also in the larger context of developing SCWRs and their associated calculational tools.

### 9.2.1 New Experiments at the PROTEUS Zero-Power Facility

**Experiments Corresponding Closer to Power Reactor Conditions** Although the code validation carried out for CASMO-4E and MCNPX has been very successful for the configurations

investigated in PROTEUS, it has been seen that there are considerable differences in neutron spectra between the PROTEUS reference lattice and the latest SCWR assembly designs under power reactor conditions. One of the features of the experimental setup causing this has been that no distinction was made between coolant and moderator because of the lack of structural materials. New experiments should thus be conducted, in which structures are introduced into the lattice as separator between low density coolant and high density moderator. A coolant with a density comparable to that in an SCWR assembly under power reactor conditions could be simulated by using an appropriate mixture of heavy and light water. The neutron spectrum would become much harder, and code validation would then be achieved for configurations which resemble the power reactor situation more closely.

**Extension of the SCWR Related Database** In order to better qualify the neutronics codes, other types of integral measurements, as well as test zone configurations, should be introduced into the experimental program. Foil measurements, for example, can not only characterize the reaction rates more precisely, but can also be applied to the determination of within-pin radial and azimuthal distributions. The latter are of particular interest, given the heterogeneous layout of SCWR assemblies. Additionally, axial reaction rate distributions should be measured, which is important due to the strongly varying coolant properties along the vertical axis. To simulate the dependence of the coolant density with the height, one could insert plastics with different hydrogen densities or use axially segmented water tanks. Furthermore, experiments could be planned to investigate the effectiveness of alternative control absorber materials.

Besides the extension of the experimental database through the measurement of additional parameters, analytical aspects could be expanded as well. One should focus on alternative deterministic codes which could be validated against the experiments. By doing so, it would become possible to compare the different deterministic treatments (e.g. of  $^{238}\text{U}$  resonance capture).

**Experiments with More Representative SCWR Assembly Designs** As mentioned above, the SCWR-like test lattice configuration investigated currently differs significantly from the lattice layout of one of the currently proposed SCWR assemblies, viz. the European design, due to the double-row geometry employed. A significantly smaller water channel (as compared to the PROTEUS lattice) is surrounded by two rows of fuel pins. Outside this double row, a moderator gap separates the assembly from its neighbors, thus providing thermal neutrons to the outer row of fuel pins, which is not adjacent to the moderator channel in the center. Such a design could be implemented in the PROTEUS test zone. Due to the considerably reduced  $k_{\infty}$  value of the European assembly (1.243, instead of 1.476 for the current PROTEUS test lattice), the entire test zone could be filled with such a lattice arrangement without jeopardizing the operational limits of the PROTEUS reactor.

There are, of course, other advantages of having a larger test zone in PROTEUS. The SCWR-specific neutron spectrum would extend further out radially, making it possible to implement

other types of experiments (e.g. in relation to control rod worths) more easily.

### 9.2.2 Other Aspects

**Clarification of PROTEUS Graphite Specifications** It has been seen that the whole-reactor calculations with MCNPX, using the current specifications for the graphite regions of PROTEUS, overestimate  $k_{\text{eff}}$  by  $\sim 300$  pcm to 800 pcm depending on the studied configuration. The overestimation was demonstrated to be linearly correlated to the number of fuel pins loaded into the C-driver. By adjusting the value of the equivalent boron-10 concentration to account for the graphite impurities, one was able to correct the overestimation of the C-driver fuel pin worths. The resulting boron-10 concentration, however, is 3 to 4 times larger than that assumed so far, which appears to be in contradiction with the past measurements. To clarify the situation, two actions are recommended for the future:

1. Past PROTEUS configurations, with different numbers of C-driver and D<sub>2</sub>O fuel pins [5], need to be investigated to confirm that the  $k_{\text{eff}}$  predictions of the MCNPX whole-reactor model are still linearly correlated with the number of loaded C-driver pins and that the boron concentration determined in this work corrects for this linear trend.
2. New measurements should be carried out for different representative blocks of the PROTEUS graphite. This would allow one to determine the equivalent boron concentration necessary to simulate the graphite zone properties properly, i.e. in correspondence to the current positioning of the individual graphite blocks.

**CASMO-4E Overestimation of  $C_8$  in the Gd-poisoned Fuel Pin** As noted above, CASMO-4E predictions of reaction rate distributions have been found - via reduced geometry comparisons for the various configurations - to be generally in good agreement with MCNPX. One exception has been the  $^{238}\text{U}$  capture rate in the gadolinium-poisoned fuel pin introduced into the central position of the reference lattice. While the MCNPX whole-reactor calculation yielded agreement with experiment within the  $1\sigma$  uncertainty, the comparison between the reduced geometry models showed that CASMO-4E overestimates  $C_8$  in the Gd-poisoned pin by  $\sim 3\%$ . This overestimation can be attributed to several aspects of the experimental setup. Thus, for example, the Gd-pin employed had a diameter  $\sim 20\%$  smaller than the other pins, and was positioned at an intersection of rows and columns of fuel pins. It is assumed that the discrepancy stems from the resonance treatment of the fuel pin by the deterministic code. However, this hypothesis needs to be verified.

**Neutronics / Thermal-Hydraulics Coupling** The validation of the neutronics design of an advanced reactor concept, such as the SCWR, clearly needs to go hand-in-hand with corresponding efforts on the thermal-hydraulics side. The latter aspects are very challenging for the SCWR,

considering the large coolant density changes in the core, as also the multiple flow paths foreseen for the fluid (see Subsec. 2.2.2).

Once both types of calculational tools, i.e. neutronics and thermal-hydraulics, have been adequately validated from the viewpoint of static behavior, the safety case for an SCWR prototype would need to consider the validation of reactor dynamics calculations. Here, experiments would be needed to validate the complex neutronics / thermal-hydraulics coupling that, via reactivity feedback effects, determines the power evolution during hypothetical reactor transients. Such experiments would clearly have to be conducted in facilities other than of the type represented by PROTEUS.

# Bibliography

- [1] F. Jatuff, K. Macku, and R. Chawla. On the accuracy of reactor physics calculations for square HPLWR fuel assemblies. *Annals of Nuclear Energy*, 33:198–207, 2006.
- [2] F. Tani. *Decomposition Analysis of Reactivity Effect Predictions for Modern LWR Fuel*. PhD thesis, École Polytechnique Fédérale de Lausanne, 2006.
- [3] K. Kamei, A. Yamaji, Y. Ishiwatari, Y. Oka, and J. Liu. Fuel and Core Design of Super Light Water Reactor with Low Leakage Fuel Loading Pattern. *Journal of Nuclear Science and Technology*, 43(2):129–139, 2006.
- [4] K. Fischer, T. Schulenberg, and E. Laurien. Design of a Supercritical Water-Cooled Reactor with a Three-Pass Core Arrangement. *Nuclear Engineering and Design*, 239:800–812, 2009.
- [5] M. Plaschy, M. Murphy, F. Jatuff, G. Perret, R. Seiler, and R. Chawla. Validation of Monte Carlo Predictions of LWR-PROTEUS Safety Parameters Using an Improved Whole-Reactor Model. *Annals of Nuclear Energy*, 39:1536–1543, 2009.



# Appendix A: Reduced Geometry Input Decks for the Unperturbed Configuration

## A.1 CASMO-4E Input

```
* Standard input file for CASMO calculations related to the Ph.D. work
* of D. Rätz (Experiments at PROTEUS)
* SCWR-like lattice, south-east quadrant
* Date: 2010 12 17, dominik.raetz@psi.ch
```

```
TTL * SEG SCWR square lattice, driver fuel rods, DHO mixture
```

```
TFU=293 TMO=293
```

```
PWR 21 1.3400 28.610 0.0000 0.0000 0.0000 0.0000 4 1
```

```
COO 1.0351 / 1001=4.49E22, 1002=2.19E22, 8000=3.34E22 * In-channel
```

```
CAN 1.8628 / 13000=100.0 * Aluminum clad smeared
```

```
* out with "vacuum gap"
```

```
FUE 1 10.3298 / 5.00
```

```
* 5% enriched UO2 fuel
```

```
PIN 1 0.50900 0.61000 / '1' 'CAN'
```

```
PIN 2 0.50900 0.61000 / 'COO' 'COO'
```

```
LPI
```

```
1 1 1 1 1 1 1 1 1 1 1
1 2 2 2 2 1 2 2 2 2 1
1 2 2 2 2 1 2 2 2 2 1
1 2 2 2 2 1 2 2 2 2 1
1 2 2 2 2 1 2 2 2 2 1
1 2 2 2 2 1 2 2 2 2 1
1 1 1 1 1 1 1 1 1 1 1
1 2 2 2 2 1 2 2 2 2 1
1 2 2 2 2 1 2 2 2 2 1
1 2 2 2 2 1 2 2 2 2 1
1 2 2 2 2 1 2 2 2 2 1
1 2 2 2 2 1 2 2 2 2 1
1 1 1 1 1 1 1 1 1 1 1
```

PDE 0.001	* power density
THE=0	* No thermal expansion
XEN 0	* Xe free
XPO 'FISS' 'POW' / 'OUT'	* power rate maps
QUA 'NEU' /,,,0.02/,,,0.02/,,,0.02	* refine mesh of characteristics
FRR 92235 92238 92234	* reaction rate maps
AVE 'CELL' / 1 0 0 1	
RRI	* reaction rates for isotopes
RRX 1001 1002 8000 13000 92238	* microzone reaction rates
MND 92235 92238	* number density maps
DEP 0	* depletion (burnup) points
STA	
END	



## A.2 MCNPX Input

```

*** Core III.4 Calculation reduced geometry PhD Thesis ***
c square fuel assembly with 4x4 water canals,
c and driver fuel rods (5w% enriched, Al cladding)
c Symmetry: 1/4 of assembly, S-E sector
c Date: 2010 12 03, Dominik Rätz
c Total height = 26.324 cm
c
c Driver Fuel Rod Universe
01 1 6.925466-2 -1 -75 74 u=1 imp:n=1 $ UO2 5.00% U5
02 1 6.925466-2 (-1 -74):(-1 75) u=1 imp:n=1 $ UO2 5.00% U5
04 4 4.15336-2 +1 -3 u=1 imp:n=1 $ Al clad
05 5 1.002-1 +3 u=1 imp:n=1 $ DHO mixture
c
c Assembly gaps
10 5 1.002-1 +21 -33 -52 +53 +61 -73 imp:n=1 $ South mixture gap
11 5 1.002-1 +32 -33 -41 +52 +61 -73 imp:n=1 $ East mixture gap
c
c c Lattice (1/4 square fuel assembly) definition: water canals
15 5 1.002-1 +22 -26 -42 +46 +61 -73 imp:n=1 $ NW water canal
16 5 1.002-1 +27 -31 -42 +46 +61 -73 imp:n=1 $ NE water canal
17 5 1.002-1 +22 -26 -47 +51 +61 -73 imp:n=1 $ SW water canal
18 5 1.002-1 +27 -31 -47 +51 +61 -73 imp:n=1 $ SE water canal
c
c Lattice (1/4 square fuel assembly) definition: fuel cells
21 0 +21 -22 -41 +42 +61 -73 fill=1 (0.000 0.000 0.0) imp:n=1 $ A1
22 0 +22 -23 -41 +42 +61 -73 fill=1 (1.340 0.000 0.0) imp:n=1 $ B1
23 0 +23 -24 -41 +42 +61 -73 fill=1 (2.680 0.000 0.0) imp:n=1 $ C1
24 0 +24 -25 -41 +42 +61 -73 fill=1 (4.020 0.000 0.0) imp:n=1 $ D1
25 0 +25 -26 -41 +42 +61 -73 fill=1 (5.360 0.000 0.0) imp:n=1 $ E1
26 0 +26 -27 -41 +42 +61 -73 fill=1 (6.700 0.000 0.0) imp:n=1 $ F1
27 0 +27 -28 -41 +42 +61 -73 fill=1 (8.040 0.000 0.0) imp:n=1 $ G1
28 0 +28 -29 -41 +42 +61 -73 fill=1 (9.380 0.000 0.0) imp:n=1 $ H1
29 0 +29 -30 -41 +42 +61 -73 fill=1 (10.72 0.000 0.0) imp:n=1 $ I1
30 0 +30 -31 -41 +42 +61 -73 fill=1 (12.06 0.000 0.0) imp:n=1 $ J1
31 0 +31 -32 -41 +42 +61 -73 fill=1 (13.40 0.000 0.0) imp:n=1 $ K1
c
32 0 +21 -22 -42 +43 +61 -73 fill=1 (0.000 -1.340 0.0) imp:n=1 $ A2
33 0 +26 -27 -42 +43 +61 -73 fill=1 (6.700 -1.340 0.0) imp:n=1 $ F2
34 0 +31 -32 -42 +43 +61 -73 fill=1 (13.40 -1.340 0.0) imp:n=1 $ K2
35 0 +21 -22 -43 +44 +61 -73 fill=1 (0.000 -2.680 0.0) imp:n=1 $ A3
36 0 +26 -27 -43 +44 +61 -73 fill=1 (6.700 -2.680 0.0) imp:n=1 $ F3
37 0 +31 -32 -43 +44 +61 -73 fill=1 (13.40 -2.680 0.0) imp:n=1 $ K3
38 0 +21 -22 -44 +45 +61 -73 fill=1 (0.000 -4.020 0.0) imp:n=1 $ A4
39 0 +26 -27 -44 +45 +61 -73 fill=1 (6.700 -4.020 0.0) imp:n=1 $ F4
40 0 +31 -32 -44 +45 +61 -73 fill=1 (13.40 -4.020 0.0) imp:n=1 $ K4
41 0 +21 -22 -45 +46 +61 -73 fill=1 (0.000 -5.360 0.0) imp:n=1 $ A5
42 0 +26 -27 -45 +46 +61 -73 fill=1 (6.700 -5.360 0.0) imp:n=1 $ F5
43 0 +31 -32 -45 +46 +61 -73 fill=1 (13.40 -5.360 0.0) imp:n=1 $ K5
c

```

```

44  0  +21 -22 -46 +47 +61 -73 fill=1 (0.000 -6.700 0.0) imp:n=1 $ A6
45  0  +22 -23 -46 +47 +61 -73 fill=1 (1.340 -6.700 0.0) imp:n=1 $ B6
46  0  +23 -24 -46 +47 +61 -73 fill=1 (2.680 -6.700 0.0) imp:n=1 $ C6
47  0  +24 -25 -46 +47 +61 -73 fill=1 (4.020 -6.700 0.0) imp:n=1 $ D6
48  0  +25 -26 -46 +47 +61 -73 fill=1 (5.360 -6.700 0.0) imp:n=1 $ E6
49  0  +26 -27 -46 +47 +61 -73 fill=1 (6.700 -6.700 0.0) imp:n=1 $ F6
50  0  +27 -28 -46 +47 +61 -73 fill=1 (8.040 -6.700 0.0) imp:n=1 $ G6
51  0  +28 -29 -46 +47 +61 -73 fill=1 (9.380 -6.700 0.0) imp:n=1 $ H6
52  0  +29 -30 -46 +47 +61 -73 fill=1 (10.72 -6.700 0.0) imp:n=1 $ I6
53  0  +30 -31 -46 +47 +61 -73 fill=1 (12.06 -6.700 0.0) imp:n=1 $ J6
54  0  +31 -32 -46 +47 +61 -73 fill=1 (13.40 -6.700 0.0) imp:n=1 $ K6
c
55  0  +21 -22 -47 +48 +61 -73 fill=1 (0.000 -8.040 0.0) imp:n=1 $ A7
56  0  +26 -27 -47 +48 +61 -73 fill=1 (6.700 -8.040 0.0) imp:n=1 $ F7
57  0  +31 -32 -47 +48 +61 -73 fill=1 (13.40 -8.040 0.0) imp:n=1 $ K7
58  0  +21 -22 -48 +49 +61 -73 fill=1 (0.000 -9.380 0.0) imp:n=1 $ A8
59  0  +26 -27 -48 +49 +61 -73 fill=1 (6.700 -9.380 0.0) imp:n=1 $ F8
60  0  +31 -32 -48 +49 +61 -73 fill=1 (13.40 -9.380 0.0) imp:n=1 $ K8
61  0  +21 -22 -49 +50 +61 -73 fill=1 (0.000 -10.72 0.0) imp:n=1 $ A9
62  0  +26 -27 -49 +50 +61 -73 fill=1 (6.700 -10.72 0.0) imp:n=1 $ F9
63  0  +31 -32 -49 +50 +61 -73 fill=1 (13.40 -10.72 0.0) imp:n=1 $ K9
64  0  +21 -22 -50 +51 +61 -73 fill=1 (0.000 -12.06 0.0) imp:n=1 $ A10
65  0  +26 -27 -50 +51 +61 -73 fill=1 (6.700 -12.06 0.0) imp:n=1 $ F10
66  0  +31 -32 -50 +51 +61 -73 fill=1 (13.40 -12.06 0.0) imp:n=1 $ K10
c
67  0  +21 -22 -51 +52 +61 -73 fill=1 (0.000 -13.40 0.0) imp:n=1 $ A11
68  0  +22 -23 -51 +52 +61 -73 fill=1 (1.340 -13.40 0.0) imp:n=1 $ B11
69  0  +23 -24 -51 +52 +61 -73 fill=1 (2.680 -13.40 0.0) imp:n=1 $ C11
70  0  +24 -25 -51 +52 +61 -73 fill=1 (4.020 -13.40 0.0) imp:n=1 $ D11
71  0  +25 -26 -51 +52 +61 -73 fill=1 (5.360 -13.40 0.0) imp:n=1 $ E11
72  0  +26 -27 -51 +52 +61 -73 fill=1 (6.700 -13.40 0.0) imp:n=1 $ F11
73  0  +27 -28 -51 +52 +61 -73 fill=1 (8.040 -13.40 0.0) imp:n=1 $ G11
74  0  +28 -29 -51 +52 +61 -73 fill=1 (9.380 -13.40 0.0) imp:n=1 $ H11
75  0  +29 -30 -51 +52 +61 -73 fill=1 (10.72 -13.40 0.0) imp:n=1 $ I11
76  0  +30 -31 -51 +52 +61 -73 fill=1 (12.06 -13.40 0.0) imp:n=1 $ J11
77  0  +31 -32 -51 +52 +61 -73 fill=1 (13.40 -13.40 0.0) imp:n=1 $ K11
c
100 0  -21:33:41:-53:-61:73      imp:n=0          $ out of the real world
c
c
c          ++++++ first empty line++++++
1      cz  0.5090      $ driver fuel rod pellet outer radius
3      cz  0.6100      $ driver fuel rod clad outer radius
c
c  11      cz  1.296033 $ inner radius guide tube
c  12      cz  1.396033 $ outer radius guide tube
c  13      cz  0.6980165 $ radius of absorber rod
c
*21    px      0.000    $ box containing the system
*33    px      14.305
*41    py      0.000
*53    py     -14.305
61     pz     -13.162
73     pz      13.162
74     pz     -8.000    $ Planes for tally
75     pz      8.000    $ Planes for tally

```

```

c
22    px    0.6700
23    px    2.0100
24    px    3.3500
25    px    4.6900
26    px    6.0300
27    px    7.3700
28    px    8.7100
29    px    10.0500
30    px    11.3900
31    px    12.7300
32    px    14.0700
c
42    py    -0.6700
43    py    -2.0100
44    py    -3.3500
45    py    -4.6900
46    py    -6.0300
47    py    -7.3700
48    py    -8.7100
49    py    -10.0500
50    py    -11.3900
51    py    -12.7300
52    py    -14.0700
c
c          ++++++++ 2nd blank line follows ++++++++

c      UO2 5% enriched D2O&C zone   driver rods (from table-4 TM-41-98-07)
m1      92235.70c 1.1613-3
        92238.70c 2.1878-2
        13027.70c 1.37360-4
        8016.70c 4.6078-2
c      Al-cladding
m4      13027.70c 4.15336-2
c
c -- d2o-h20 mixture Phase II (private communication: Mr. Peter Grimm)
m5      1001.70c 4.49E-02
        1002.70c 2.19E-02
        8016.70c 3.34E-02 $ New for III-4 32.8%
mt5     lwtr.70t hwtr.70t
c
c      Materials for tally purposes
m35     92235.70c 1.0  $ U235 for tallies
m38     92238.70c 1.0  $ U238 for tallies
c
c
mode     n
kcode    1500000    1.0    30    1030
ksrc      0.000    0.000 0.0 1.340    0.000 0.0 2.680    0.000 0.0
          4.020    0.000 0.0 5.360    0.000 0.0 6.700    0.000 0.0
          8.040    0.000 0.0 9.380    0.000 0.0 10.72    0.000 0.0
          12.06    0.000 0.0 13.40    0.000 0.0 0.000   -1.340 0.0
          6.700   -1.340 0.0 13.40   -1.340 0.0 0.000   -2.680 0.0
          6.700   -2.680 0.0 13.40   -2.680 0.0 0.000   -4.020 0.0
          6.700   -4.020 0.0 13.40   -4.020 0.0 0.000   -5.360 0.0
          6.700   -5.360 0.0 13.40   -5.360 0.0 0.000   -6.700 0.0
          1.340   -6.700 0.0 2.680   -6.700 0.0 4.020   -6.700 0.0

```

```

5.360 -6.700 0.0 6.700 -6.700 0.0 8.040 -6.700 0.0
9.380 -6.700 0.0 10.72 -6.700 0.0 12.06 -6.700 0.0
13.40 -6.700 0.0 0.000 -8.040 0.0 6.700 -8.040 0.0
13.40 -8.040 0.0 0.000 -9.380 0.0 6.700 -9.380 0.0
13.40 -9.380 0.0 0.000 -10.72 0.0 6.700 -10.72 0.0
13.40 -10.72 0.0 0.000 -12.06 0.0 6.700 -12.06 0.0
13.40 -12.06 0.0 0.000 -13.40 0.0 1.340 -13.40 0.0
2.680 -13.40 0.0 4.020 -13.40 0.0 5.360 -13.40 0.0
6.700 -13.40 0.0 8.040 -13.40 0.0 9.380 -13.40 0.0
10.72 -13.40 0.0 12.06 -13.40 0.0 13.40 -13.40 0.0

c
print 40
c -30 -50 -70 -72 -85 -98 -100 -110 -120 -126 -130
c -140 -160 -161 -162 -175
c
c **** n tallies for capture and fission rate calculations ****
c Total absorption = -2
c Total fission = -6
c fission x v = (-6 -7)
c capture = 102
c n-heat deposition =106
c
c *** tallies in NW subbundle ***
f14:n (1 < 21 ) $ A1
(1 < 22 ) $ B1
(1 < 23 ) $ C1
(1 < 24 ) $ D1
(1 < 25 ) $ E1
(1 < 26 ) $ F1
(1 < 27 ) $ G1
(1 < 28 ) $ H1
(1 < 29 ) $ I1
(1 < 30 ) $ J1
(1 < 31 ) $ K1
(1 < 32 ) $ A2
(1 < 33 ) $ F2
(1 < 34 ) $ K2
(1 < 35 ) $ A3
(1 < 36 ) $ F3
(1 < 37 ) $ K3
(1 < 38 ) $ A4
(1 < 39 ) $ F4
(1 < 40 ) $ K4
(1 < 41 ) $ A5
(1 < 42 ) $ F5
(1 < 43 ) $ K5
(1 < 44 ) $ A6
(1 < 45 ) $ B6
(1 < 46 ) $ C6
(1 < 47 ) $ D6
(1 < 48 ) $ E6
(1 < 49 ) $ F6
(1 < 50 ) $ G6
(1 < 51 ) $ H6
(1 < 52 ) $ I6
(1 < 53 ) $ J6
(1 < 54 ) $ K6

```

```
(1 < 55 ) $ A7
(1 < 56 ) $ F7
(1 < 57 ) $ K7
(1 < 58 ) $ A8
(1 < 59 ) $ F8
(1 < 60 ) $ K8
(1 < 61 ) $ A9
(1 < 62 ) $ F9
(1 < 63 ) $ K9
(1 < 64 ) $ A10
(1 < 65 ) $ F10
(1 < 66 ) $ K10
(1 < 67 ) $ A11
(1 < 68 ) $ B11
(1 < 69 ) $ C11
(1 < 70 ) $ D11
(1 < 71 ) $ E11
(1 < 72 ) $ F11
(1 < 73 ) $ G11
(1 < 74 ) $ H11
(1 < 75 ) $ I11
(1 < 76 ) $ J11
(1 < 77 ) $ K11
fm14  (1.0 35 (102) (-6)) $ U235 with unity numb. density
      (1.0 38 (102) (-6)) $ U238 with unity numb. density
c
e0    15.0
c
prdmp 70 70 0 2
```



# Acknowledgements

This research was carried out in the Laboratory for Reactor Physics and Systems Behavior (LRS) at the Paul Scherrer Institute (PSI), in the framework of the collaboration between PSI, EPFL and swissnuclear. Although, my name is the only one appearing on the authors list of this thesis, I'm fully aware that it would not have been possible to succeed without extensive help from many other people. I would like to express my most sincere gratitude to all of you and let you all know that I am deeply indebted to you!

- First, I would like to thank my beloved wife Regula and my two daughters Lia and Anina for their love and endless support over the many years of this endeavor. The three of you were my light in the dark and the driving force behind my determination to stay focused on the task. I love you with all my heart!
- I would like to thank Prof. Rakesh Chawla for giving me the opportunity to do this work, for taking me under his wings and directing this thesis, and for spending endless hours editing my work.
- Thank you, Dr. Kelly Jordan, for supervising my work, for supporting me throughout the years. Thank you for many fruitful discussions about scientific and other matters. It has been a pleasure working with you!
- And thank you, Dr. Gregory Perret, for answering many questions, for your dedication to science and work, and for your huge support in whatever matter I brought to you. Also, thank you for an unforgettable night in Interlaken!
- I would also like to thank the former group leaders of the experimental reactor physics group, Dr. Fabian Jatuff and Mike Murphy, who have largely contributed to this thesis. Fabian, thank you for your support even after you left, for your valuable advice in many matters and for your motivating nature. Mike, thank you for sharing your, what seems to me, endless knowledge about PROTEUS and reactor physics experiments. Without you, the ambitious measurement schedule could not have been kept.
- Thank you, Dr. Oliver Köberl, for allowing me to perform the experiments in your reactor and for many discussions on various subjects. Also, please accept my apologies for literally stepping on your toes.

- And thank you, Mr. Grimm, for sharing your profound knowledge of CASMO-4E, for answering many questions, and for helping to solve key problems in my work.
- I would like to thank the operational staff of PROTEUS, Markus Fassbind, Manfred Zimmermann, and Alex Stephan, for providing a fully functioning reactor and for the endless hours of your work during the experimental campaigns.
- I would also like to thank Prof. Olivier Schneider, Dr. Fabiàn Jatuff, and Prof. Gérald Rimpault for accepting to form the jury for this thesis.
- Last, but most certainly not least, I would like to thank my parents - my own, as well as my in-laws - for their all-round support not only during the doctoral work, but during my entire education. Thank you for making it all possible!



# Curriculum Vitæ

Dominik Rätz  
Mattenstrasse 3  
CH-4410 Liestal  
Mobile: +41 79 405 21 85  
Email: dominik.raetz@psi.ch

born, October 4<sup>th</sup>, 1982  
married  
Swiss



---

## Education

- Ph.D. studies at the Doctoral School of the Swiss Federal Institute of Technology, Lausanne (EPFL) December 2011
- Master of Science in Physics from the Swiss Federal Institute of Technology, Zurich (ETHZ); major in Reactor Physics March 2008
- General qualification in Mathematics for university entrance from Liestal High School; received mathematics award December 2002

## Professional Experience

- Ph.D. research at the Paul Scherrer Institute (PSI), Villigen, on “Neutronics Experiments and Analysis Related to Strong Moderation Heterogeneity in LWRs”; directed by Prof. R. Chawla March 2008–  
March 2011
  - Planning and execution of reactor physics experiments
  - Preparation and analysis of the obtained results
  - Probabilistic and deterministic calculations and comparison with experimental results (validation of the computer codes)
- Diploma thesis in Physics at the Paul Scherrer Institute (PSI), Villigen, on “Sub-mm Membrane Resistance in Polymer Electrolyte Fuel Cells,” supervised by M. Reum und Dr. F. Büchi October 2007–  
January 2008

- Internship at Swiss Federal Institute of Technology, Zurich: October 2006–  
“Feasibility study for fast gamma-tomography,” supervised by February 2007  
Prof. H.M. Prasser
- Paul Scherrer Institute (PSI), Villigen: Seven months February–  
internship in particle physics, including experiments at August 2003  
Villigen and at Grenoble, France; supervised by Dr. Klaus  
Kirch

## Publications

- D. Rätz, K.A. Jordan, A.-S. Bayard, G. Perret, and R. Spring 2012  
Chawla, “*Experimental investigation of moderator density  
variation effects in an SCWR-like fuel lattice*,” **Nuclear  
Engineering and Design**, Article under review, 2011
- D. Rätz, K.A. Jordan, G. Perret, and R. Chawla, November 2011  
“*Experimental Validation of Control Rod Related  
Perturbations of Moderator Regions in an SCWR-Like Fuel  
Lattice*,” **Annals of Nuclear Energy** **38**, p.2319-2332, 2011
- D. Rätz, K.A. Jordan, M.F. Murphy, G. Perret, and R. April 2011  
Chawla, “*Comparison of Measured and Calculated Reaction  
Rate Distributions in an SCWR-Like Test Lattice*,” **Annals  
of Nuclear Energy** **38**, p. 794-801, 2011
- D. Rätz, K.A. Jordan, and R. Chawla, “*Comparison Between October 2010  
Calculations and Experiments for an SCWR-Like Fuel  
Lattice with Perturbed Moderator Regions*,” **Proceedings of  
SNA + MC 2010**, Tokyo, Japan, October 17-21, 2010
- D. Rätz, “*Calculation/Experiment Comparison for an “LWR” May 2010  
Lattice with Strongly Heterogeneous Moderation*,” **PSI NES  
Ph.D. Day 2010**, Villigen-PSI, Switzerland, May 26, 2010  
**Best Paper award received**
- D. Rätz, K.A. Jordan, M.F. Murphy, G. Perret, and R. May 2010  
Chawla, “*Experimental Validation of Reaction Rate  
Distributions in an SCWR-Like Fuel Lattice at PROTEUS*,”  
**Proceedings of PHYSOR 2010**, Pittsburgh,  
Pennsylvania, USA, May 9-14, 2010
- D. Rätz, “*Neutronics Experiments Related to Strong June 2009  
Moderation Heterogeneity in LWRs*,” **PSI NES Ph.D. Day  
2009**, Villigen-PSI, Switzerland, June 16, 2009  
**Best Paper award received**
- K. Kirch, D. Rätz et al., “*An apparatus for the investigation July 2004  
of solid D<sub>2</sub> with respect to ultra-cold neutron sources*,”  
**Nuclear Instruments & Methods in Physics Research  
A533**, p. 491-504, 2004